UNIVERSITY OF AMSTERDAM

UvA-DARE (Digital Academic Repository)

Spatial, temporal and functional analysis of brain damage after microembolization

Georgakopoulou, T.

Publication date
2023

Document Version
Final published version

Link to publication

Citation for published version (APA):
Georgakopoulou, T. (2023). *Spatial, temporal and functional analysis of brain damage after microembolization*. [Thesis, fully internal, Universiteit van Amsterdam].

General rights
It is not permitted to download or to forward/distribute the text or part of it without the consent of the author(s) and/or copyright holder(s), other than for strictly personal, individual use, unless the work is under an open content license (like Creative Commons).

Disclaimer/Complaints regulations
If you believe that digital publication of certain material infringes any of your rights or (privacy) interests, please let the Library know, stating your reasons. In case of a legitimate complaint, the Library will make the material inaccessible and/or remove it from the website. Please Ask the Library: https://uba.uva.nl/en/contact, or a letter to: Library of the University of Amsterdam, Secretariat, Singel 425, 1012 WP Amsterdam, The Netherlands. You will be contacted as soon as possible.

UvA-DARE is a service provided by the library of the University of Amsterdam (https://dare.uva.nl)

Download date:31 Aug 2023

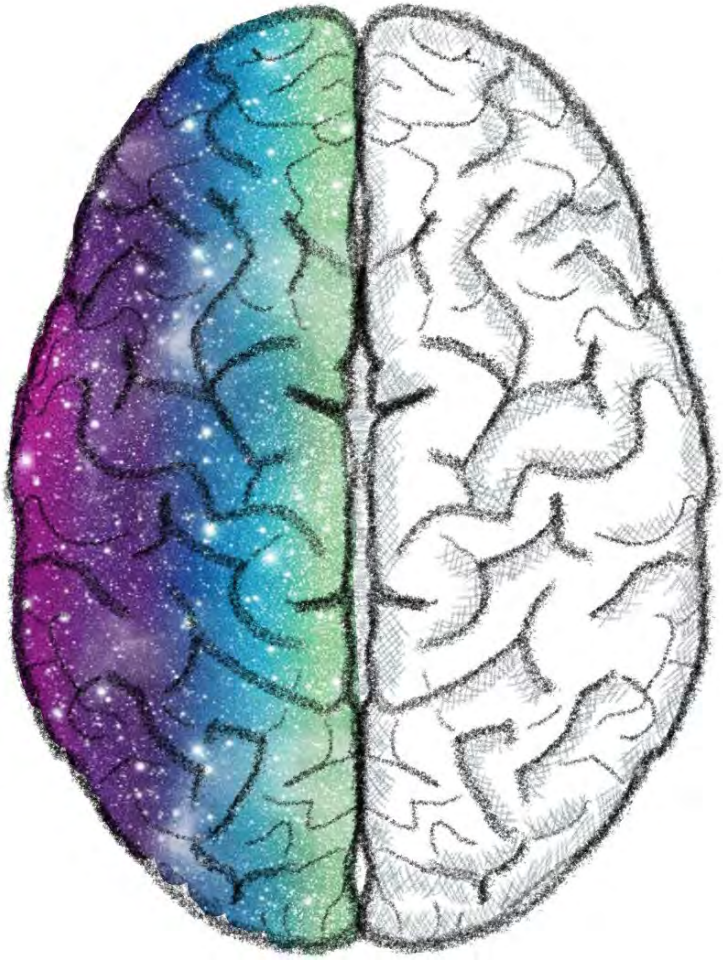

Spatial, temporal and functional analysis of brain damage after microembolization

Theodosia Georgakopoulou

Οξείες Οδύνες του Εγκεφάλου

"Ετέρη νούσος ην ύδωρ επί τω εγκεφάλω γένηται, οδύνη οξείη ίσχει διά του βρέγματος και των κροτάφων άλλοτε άλλη, και ρίγος και πυρετός άλλοτε και άλλοτε, και τας χώρας των οφθαλμών αλγέει, και αμβλυώσσει, και η κόρη σχίζεται, και δοκέει εκ του ενός δύο οράν... και ην αναστή, σκοτοδινίη μιν λαμβάνει... και τα ώτα τέτριγε... και εμέει σίελα και λάπην, ενιότε δε και τα σιτία" (1).

Acute brain suffering

"There is also another disease, which appears with a concentration of fluids within the brain, acute strong pain in temporal and/or parietal lobe area, with a simultaneously appearance of shivering and fever in waves. The patient feels a kind of anguish pain in the area of his eyes, his vision is afflicted, the eye pupil is divided and he thinks that he sees two objects instead of one. When he attempts to rise from his position he is conquered by vertigo, his ears bell, he vomits, while sometimes looses saliva, phlegm, and aliments" (1).

Hippocrates over "stroke"

1. Tsoucalas, G., Papaioannou, T. G. & Karamanou, M. The Hippocratic Doctrine of "the Acute Brain Suffering" as the Brain Stroke. *Journal of Stroke and Cerebrovascular Diseases* **28, 412-417 (2019).**

ISBN: 978-94-6469-369-0

The studies described in this thesis were carried out at the department of Biomedical Engineering and Physics of the Amsterdam UMC, location Academic Medical Center (AMC), University of Amsterdam, Amsterdam, The Netherlands. This work was funded by the European Union's Horizon 2020 research and innovation programme, the INSIST project, under grant agreement No777072

Financial support by the Dutch Heart Foundation for the publication of this thesis is gratefully acknowledged. Additional financial support was kindly provided by the Academic Medical Center.

Hartstichting

Cover (front) - Schematic of a human brain. Made in Microsoft 365 - Powerpoint and Paint.
Lay-out and cover design: Theodosia Georgakopoulou
Printing: Proefschrift Maken | www.proefschriftmaken.nl

Copyright © 2023 by T. Georgakopoulou.
All rights reserved. No part of this publication may be reproduced, stored or transmitted in any way without prior permission from the author.

SPATIAL, TEMPORAL AND FUNCTIONAL ANALYSIS OF BRAIN DAMAGE AFTER MICROEMBOLIZATION

ACADEMISCH PROEFSCHRIFT

ter verkrijging van de graad van doctor
aan de Universiteit van Amsterdam
op gezag van de Rector Magnificus
prof. dr. ir. P.P.C.C. Verbeek
ten overstaan van een door het College voor Promoties ingestelde commissie,
in het openbaar te verdedigen in de Agnietenkapel
op vrijdag 7 juli 2023, te 13.00 uur

door Theodosia Georgakopoulou
geboren te KATERINI

PROMOTIECOMMISSIE

Promotores:	prof. dr. A.G.J.M. van Leeuwen	AMC-UvA
	prof. dr. H.A. Marquering	AMC-UvA
Co-promotor:	dr. E.N.T.P. Bakker	AMC-UvA
Overige leden:	prof. dr. ir. A.G. Hoekstra	Universiteit van Amsterdam
	prof. dr. J.D. van Buul	Universiteit van Amsterdam
	dr. J. Coutinho	AMC-UvA
	prof. dr. R.M. Dijkhuizen	Universiteit Utrecht
	dr. ir. J.J. Wentzel	Erasmus MC

Faculteit der Geneeskunde

TABLE OF CONTENTS

Chapter 1	Introduction and scope of the thesis	**7**
Chapter 2	Quantification of hypoxic regions distant from occlusions in cerebral penetrating arteriole trees	**17**
Chapter 3	Quantitative 3D analysis of tissue damage in a rat model of microembolization	**45**
Chapter 4	Recovery of hypoxic regions in a rat model of microembolism	**69**
Chapter 5	Perivascular clearance of blood proteins after blood-brain barrier disruption in a rat model of micro-infarcts	**83**
Chapter 6	Microembolus clearance through angiophagy is an auxiliary mechanism preserving tissue perfusion in the rat brain	**99**
Chapter 7	Extravasation of biodegradable microspheres in the rat brain: a platform for sustained drug delivery?	**125**
Chapter 8	General discussion	**147**
Chapter 9	Summary	**157**
	Samenvatting	**159**
	Author affiliations	**162**
	Portfolio	**166**
	Curriculum vitae	**170**
	Dankwoord	**172**

Chapter 1

INTRODUCTION AND SCOPE OF THE THESIS

INTRODUCTION

The human brain is a complex organ that forms the operation and command center of our body. Besides essential functions such as breathing, heart rate and balance, higher-order capacities like cognition and behavior are all regulated by the brain. By sending electrical signals to peripheral organs and structures, the brain manages to orchestrate and control the human body. The building blocks of the brain are the neurons, which are responsible for the signal transfer and the glial cells, which support the neuronal actions. Provided that nutrients and oxygen are delivered to the brain, the building blocks of the brain communicate and interact with each other. In order to perform its daily tasks, the human brain consumes 20% of the body's glucose and oxygen (1). Since the brain lacks a storage reservoir (2), energy substrates need to be transferred constantly through an intricate network of arteries, arterioles, and highly interconnected capillaries (3). Aging, lack of exercise, cardiovascular conditions or a combination of these factors can eventually hinder or compromise brain perfusion and impair homeostasis. In this thesis, we address the impact of compromised perfusion at the arteriole level and the contribution of recovery mechanisms to homeostasis.

Stroke, thrombectomy and microembolization

Among the cerebrovascular diseases that cause hypoperfusion, the most common is stroke. Stroke forms a major medical issue counting millions of cases globally per year (4). It is a leading cause of disability and death (5) and has an increasing incidence in developing countries (6). Stroke can be broadly classified into acute ischemic stroke (AIS) and hemorrhagic stroke. AIS is caused by a thromboembolic occlusion of a cerebral artery and represents ~71% of all stroke cases worldwide (7). As a result of the vessel occlusion, hypoperfusion and limited oxygenation of the corresponding brain region leads to neuronal cell death and neurological deficits such as hemiparesis (unilateral weakness or loss of strength), hemianaesthesia (unilateral numbness) and aphasia (language impairment).

Due to the limited capacity of the brain to store oxygen and nutrients, time is crucial for the survival of the neuronal and glial cells in case of a stroke. For this reason, AIS patients should be treated within a certain time window (up to 24h) after the manifestation of the symptoms (4, 8). The current therapies of AIS include intravenous thrombolysis by administration of alteplase (rtPA) and thrombectomy; the mechanical removal of the thrombus (Fig. 1). Both therapies aim to reestablish blood flow. RtPA administration within 4.5h of AIS increases the odds of good clinical outcome (Modified ranking scale (mRS) 0–2) by about a third. However, rtPA administration has some critical limitations: (i) it must be administered within a time frame of 4.5h, (ii) it has many contraindications such as recent surgery, active bleeding and coagulation abnormalities (9) and (iii) its effectivity depends on thrombus composition and size (10). In an attempt to improve clinical and functional outcome of AIS patients, intra-arterial thrombolysis and first-generation mechanical thrombectomy devices have been introduced in AIS therapy with limited success (11, 12). Since the incorporation of second-generation thrombectomy devices, such as thrombus aspiration and stent retrievers, a strong improvement in clinical and

functional outcomes of AIS patients has been shown. In particular, the combination of thrombectomy (with second-generation devices) and intravenous thrombolysis within 6h of AIS increases recanalization and functional independence (4).

Despite the technological innovations in AIS treatment (13-15), only a subgroup of properly selected patients benefits from endovascular thrombectomy (16). From the treated patients ~50% show signs of early recovery, but many still fail to reach functional independence within 90 days (17). Poor collateral circulation correlates with poor functional outcome, but collateral status alone cannot explain the discrepancy between successful recanalization and poor clinical outcome (18). There is an urgent need to shed light on other possible factors that contribute to poor recovery.

Like all surgical interventions, thrombectomy is accompanied by a number of risks. During the removal of the thrombus, there is a high risk of vessel wall injury (19) which in turn can cause continuous embolization. In addition, a shower of microemboli might be released to the downstream circulation due to fragmentation of the initial thrombus (Fig. 1) (20, 21). Other sources of microembolization could be the same as the one causing the initial AIS event, such as heart disorders (atrial fibrillation) or upstream atherosclerotic lesions (20). A shower of microemboli that releases into the downstream circulation could potentially cause additional tissue damage, which could partly explain the poor recovery of AIS patients. This thesis lays emphasis on the quantification of local effects caused by multiple micro-occlusions as a consequence of microembolization. Such data could function as a basis for the improvement of medical devices used in thrombectomy or foster alternative strategies.

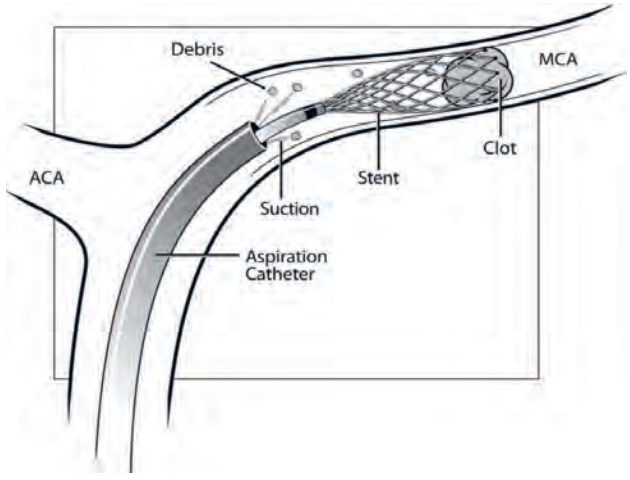

Figure 1. Schematic diagram of thrombectomy, the surgical removal of a thrombus. *Fragmentation of the initial thrombus (debris) is a possible complication. MCA: Middle cerebral artery, ACA: Anterior cerebral artery. This figure is reproduced with permission from T. M. Dumont et al., J Neurointerv Surg. 2014 (22).*

Blood brain barrier permeability and edema clearance

A highly balanced chemical composition of the brain microenvironment is required to secure proper neuronal functioning. Like a filter that allows only a certain size of components to flow through, the mammalian brain possesses such a physical barrier, called the blood brain barrier (BBB). The BBB separates the peripheral circulation from the brain tissue by controlling the substances that enter the brain parenchyma. The discovery of the BBB came from experiments where peripherally injected dyes managed to stain peripheral organs but failed to stain the brain tissue (23). In order to control the entrance of blood components, the BBB consists of highly specialized endothelial cells connected to each other with tight junctions (intercellular adhesion protein complexes) and lacking fenestrations (small pores) (Fig. 2). These characteristics differentiate brain endothelial cells from the "leaky" endothelial cells of the periphery. Owing to these characteristics, they can perform functions such as selective passage of blood components, protection against neurotoxins, neurotransmitter regulation, and maintenance of homeostasis and brain nutrition (24).

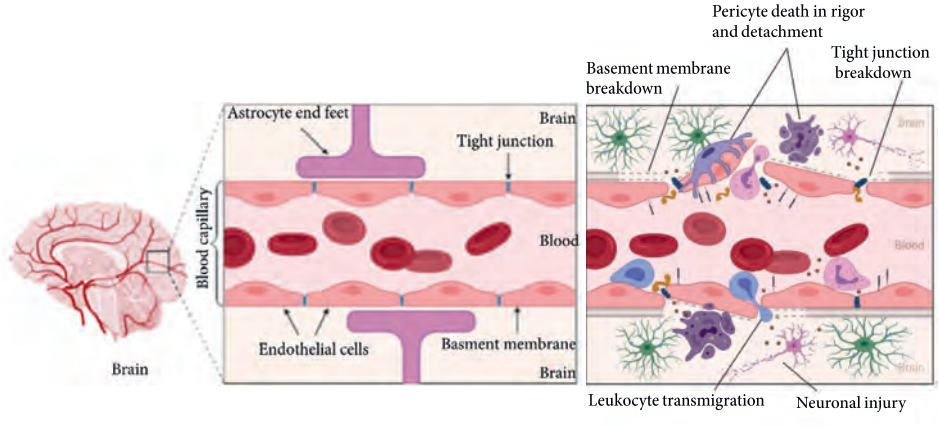

Figure 2. *Schematic diagram of the brain, with the blood brain barrier under physiological (left) and pathological (right) conditions. Left figure reproduced from A. Alahmari, Neural Plasticity. 2021 (25) and right figure adapted from A. Patabendige et al., Int. J. Mol. Sci. 2021 (26).*

Under pathological conditions, BBB impairment leads to extended permeability and therefore dysregulation of the fluid balance in the brain (Fig. 2) (27). BBB disruption is a typical pathological cascade triggered by AIS and is characterized by leakage of blood components (erythrocytes, albumin, immunoglobulin G (IgG), ions) and water into the brain parenchyma. The water and ion imbalance leads in turn to cerebral edema (28, 29). The uncontrolled entrance and accumulation of immune cells further triggers inflammatory responses and aggravates brain injury (30).

To prevent further neuronal damage, the brain has to remove the dead cells, edema and surplus of blood components. The interstitial space of peripheral organs (lungs, muscles etc.) is cleared through the lymphatic system and the produced debris is guided to the

systemic circulation (31). However, the brain lacks lymphatic vessels, but has its own cleaning system; the glymphatic (glia+lymphatic) system. Through an intricate network of pathways, called perivascular spaces, which align the existing cerebral vasculature (32), the brain manages to clean the metabolic waste produced daily (Fig. 3). According to the theory of glymphatics the debris from the interstitial fluid (ISF) in the brain parenchyma is removed through the perivascular spaces (along the vessels) and transferred to the cerebrospinal fluid (CSF), which surrounds the brain and spinal cord (32). The continuous recycling and refreshing of the fluids ensures the clearance of the brain in both physiological and pathological conditions. In the past years, several theories developed regarding the glymphatic flow direction in the ISF, perivascular spaces and CSF, but the fluid movement in the brain is still debated (33-35). In the current thesis, we studied the role of glymphatics in the clearance of IgG after microembolization.

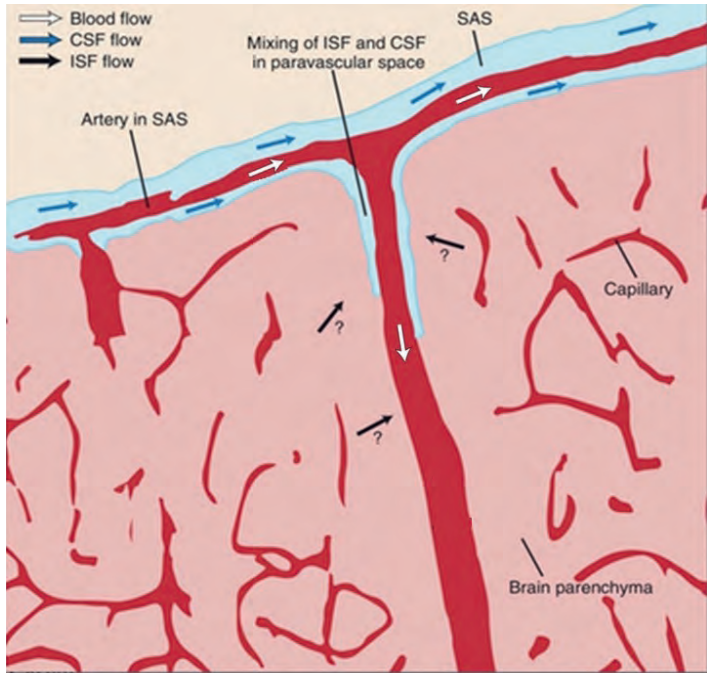

***Figure 3. Schematic diagram of the brain cortex, with a perivascular space surrounding a penetrating artery**. Brain fluids circulate in the brain parenchyma, perivascular space and subarachnoid space (SAS). Since the direction of ISF flow is still debated, question marks were added next to the black arrows. CSF: cerebrospinal fluid, ISF: interstitial fluid. Adapted from E. Bakker et al., Exp Physiol. 2019 (36).*

Reperfusion mechanisms

Our brain has the ability to cope with pathological stimuli such as (micro-)occlusions of cerebral arteri(ol)es to rescue tissue at risk. Micro-occlusions are a result of thromboemboli, or thrombus formation in the vessel wall. To maintain homeostasis after a micro-occlusion, internal protection mechanisms that aim to restore blood flow are recruited. The main mechanism includes the fibrinolytic system, which can resolve a thrombus using an active

enzyme named plasmin and the hemodynamic pressure which facilitates fibrinolysis by pushing and washing out the lysed fragments (37). Because plasmin is fibrin specific, erythrocyte-rich thrombi (10) or cholesterol crystals may be less susceptible to lysis.

In cases of a resistant thrombus, another mechanism may take over. Evidence coming from rodent experiments revealed an until recently unknown mechanism which restores blood flow (37). Angiophagy is the extravasation of the thrombus from the vessel to the brain parenchyma. In an attempt to reestablish tissue perfusion, endothelial cells reorganize, engulf the embolus and remove it to the brain parenchyma. Angiophagy is activated within 24h after multiple occlusions of the cerebral vasculature and depends on the size of the thrombus, thrombus composition and vessel location (37, 38).

In silico trials

This thesis is part of the INSIST (*IN Silico* clinical trials for the treatment of acute Ischemic STroke) consortium, a European multidisciplinary collaboration between research groups (list of INSIST investigators- **Chapter 9**). Using the expertise of various research fields, ranging from clot mechanics and blood flow modelling to thrombectomy simulations and brain tissue pathology, INSIST aims to (partly) replace traditional clinical trials with computer simulated (*in silico*) AIS clinical trials (39). In order to perform *in silico* AIS clinical trials, a virtual population has been made based on real (anonymous) patient data. From this pool, a virtual patient can be selected and a patient-specific virtual clinical trial can take place by clicking on a button. The aim of the trial is to predict the outcome as well as the efficacy of the treatment without using human patients or rodent models. The contribution of the current work to the pipeline of *in silico* clinical trials is the quantification of brain damage following microembolization and the fine-tuning of *in silico* modelling related to tissue perfusion and oxygenation after micro-occlusions.

SCOPE OF THE THESIS

The aim of this thesis is to assess brain tissue damage in terms of ischemia, hypoxia and infarction caused by a shower of microemboli. We quantified the spatial relationship between microsphere position and resulting brain damage in order to map the contribution of microembolization to brain tissue damage following thrombectomy. Recovery mechanisms such as angiophagy and clearance of endogenous IgG were also examined. A better understanding of these processes could lead to improvement of the current thrombectomy medical devices as well as to new therapeutic ways of rescuing tissue at risk by using angiophagy to transfer compounds into the brain parenchyma.

In **chapter 2**, we studied the effects of micro-occlusions on brain tissue using both *in vivo* and *in silico* experiments. In particular, we quantified the relationship between hypoxic regions and occlusion site in cerebral penetrating arterial trees. Spatial analysis in a rat model of microembolization, where 25 μm (in diameter) microspheres were injected into the brain, was compared to computer modelling calculations of *in silico* cerebral cortical columns. In **chapter 3**, we determined the extent of damage on brain

tissue caused by different sizes of microemboli. We quantified the relationship between microspheres and tissue damage using a novel spatial analysis. In a rat model, a mixture of microsphere sizes (15, 25 and 50 µm diameter) was injected in the brain. The intervention hemisphere was partly reconstructed using confocal images and a point-pattern spatial analysis was applied between occlusion site and the hypoxic or infarcted regions. In **chapter 4**, we mapped brain tissue damage over time due to microembolization in terms of ischemia, hypoxia and infarction. The total volume of ischemia, hypoxia and infarction was calculated, and the course of the lesions was monitored for a period of seven days, following microembolization with a mixture of microsphere sizes. In **chapter 5**, the effects of micro-occlusions on perfusion and tissue viability were analyzed 24h post-surgery. In addition clearance of endogenous IgG was evaluated based on histological analysis and confocal imaging. Three groups of rats were injected with microspheres in the brain. Each group received another size of microspheres (15, 25, 50 µm diameter). **Chapter 6** studied angiophagy using both *in vitro* and *in vivo* experiments. Micro-occlusions were introduced by injecting a mixture of microsphere sizes in a rat model and the process of angiophagy was quantified in a course of 7 days. The molecular mechanism behind angiophagy was examined using cell cultures of human (brain) endothelial cells. In **chapter 7**, we evaluated the extent to which the process of angiophagy could be used as a transport medium for therapeutical compounds in the brain parenchyma. Three types of biodegradable microspheres having different characteristics and the same diameter (~13 µm) were injected in the brain. Using immunohistochemistry and confocal microscopy, we evaluated the extravasation rate of biodegradable microspheres and assessed tissue damage 14 days after microembolization. Finally, in **chapter 8** the findings of this thesis and future perspectives are further discussed.

REFERENCES

1. Sokoloff, L. The metabolism of the central nervous system in vivo. *Handbook of physiology, section I, neurophysiology* **3**, 1843-1864 (1960).
2. Tarumi, T. & Zhang, R. PMC5874160; Cerebral blood flow in normal aging adults: cardiovascular determinants, clinical implications, and aerobic fitness. *J. Neurochem.* **144**, 595-608 (2018).
3. Duvernoy, H. M., Delon, S. & Vannson, J. L. Cortical blood vessels of the human brain. *Brain Res. Bull.* **7**, 519-579 (1981).
4. Hankey, G. J. Stroke. *Lancet* **389**, 641-654 (2017).
5. Luengo-Fernandez, R. *et al*. PMC4946627; Population-based study of disability and institutionalization after transient ischemic attack and stroke: 10-year results of the Oxford Vascular Study. *Stroke* **44**, 2854-2861 (2013).
6. Campbell, B. C. V. *et al.* Ischaemic stroke. *Nat Rev Dis Primers* **5**, 70 (2019).
7. Feigin, V. L. *et al*. PMC6247346; Global, Regional, and Country-Specific Lifetime Risks of Stroke, 1990 and 2016. *N. Engl. J. Med.* **379**, 2429-2437 (2018).
8. Beckhauser, M. T. *et al.* Extended Time Window Mechanical Thrombectomy for Acute Stroke in Brazil. *J Stroke Cerebrovasc Dis* **29**, 105134 (2020).
9. Emberson, J. *et al.* PMC4441266; Effect of treatment delay, age, and stroke severity on the effects of intravenous thrombolysis with alteplase for acute ischaemic stroke: a meta-analysis of individual patient data from randomised trials. *Lancet* **384**, 1929-1935 (2014).
10. Wohner, N. *et al.* PMC3339800; Lytic resistance of fibrin containing red blood cells. *Arterioscler. Thromb. Vasc. Biol.* **31**, 2306-2313 (2011).
11. Broderick, J. P. *et al.* PMC3651875; Endovascular therapy after intravenous t-PA versus t-PA alone for stroke. *N. Engl. J. Med.* **368**, 893-903 (2013).

12. Ciccone, A. *et al.* PMC3708480; Endovascular treatment for acute ischemic stroke. *N. Engl. J. Med.* **368**, 904-913 (2013).
13. Hu, Y. C. & Stiefel, M. F. Force and aspiration analysis of the ADAPT technique in acute ischemic stroke treatment. *J Neurointerv Surg* **8**, 244-246 (2016).
14. Nogueira, R. G. *et al.* PMC4176618; Trevo versus Merci retrievers for thrombectomy revascularisation of large vessel occlusions in acute ischaemic stroke (TREVO 2): a randomised trial. *Lancet* **380**, 1231-1240 (2012).
15. Bhaskar, S., Stanwell, P., Cordato, D., Attia, J. & Levi, C. PMC5771207; Reperfusion therapy in acute ischemic stroke: dawn of a new era? *BMC Neurol.* **18**, 8 (2018).
16. Meurer, W. J., Barth, B. E., Gaddis, G., Vilke, G. M. & Lam, S. H. Rapid Systematic Review: Intra-Arterial Thrombectomy ("Clot Retrieval") for Selected Patients with Acute Ischemic Stroke. *J. Emerg. Med.* **52**, 255-261 (2017).
17. Goyal, M. *et al.* Endovascular thrombectomy after large-vessel ischaemic stroke: a meta-analysis of individual patient data from five randomised trials. *Lancet* **387**, 1723-1731 (2016).
18. Leng, X. *et al.* Impact of Collateral Status on Successful Revascularization in Endovascular Treatment: A Systematic Review and Meta-Analysis. *Cerebrovasc. Dis.* **41**, 27-34 (2016).
19. Abraham, P. *et al.* Vessel wall signal enhancement on 3-T MRI in acute stroke patients after stent retriever thrombectomy. *Neurosurg Focus* **42**, E20 (2017).
20. Sheriff, F. *et al.* Microemboli After Successful Thrombectomy Do Not Affect Outcome but Predict New Embolic Events. *Stroke*, Strokeaha119025856 (2019).
21. Farina, F. *et al.* Prognostic Role of Microembolic Signals After Endovascular Treatment in Anterior Circulation Ischemic Stroke Patients. *World Neurosurg* **110**, e882-e889 (2018).
22. Dumont, T. M., Mokin, M., Sorkin, G. C., Levy, E. I. & Siddiqui, A. H. Aspiration thrombectomy in concert with stent thrombectomy. *Journal of NeuroInterventional Surgery* **6**, e26 (2014).
23. Liebner, S., Czupalla, C. J. & Wolburg, H. Current concepts of blood-brain barrier development. *Int. J. Dev. Biol.* **55**, 467-476 (2011).
24. Ballabh, P., Braun, A. & Nedergaard, M. The blood-brain barrier: an overview: structure, regulation, and clinical implications. *Neurobiol. Dis.* **16**, 1-13 (2004).
25. Alahmari, A. Blood-Brain Barrier Overview: Structural and Functional Correlation. *Neural Plast.* **2021**, 6564585 (2021).
26. Patabendige, A., Singh, A., Jenkins, S., Sen, J. & Chen, R. Astrocyte Activation in Neurovascular Damage and Repair Following Ischaemic Stroke. *International Journal of Molecular Sciences* **22**, 4280 (2021).
27. Zhao, Z., Nelson, A. R., Betsholtz, C. & Zlokovic, B. V. PMC4655822; Establishment and Dysfunction of the Blood-Brain Barrier. *Cell* **163**, 1064-1078 (2015).
28. Khatri, R., McKinney, A. M., Swenson, B. & Janardhan, V. Blood-brain barrier, reperfusion injury, and hemorrhagic transformation in acute ischemic stroke. *Neurology* **79**, 52 (2012).
29. Chen, S., Shao, L. & Ma, L. PMC8415457; Cerebral Edema Formation After Stroke: Emphasis on Blood-Brain Barrier and the Lymphatic Drainage System of the Brain. *Front Cell Neurosci* **15**, 716825 (2021).
30. Shi, K. *et al.* Global brain inflammation in stroke. *Lancet Neurol* **18**, 1058-1066 (2019).
31. Liao, S. & Padera, T. P. PMC3780287; Lymphatic function and immune regulation in health and disease. *Lymphat Res Biol* **11**, 136-143 (2013).
32. Iliff, J. J. & Nedergaard, M. PMC3699410; Is there a cerebral lymphatic system? *Stroke* **44**, 93 (2013).
33. Rasmussen, M. K., Mestre, H. & Nedergaard, M. PMC6261373; The glymphatic pathway in neurological disorders. *Lancet Neurol* **17**, 1016-1024 (2018).
34. Abbott, N. J., Pizzo, M. E., Preston, J. E., Janigro, D. & Thorne, R. G. The role of brain barriers in fluid movement in the CNS: is there a 'glymphatic' system? *Acta Neuropathol* **135**, 387-407 (2018).
35. Hladky, S. B. & Barrand, M. A. PMC8815211; The glymphatic hypothesis: the theory and the evidence. *Fluids Barriers CNS* **19**, 9 (2022).
36. Bakker, E., Naessens, D. M. P. & VanBavel, E. PMC6618149; Paravascular spaces: entry to or exit from the brain? *Exp. Physiol.* **104**, 1013-1017 (2019).
37. Grutzendler, J. Angiophagy: mechanism of micro-vascular recanalization independent of the fibrinolytic system. *Stroke* **44**, 84 (2013).
38. van der Wijk, A. E. *et al.* Extravasation of Microspheres in a Rat Model of Silent Brain Infarcts. *Stroke* **50**, 1590-1594 (2019).
39. Konduri, P. R., Marquering, H. A., van Bavel, E. E., Hoekstra, A. & Majoie, C. PMC7525145; In-Silico Trials for Treatment of Acute Ischemic Stroke. *Front Neurol* **11**, 558125 (2020).

Chapter 2

QUANTIFICATION OF HYPOXIC REGIONS DISTANT FROM OCCLUSIONS IN CEREBRAL PENETRATING ARTERIOLE TREES

Yidan Xue[1#], Theodosia Georgakopoulou[2#], Anne-Eva van der Wijk[2], Tamás I. Józsa[1], Ed van Bavel[2§], Stephen J. Payne[1,3§]

[1] Institute of Biomedical Engineering, Department of Engineering Science, University of Oxford, Oxford, UK

[2] Amsterdam UMC, University of Amsterdam, Biomedical Engineering and Physics, Amsterdam Cardiovascular Sciences, Meibergdreef 9, Amsterdam, The Netherlands

[3] Institute of Applied Mechanics, National Taiwan University, Taiwan

[#] These authors are joint first authors

[§] These authors are joint senior authors

PLoS Comput Biol. (2022) 18(8):e1010166

ABSTRACT

The brain function depends on the continuous oxygen supply through the bloodstream inside the microvasculature. Occlusions in the microvascular network will disturb the oxygen delivery in the brain and result in hypoxic tissues that can lead to infarction and cognitive dysfunction. To aid in understanding the formation of hypoxic tissues caused by micro-occlusions in the penetrating arteriole trees, we use rodent experiments and simulations of human vascular networks to study the spatial correlations between the hypoxic regions and the occlusion locations. Our results suggest that hypoxic regions can form distally from the occlusion site, which agrees with the previous observations in the rat brain. These distant hypoxic regions are primarily due to the lack of blood flow in the brain tissues downstream of the occlusion. Moreover, a reasonable agreement of the spatial relationship is found between the experiments and the simulations, which indicates the applicability of *in silico* models to study the effects of microemboli on the brain tissue.

INTRODUCTION

Due to the high metabolic demands and its limited capacity for storage, the mammalian brain depends on near constant cerebral blood flow (CBF) to sustain sufficient nutrient and oxygen delivery (1). Adequate CBF is maintained by the process of cerebral autoregulation (the response of cerebral vessels to blood pressure changes) (2). Based on local neuronal activation (3), tissue oxygenation is ensured by a compact and complex microvascular network of arterioles and capillaries (4).

The acute effects that follow a sudden CBF reduction, such as loss of consciousness in case of a syncope (5) and irreversible neurological damage in case of a cardiac arrest or acute ischemic stroke (AIS) (6, 7), underline the brain's vulnerability to anoxia. Next to global CBF disruption and large vessel occlusion, cerebral micro-infarcts can also lead to detectable brain damage (8). Such micro-infarcts can result from microemboli (9), which can be released into the cerebral circulation under a number of conditions, including atrial fibrillation, unstable plaques (10), or endovascular treatment (the mechanical removal of a thrombus in AIS patients) (11). However, due to the low resolution of brain imaging techniques, cerebral micro-infarcts in humans are mainly discovered only after post-mortem examination.

Evidence of the effects of micro-occlusions on brain tissue thus primarily comes from rodent studies. Such studies have shown that micro-occlusions, formed in response to the intra-arterial injection of microemboli, can lead to multiple regions of ischemia, hypoxia and infarction (12–17), cognitive dysfunction (18, 19), blood brain barrier permeability, astrogliosis and inflammation (20, 21). Using a sophisticated photothrombotic technique which selectively occludes individual penetrating arterioles, Shih et al. (2013) not only monitored the formation and progress of a single microinfarct but also assessed the resulting cognitive deficits (22). Such experiments have also confirmed that arterioles have a poor network of anastomoses (23).

Despite these studies, little quantitative information exists on the relationship between micro-occlusion sites, ischemic territory, and hypoxic area. Given the known vulnerability of penetrating arterioles to obstruction and the distant effects of a single microinfarct on the surrounding tissue (24), it is important to quantify both the extent to which blood vessel architecture affects tissue oxygenation, and how blood vessel architecture and clot location determine the fate of brain tissue viability after blood flow obstruction. A better understanding of brain oxygenation is not only relevant for an improved understanding of the response of the circulation to stimuli but can serve as a starting point for treatment of cerebrovascular diseases (2, 25). For instance, quantitative data on brain tissue damage caused by microemboli could lead to the improvement of medical devices used for post-AIS endovascular treatment.

To this end, numerical models have recently been developed to aid in understanding the structure of cerebral microvasculature (26–35), and the effects of micro-occlusions on blood flow (35–38) and oxygen transport (39, 40). In our previous work, we simulated the oxygen transport in cerebral capillary cubes using the Green's function method (32) and quantified the tissue hypoxia responding to different level of micro-occlusions (40).

However, the penetrating arterioles were not included in the previous model, which limited the length scale that it was able to represent and thus made it difficult to compare predictions to the microembolization experiments (17, 41) that aim at the penetrating arterioles (42).

In the present study, we thus investigated further the effects of micro-occlusions in penetrating arteriole trees (the vessels between the capillaries and the pial circulation) on tissue hypoxia using both experimental and numerical methods. In our animal experiments, we injected 25 μm (in diameter) polystyrene microspheres through the common carotid artery (CCA) of rat models, which led to tissue ischemia and hypoxia. Then we reconstructed part of the intervention hemisphere in each animal and segmented the locations of microspheres and hypoxic regions in a 3D coordinate system. In our simulations, we constructed a number of human cortical column networks, which were then occluded by microspheres of the same size, and the Green's function method was applied to simulate oxygen transport. Two novel distance analyses were conducted to investigate the spatial relationship between hypoxic regions and occlusion sites in both experiments and simulations in an identical manner. This enabled direct comparisons to be made between experimental and numerical results and thus to quantify the relationship between the locations of micro-occlusions and hypoxic regions. These results will be valuable in further understanding the response of cerebral tissue to micro-occlusions.

METHODS

Animal experiments

Ethics statement

All animal experiments were approved by the ethics committee of the University of Amsterdam, Academic Medical Center (permit number: DMF321AA). For the required procedures, the ARRIVE guidelines and European Union guidelines for the care of laboratory animals (Directive 2010/63/EU) were followed.

Animal surgeries

Six Wistar rats (n=6, 50% female, 16-20 weeks old, Charles River) were used. The animals received *ad libitum* food and water and were pair-housed in standard plastic cages with a 12h:12h light-dark cycle. Surgeries were performed exactly as described earlier by Georgakopoulou et al. (2021) (41). Briefly, animals were anesthetized with a mixture of 100% oxygen and isoflurane (Isoflutek 1000 mg/g; Laboratorios Karizoo SA, Barcelona, Spain). After exposure of the left CCA at the bifurcation level, the external carotid artery and occipital artery were temporarily ligated with a surgical suture (size 6.0). To mimic microembolization, 200 μl of fluorescent microspheres (DiagPoly™ Custom made Plain Fluorescent Microparticles, Excitation wavelength 656 nm, Emission wavelength 674 nm, Creative Diagnostics®, Shirley, NY; approximately 5500 microspheres of 25 μm in diameter) resuspended in a sterile 2% bovine serum albumin solution of phosphate buffered saline (PBS), was injected via the left CCA using an insulin syringe (29G) as shown in Fig.

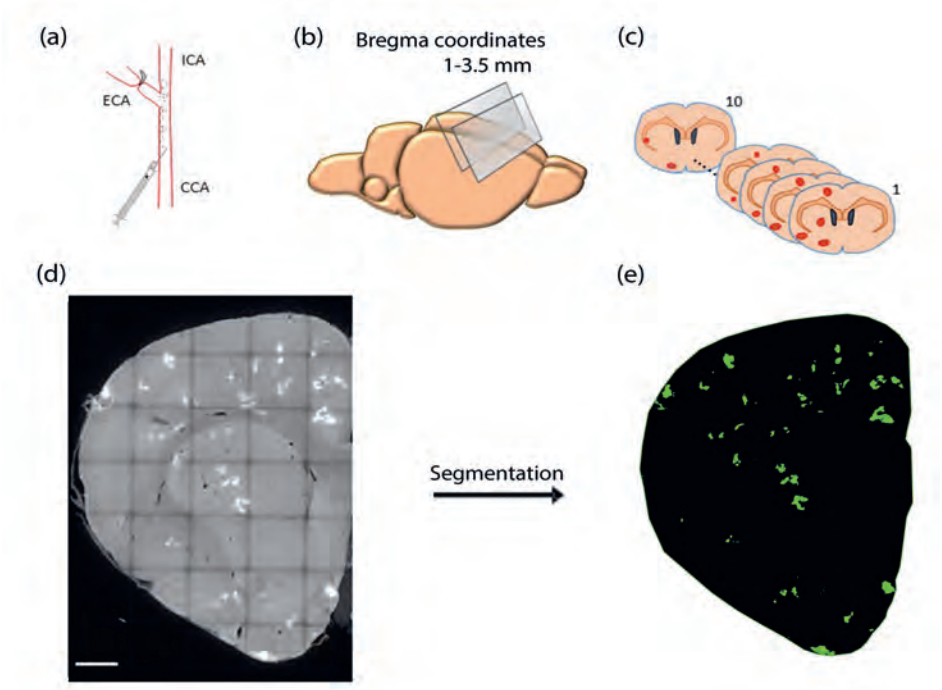

***Figure 1.* (a)** *Microembolization model: Injection of microspheres via left common carotid artery (CCA).* **(b)** *Brain sections (50 µm thick) were made between 1-3.5 mm bregma coordinates.* **(c)** *Ten consecutive coronal brain sections were selected for the brain damage reconstruction. Brain tissue damage (in red) was mainly confined on the intervention hemisphere.* **(d)** *Maximum intensity projection (MIP) of a 50 µm thick coronal brain section of the intervention hemisphere with hypoxic regions (white). Tilescan image was made using confocal imaging, Scale bar = 1000 µm.* **(e)** *The same brain section as in (d) after the segmentation of hypoxic regions (green) in the IMARIS software. CCA - common carotid artery. ICA - internal carotid artery. ECA - external carotid artery.*

1(a). Microspheres were lodged in the left hemisphere, leaving the right hemisphere as a control, as depicted in Fig. 1(c).

Tissue preparation and immunohistochemistry

Animals were killed 24h post-surgery. Pimonidazole hydrochloride (60 mg/kg; Hypoxyprobe Pacific Blue Kit, HP15-x, Burlington, MA) was used as a marker of hypoxia and lectin (1 mg/kg; DyLight 594 labeled lycopersicon Esculentum tomato, Vector Laboratories, DL-1177, Burlingame, CA) as a marker of ischemia (17). Pimonidazole hydrochloride is a probe which binds to cells that have a partial pressure of oxygen (PO_2) smaller than 10 mmHg and lectin is a dye which stains perfused blood vessels intravenously. Brain removal, brain pre-processing, and immunohistochemistry of brain sections (50 µm thick) were performed as described previously (17). Mouse anti-pimonidazole (Hypoxyprobe Pacific Blue Kit, HP15-x, 1:500) antibody was used to detect Hypoxyprobe and hence to visualize hypoxia.

3D reconstruction of intervention hemisphere

For the spatial analysis between microspheres and brain damage, a 500 μm thick volume of the intervention hemisphere was reconstructed. Ten consecutive coronal brain sections (50 μm thick) devoid of tearing were selected from the forebrain between 1 and 3.5 mm of the bregma as shown in Fig. 1(b) and 1(c). Tilescan z-stack images (resolution: x,y: 3 μm and z: 5 μm) of the intervention hemisphere were acquired using a confocal laser scanning microscope SP8 (Leica Microsystems, Wetzlar, Germany) with a 10x objective. To facilitate alignment, the z-stack images were converted to maximum intensity projection (MIP) images as depicted in Fig. 1(d). To this end, the ImageJ software (Rasband, W.S., ImageJ, U. S. National Institutes of Health, Bethesda, Maryland, USA) was utilised, whereas MIP images were aligned using the AMIRA software (Visage Imaging, Inc., San Diego, CA, USA). The resultant z-resolution was thus 50 μm.

Segmentation of microspheres, ischemic and hypoxic regions

Reconstructed brain volumes of the intervention hemisphere were inserted in IMARIS 9.3, a 3D analysis software (Bitplane Inc., St. Paul, MN, USA) and the spot creation wizard and surface creation wizard were used to automatically segment microspheres and hypoxic regions respectively (Fig. 1(e)). Ischemic regions were segmented manually by an experienced researcher. The segmented volumes were exported from IMARIS as numbers in excel files and as .tiff binary images, separate for each segmented element (microspheres, ischemic and hypoxic regions). To quantify how deep in the cortex microspheres were lodged, we manually calculated their distance from the cortical surface, using Leica LAS X software (Leica Microsystems, Germany).

Custom Python codes were used to locate the microspheres and hypoxic regions in the .tiff images to enable distance computations. The 2D binary MIP images were then converted to 3D based on the given z-coordinate of the centre of the coronal brain sections. Images of hypoxic regions were downsampled into $15\times15\times50$ μm^3 voxels to enable direct comparison with the $15\times15\times15$ μm^3 resolution employed in the simulations, as described in the following subsection.

Computational models

Physiologically representative cortical columns

To simulate the oxygen transport in a cortical column supplied by a single penetrating arteriole, existing models of penetrating arterioles (34) and capillaries (33) were coupled together. Note that these networks were generated from human cerebral microvasculature data (43–45). To represent a tissue volume of $375\times375\times1500$ μm^3, four periodic 375 μm capillary cubes were stacked along the depth of the cortical column. A penetrating arteriole model was then placed at the centre of the column with its inlet aligned with the cortical surface. The branches of the arteriole tree outside the column were trimmed and the boundary nodes were each connected to the closest node of the capillary network. Figure 2 displays typical examples of: (a) a capillary network; (b) a penetrating arteriole

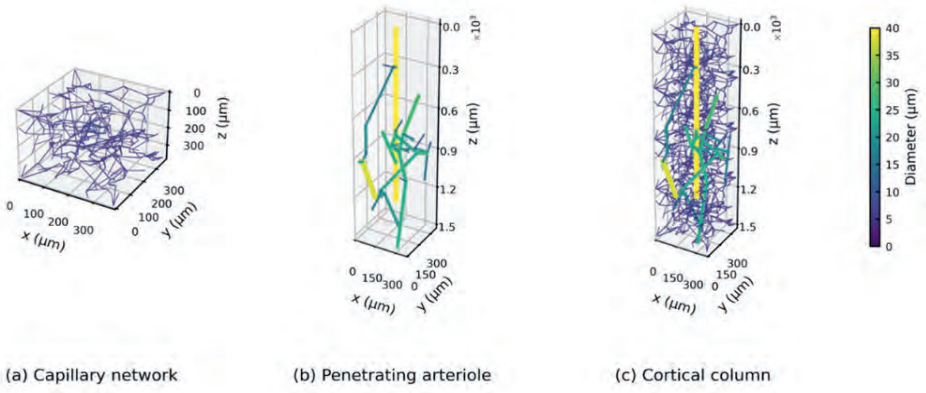

Figure 2. *Geometry of* ***(a)*** *a capillary network,* ***(b)*** *a penetrating arteriole and* ***(c)*** *a cortical column built from the penetrating arteriole and the capillary cubes.*

tree; and (c) a typical cortical column assembled from these two networks. The geometric information of the 10 example cortical columns generated here is summarised in Table 1.

Table 1. *Geometric information of cortical columns.*

	Simulation	**Literature**
Surface density of arterioles	7.11/mm^2	5.63-10/mm^2 (44, 46)
Vessel density	10846±163/mm^3	10129/mm^3 (47)
Vascular volume fraction	2.82±0.22 %	2.70 % (47)

Blood flow simulation

The blood flow in the microvasculature is assumed to be in quasi steady state. The flow is also assumed to be purely laminar because of the low Reynolds number of about 0.50 in arterioles and about 0.003 in capillaries (48). In addition, it was assumed that the flow was fully developed and axisymmetric with zero velocity components in the radial and circumferential directions. Hence the Hagen-Poiseuille equation for blood flow in each vessel can be used:

$$\frac{\Delta p}{Q} = \frac{8\mu L}{\pi r^4} \qquad \text{Equation 1}$$

where Δp is the pressure drop along the vessel, Q is the flow rate, L and r are the vessel length and radius and μ is the blood viscosity, which is an empirical function of vessel diameter and haematocrit (49). The haematocrit was taken to be a constant value of 0.45 (33, 40) and the plasma viscosity was taken to be 1.20 mPa·s (34,50).

Note that we assume constant haematocrit here, despite there being multiple studies showing that the haematocrit is not evenly distributed at microvascular bifurcations due to phase separation (51, 52). However, previous studies have shown that the effects of phase separation on blood flow at the length scale modelled here are likely to be second order (53, 54). We also further tested different phase separation models on oxygen transport simulations, the effects of which on tissue oxygenation were found to be of only secondary importance (results not presented here).

Since there is a linear relationship between pressure drop and flow rate in each vessel, the flow field can be solved by using a set of linear equations. Hence an n×n conductance matrix Γ can be defined for the network as

$$\Gamma_{ij} = \frac{Q_{ij}}{p_i - p_j} = \frac{\pi r_{ij}^4}{8\mu_{ij} L_{ij}} \quad \text{Equation 2}$$

where n is the total number of vertices of blood vessels in the network and Q_{ij} is the flow rate from *i* to *j*. Γ_{ij} is zero if there is no connection between nodes *i* and *j*. Then conservation of mass at each node yields

$$\sum_{j=1}^{n} (p_i - p_j)\Gamma_{ij} = S_i \quad \text{Equation 3}$$

where S*i* is the source term at node *i*.

By coupling Eqs. 2 and 3 and setting the boundary conditions, the pressure at each node and the flow rate in each blood vessel can be solved using a standard linear solver. In this study, all boundary nodes were assumed to have the same pressure, except for the arteriole inlet node at the top of the column. The blood pressure difference between arteriole inlet and boundary nodes was adjusted to maintain a normal perfusion of 55 mL/100 mL/min in each column (55). All blood flow simulations were carried out using custom Python scripts.

Oxygen transport simulation

Oxygen transport simulations were performed using the Green's function method (32, 56). This method has recently been implemented in several studies on cerebral oxygen transport (26, 31, 40). In the Green's function method, blood vessels are represented by discrete oxygen sources and the tissue region is divided into cuboidal elements which act as oxygen sinks. Inside blood vessels, the blood oxygen concentration (C_b) can be represented as a sum of oxygen dissolved in plasma and oxygen carried by haemoglobin as

$$C_b = \alpha_b P_b + C_{Hb} HS \quad \text{Equation 4}$$

where a_b is the blood oxygen solubility, P_b is the blood PO_2, C_{Hb} is the oxygen binding capacity per unit volume of red blood cells and S is the oxygen saturation of haemoglobin. S has a non-linear relationship with blood PO_2:

$$S = \frac{P_b^N}{P_{50}^N + P_b^N} \quad \text{Equation 5}$$

where N is the Hill equation exponent and P_{50} is the PO_2 at half maximal haemoglobin saturation.

The oxygen transport in brain tissue can be simplified to a diffusion-reaction equation:

$$D_t \alpha_t \nabla^2 P_t = M \quad \text{Equation 6}$$

where D_t, α_t and P_t are the oxygen diffusion coefficient, the oxygen solubility and PO_2 in brain tissue, respectively. Metabolic rate of oxygen (M) and tissue PO_2 are assumed to follow a Michaelis-Menten relationship:

$$M = \frac{M_0 P_t}{P_t + P_0} \quad \text{Equation 7}$$

where M_0 is the maximum metabolic rate of oxygen and P_0 is the Michaelis constant which is the tissue PO_2 when M is half of M_0.

According to the potential theory, a Green's function $G(\mathbf{x},\mathbf{x}^*)$ can be defined between a point source $\mathbf{x}^* = (x^*_1,x^*_2,x^*_3)$ and a point in tissue $\mathbf{x} = (x_1,x_2,x_3)$. In an infinite domain, the solution of the Green's function is

$$G(\mathbf{x},\mathbf{x}^*) = \frac{1}{4\pi D_t \alpha_t |\mathbf{x}-\mathbf{x}^*|} \quad \text{Equation 8}$$

By integrating the potentials of oxygen from all sources, the PO_2 within each tissue element can be solved easily. Full details of the numerical implementation of the Green's function method can be found in (32, 56).

The Green's function method was applied to our cortical columns using an open-source C++ package (https://physiology.arizona.edu/people/secomb/greens) developed by Secomb et al. (2004) (32). Custom Python scripts were written to read the network geometry and to post-process the simulation results. The blood PO_2 at arteriole inlet was set as 90 mmHg (31). The tissue region in each column was discretised into voxel of 15×15×15 μm³. All model parameters were taken to be the same as used in Secomb et al. (2004) (32), except for the maximum metabolic rate of oxygen, which was adjusted to $M_0 = 6.72\times10^{-4}$ cm³ oxygen/cm³ tissue/s based on human data (30), to be consistent with our previous numerical study (40).

Blockage simulation

To simulate occlusion in the arteriole tree, a bead with a size of 25 μm was introduced at the arteriole inlet of each of the 10 cortical columns. The bead was assumed to be carried by the blood flow and to be trapped at the inlet of the first vessel that it reached with a diameter smaller than the bead size of 25 μm. This setup led to 6-15 occlusion scenarios in each cortical column, due to different column geometries, which resulted in a total of 91 scenarios in 10 columns. Here we simply assume that the probability of each blockage in a column is the same since there is currently no suitable bead transport model in the cerebral microvasculature. In addition, only one bead is assumed to be present in each arteriole due to the low bead density found in animal experiments (0.43/column, Section 3.1). Hence, we assume that there are only two situations of the cortical column supplied by one penetrating arteriole: one bead or no bead. After the blockage simulation, the hypoxic regions were identified in each column as the tissue voxels with a PO_2 smaller than 10 mmHg, i.e., matching the experimental setting.

Distance calculations for both experimental and simulated data

Two types of distance analysis were performed to establish spatial relationships between vessel blockages and hypoxic regions, namely the pixel-based Gx function and the hypoxic intensity. These two analyses were conducted in identical ways in the *in vivo* experiments

and *in silico* simulations, which enables high-fidelity comparisons to be made between the two. Note that the regions outside of the brain tissue in experiments and outside of the cortical columns in simulations were excluded from these distance analyses.

The pixel-based Gx function is defined here as the cumulative fraction of distances from the hypoxic regions to their closest microspheres:

$$\text{Pixel-based Gx}(d) = P(\delta < d) \qquad \text{Equation 9}$$

where d is the distance, P is the probability and δ is the distance from a hypoxic pixel to its closest microsphere. Note that this analysis is different from the Gx function conducted in our previous study, which used the centre of each hypoxic region instead (41). In the simulations, the small number of voxels with PO_2 below 10 mmHg under healthy condition were excluded from the pixel-based Gx function analysis.

The hypoxic intensity is defined as the volume fraction of hypoxic tissue in a sphere of a certain radius around a microsphere, which is thus a function of distance. Around each microsphere the hypoxic intensity was calculated up to a radius of 500 μm with a step size of 50 μm. In each cortical column, the hypoxic intensity was averaged for all possible blockage sites since we have assumed the same probability of each blockage scenario in each column.

To investigate the spatial correlations between hypoxic regions and microspheres in the experiments, we ran Monte-Carlo simulations of microspheres; these simulations provided the control situation against which we compared the randomness of the distributions obtained here. The control points were randomly generated in the intervention hemisphere in each animal, where the density of points was equal to the *in vivo* bead density in the same brain region. Then the same hypoxic intensity analyses were conducted around these control points, which were compared against the hypoxic intensity calculated in experiments.

RESULTS

Ischemic and hypoxic distribution patterns after blocking the cerebral arterioles in a rat model of microembolization

Table 2 shows the number and density of microspheres and the resulting ischemia and hypoxia per animal. The density of 25 μm microsphere of 2.03/mm^3 (average of 6 animals) results in a volume fraction of 1.66×10^{-5} mL beads per mL cerebral tissue. If we assume that the beads are entirely present in a territory of 100 mL supplied by a middle cerebral artery in a human, the total thrombus volume will be 1.66×10^{-3} mL. This value is significantly smaller than a typical thrombus volume of 0.17 mL (57), which indicates that the micro-occlusions considered in this study correspond to a case where only about 1% of a larger thrombus is embolised during thrombectomy and thrombolysis.

A typical example of a blocked arteriole is shown in Fig. 3 where a single 25 μm microsphere blocks an arteriole of similar size and leads to ischemia (absence of lectin staining; red) and hypoxia (green). Since the animals are killed 24h post-surgery, neuronal cell death has already taken place which explains in some cases the absence of hypoxic cells from the lesion core. The implications of this will be discussed later.

Table 2. *Number and density of microspheres, total brain volume and % of ischemia and hypoxia per animal. These numbers were measured in the reconstructed brain volumes with a thickness of 500 µm.*

Animal	Number of microspheres	Microspheres density (1/mm³)	Total volume of 10 brain sections (mm³)	% of hemisphere being ischemic	% of hemisphere being hypoxic
1	25	1.23	20.32	0.51%	0.81%
2	41	1.97	20.86	1.90%	1.40%
3	47	1.89	24.84	2.69%	2.38%
4	26	1.29	20.18	0.64%	0.30%
5	88	4.07	21.61	2.19%	1.68%
6	35	1.73	20.28	0.98%	1.15%

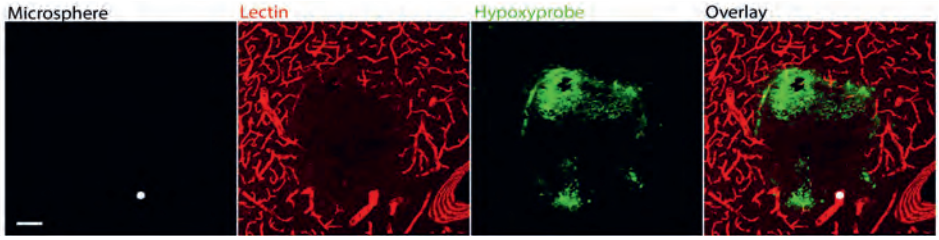

Figure 3. *Maximum intensity projection (MIP) of a 50 µm thick brain section of the intervention hemisphere showing a typical example of a 25 µm (diameter) microsphere causing ischemia (absence of lectin; red) and hypoxia (green) in the rat brain. Scale bar = 100 µm.*

Figure 4 shows the distribution of microspheres (white) and the resulting ischemic (red) and hypoxic (green) regions in each animal. Due to the stochastic nature of the microsphere distribution the resulting ischemia and hypoxia are not confined to one brain region but are dispersed throughout the brain structures (Cortex, Striatum, Corpus callosum). We found that 73% of the microspheres were lodged in the cortex with the remaining found in deeper brain structures. From the microspheres lodged in the cortex only 0.07% were found on the cortical surface and the majority were lodged at a mean distance of 940.70 ±122.50 µm from the cortical surface. Although ischemia and hypoxia are distributed heterogeneously, there is a reasonable match (36.10±5.30% of hypoxic regions are also ischemic) between the two in the affected brain hemisphere within each animal (yellow colour in overlay channel Fig. 4).

3D distance analysis reveals two patterns of hypoxic intensity and a strong correlation between microspheres and hypoxic damage

In a previous study where a mixture of microspheres was injected via the CCA we found a spatial correlation over hundreds of micrometres between microspheres and centroids of hypoxic regions by applying a point-pattern 3D distance analysis (41). However, this experimental setup was not suitable to isolate the effects of a single microsphere or a single size of microspheres on brain tissue oxygenation. Thus, here we only injected one size of microspheres and used a different approach for the 3D distance analysis. In particular, we

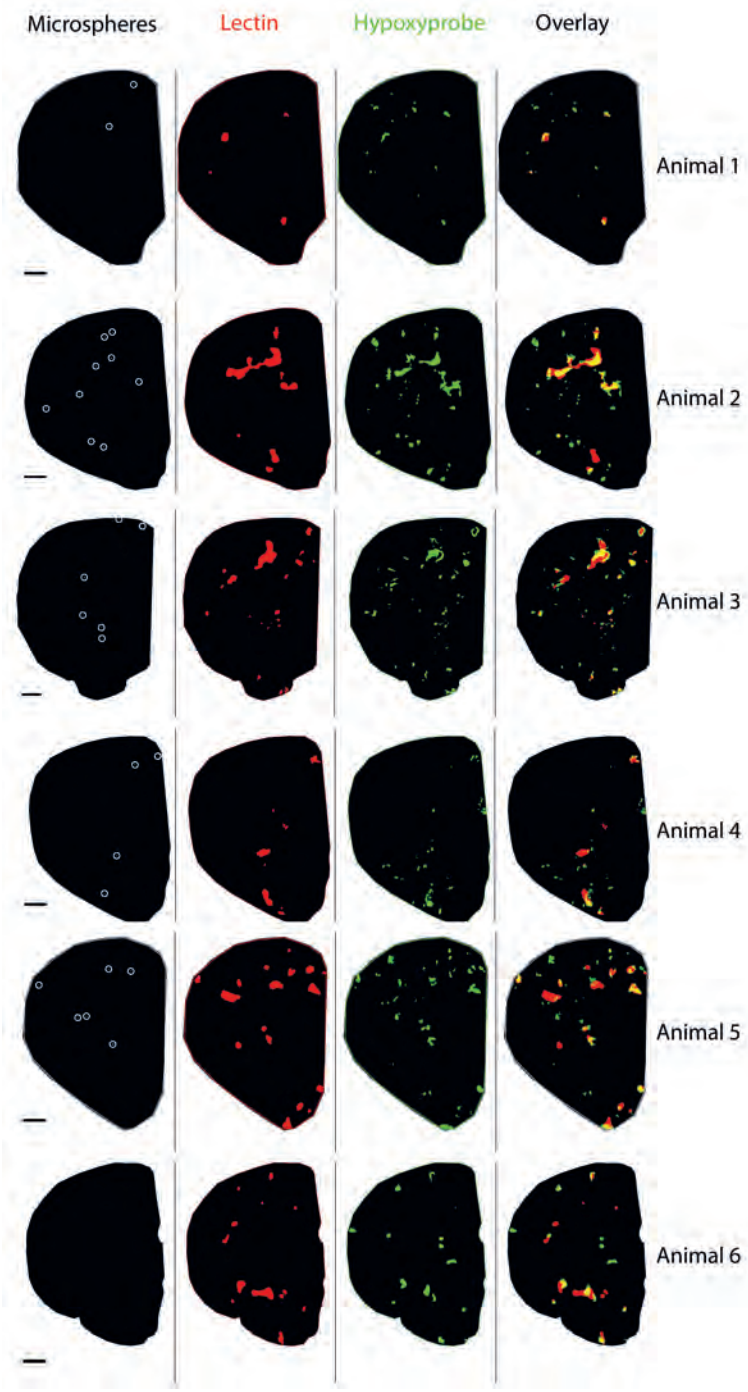

Figure 4. Per animal a representative segmented brain section of the intervention hemisphere. *From left to right: microspheres (centre of white circles), ischemia (lectin; red), hypoxia (hypoxyprobe; green) and overlay of the three channels. In yellow is shown the overlap between ischemia and hypoxia. Scale bar = 1000 μm.*

measured the hypoxic intensity as a function of the distance from each microsphere, where each hypoxic intensity curve thus represents the distribution of hypoxic regions around a single 25 µm microsphere.

As shown in Fig. S1 (Supplementary Information), there are cases in all 6 animals where hypoxic intensity decreases to less than half within the first 200 µm and cases where hypoxic intensity starts from zero and reaches 10-20% within the first 200 µm. To elucidate this phenomenon, we categorised the hypoxic intensity patterns into two types (Fig. 5(a)), based on the criterion of whether the slope is negative when the radius increases from 50 to 100 µm (Type A: accounting for 30.90% of the cases when considering all 6 animals), or positive (Type B: 69.10% of the cases). Note that the cases of full hypoxia and no hypoxia inside a radius of 100 µm were categorised as type A and type B respectively. Representative examples for both types are shown in a 2D schematic in Fig. 5(b).

To further investigate whether the hypoxic regions form locally or distally around the microspheres, we categorised the two types of hypoxic intensity into four subtypes based on the presence or absence of hypoxic regions within 100 µm of the microsphere. The percentage of each subtype in all 6 animals is listed in Table 3. Hypoxic regions are absent within 100 µm of the microsphere in the majority of the type B cases, which also account for 49.20% of all cases. Thus, approximately half of the 25 µm microspheres did not lead

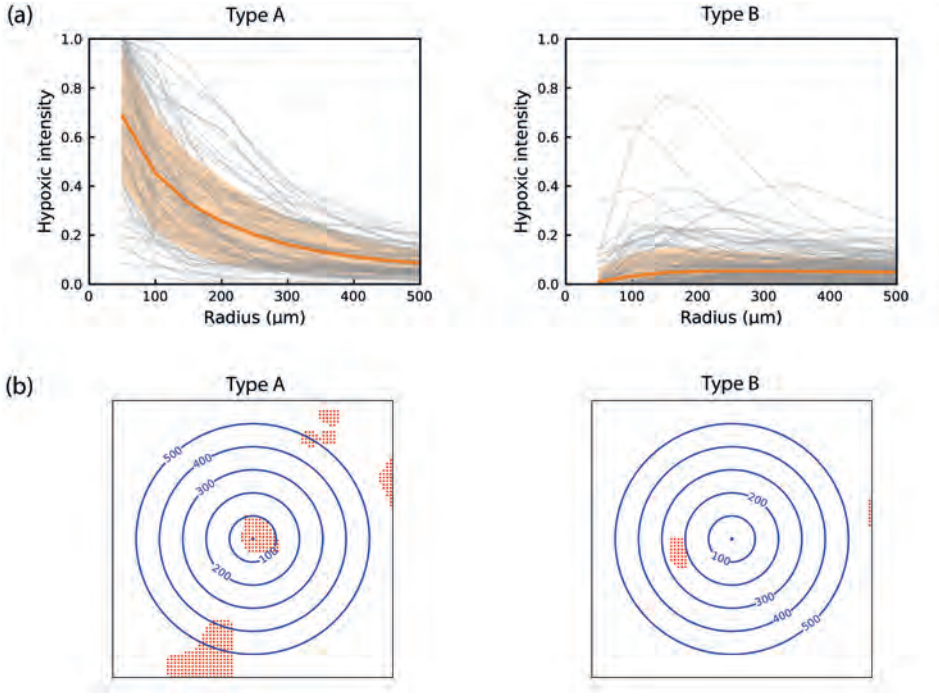

***Figure 5.* (a)** *Two types of hypoxic intensity. Type A is characterised by negative slope and Type B by positive slope. Mean ± standard deviation (filled areas) (all microspheres of n=6 animals).* **(b)** *Representative examples of the two types of hypoxic intensity. A 2D schematic of the 3D hypoxic intensity analysis. Using a microsphere as a starting point, the number of hypoxic pixels (red) were calculated in spheres of increasing radius (blue concentric circles).*

to local hypoxia in our experiments.

Table 3. *Percentage of cases of type A and type B hypoxic intensity with or without hypoxic regions within 100 µm of the microsphere.*

	Type A	**Type B**
Hypoxic regions present within 100 µm of the microsphere (local hypoxia)	30.90%	19.90%
Hypoxic regions absent within 100 µm of the microsphere (no local hypoxia)	/	49.20%

Next, we tested whether there was a correlation between occlusion site and hypoxic pixels. To do this, we ran Monte-Carlo simulations using random control points. The Monte-Carlo simulations shown in Fig. 6 for all animals are found to give results that are below the curves of the experimental data: this thus indicates a degree of correlation between individual microspheres and resulting hypoxic regions. Note that in the experimental results we introduced only the hypoxic intensity calculations; the pixel-based Gx function results will be presented in Section 3.5.

It should be noted that these distance calculations do not consider the vessel architecture. Due to tissue deformation and other technical issues such as brain section alignment, blood vessel reconstructions based on confocal imaging of brain sections are not sufficiently accurate. Even in a brain tissue made transparent by means of clearing techniques, blood vessel segmentation remains challenging. This knowledge gap is thus addressed using the numerical simulations presented below.

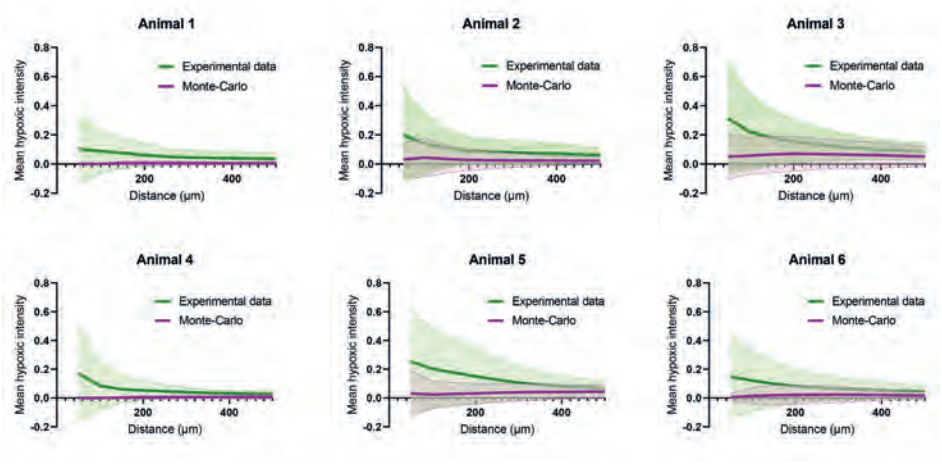

Figure 6. Per animal experimental data versus Monte-Carlo simulations. *Monte-Carlo simulations: hypoxic intensity as a function of the distance from random control points. Mean ± standard deviation (filled areas) (all microspheres or control points of n=6 animals).*

Heterogeneous distribution of tissue oxygenation in the cortical column

Figure 7 shows the tissue oxygenation in a typical cortical column as solved by the Green's function method. The simulations suggest that oxygen is distributed highly heterogeneously in the tissue within a cortical column. However, it is highly coupled with the microvascular geometry, especially the geometry of the arteriole tree.

To investigate the effects of arteriole and capillary geometries on oxygen transport, we performed two simulations: one in a cortical column with the same arteriole structure as shown in Fig. 7(a) but using a different capillary network (Supplementary Information Fig. S2), and the other in a cortical column using the same capillary geometry but connected to a different arteriole tree (Supplementary Information Fig. S3). The change in capillary geometry or arteriole geometry leads to a root-mean-square difference of 9.70 or 15.90 mmHg for PO_2 in each tissue voxel in the column, respectively. However, these local variations were found to only have negligible effects on the overall PO_2 distribution in the column (Supplementary Information Fig. S4).

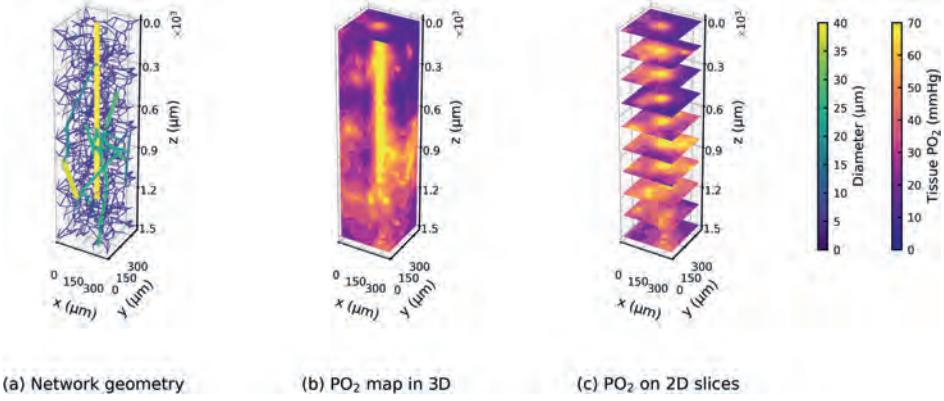

Figure 7. *The geometry of a typical cortical column* **(a)** *and its tissue oxygenation* **(b, c)** *solved by the Green's function method.*

Response of tissue oxygenation to blockage on the arteriole tree

Figure 8 displays three different 25 μm blockage scenarios in the same cortical column, where the blockage locations are indicated by blue spheres. The micro-blockage leads to perfusion drops in the downstream vessels and corresponding regions. The reduction in blood flow (in dark grey) because of the occlusion site is strongly heterogeneous in the column. In addition, the relative perfusion drop in the whole column is 18.50% (a), 50.70% (b) and 8.20% (c) respectively in these three blockage scenarios; this value is thus highly dependent on the blockage location and the specific downstream microvasculature.

The tissue PO_2 drop is also distributed unevenly in the column. However, the regions of tissue PO_2 drop (in red), which are primarily located around the blood vessels with largest flow rate drops (in dark grey), match those of reduced perfusion closely. The PO_2 drop then leads to hypoxic regions (PO_2 smaller than 10 mmHg), which are shown as red dots in the bottom row of Fig. 8. The tissues near the column centre are found to be unlikely to become hypoxic, due to the oxygen supply from the penetrating arteriole trunk. These simulations thus indicate that the tissue hypoxia caused by occlusion in the arteriole tree is mainly due to the perfusion shortage that occurs in the region downstream of the occlusion site.

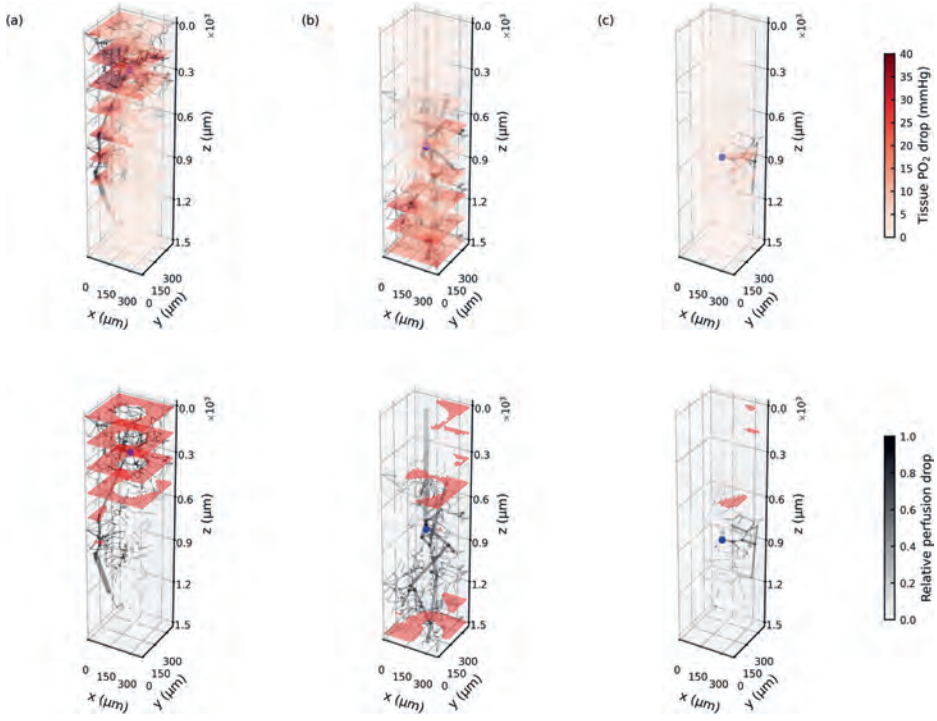

Figure 8. *The top row shows the drops in relative perfusion and tissue oxygenation in response to 3 different 25 μm blockages (blue sphere) in the same arteriole tree. The bottom row shows the hypoxic regions (PO_2 smaller than 10 mmHg, coloured in red) in response to the same blockages.*

Comparisons between simulations and experiments show agreements on pixel-based Gx function and discrepancies on hypoxic intensity

Figure 9 presents the results of two distance analyses in both experiments and simulations. The pixel-based Gx function has a consistent sigmoidal shape in each animal in experiments (Fig. 9(a)) and in each cortical column in simulations (Fig. 9(b)). This results in small standard deviations between each animal and between each cortical column as shown in Fig. 9(c). In addition, there is a close match for the pixel-based Gx function between experiments and simulations in that they both reach 50% at around 300 μm and reach about 90% at 800 μm. However, the experimental curve is found to start to increase at shorter distances than in the simulations, which indicates that there are more hypoxic regions in the vicinity of occlusion sites in experiments than was found in the simulations.

These discrepancies are more clearly shown in the hypoxic intensity results. The experimental hypoxic intensity curves decrease as the radius increases (Fig. 9(d)), however, most of the simulated hypoxic intensity curves increase at the start (Fig. 9(e)). The reason for this difference is that the experiments have more type A hypoxic intensity (30.9%), while there is only one case out of 91 simulations that is type A (Supplementary Information Fig. S5). This discrepancy leads to some significant differences between experiments and simulations (Fig. 9(f)). The standard deviation of the hypoxic intensity is

also larger than that of the pixel-based Gx function in both experiments and simulations. These results will be further discussed in the next section.

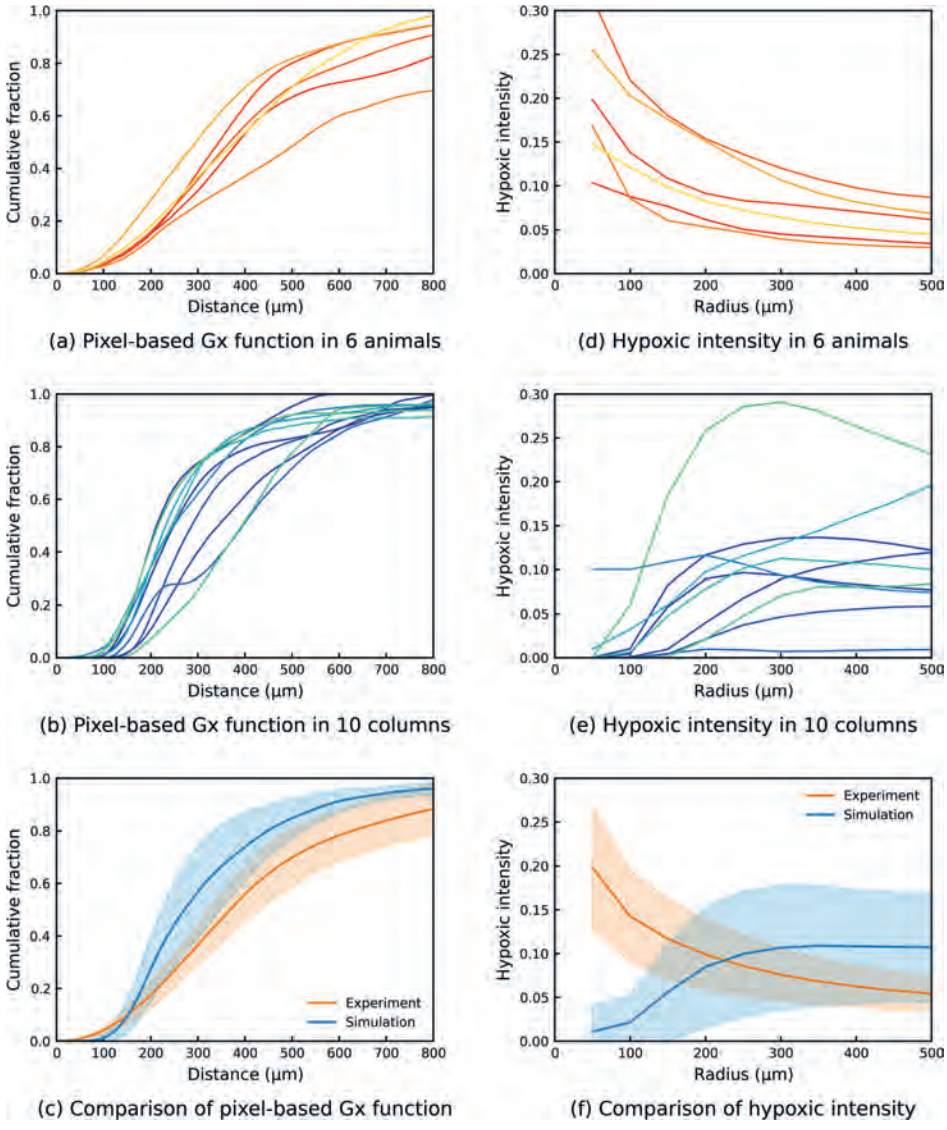

Figure 9. Comparisons of pixel-based Gx function and hypoxic intensity between experiments and simulations. *The error bar of experiments shows the standard deviation between 6 animals. The error bar of simulation shows the standard deviation between 10 cortical columns.*

DISCUSSION

In this study, we examined the effects of micro-occlusions in the cerebral penetrating arteriole trees on tissue hypoxia using both *in vivo* animal experiments and *in silico* simulations. Two novel distance analyses, namely hypoxic intensity and pixel-based Gx function, were

carried out identically in both experiments and simulations. The first method focuses on the distribution of hypoxic regions around each microsphere. By comparison, the latter one zooms out to examine the cumulative fraction of distance between the microsphere and the resultant hypoxic regions in the reconstructed or simulated brain tissue volumes. To the best of our knowledge, this is the first study on the spatial relationships between occlusion sites and hypoxic regions that combines both experimental and numerical methods, and the first that considers occlusions over different generations of the penetrating arteriole trees.

Fair agreement in pixel-based Gx function results have been shown between experiments and simulations. These results suggest that hypoxic regions can form distally from the occlusion sites, in agreement with previous experimental findings using mixed microspheres of several sizes (41). However, other discrepancies in hypoxic intensity have been shown between experiments and simulations. We thus further categorised the hypoxic intensity into two types, where type A decreases and type B increases as the radius increases from 50 to 100 μm. Type A hypoxic intensity represents the scenarios when significant hypoxic regions present near the occlusion site, whereas type B represents the cases when most hypoxic regions form far away from the occlusion site. Type B hypoxic intensity was found to be the dominant case in both experiments (69.1%) and simulations (98.9%). This finding also agrees with the pixel-based Gx function that more than 90% of the hypoxic regions are more than 150 μm from the microsphere instead of around the occlusion site.

Reasonable agreement between ischemic and hypoxic regions

Using a rat model of microembolization we assessed the percentage of overlap between ischemia and hypoxia in a limited brain volume of the affected hemisphere, 24h post-surgery. We found ischemic regions which were not hypoxic, hypoxic regions which were not ischemic and a 36.1±5.3% overlap between ischemia and hypoxia. In our previous work where we injected a mixture of microsphere sizes and killed the animals after 1, 3 and 7 days we found that infarction volume at day 7 was similar to that of day 1, suggesting that infarction develops within 24h after microembolization (17). As a consequence, we missed in our data the cells which had already undergone cell death. This pathology can explain the ischemic regions which were not hypoxic. In cases where hypoxic regions did not overlap with ischemia, we think that larger ischemic regions, which are formed due to multiple occlusions of the same or different arterial trees, are likely responsible for these results. Hypoxic regions could span beyond the analysed tissue (500 μm thick). As a result, we detect only the hypoxia in our analysed brain tissue, while the ischemic source is further away in the z-direction. Considering the pathological process of infarct growth and the distal effects of large ischemic regions, the overlap between ischemia and hypoxia in our experiments is reasonable.

Distal hypoxic regions

In the experimental data we found both local (<100 μm, 50.8% of all cases) and distal (>100 μm, 49.2% of all cases) effects due to micro-occlusions. Contrary to previous *in*

vivo rodent studies where the occlusion site was highly correlated to brain tissue damage (22–24), we found distal effects after occlusion of penetrating arteriole branches using a rat model of microembolization (41). Our simulations suggest that a 25 µm microsphere will occlude a branch of the penetrating arteriole, which will lead to hypoperfusion downstream of the occlusion site in the corresponding cortical column (Fig. 8). The hypoperfusion will then result in distal tissue hypoxia from the occlusion site. This fenomenon is partially supported by the overlap between ischemic and hypoxic regions in the experiments.

According to blood vessel diameter measurements, rat penetrating arterioles range in size from 10-30 µm (22). By injecting microspheres of 25 µm in diameter we should have been able to target the first few branches of penetrating arterioles. We however detected most of the microspheres lodged at a distance > 500 µm below the cortical surface. This discrepancy could be explained by the arterial wall elasticity in combination with the blood flow which may push the microspheres distally from the cortical surface (58). Since we did not consider the vessel architecture directly, microspheres could block either a penetrating arteriole at a lower level or branches of a penetrating arteriole. Even in the cases where the perfusion volumes may be smaller, the effects of blocked arterioles span a greater distance than was found in *in vivo* occlusions of penetrating arterioles using photothrombosis (22,23).

To understand the discrepancy found between microembolization and the photothrombotic model we address here some differences between the two techniques. Firstly, in the current experimental study, microspheres are lodged not only in the cortex but also in deep brain structures. Whereas cortical columns are thoroughly examined under controlled circumstances, deeper brain structures and their vessel architecture, perfusion and oxygenation are poorly investigated due to limited depth resolution of live imaging techniques (59). In addition, despite the high resolution gained by tissue clearing or other modern techniques (60–62), effective image segmentation remains challenging (63). Secondly, in our microembolization model the tissue hypoxia can be a result of multiple occluded arteriole(s). In the distance calculations both cases were included, and no distinction was made between the two, since we did not consider blood vessel architecture and could not trace back the effects of every microsphere. Thirdly, we looked at hypoxia 24h after microembolization, missing the tissue where neuronal cell death has already taken place. Lastly, some microspheres may not necessarily lead to ischemia or hypoxia, because of a certain degree of collateralization. As a result, microspheres without any detectable brain damage may wrongly be matched to tissue hypoxia created by other occlusion(s). However, we can exclude this scenario based on our simulations, where most single penetrating arteriole occlusions (98.9%) led to distal hypoxic regions thus confirming the experimental findings. Taken together, the inclusion of deep brain structures in our distance analysis and the synergistic effect of multiple occluded arterioles (41) could explain the discrepancies found between the microembolization versus photothrombotic model, although further detailed work will be required to establish this more accurately.

Comparisons between simulations and experiments

In this study, numerical simulations were matched with experiments as closely as possible to enable high fidelity comparisons and validations between the two. The validation of *in silico* models against *in vivo* experimental data remains a challenging step for most biomedical simulations, especially for non-linear scenarios like drug delivery and oxygen transport which can result in highly heterogeneous distribution of these substances in tissues. In a recent study, Hartung et al. (2021) (39) simulated blood flow and oxygen transport using the reconstructed microvasculature from *in vivo* images, which led to a very good agreement between the simulated oxygen fields and the two-photon oxygen images. This validation (39) focused on tissue oxygenation under healthy scenarios, thus our work provides a further investigation into the pathological effects of micro-occlusions on tissue hypoxia by comparing the spatial relationships. The validation indicates that the modelling approach is an appropriate one for this scenario and thus supports its wider use in understanding the response of brain tissue to microemboli.

As part of the INSIST (*IN Silico* clinical trials for the treatment of acute Ischemic STroke) project (64), we are developing computational models of AIS at multiple scales to aid in optimising AIS treatments and developing medical devices. The micro-scale models presented here and in previous works (37, 40) can in the future be coupled with organ-scale models of AIS (65–67) and play a key role in predicting the secondary tissue damage caused by microthrombi after an unsuccessful thrombectomy (68–70).

We next highlight several differences between the experimental and numerical setups. The cerebral microvascular networks used in the simulations (33, 34) were generated from the statistical data of the human brain (43–45). However, the experiments were conducted in rat brains. Despite topological similarities between human and rodent networks, the human capillaries have been found to have longer vessels and larger spacings between vessels than rodent capillaries (71). In addition, the venules were not included in the simulations, because the occlusions are primarily on the arteriole side. These geometrical differences can potentially lead to discrepancies between simulations and experiments, which should be quantified in future work.

In addition, the blood flow and oxygen transport models in this study are purely steady and passive. However, the hypoxic regions were measured and segmented 24h after the microembolization in experiments. In this time interval, the brain can have active responses to vessel blockage and tissue ischemia and hypoxia including autoregulation (72, 73), pericyte constriction (42, 74), microsphere clearance (75, 76) and pathological response like infarct formation (17). These time-dependent events were not considered in the simulations but should be included in future studies.

Discrepancies of hypoxic intensity have been shown between simulations and experiments, which are mainly since there are more type B hypoxic intensity trends found in the simulations than in the experiments. This discrepancy can be partially explained by the differences between the two that we have discussed previously. In the simulations, it is assumed that the bead occludes a branch of the penetrating arteriole with a diameter smaller than 25 μm at the vessel inlet, which tends to be near the column centre. As shown

in Fig. 8, the hypoxic regions are mainly caused by the hypoperfusion in the regions downstream of the occlusion site and at the column boundary, which will lead to a type B hypoxic intensity. However, in the experiments, microspheres were found to be lodged further away from the cortex surface (mean ± st.dev. = 940.70 ± 122.50 µm), probably due to the vessel wall elasticity in combination with the blood flow. The occlusions will thus more readily happen at the arteriole-capillary transition or the capillary scale. In such a case, more hypoxic regions may form locally (type A) instead of in the regions downstream of the occlusion (type B) in the experiments. It thus leads to fewer type B cases in the experiments than the simulations. In addition, these effects are found to be relatively minor on the pixel-based Gx function, because the hypoxic regions caused by a capillary occlusion tend to be much smaller than these caused by a penetrating arteriole occlusion, which thus only contribute insignificantly to the pixel-based Gx function using the cumulative fraction. However, these hypotheses need further investigations when a fuller description of the vascular geometry is available.

Limitations

One of the major experimental limitations is the z-resolution of the individual coronal brain sections. Although initially a z-step of 5 µm was used when taking the confocal overview images, the z-resolution changed to 50 µm when converting the images to MIP for the 3D reconstruction of the brain tissue. Due to the low z-resolution and technical issues such as the deformation of brain sections, no blood vessel geometry was considered in the experimental data. In addition to the limited z-resolution of individual brain sections, the total z-dimension of the reconstructed brain volume (500 µm), was low compared to the x and y dimensions (7000-8000 µm). As a result, the contribution of microspheres outside the reconstructed brain region to tissue hypoxia was hard to predict. This is something that could add uncertainty to the experimental findings. We tackled these limitations by incorporating *in silico* models of cortical columns and comparing the experimental data as closely as possible to the simulations.

One of the steps in our distance analysis workflow involved the segmentation of brain sections to include the brain anatomy in the calculations. Despite gentle handling of the brain tissue during the staining procedure we could not avoid one section of animal 3 becoming broken. For this particular case, we thus used the previous section instead, since the total area and anatomy of consecutive sections were found to be very similar.

One limitation of the simulations is the assumption of one bead or no bead per column, due to the low bead density in the experiments. However, more beads can occlude the same column and the combined effects of multiple blockages on hypoxic regions could affect both the hypoxic intensity and the pixel-based Gx function. Moreover, the occlusions were found to be very mild in the study when we compared the thrombus volume in our models with the thrombus volume measured by clinics. This indicates that there will tend to be more severe micro-occlusions caused by thrombus fragments after an unsuccessful thrombectomy. Hence, we need to be cautious in applying the results presented in this paper directly to clinical studies.

Another limitation is the assumption of the same probability of possible bead locations in the same column since there is currently no available bead transport model in the cerebral microvasculature. This has also been a limitation in our recent studies on the effects of cerebral microthrombi on blood flow and oxygen transport (37, 40). The microemboli transport model will thus need to be developed and coupled with current oxygen transport models in future work.

FUNDING

This work was partially funded by the European Union's Horizon 2020 research and innovation programme, the INSIST project, under grant agreement No 777072.

COMPETING INTERESTS

The authors have declared that no competing interests exist.

REFERENCES

1. Tarumi, T. & Zhang, R. Cerebral blood flow in normal aging adults: cardiovascular determinants, clinical implications, and aerobic fitness. *J Neurochem* **144**, 595–608 (2018).
2. Claassen, J. A. H. R., Thijssen, D. H. J., Panerai, R. B. & Faraci, F. M. Regulation of cerebral blood flow in humans: physiology and clinical implications of autoregulation. *Physiol Rev* **101**, 1487–1559 (2021).
3. Boas, D. A. *et al.* Can the cerebral metabolic rate of oxygen be estimated with near-infrared spectroscopy? *Phys Med Biol* **48**, 2405–2418 (2003).
4. Duvernoy, H. M., Delon, S. & Vannson, J. L. Cortical blood vessels of the human brain. *Brain Res Bull* **7**, 519–579 (1981).
5. Sutton, R. Reflex syncope: Diagnosis and treatment. *J Arrhythm* **33**, 545–552 (2017).
6. Andersen, L. W., Holmberg, M. J., Berg, K. M., Donnino, M. W. & Granfeldt, A. In-Hospital Cardiac Arrest. *JAMA* **321**, 1200 (2019).
7. Hankey, G. J. Stroke. *The Lancet* **389**, 641–654 (2017).
8. van Veluw, S. J. *et al.* Detection, risk factors, and functional consequences of cerebral microinfarcts. *Lancet Neurol* **16**, 730–740 (2017).
9. Goldberg, I., Auriel, E., Russell, D. & Korczyn, A. D. Microembolism, silent brain infarcts and dementia. *J Neurol Sci* **322**, 250–253 (2012).
10. Vuković-Cvetković, V. Microembolus Detection by Transcranial Doppler Sonography: Review of the Literature. *Stroke Res Treat* **2012**, 1–7 (2012).
11. Sheriff, F. *et al.* Microemboli After Successful Thrombectomy Do Not Affect Outcome but Predict New Embolic Events. *Stroke* **51**, 154–161 (2020).
12. Grutzendler, J. Angiophagy: mechanism of microvascular recanalization independent of the fibrinolytic system. *Stroke* **44**, S84-6 (2013).
13. Mayzel-Oreg, O. *et al.* Microsphere-induced embolic stroke: An MRI study. *Magn Reson Med* **51**, 1232–1238 (2004).
14. Miyake, K., Takeo, S. & Kaijihara, H. Sustained decrease in brain regional blood flow after microsphere embolism in rats. *Stroke* **24**, 415–20 (1993).
15. Rapp, J. H. *et al.* Cerebral Ischemia and Infarction From Atheroemboli <100 μm in Size. *Stroke* **34**, 1976–1980 (2003).
16. Tsai, M.-J., Tsai, Y.-H. & Kuo, Y.-M. Characterization of the pattern of ischemic stroke induced by artificial particle embolization in the rat brain. *Biomaterials* **32**, 6381–6388 (2011).
17. Georgakopoulou, T., van der Wijk, A.-E., Bakker, E. N. T. P. & VanBavel, E. Recovery of Hypoxic Regions in a Rat Model of Microembolism. *Journal of Stroke and Cerebrovascular Diseases* **30**, 105739 (2021).
18. Lyden, P. D., Zivin, J. A., Chabolla, D. R., Jacobs, M. A. & Gage, F. H. Quantitative effects of cerebral infarction on spatial learning in rats. *Exp Neurol* **116**, 122–132 (1992).
19. Zhang, H.-A. *et al.* Evaluation of Hippocampal Injury and Cognitive Function Induced by

Embolization in the Rat Brain. *Anat Rec* **296**, 1207–1214 (2013).

20. Rapp, J. H. *et al*. Microemboli Composed of Cholesterol Crystals Disrupt the Blood-Brain Barrier and Reduce Cognition. *Stroke* **39**, 2354–2361 (2008).
21. van der Wijk, A. E. *et al*. Microembolus clearance through angiophagy is an auxiliary mechanism preserving tissue perfusion in the rat brain. *Acta Neuropathol Commun* **8**, 1–14 (2020).
22. Shih, A. Y. *et al*. The smallest stroke: Occlusion of one penetrating vessel leads to infarction and a cognitive deficit. *Nat Neurosci* **16**, 55–63 (2013).
23. Nishimura, N., Schaffer, C. B., Friedman, B., Lyden, P. D. & Kleinfeld, D. Penetrating arterioles are a bottleneck in the perfusion of neocortex. *Proceedings of the National Academy of Sciences* **104**, 365–370 (2007).
24. Taylor, Z. J. *et al.* Microvascular basis for growth of small infarcts following occlusion of single penetrating arterioles in mouse cortex. *Journal of Cerebral Blood Flow & Metabolism* **36**, 1357–1373 (2016).
25. Beishon, L. *et al.* Vascular and haemodynamic issues of brain ageing. *Pflugers Arch* **473**, 735–751 (2021).
26. Celaya-Alcala, J. T. *et al*. Simulation of oxygen transport and estimation of tissue perfusion in extensive microvascular networks: Application to cerebral cortex. *Journal of Cerebral Blood Flow & Metabolism* **41**, 656–669 (2021).
27. Goirand, F., le Borgne, T. & Lorthois, S. Network-driven anomalous transport is a fundamental component of brain microvascular dysfunction. *Nat Commun* **12**, 7295 (2021).
28. Gould, I. G., Tsai, P., Kleinfeld, D. & Linninger, A. The capillary bed offers the largest hemodynamic resistance to the cortical blood supply. *Journal of Cerebral Blood Flow and Metabolism* **37**, 52–68 (2017).
29. Linninger, A. A. *et al.* Cerebral microcirculation and oxygen tension in the human secondary cortex. *Ann Biomed Eng* **41**, 2264–2284 (2013).
30. Payne, S. J. & Lucas, C. Oxygen delivery from the cerebral microvasculature to tissue is governed by a single time constant of approximately 6 seconds. *Microcirculation* **25**, e12428 (2018).
31. Secomb, T. W., Bullock, K. v, Boas, D. A. & Sakadžić, S. The mass transfer coefficient for oxygen transport from blood to tissue in cerebral cortex. *Journal of Cerebral Blood Flow & Metabolism* **40**, 1634–1646 (2020).
32. Secomb, T. W., Hsu, R., Park, E. Y. H. & Dewhirst, M. W. Green's function methods for analysis of oxygen delivery to tissue by microvascular networks. *Ann Biomed Eng* **32**, 1519–1529 (2004).
33. El-Bouri, W. K. & Payne, S. J. Multi-scale homogenization of blood flow in 3-dimensional human cerebral microvascular networks. *J Theor Biol* **380**, 40–47 (2015).
34. El-Bouri, W. K. & Payne, S. J. A statistical model of the penetrating arterioles and venules in the human cerebral cortex. *Microcirculation* **23**, 580–590 (2016).
35. El-Bouri, W. K. & Payne, S. J. Investigating the effects of a penetrating vessel occlusion with a multi-scale microvasculature model of the human cerebral cortex. *Neuroimage* **172**, 94–106 (2018).
36. Cruz Hernández, J. C. *et al*. Neutrophil adhesion in brain capillaries reduces cortical blood flow and impairs memory function in Alzheimer's disease mouse models. *Nat Neurosci* **22**, 413–420 (2019).
37. El-Bouri, W. K., MacGowan, A., Józsa, T. I., Gounis, M. J. & Payne, S. J. Modelling the impact of clot fragmentation on the microcirculation after thrombectomy. *PLoS Comput Biol* **17**, e1008515 (2021).
38. Schmid, F., Conti, G., Jenny, P. & Weber, B. The severity of microstrokes depends on local vascular topology and baseline perfusion. *Elife* **10**, (2021).
39. Hartung, G. et al. Voxelized simulation of cerebral oxygen perfusion elucidates hypoxia in aged mouse cortex. *PLoS Comput Biol* **17**, e1008584 (2021).
40. Xue, Y., El-Bouri, W. K., Józsa, T. I. & Payne, S. J. Modelling the effects of cerebral microthrombi on tissue oxygenation and cell death. *J Biomech* **127**, 110705 (2021).
41. Georgakopoulou, T. *et al*. Quantitative 3D Analysis of Tissue Damage in a Rat Model of Microembolization. *J Biomech* **128**, 110723 (2021).
42. Hartmann, D. A., Coelho-Santos, V. & Shih, A. Y. Pericyte Control of Blood Flow Across Microvascular Zones in the Central Nervous System. *Annu Rev Physiol* **84**, 1–24 (2022).
43. Cassot, F., Lauwers, F., Fouard, C., Prohaska, S. & Lauwers-Cances, V. A novel three-dimensional computer-assisted method for a quantitative study of microvascular networks of the human cerebral cortex. *Microcirculation* **13**, 1–18 (2006).
44. Cassot, F. *et al.* Branching patterns for arterioles and venules of the human cerebral cortex. *Brain Res* **1313**, 62–78 (2010).
45. Lorthois, S., Lauwers, F. & Cassot, F. Tortuosity and other vessel attributes for arterioles and venules of the human cerebral cortex. *Microvasc Res* **91**, 99–109 (2014).
46. Risser, L., Plouraboué, F., Cloetens, P. & Fonta, C. A 3D-investigation shows that angiogenesis in primate cerebral cortex mainly occurs at capillary level. *International Journal of Developmental Neuroscience* **27**, 185–196 (2009).
47. Lauwers, F., Cassot, F., Lauwers-Cances, V., Puwanarajah, P. & Duvernoy, H. Morphometry

of the human cerebral cortex microcirculation: General characteristics and space-related profiles. *Neuroimage* **39**, 936–948 (2008).

48. *Cardiovascular Mathematics*. vol. 53 (Springer Milan, 2009).

49. Pries, A. R., Neuhaus, D. & Gaehtgens, P. Blood viscosity in tube flow: dependence on diameter and hematocrit. *American Journal of Physiology-Heart and Circulatory Physiology* **263**, H1770–H1778 (1992).

50. Windberger, U., Bartholovitsch, A., Plasenzetti, R., Korak, K. J. & Heinze, G. Whole blood viscosity, plasma viscosity and erythrocyte aggregation in nine mammalian species: Reference values and comparison of data. *Exp Physiol* **88**, 431–440 (2003).

51. Pries, A. R., Ley, K., Claassen, M. & Gaehtgens, P. Red cell distribution at microvascular bifurcations. *Microvasc Res* **38**, 81–101 (1989).

52. Gould, I. G. & Linninger, A. A. Hematocrit Distribution and Tissue Oxygenation in Large Microcirculatory Networks. *Microcirculation* **22**, 1–18 (2015).

53. Su, S.-W. Modelling Blood Flow and Oxygen Transport in the Human Cerebral Cortex. (2012).

54. Freear, A., El-Bouri, W. K. & Payne, S. J. Quantifying the effects of haematocrit variability in cerebral microvascular networks. in VPH2020 (2020).

55. Heijtel, D. F. R. *et al.* Accuracy and precision of pseudo-continuous arterial spin labeling perfusion during baseline and hypercapnia: A head-to-head comparison with 15O H2O positron emission tomography. *Neuroimage* **92**, 182–192 (2014).

56. Hsu, R. & Secomb, T. W. A Green's function method for analysis of oxygen delivery to tissue by microvascular networks. *Math Biosci* **96**, 61–78 (1989).

57. Baek, J.-H. *et al.* Predictive value of thrombus volume for recanalization in stent retriever thrombectomy. *Sci Rep* **7**, 15938 (2017).

58. Zhu, L. *et al.* Do Microemboli Reach the Brain Penetrating Arteries? *Journal of Surgical Research* **176**, 679–683 (2012).

59. Esipova, T. v. *et al.* Oxyphor 2P: A High-Performance Probe for Deep-Tissue Longitudinal Oxygen Imaging. *Cell Metab* **29**, 736-744.e7 (2019).

60. Gómez-de Frutos, M. C. *et al.* Identification of brain structures and blood vessels by conventional ultrasound in rats. *J Neurosci Methods* **346**, 108935 (2020).

61. Lugo-Hernandez, E. *et al.* 3D visualization and quantification of microvessels in the whole ischemic mouse brain using solvent-based clearing and light sheet microscopy. *Journal of Cerebral Blood Flow & Metabolism* **37**, 3355–3367 (2017).

62. Zhang, M. Q. *et al.* Three-dimensional visualization of rat brain microvasculature following permanent focal ischaemia by synchrotron radiation. *Br J Radiol* **87**, 20130670 (2014).

63. Zhang, L.-Y. *et al.* CLARITY for High-resolution Imaging and Quantification of Vasculature in the Whole Mouse Brain. *Aging Dis* **9**, 262 (2018).

64. Konduri, P. R., Marquering, H. A., van Bavel, E. E., Hoekstra, A. & Majoie, C. B. L. M. In-Silico Trials for Treatment of Acute Ischemic Stroke. *Front Neurol* **11**, 1–8 (2020).

65. Józsa, T. I. *et al.* A porous circulation model of the human brain for in silico clinical trials in ischaemic stroke. *Interface Focus* **11**, 20190127 (2021).

66. Padmos, R. M. *et al.* Coupling one-dimensional arterial blood flow to three-dimensional tissue perfusion models for in silico trials of acute ischaemic stroke. *Interface Focus* **11**, 20190125 (2021).

67. Józsa, T. I., Padmos, R. M., El-Bouri, W. K., Hoekstra, A. G. & Payne, S. J. On the Sensitivity Analysis of Porous Finite Element Models for Cerebral Perfusion Estimation. *Ann Biomed Eng* (2021) doi:10.1007/s10439-021-02808-w.

68. Miller, C. *et al.* In silico trials for treatment of acute ischemic stroke: Design and implementation. *Comput Biol Med* **137**, 104802 (2021).

69. Luraghi, G. *et al.* Applicability assessment of a stent-retriever thrombectomy finite-element model. *Interface Focus* **11**, 20190123 (2021).

70. Luraghi, G. *et al.* The first virtual patient-specific thrombectomy procedure. *J Biomech* **126**, 110622 (2021).

71. Smith, A. F. *et al.* Brain capillary networks across species: A few simple organizational requirements are sufficient to reproduce both structure and function. *Front Physiol* **10**, 1–22 (2019).

72. Payne, S. *Cerebral Autoregulation*. (Springer International Publishing, 2016). doi:10.1007/978-3-319-31784-7.

73. Payne, S. J. *Cerebral Blood Flow and Metabolism*. (WORLD SCIENTIFIC, 2017). doi:10.1142/10463.

74. Hall, C. N. *et al.* Capillary pericytes regulate cerebral blood flow in health and disease. *Nature* **508**, 55–60 (2014).

75. van der Wijk, A.-E. *et al.* Extravasation of Microspheres in a Rat Model of Silent Brain Infarcts. *Stroke* **50**, 1590–1594 (2019).

76. Reeson, P., Choi, K. & Brown, C. E. VEGF signaling regulates the fate of obstructed capillaries in mouse cortex. *Elife* **7**, 1–26 (2018).

SUPPLEMENTARY INFORMATION

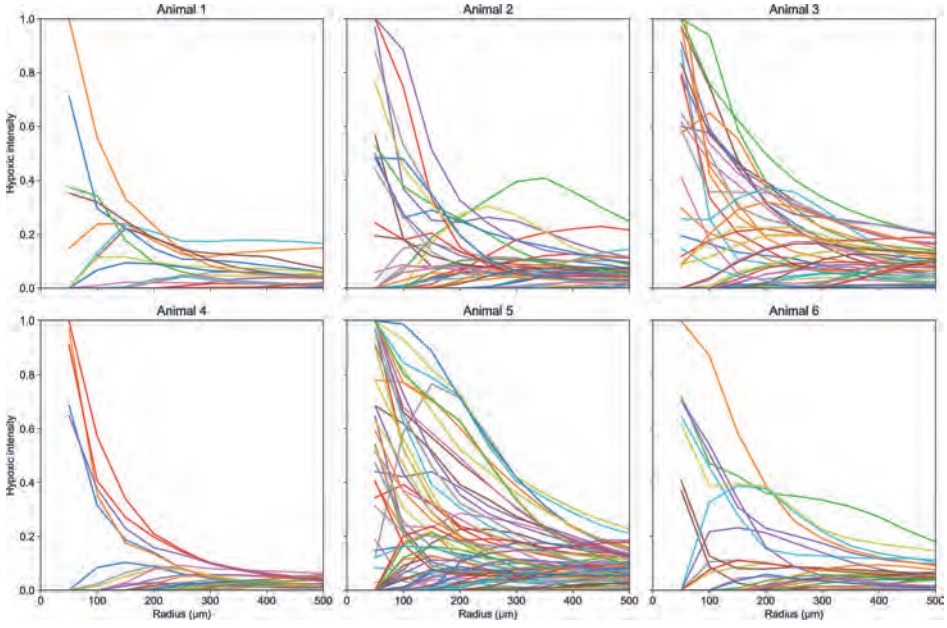

Figure S1. *Per animal the mean hypoxic intensity as a function of the distance from a microsphere.*

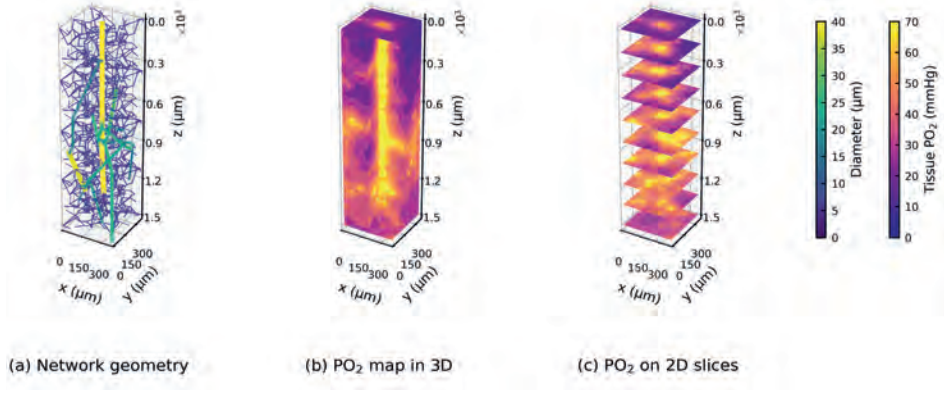

Figure S2. *The geometry of a column with the same arteriole geometry as shown in Fig. 7(a) but different capillary geometry* **(a)** *and its tissue oxygenation* **(b, c)**.

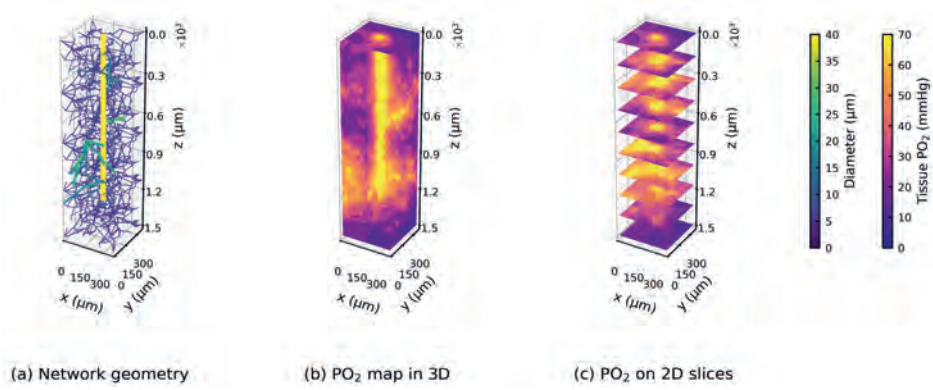

Figure S3. *The geometry of a column with the same capillary geometry as shown in Fig. 7(a) but different arteriole geometry* **(a)** *and its tissue oxygenation* **(b, c)**.

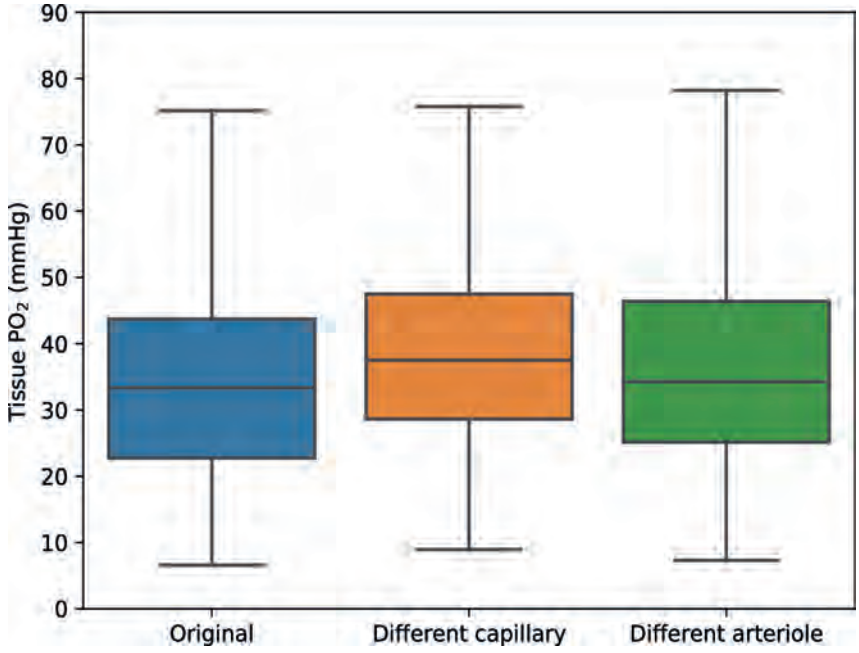

Figure S4. *Tissue PO_2 distribution in cortical columns shown in Figs. 7, S2 (using a different capillary cube) and S3 (using a different penetrating arteriole tree). The box shows the quartiles of the data (25%, 50% and 75%) and the whiskers min and max.*

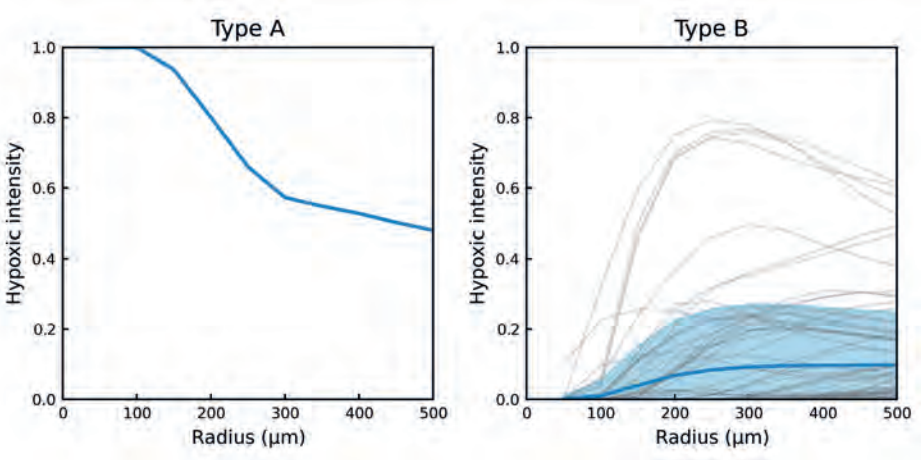

Figure S5. *Two types of hypoxic intensity in simulations.*

https://doi.org/10.1371/journal.pcbi.1010166.s006

S1 Data. *Manuscript data of pixel-based Gx function and hypoxic intensity in simulations and experiments.*

Chapter 3

QUANTITATIVE 3D ANALYSIS OF TISSUE DAMAGE IN A RAT MODEL OF MICROEMBOLIZATION

Theodosia Georgakopoulou[1], Anne-Eva van der Wijk[1], Erik N. T. P. Bakker[1], Ed van Bavel[1], on behalf of the INSIST investigators

[1] Amsterdam UMC, University of Amsterdam, Biomedical Engineering and Physics, Amsterdam Cardiovascular Sciences, Meibergdreef 9, Amsterdam, The Netherlands

J Biomech. (2021) 128:110723

ABSTRACT

There is a discrepancy between successful recanalization and good clinical outcome after endovascular treatment in acute ischemic stroke patients. During removal of a thrombus, a shower of microemboli may release and lodge to the distal circulation. The objective of this study was to determine the extent of damage on brain tissue caused by microemboli. In a rat model of microembolization, a mixture of microsphere sizes (15, 25 and 50 μm diameter) was injected via the left internal carotid artery. A 3D image of the left hemisphere was reconstructed and a point-pattern spatial analysis was applied based on G- and K-functions to unravel the spatial correlation between microsphere locations and the centroids of the induced hypoxic or infarcted regions. We show a spatial correlation between microsphere location and hypoxic or infarcted regions spreading up to a distance of 1000-1500 μm. These results imply that microemboli, which individually may not always be harmful, can interact and result in local areas of hypoxia or even infarction when lodged in large numbers.

INTRODUCTION

Among cardiovascular diseases, stroke is the second leading cause of death and the third leading cause of disability worldwide. Acute ischemic stroke (AIS; i.e. thrombotic or embolic occlusion of a cerebral artery) accounts for about 80% of stroke cases (1). In the past years, next to thrombolysis, endovascular treatment (EVT) has been included in the standard treatment of AIS. During EVT, the thrombus is removed by aspiration catheters or stent retrievers, more recently extended with proximal flow arrest and aspiration (2). EVT results in the majority of cases (up to 95%) in successful recanalization of the occluded vessel (3). However, a large proportion of the patients (63%) has poor functional outcome (4), which may be caused by suboptimal local perfusion of the brain tissue (5).

Despite the improvement of EVT devices, embolization of the distal arterial bed by fragments of the initial thrombus might occur (6, 7). This hypothesis is supported by *in vitro* models of EVT where during removal of a thrombus thousands of microemboli (<50 µm) release (8). While thrombolysis is performed prior to EVT in eligible patients (i.e. within 4.5h after symptom onset (9), it is unclear whether all microemboli resulting from EVT are lysed (10).

While occlusions caused by mm-size emboli will clearly contribute to poor reflow in the tissue downstream territory, it is much less clear what the effect is of the numerous small fragments. Given the syncytial nature of the capillary bed and the possibility for oxygen transfer by diffusion, the smallest fragments may be less harmful. Optimal design of clot retriever device therefore requires information on the effects of these smaller fragments. In particular, there is much attention for the development of *in silico* clinical trials on new intervention strategies in ischemic stroke (11). Such trials require a detailed and quantitative understanding of local tissue damage by micro-occlusions in order to contribute to the improvement of device design.

In a previous study, we found that polystyrene microspheres (MS) occlude arteriole-sized vessels in the brain, leading to tissue hypoxia and infarction after 24h (12). In the present study, we used this rat model of impermeable thrombi to quantify spatial characteristics of tissue damage following microembolization of the brain. We reconstructed a brain volume of the intervention hemisphere and segmented and quantified the brain damage. Subsequently, we studied the spatial distribution of microemboli and hypoxic or infarcted regions and explored their spatial relationships in the brain.

METHODS

Detailed Methods, including all experimental procedures and the spatial analysis of MS and brain damage can be found in the Supplementary Information.

In short, we injected MS in the brain of six rats (3 male, 3 female). Buprenorphine (Temgesic™, 0.05 mg/kg, Schering-Plough, Welwyn Garden City, Hertfordshire, UK) was used as analgesic and the animals were anesthetized with 2-2.5% isoflurane in 1 L/min O_2. The 3D spatial distribution of MS locations and centroids of hypoxic (HYP) and infarcted (INF) regions was tested using a point-pattern analysis based on the G- and

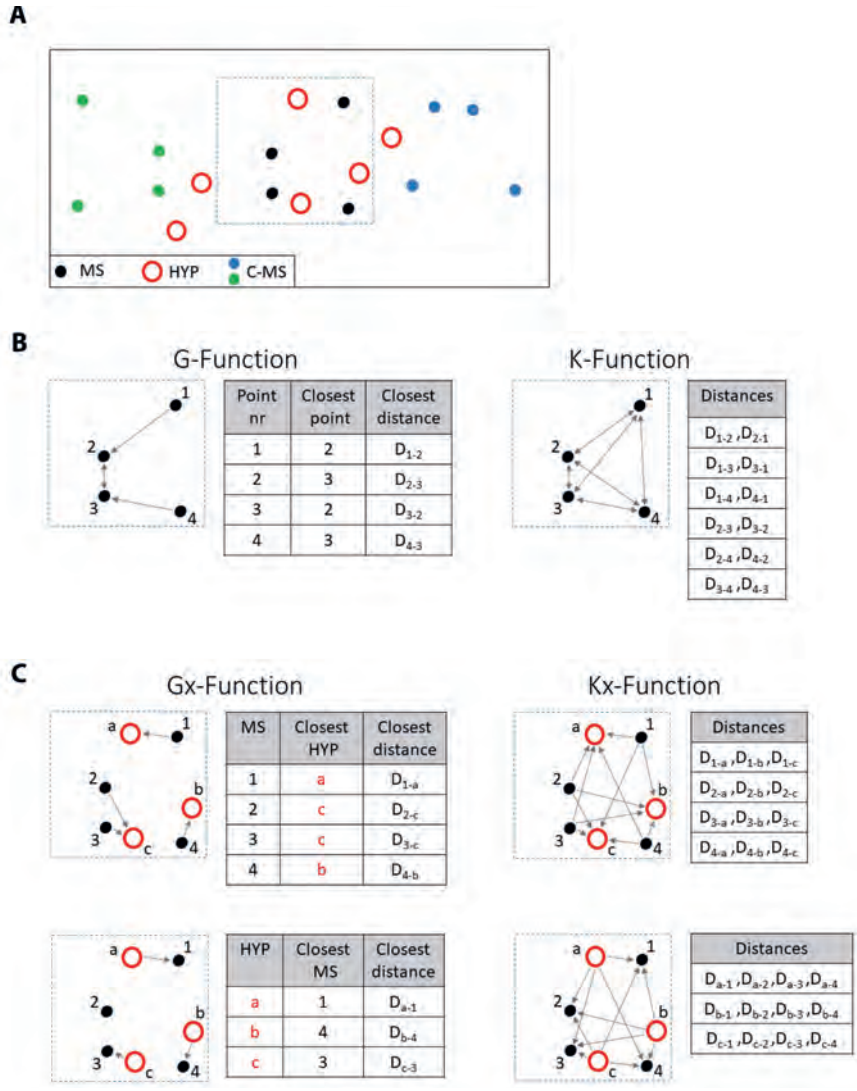

Figure 1. Schematic explanation of spatial analysis. (A) *The experimental data depicted as black filled circles (MS), and red open circles (HYP) and two scenarios of the generated data depicted as blue or green filled circles (C-MS). For the Monte-Carlo simulations, the generation of C-MS was repeated 250 times. Note that the generated C-MS have similar distribution of interparticle distances as the experimental MS data. G- and K-functions were used to describe the spatial relations within and between experimental and generated data. The experimental points within the dotted area are used to explain these functions in the following panels.* ***(B)*** *G-function: Per MS, the closest neighbor was detected and the distance (grey arrows) was determined as shown in the table. The G-function is the cumulative density function of these nearest neighbor distances. K-function: Grey arrows indicate the distances from all MS to all other MS (see table). The K-function is the cumulative density function of all these distances.* ***(C)*** *Gx-function: Grey arrows indicate distances from MS to their nearest HYP (upper panel) and vice versa (lower panel). Per MS or HYP, the closest neighbor is detected and the distance is determined as shown in the tables. The Gx-function is the cumulative density function of the nearest neighbor distances. Kx-function: arrows indicate distances from MS to all HYP (upper panel) and from HYP to all MS (lower panel). Note that for Kx but not Gx, the distances are the same whether measured from MS or HYP (see tables). The cumulative densities of all the distances are the Kx-function. MS: Microspheres, HYP: Hypoxic centroids, C-MS: Generated control points for MS.*

K-functions (Fig. 1). These are cumulative density functions of respectively the nearest neighbor distances (NND) and all distances between point events. The point events could be homogeneous (e.g. only MS) or heterogeneous (e.g. MS and HYP). The latter are denoted as cross-G (Gx) and cross-K (Kx) functions. The experimental distributions were tested against Monte-Carlo simulations of control locations for MS or HYP based on null hypotheses (H_0).

Prior to the calculation of Gx- and Kx-functions, the spatial distribution of MS in the brain was tested. Thereto, MS distributions were compared to the H_0 of purely randomly dispersed points, generated with Monte-Carlo simulations. As this analysis showed significant clustering of MS in the brain tissue, we generated control locations (C-MS) with similar G- and K-functions as the MS. The same procedure was repeated for the generation of control points representing HYP (C-HYP). These generated clustered control points were then used to evaluate the spatial relation between MS and HYP based on the Gx- and Kx-functions. For the spatial relation between MS and INF, the analysis was limited to the calculation of Gx- and Kx-functions for distances from INF to either MS or C-MS, due to the low INF numbers.

RESULTS

Stochastic nature of MS-induced hypoxic regions distribution

Figure 2 provides an example of the distribution of MS and their effect on local hypoxia. Figure 2C demonstrates a 50 µm thick section, with clearly discernible MS and demarcated zones of hypoxia. Figure 2D shows x and y coordinates of MS and HYP, based on the full stacked image of 10 consecutive histological sections, totaling 500 µm. As can be seen, the spatial relationship between MS and the consequent hypoxia appeared to be quite diffuse, rather than a one-on-one relationship between MS and hypoxic regions in the near vicinity. In addition, MS appeared to be clustered.

Size distribution of hypoxic and infarcted regions

The number of MS that reached the brain varied between animals, ranging from 43 to 190 per reconstructed brain volume (Table 1 and Supplementary Information Table S1). All animals had signs of hypoxia and infarction (Table 1 and Supplementary Information Fig. S1). On average, 82±41 hypoxic regions and 4±2 infarctions were detected in the reconstructed hemispheres. Only 10% of the hypoxic regions was ≥0.01 mm^3, whereas the majority of infarcted regions was ≥0.01 mm^3 (Fig. 3A) and infarctions were ~30 times larger in size (Fig. 3B).

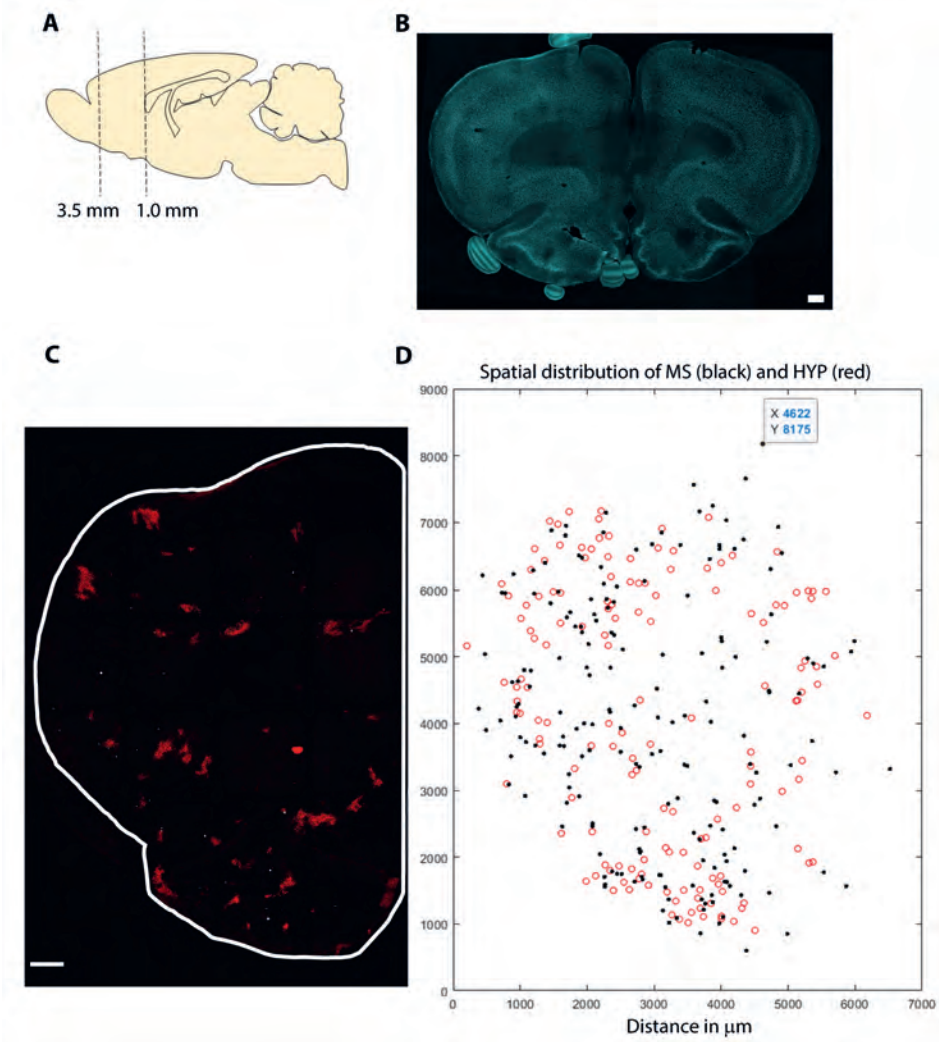

***Figure 2.* (A)** *Schematic drawing of a rat brain. Dashed lines indicate the bregma coordinates where the brain sections were made. Only ten consecutive sections were selected for the reconstruction of the brain volume.* **(B)** *Representative 50 µm thick coronal section stained with NeuN antibody indicating the anatomy of the brain structures. Scale bar = 500 µm.* **(C)** *Maximum intensity projection of the same 50 µm thick coronal section as in (B) of only the intervention hemisphere. Distribution of MS (white dots) of different sizes and hypoxic regions (red). Scale bar = 500 µm.* **(D)** *Spatial 2D distribution of MS (black points) and HYP (red circles) of a reconstructed brain hemisphere (500 µm thick). MS: Microspheres, HYP: Hypoxic centroids.*

Table 1. *Number and density of MS lodged in 500 µm thick reconstructed brain volumes and the numbers of the hypoxic and infarcted regions per animal (N=6 animals). MS: Microspheres.*

Animal	Number of lodgded MS/ (MS density (MS/mm³))	Number of hypoxic regions	Number of infarcted regions
1	190 (10.6)	152	5
2	81 (4.9)	83	2
3	43 (2.3)	27	6
4	79 (4.3)	70	1
5	115 (5.9)	67	4
6	105 (3.9)	94	4

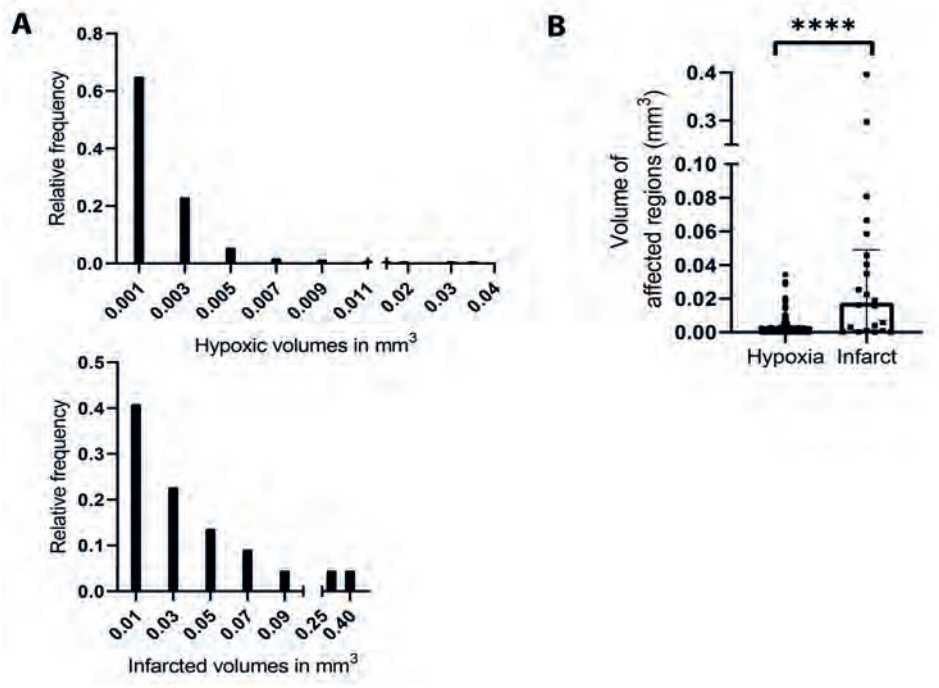

Figure 3. Comparison between hypoxic and infarcted regions. (A) *Size distribution of hypoxic (upper graph) and infarcted (lower graph) regions, as measured in a 500 µm reconstructed volume of the intervention hemisphere.* ***(B)*** *Hypoxic regions caused by microembolization are significantly smaller than the infarcted regions. Data are depicted as median with interquartile range. ****P<0.0001, Mann-Whitney. Pooled data from six animals (N=6).*

Correlation between MS density and brain damage

Considering the variable number of MS detected in the brain between animals, we assessed whether there is a correlation between MS density and 1) the total volume and 2) the number of hypoxic and infarcted regions. Figure 4A shows a positive correlation between MS density and hypoxia, both in terms of number of hypoxic regions and hypoxic volume (Fig. 4A; left graph: Pearson R^2=0.87, P=0.024 and right graph: Pearson R^2=0.91, P=0.003). In contrast, MS density was not correlated with the number of infarcted regions (Fig. 4B; left graph: Pearson R^2=0.02, P=0.809), nor with the total infarcted volume (Fig. 4B; right graph: Pearson R^2=0. 51, P=0.111). Notably, the total infarcted volume correlated with the total hypoxic volume (Fig. 4C Pearson R^2=0. 68, P=0.042).

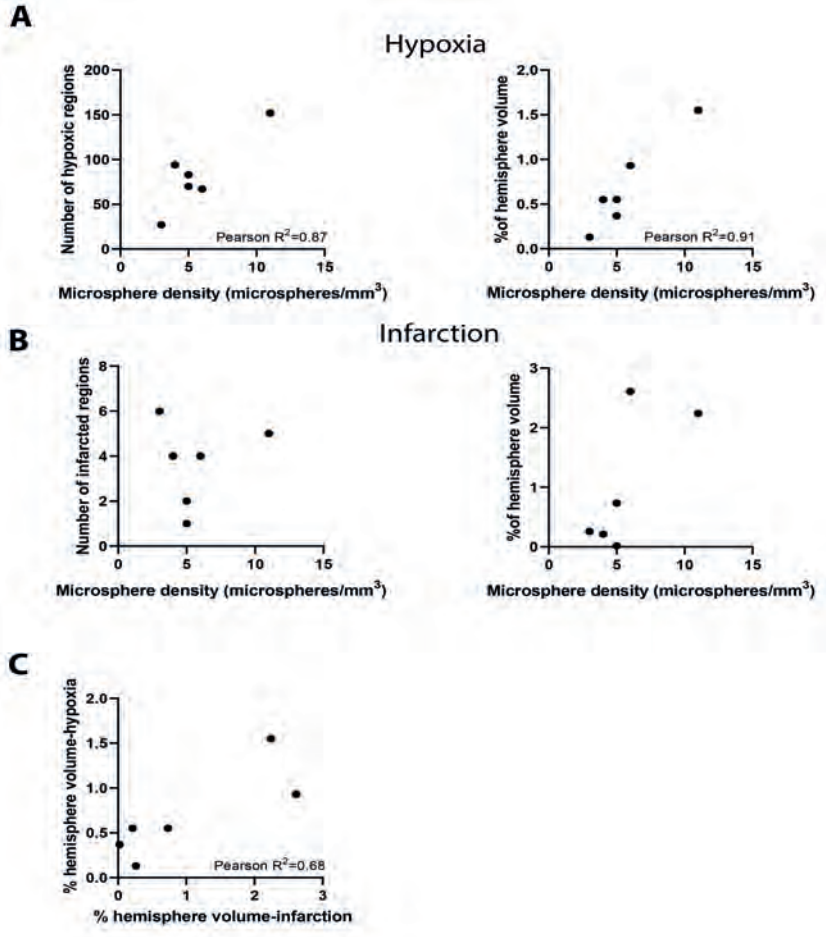

Figure 4. Correlation between MS density and number or total volume of hypoxic or infarcted regions in a 500 µm reconstructed volume of the intervention hemisphere. ***(A)*** *Significant positive correlation between MS density and number (left graph; Pearson's correlation coefficient, R^2=0.87, *P=0.024) or total volume of hypoxic regions (right graph; Pearson's correlation coefficient, R^2 = 0.91, **P < 0.01).* ***(B)*** *No significant correlation between MS density and the number (left graph) or total volume (right graph) of infarcted regions.* ***(C)*** *Significant positive correlation between total hypoxic volume and total infarcted volume (Pearson's correlation coefficient, R^2=0.68, *P=0.042). N=6 animals. MS: Microspheres.*

Point-pattern spatial analysis of MS and tissue hypoxia or infarction

Based on the above observations, we conducted a point-pattern spatial statistical analysis of our data. First, we tested whether MS or HYP were clustered. Figure 5A-B shows representative G- and K-functions (black) of the experimental spatial distributions of MS. Also shown are the G- and K-functions of fully randomly distributed control points (blue), generated by Monte-Carlo simulations (250 repeats). All functions were left-shifted as compared to the random controls, indicating that MS locations were clustered in this

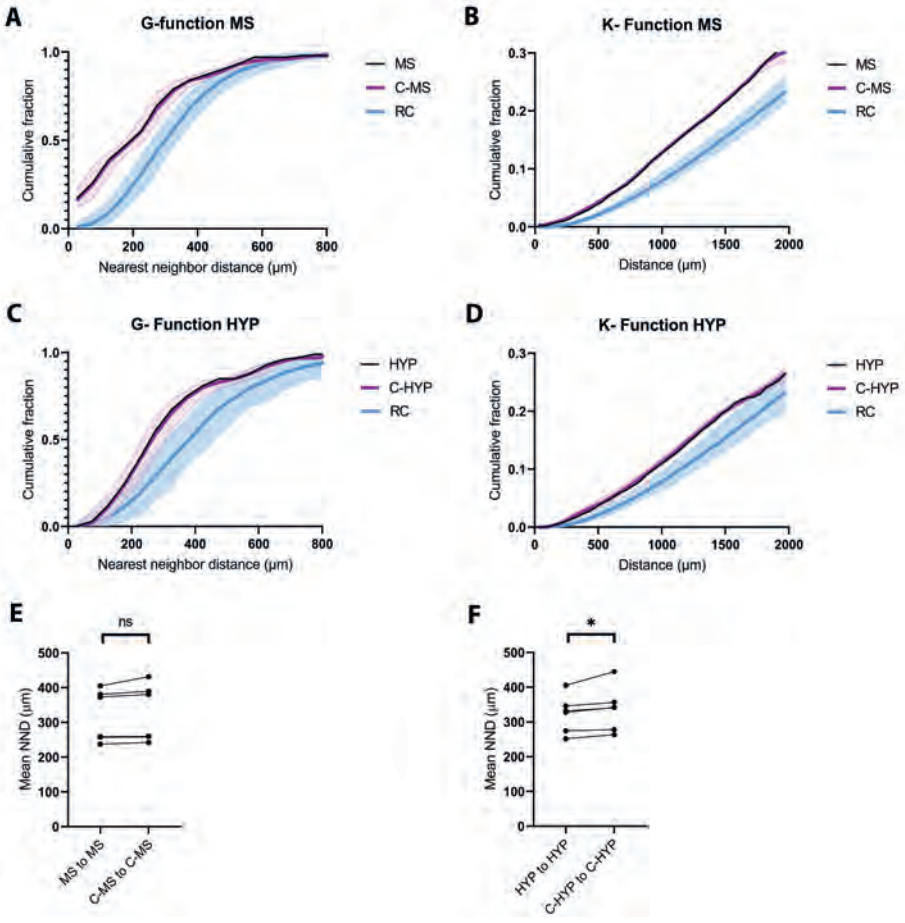

Figure 5. Representative example of MS or HYP clustering and generation of 'clustered' control points for MS and HYP. (A) *G-Function: Cumulative densities of NND between MS (black curve; experimental data) versus RC (blue curve, simulated data) and C-MS (magenta curve; simulated data).* ***(B)*** *K-Function: Cumulative densities of distances between all MS versus RC and C-MS.* ***(C)*** *G-Function: Cumulative densities of NND between HYP versus RC and C-HYP.* ***(D)*** *K-Function: Cumulative densities of distances between all HYP versus RC or C-HYP.* ***(E,F)*** *Pairwise comparisons of mean NND between experimental data and C-MS or C-HYP. Lines connect dots corresponding to mean NND measured in the intervention hemisphere of the same individual rats. ns = not significant, *P<0.05 paired t-test, N=6 animals. The filled area indicates confidence intervals. RC: Randomly generated (i.e. with homogeneous probability over the tissue and independently from each other) control points, MS: Microspheres, C-MS: Control points for MS, HYP: Hypoxic centroids, C-HYP: Control points for HYP, NND: Nearest neighbor distances.*

example. The curves were significantly different over a large distance range (Fischer's method, n=6 animals, data not shown). The same analysis was done for HYP, with similar results (Fig. 5C-D; black and blue).

In order to analyze the spatial correlations between MS and HYP, we therefore attempted to generate clustered control points with equal G- and K-functions. As indicated by the mean and confidence interval of these generated clustered control points (Fig. 5A-D, magenta), tight matches of the G- and K-functions to the experimental data were obtained.

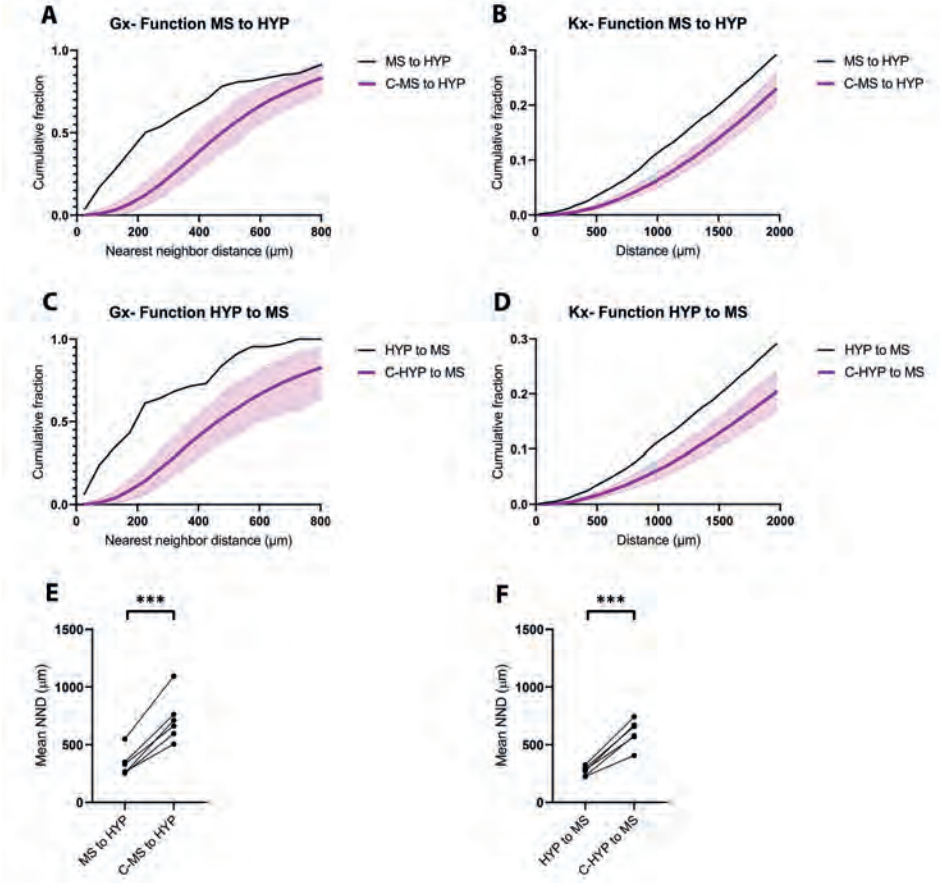

Figure 6. Representative examples of clustering between MS and HYP and pairwise comparisons of mean NND. (A) *Gx-function: Cumulative densities of NND between MS and HYP (black curve; experimental data) and between C-MS and HYP (magenta curve; simulated data).* ***(B)*** *Kx-function: Cumulative densities of distances between all MS and HYP and between all C-MS and HYP. Note, Kx-function for distances between all MS and HYP is the same as HYP and MS.* ***(C)*** *Gx-function: Cumulative densities of NND between HYP and MS and between C-HYP and MS.* ***(D)*** *Kx-function: Cumulative densities of distances between all HYP and MS and between all C-HYP and MS.* ***(E, F)*** *Pairwise comparisons between mean NND from MS or C-MS to HYP and between mean NND from HYP or C-HYP to MS. Lines connect dots corresponding to NND measured in the intervention hemisphere of the same individual rats. ***P<0.001 paired t-test, N=6 animals. The filled area indicates confidence intervals. MS: Microspheres, C-MS: Control points for MS, HYP: Hypoxic centroids, C-HYP: Control points for HYP, NND: Nearest neighbor distances.*

Figure 5E-F shows the mean NND of experimental data versus the clustered control points for the six animals. These distances were different between animals, related to the total number of MS and HYP. For five out of six experiments, the NND of the generated points tightly matched that of the data, with somewhat less matching in the sixth case.

Next, we set out to study the spatial relationship between MS and HYP, first by analyzing the distances from MS to HYP (Fig. 6A-B) and then from HYP to MS (Fig. 6C-D). Representative Gx- and Kx-functions of the experimental spatial distributions (black) between MS and HYP, versus the simulated spatial distributions (magenta) between C-MS and HYP are shown in Fig. 6A-B. Figure 6A demonstrates substantial variation in experimental NND (black), with 50% of the closest HYP being further away than 200 µm from MS. Still, comparison to the Monte-Carlo simulations (magenta) that were based on absence of spatial correlation, revealed that HYP are closer to MS than to C-MS. This finding indicates a spatial correlation between MS and their closest HYP for this example. Spatial correlation was also confirmed in the Kx-function between MS and all HYP, as shown in Fig. 6B. There, the experimental spatial distribution of distances between MS and HYP (black), was left-shifted compared to the simulated data (magenta) up to tested distances of 2000 µm. Similar results were found in the reverse distance analysis, from HYP to either their closest MS (Fig. 6C), or all MS (Fig. 6D) for this particular example. Figure 6E-F shows the mean NND of experimental data versus the Monte-Carlo simulated data for the six animals. Pairwise comparison of mean NND of MS or C-MS to HYP indicates that the closest HYP were on average 389 ± 107 µm closer to MS than control points (Fig. 6E; P=0.0003, paired t-test). MS were found to be on average 332 ± 87 µm closer to HYP than control points (Fig. 6F; P=0.0002, paired t-test).

Figure 7 shows the difference between experimental Gx- and Kx-functions and their Monte-Carlo simulations for the six animals (ΔGx and ΔKx respectively). ΔGx was significantly positive up to the tested distance of 800 µm (Fig. 7A). Note that the majority of MS and HYP clustering took place within the first 200 µm. ΔKx was significantly positive up to the tested distance of 2000 µm, with the plateau around 1500 µm (Fig. 7B). Similar spatial correlations were found for the reverse analysis of MS to their closest HYP (Fig. 7C) or all HYP (Fig. 7D). Taken together, the above data demonstrate a spatial correlation over hundreds of micrometers between MS and HYP.

Lastly, we tested the spatial relation between MS and INF. Figure 8 shows the ΔGx and ΔKx curves for the six animals, between experimental data and their Monte-Carlo simulations. Figure 8A shows that clustering of INF and their closest MS, is maximal at a distance of 200 µm. Figure 8B shows a correlation between MS and INF up to a distance of 2000 µm with a maximum at 1000 µm.

DISCUSSION

Our study addressed effects of microvascular occlusions as could occur after EVT, and provides quantitative spatial data on tissue hypoxia and infarction. In particular, we found that microembolization caused numerous hypoxic and a few infarcted regions, in the wide

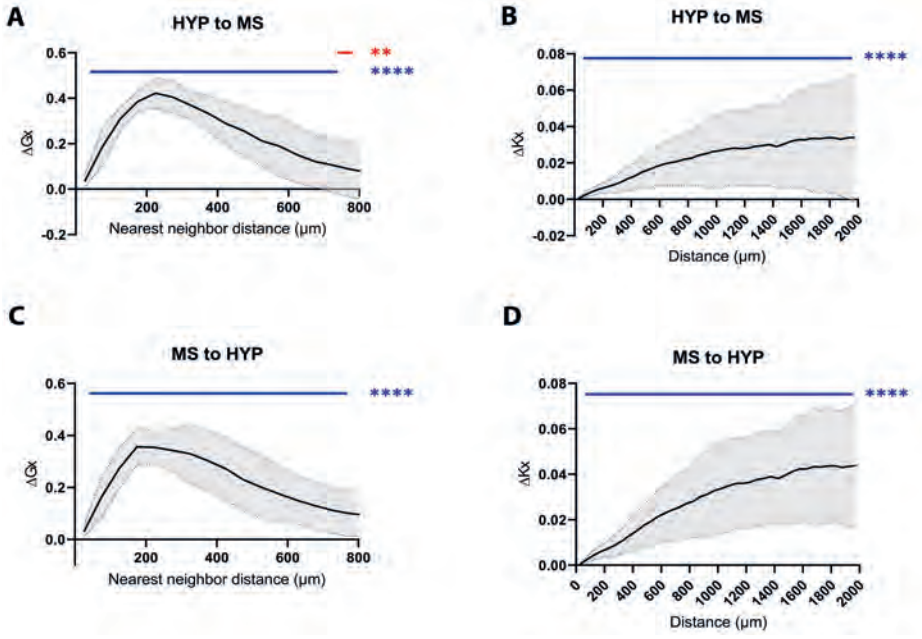

Figure 7. Experimental data minus average of Monte-Carlo simulations. (A) *ΔGx-function: Cumulative densities of NND between HYP and MS (experimental data) minus mean cumulative densities of NND between C-HYP and MS (simulated data, assuming no relation between MS and HYP).* **(B)** *ΔKx-function: Cumulative densities of distances between all HYP and MS (experimental data) minus mean cumulative densities of distances between all C-HYP and MS (simulated data).* **(C)** *ΔGx-function: Cumulative densities of NND between MS and HYP (experimental data) minus mean cumulative densities of NND between C-MS and HYP (simulated data).* **(D)** *ΔKx-function: Cumulative densities of distances between all MS and HYP (experimental data) minus mean cumulative densities of distances between all C-MS and HYP (simulated data). The filled area indicates standard deviation for the ΔGx- or ΔKx-functions over the six animals. The data in B and D are equal by definition, but the Monte-Carlo simulations are not. MS: Microspheres, C-MS: Generated control for MS, HYP: Hypoxic centroids, C-HYP: Generated control for HYP, NND: Nearest neighbor distances. **P<0.01(red horizontal lines above the curve indicate to which distance interval the significance of the data is **P<0.01), ****P<0.0001(blue horizontal lines above the curve indicate to which distance interval the significance of the data is ****P<0.0001) Fischer's method p-value, N=6 animals.*

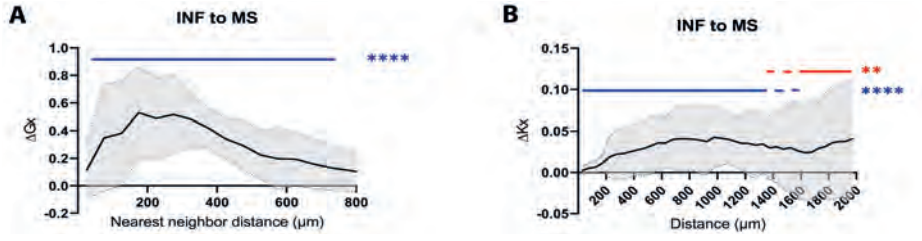

Figure 8. Experimental data minus average of Monte-Carlo simulations. (A) *ΔGx-function: Cumulative densities of NND between INF and MS (experimental data) minus mean cumulative densities of NND between INF and C-MS (simulated data).* **(B)** *ΔKx-function: Cumulative densities of distances between all INF and MS (experimental data) minus mean cumulative densities of distances between all INF and C-MS (simulated data). The filled area indicates standard deviation for the ΔGx- or ΔKx-functions over the six animals. MS: Microspheres, INF: Infarcted centroids, C-MS: Generated control points for MS, NND: Nearest neighbor distances. **P<0.01(red horizontal lines above the curve indicate to which distance interval the significance of the data is **P<0.01), ****P<0.0001(blue horizontal lines above the curve indicate to which distance interval the significance of the data is ****P<0.0001) Fischer's method p-value, N=6 animals.*

vicinity around lodged MS. The effects of MS were highly stochastic in nature, with respect to both volume of affected tissue and distance from MS. A point-pattern analysis between MS locations and centroids of HYP or INF revealed a spatial correlation over hundreds of micrometers. To our knowledge, these data are unique and map the complex interactions of multiple arterial occlusions due to lodged MS.

Justification of spatial analysis and interpretation of spatial correlations

The relationship between occlusion and brain damage is complex and depends on the geometry of the vascular bed. A shower of microemboli sized between 15 µm and 50 µm targets the vascular bed at the level of penetrating arteries, arterioles and capillaries. Penetrating arteries (20-90 µm diameter) bridge the pial vascular network of the brain surface with the intracortical microvascular network (7-20 µm diameter) (13). In contrast to the highly anastomosing architecture of both the pial and intracortical vascular networks, the penetrating arteries are mostly lacking anastomoses (14). Thus, occlusions in the network at particularly this level, because of a microembolic shower, could lead to blood flow reduction and micro-infarcts.

In order to determine the spatial relationship of MS with damage resulting from obstruction of the microvasculature, we applied a point-pattern spatial analysis. The difference of the Gx-functions from their Monte-Carlo simulations, which assumed no relation between MS and hypoxic regions, was maximal for a distance (NND) of ~200 µm (Fig. 7A,C). This finding indicates that a single MS induces a risk for hypoxia in a surrounding tissue sphere that extents up to this distance. For the Kx-function, the difference with the control (Fig. 7B,D) continued to increase up to the largest analyzed distance of 2000 µm, with most of the effect up to ~1500 µm. This finding shows that up to this distance the number of MS surrounding hypoxic areas was larger than expected based on uncorrelated distributions of spheres and hypoxic areas and that even distant MS still may cause tissue hypoxia. In an attempt to explain these results, we propose that risk zones of two or more MS extend towards each other. Figure 9 provides a schematic representation of this effect. Such a cooperative effect of multiple MS could relate to the blocking of the vascular bed at multiple entrance vessels to a tissue area that then becomes hypoxic. These entrance vessels could be arterioles, small local collaterals or part of the continuous capillary bed. However, a more careful interpretation of the current data requires simulation of these processes, based on vascular topology data.

We included in our analysis three MS sizes, which in turn block the vessels at different levels and thus most likely exert their effects to different distances relative to the site of occlusion (15). Tissue damage resulting from microvascular occlusions depends on the clot location. Thus, it has been shown that occlusion of a single pial vessel or a single capillary results in focal ischemia and is rather harmless (16, 17). In contrast, penetrating vessels are a critical bottleneck in cortical blood flow, affecting blood flow in a large region downstream of an occlusion (14) and leading to micro-infarcts (17). Data coming from single penetrating artery occlusions show that brain damage spans up to a radius of ~230 µm and a depth of ~1200 µm relative to the pial surface (cortical columns) (17). The radii

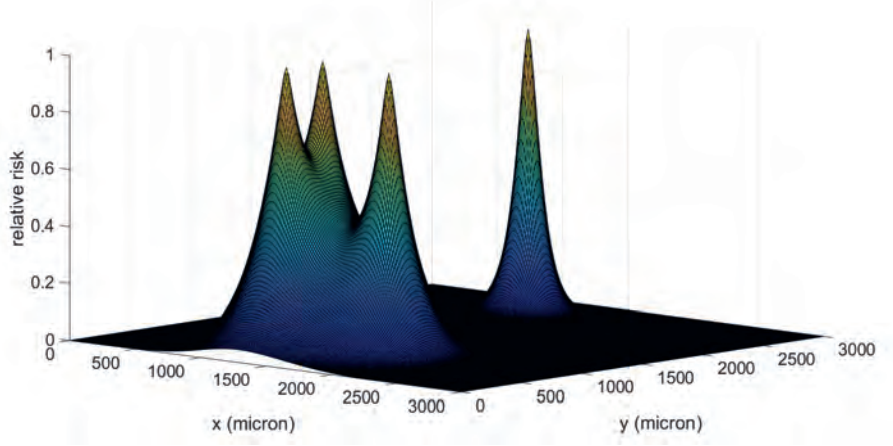

Figure 9. Illustration of the spatial analysis interpretation. *Indicated is the combined effect of four MS on the risk of developing hypoxia in the surrounding tissue. Each microsphere (MS) induces a risk that becomes smaller with increasing distance. An isolated MS at the right causes a risk for hypoxia that extends to around 200 µm, explaining the ΔGx-function. Three relatively close MS on the left generate a much broader risk profile, reflecting a collaborative effect and explaining the shallow and extended ΔKx-function.*

of influence found in the current study are of the same order. One might suspect that the extent of the brain damage caused by the largest MS could partly explain the large radii found here, in the sense that the damage caused by the larger may overshadow the effect of the smaller ones. However, we believe that this is highly unlikely, firstly because the majority of MS in our model is of 15 µm and secondly due to the shape and distribution of hypoxic regions in the intervention hemisphere, where they do not necessarily originate from the brain surface as cortical column-shaped regions. Consequently, we believe that there is a cooperative effect between the smaller MS, which spreads in the brain tissue. In a future study, we aim to isolate the effect of different MS sizes on brain tissue damage by injecting each MS size separately per group.

In addition to the high number of hypoxic regions, we observed a few much larger infarcted regions. MS were clustered around infarcts, with Gx- and Kx-functions (Fig. 8) that resemble those of the hypoxic areas (Fig. 7), and we suggest that also the infarct zones were caused by the interactive effects of multiple MS in the wide surrounding. The large size and small number suggest that the infarcted regions develop from merging hypoxic zones. Yet, it is not obvious from the data if and how the local and more remote MS affect this process.

Limitations of the study

We investigated hypoxia and infarction only at 24h after microembolization. Other timepoints could provide insight into the progression of hypoxia towards infarction or recovery. Of interest, in a previous study, total hypoxic volume became less after 7 days, without a growth in infarct volume in this microembolization model, pointing at recovery (12). For the full analysis and understanding of such events several factors should be taken

into account, in addition to the size and number of MS (18). These include the arterial topology and notably the percentage of anastomosing arteries per arterial level (13). Although the segmentation of the numerous arterioles and capillaries and the generation of reliable connectivity between these segments are major technical obstacles, microvascular network data could help building more detailed mechanistic models. Moreover, further experimental work is needed. We are currently developing techniques for clearing of brain tissue and 3D imaging of much larger volumes by light sheet microscopy (19, 20). Another aspect not addressed in the current study is the differential vulnerability of brain regions to an ischemic environment (21, 22), notably the difference between gray and white matter.

When we designed these experiments, we expected to find a much more localized spatial relation between lodged MS and the induced hypoxic and infarcted areas. We do not believe that the wide dispersion results from experimental noise. Thus, as shown in Fig. 2 the hypoxia staining is characterized by clearly discernable zones. While the estimated number and volumes of these hypoxic regions depend on segmentation choices, the stochastic nature of the spatial correlations is expected to be rather insensitive to the segmentation procedure. Indeed, in an alternative approach (not shown) we determined mean hypoxia fluorescence as a function of distance from the MS on a pixel basis, avoiding the need for segmentation. This type of analysis resulted in a profile that is consistent with the Kx-function. It remains to be tested whether the stochastic effects of lodged MS are homogeneous over the tissue and equal in all directions

Since we used tissue volumes of 500 µm in thickness, we expect that MS outside this volume have influenced the hypoxia and infarct patterns. The contribution of these MS is hard to establish, but is expected to add noise to spatial relationships when considering larger distances. Some care should therefore be taken in interpretation of the distribution functions at large distances. At small distances, where these boundary effects are less relevant, we found clear differences in the Gx- and Kx-functions compared to those of the control points. We therefore suggest that the stochastic spatial relation between lodged MS and hypoxia is a direct consequence of the effects of the MS on perfusion, with resulting hypoxia depending on the balance of oxygen delivery (by remaining perfusion or diffusion) and oxygen consumption (23).

The spatial distribution analysis between homogeneous point events showed clustering of MS. This complicated the statistical analysis but we believe that by including clustering in the Monte-Carlo simulations we adequately accounted for this. Numerous studies in the past applied MS infusion in order to determine the flow distribution in the brain and other organs (24) and showed regional cerebral blood flow variations (25). The fact that MS are distributed according to the flow, together with the heterogeneity in vascular density between gray and white matter (26), could partly explain why MS were clustered. Since we compensate for clustering among MS in our analysis, possible fluctuations of the cerebral blood flow due to isoflurane-induced vasodilation (during MS injection), are not very likely to affect the spatial relation between MS and induced brain damage.

The number of MS found in the brain varied between the animals. We believe that this may be caused by the temporal ligation of external carotid artery and lifting of the

common carotid artery (with a suture placed under it) during the surgery. Even though it is hard to trace back all injected MS, we believe that this intervention may have temporarily led to blood flow redistribution between the brain regions, or partial reflux of MS after the injection.

The variation in the number of lodged MS between the animals had an effect on the extent of the brain damage. Therefore, we checked the correlation between MS density and resulting brain damage and found significant positive correlation for hypoxia, but not for infarction. Since the varying number of MS affects both the number and total volume of hypoxic regions, it seems that the numerous but smaller MS sizes also contribute to the generation of local hypoxia. The absence of correlation between MS density and the number of infarcted regions could be attributed to the low number of infarcted regions and the low number of experiments (N=6). However, there is a trend to positive correlation between MS density and total infarcted volume, though not significant (Fig. 4B right graph) and a significant correlation between total infarcted and total hypoxic volume (Fig. 4C).

Conclusion

We applied a 'black box' analysis of MS effects on brain tissue. We found that these MS have very stochastic effects on brain tissue over a relatively large distance, with an amplified effect of multiple MS. This work provides quantitative data on MS-induced tissue hypoxia and infarction that could serve for building *in silico* models of stent retrievers and aspiration catheters, which can be used for platforms like *IN Silico* trials for treatment of acute Ischemic STroke (INSIST).

ACKNOWLEDGEMENTS

INSIST investigators

Charles Majoie[1], Henk Marquering[6], Ed van Bavel[6], Alfons Hoekstra[14], Diederik Dippel[2], Hester Lingsma[4], Aad van der Lugt[3], Noor Samuels[2,3,4], Nikki Boodt[2,3,4], Yvo Roos[1], Simon de Meyer[5], Senna Staessens[5], Sarah Vandelanotte[5], Praneeta Konduri[1,6], Nerea Arrarte Terreros[1,6], Bastien Chopard[7], Franck Raynaud[7], Remy Petkantchin[7], Mikhail Panteleev[11], Alexey Shibeko[11], Karim Zouaoui Boudjeltia[15], Vanessa Blanc-Guillemaud[8], Francesco Migliavacca[9], Gabriele Dubini[9], Giulia Luraghi[9], Jose Felix Rodriguez Matas[9], Sara Bridio[9], Patrick Mc Garry[10], Michael Gilvarry[12], Ray McCarthy[12], Kevin Moerman[10], Behrooz Fereidoonnezhad[10], Anushree Dwivedi[12], Sharon Duffy[12], Stephen Payne[13], Tamas Jozsa[13], Sissy Georgakopoulou[6], Raymond Padmos[14], Victor Azizi[14], Claire Miller[14], Max van der Kolk[14]

Affiliations

[1] Department of Radiology and Nuclear Medicine, Amsterdam University Medical Centers, location AMC, Amsterdam

[2] Department of Neurology, Erasmus MC University Medical Center, PO Box 2040, 3000 CA Rotterdam, the Netherlands

[3] Department of Radiology, Erasmus MC University Medical Center, PO Box 2040, 3000 CA Rotterdam, the Netherlands
[4] Department of Public Health, Erasmus MC University Medical Center, PO Box 2040, 3000 CA Rotterdam, the Netherlands
[5] Laboratory for Thrombosis Research, KU Leuven Campus Kulak Kortrijk, Kortrijk, Belgium
[6] Department of Biomedical Engineering & Physics, Amsterdam University Medical Centers, location AMC, Amsterdam
[7] Computer Science Department, University of Geneva, CUI, 7 route de Drize, 1227 Carouge, Switzerland
[8] Institut de Recherches Internationales Servier, Coubevoie Cedex, France
[9] Department of Chemistry, Materials and Chemical Engineering 'Giulio Natta', Politecnico di Milano, Piazza Leonardo da Vinci 32, 20133 Milano, Italy
[10] National Centre for Biomedical Engineering Science, School of Engineering, National University of Ireland Galway, Ireland
[11] Faculty of computational mathematics and cybernetics, Moscow
[12] Cerenovus, Galway Neuro Technology Centre, Galway, Ireland
[13] Department of Engineering Science, University of Oxford, Parks Road, Oxford OX1 3PJ, UK
[14] Computational Science Lab, Faculty of Science, Institute for Informatics, University of Amsterdam, Amsterdam, Netherlands
[15] Laboratory of Experimental Medicine (ULB222), Faculty of Medicine, Université libre de Bruxelles, CHU de Charleroi, Belgium

SOURCES OF FUNDING

This project was funded from the European Union's Horizon 2020 research and innovation program under grant agreement No 777072 (INSIST). AEvdW was funded by Neuroscience Amsterdam (project number NDIS-2019-03)

CONFLICT OF INTEREST

The authors declare that the research was conducted in the absence of any commercial or financial relationships that could be construed as a potential conflict of interest.

AUTHOR CONTRIBUTIONS

ENTPB, EvB, AEvdW and TG designed the experiments; TG and AEvdW performed the surgeries; TG and EvB analyzed the data and wrote the manuscript; AEvdW, ENTPB and EvB contributed to editing of the manuscript. All authors read and approved the final version of the manuscript.

REFERENCES

1. Bamford, J., Sandercock, P., Dennis, M., Burn, J. & Warlow, C. Classification and natural history of clinically identifiable subtypes of cerebral infarction. *Lancet* **337**, 1521-1526 (1991).
2. Munich, S. A., Vakharia, K. & Levy, E. I. Overview of Mechanical Thrombectomy Techniques. *Neurosurgery* **85**, S60-s67 (2019).
3. Bhaskar, S., Stanwell, P., Cordato, D., Attia, J. & Levi, C. PMC5771207; Reperfusion therapy in acute ischemic stroke: dawn of a new era? *BMC Neurol.* **18**, 8 (2018).
4. Wollenweber, F. A. *et al.* Functional Outcome Following Stroke Thrombectomy in Clinical Practice. *Stroke* **50**, 2500-2506 (2019).
5. Dankbaar, J. W. *et al.* Prediction of Clinical Outcome After Acute Ischemic Stroke: The Value of Repeated Noncontrast Computed Tomography, Computed Tomographic Angiography, and Computed Tomographic Perfusion. *Stroke* **48**, 2593-2596 (2017).
6. Farina, F. *et al.* Prognostic Role of Microembolic Signals After Endovascular Treatment in Anterior Circulation Ischemic Stroke Patients. *World Neurosurg* **110**, e882-e889 (2018).
7. Sheriff, F. *et al.* Microemboli After Successful Thrombectomy Do Not Affect Outcome but Predict New Embolic Events. *Stroke*, Strokeaha119025856 (2019).
8. Arslanian, R. A. *et al.* Complete clot ingestion with cyclical ADAPT increases first-pass recanalization and reduces distal embolization. *J Neurointerv Surg* **11**, 931-936 (2019).
9. Wardlaw, J. M. *et al.* PMC3386494; Recombinant tissue plasminogen activator for acute ischaemic stroke: an updated systematic review and meta-analysis. *Lancet* **379**, 2364-2372 (2012).
10. Broocks, G. *et al.* Impact of intravenous alteplase on sub-angiographic emboli in high-resolution diffusion-weighted imaging following successful thrombectomy. *Eur. Radiol.* (2021).
11. Konduri, P. R. *et al.* In-Silico Trials for Treatment of Acute Ischemic Stroke. *Frontiers in Neurology* **11** (2020).
12. Georgakopoulou, T., van der Wijk, A. E., Bakker, E. & vanBavel, E. Recovery of Hypoxic Regions in a Rat Model of Microembolism. *J Stroke Cerebrovasc Dis* **30**, 105739 (2021).
13. Ngai, A. C. & Winn, H. R. Modulation of cerebral arteriolar diameter by intraluminal flow and pressure. *Circ. Res.* **77**, 832-840 (1995).
14. Nishimura, N., Schaffer, C. B., Friedman, B., Lyden, P. D. & Kleinfeld, D. PMC1765467; Penetrating arterioles are a bottleneck in the perfusion of neocortex. Proc. *Natl. Acad. Sci. U. S. A.* **104**, 365-370 (2007).
15. Hamilton, N. B., Attwell, D. & Hall, C. N. PMC2912025; Pericyte-mediated regulation of capillary diameter: a component of neurovascular coupling in health and disease. *Front Neuroenergetics* **2** (2010).
16. Schaffer, C. B. *et al.* PMC1324794; Two-photon imaging of cortical surface microvessels reveals a robust redistribution in blood flow after vascular occlusion. *PLoS Biol* **4**, e22 (2006).
17. Shih, A. Y. *et al.* PMC3952571; The smallest stroke: occlusion of one penetrating vessel leads to infarction and a cognitive deficit. *Nat. Neurosci.* **16**, 55-63 (2013).
18. Tsai, M. J., Tsai, Y. H. & Kuo, Y. M. Characterization of the pattern of ischemic stroke induced by artificial particle embolization in the rat brain. *Biomaterials* **32**, 6381-6388 (2011).
19. Lugo-Hernandez, E. *et al.* PMC5624395; 3D visualization and quantification of microvessels in the whole ischemic mouse brain using solvent-based clearing and light sheet microscopy. *J. Cereb. Blood Flow Metab.* **37**, 3355-3367 (2017).
20. Zhang, L. Y. *et al.* PMC5963347; CLARITY for High-resolution Imaging and Quantification of Vasculature in the Whole Mouse Brain. *Aging Dis* **9**, 262-272 (2018).
21. Pulsinelli, W. A., Brierley, J. B. & Plum, F. Temporal profile of neuronal damage in a model of transient forebrain ischemia. *Ann. Neurol.* **11**, 491-498 (1982).
22. Xu, L., Sapolsky, R. M. & Giffard, R. G. Differential sensitivity of murine astrocytes and neurons from different brain regions to injury. *Exp. Neurol.* **169**, 416-424 (2001).
23. Leithner, C. & Royl, G. PMC3887356; The oxygen paradox of neurovascular coupling. *J. Cereb. Blood Flow Metab.* **34**, 19-29 (2014).
24. Prinzen, F. W. & Bassingthwaighte, J. B. PMC3483311; Blood flow distributions by microsphere deposition methods. *Cardiovasc. Res.* **45**, 13-21 (2000).
25. Horton, R. W., Pedley, T. A. & Meldrum, B. S. Regional cerebral blood flow in the rat as determined by particle distribution and by diffusible tracer. *Stroke* **11**, 39-44 (1980).
26. Cavaglia, M. *et al.* Regional variation in brain capillary density and vascular response to ischemia. *Brain Res.* **910**, 81-93 (2001).

SUPPLEMENTARY INFORMATION

SUPPLEMENTARY METHODS

Microembolization model

Female and male Wistar rats (16 to 20 weeks old, Charles River) were used. All experiments were approved by the local committee on the Ethics of Animal Experiments of the University of Amsterdam, Academic Medical Center (permit number: DMF321AA) and were performed according to the ARRIVE guidelines and European Union guidelines for the care of laboratory animals (Directive 2010/63/EU).

Microembolization surgeries were performed exactly as described earlier by Van der Wijk et al. (2020) (1). Briefly, a mixture of fluorescent microspheres (MS) (DiagPoly™ Plain Fluorescent Polystyrene Particles, λ Ex 530 nm, λ Em 582 nm, Creative Diagnostics®, Shirley, NY; 25000 of 15 µm, 5500 of 25 µm and 625 of 50 µm MS) was injected into the left common carotid artery of anesthetized animals (isoflurane in 100% O_2), while the external carotid artery and occipital artery were temporarily ligated. The mixture of MS was administered using a 29G insulin needle over a period of 20 s. The MS sizes and numbers were in line with the size distribution of microemboli after *in vitro* EVT (2), but were limited to ≤50 µm to prevent infarction of the whole hemisphere (3). Because MS were lodged in the left hemisphere, the right hemisphere was used as a control.

Animals (n=6; 3 female, 3 male) were killed 24h post-surgery. Pimonidazole hydrochloride (60 mg/kg; Hypoxyprobe™ Pacific Blue Kit, HP15-x, Burlington, MA) was injected i.p. 90 minutes prior to euthanasia. While under anesthesia, DyLight 594 labeled tomato lectin (1 mg/kg; DyLight 594 labeled lycopersicon Esculentum tomato, Vector Laboratories, DL-1177, Burlingame, CA) was i.v. injected. Perfusion fixation was done with transcardial administration of heparinized PBS followed by 4% paraformaldehyde solution at 80 mmHg. Brains were then harvested for further processing as previously described (1).

Immunofluorescence staining of free-floating brain sections

All staining procedures were performed on an orbital shaker. After a 1h blocking step in blocking buffer (10% (v/v) normal goat serum (vector labs), 2% (v/v) TritonX-100 and 0.2% NaN_3 in PBS), brain sections (50 µm thick) were incubated with primary antibody mouse anti-NeuN (Millipore, mab377, 1:200) overnight at room temperature (RT). The following day, brain sections were washed and incubated with secondary antibody goat anti-mouse Cy5 for 2h (Molecular Probes, A10524, 1:1000), washed again and incubated with mouse anti-pimonidazole (Hypoxyprobe™ Pacific Blue Kit, HP15-x, 1:500) for 2h at RT (separate incubation to avoid cross reaction). All antibodies were dissolved in blocking buffer. Finally, brain sections were washed, mounted on microscopic slides and sealed with fluorescence mounting medium (DAKO North America Inc., s3023).

3D imaging of the brain

The sections were scanned using a confocal laser scanning microscope SP8 (Leica

Microsystems, Wetzlar, Germany) with a 10x objective. For every section, single plane tilescan images of both hemispheres and z-stack (of 5 µm steps) tilescan images of the intervention hemisphere were acquired. In order to facilitate 3D reconstruction (4), 50 µm thick consecutive coronal brain sections devoid of cutting artefacts were selected within a distance between 1 and 3.5 mm rostral from the bregma (Fig. 2A and Supplementary Information Table S2). Z-stack images were converted to maximum intensity projection (MIP) images using Image J (Rasband, W.S., ImageJ, U. S. National Institutes of Health, Bethesda, Maryland, USA) and MIP images were aligned using AMIRA software (Visage Imaging, Inc., San Diego, CA, USA) as described by De Bakker et al. (2016) (5).

Quantification of hypoxia and infarct in brain tissue

Pimonidazole hydrochloride (Hypoxyprobe™) was used as a marker of hypoxia. This probe binds to cells that have a partial oxygen pressure of ≤10 mmHg. Absence of NeuN staining was used as a marker of infarction, since anti-NeuN antibody stains healthy neurons. Reconstructed brain volumes were loaded in a 3D analysis software IMARIS 9.3 (Bitplane Inc., St. Paul, MN, USA) and the spot creation wizard was used to automatically segment MS. The hypoxic regions were segmented using the surface creation wizard and infarcted regions were segmented manually. The volumes and numbers of segmented regions and the x-, y-,z-, coordinates of MS, hypoxic centroids (HYP) and infarcted centroids (INF) were exported from IMARIS 9.3.

Spatial analysis of MS and brain damage

Our spatial analyses were based on the cumulative distribution functions of distances within and between MS and HYP or INF. Two distribution functions that are used in spatial correlation analyses between point events are the G-function and K-function (6). Figure 1 illustrates their meaning and calculation. These spatial distribution functions can be applied to distances between homogeneous point events (e.g. only MS) or heterogeneous point events (e.g. MS and HYP). We denote the latter as cross-G (Gx) and cross-K (Kx) functions.

The homogeneous G-functions and K-functions were calculated as

$$G(d) = \frac{\sum_{i \neq j} I(NND_{ij} < d)}{n} \qquad \text{Equation 1}$$

with d the distance, NND_{ij} the Euclidian distance of point event *i* to its nearest neighbor event *j*, I the indicator function (1 if true, 0 otherwise) and n the total number of point events, and

$$K(d) = \frac{\sum_{i \neq j} I(d_{ij} < d)}{n(n-1)} \qquad \text{Equation 2}$$

with d_{ij} the distance between two homogeneous point events. Gx and Kx were determined from

$$Gx(d) = \frac{\sum_{i} I(NND_i < d)}{n} \qquad \text{Equation 3}$$

and

$$Kx(d) = \frac{\sum_{i}\sum_{k} I(d_{ik} < d)}{n_i n_k} \qquad \text{Equation 4}$$

with NND_i the distance of point event *i* to its closest heterogeneous event, d_{ik} the distance

between a pair of heterogeneous events, n_i and n_k the number of point events of both types, respectively. Note that Kx is identical whether starting from MS or HYP, but Gx is not (Fig. 1). All G- and K-functions are cumulative density functions normalized to unity for distances covering the full tissue.

(cross) G- and K-functions were calculated for each animal separately and were used to test hypotheses on MS and HYP distributions. Their distribution under null hypotheses (H_0) were derived from Monte-Carlo simulations based on control locations for either MS or HYP. As control points we used selected non-hypoxic and non-infarcted voxels within the tissue boundaries of the intervention hemisphere. Per animal, the control points were equal in numbers to the numbers of MS or HYP.

The interpretation of spatial relations between MS and HYP depends on whether MS are randomly distributed in the tissue. For this reason, prior to evaluating Gx and Kx, we first tested G- and K-functions of MS distributions against the H_0 of purely randomly dispersed points, based on 250 Monte-Carlo simulations for each experiment. As these tests indicated significant clustering of MS, we designed a procedure for generation of control locations (C-MS) with similar G- and K-functions as the MS. In short, we first randomly generated as many control points as there were MS in each experiment. We then fitted their K-function by iteratively moving these individual control points in 3D towards or away from individual other points, based on the difference in K between simulation and data for the relevant distance class. We then repeated this for the G-function of nearest neighbor distances between control points. This procedure was also used for the generation of control points representing HYP (C-HYP), providing sets of Monte-Carlo simulations of MS and HYP locations with G- and K-functions matching the data. These were then used to evaluate the spatial relation between MS and HYP based on the Gx- and Kx-functions. All spatial calculations were performed using a custom-written script in MATLAB R2018b (The MathWorks, Inc., Natick, Massachusetts, United States).

Finally, we tested the spatial relation between MS and INF. However, due to the low INF numbers we skipped the steps of calculating G- and K-functions and of generating ‘clustered’ control points. We confined the analysis to the calculation of Gx- and Kx-functions for distances from INF to either MS or C-MS.

Statistics

Normally distributed data are depicted as mean ± standard deviation and non-normally distributed data as median and interquartile range. Differences in volume between hypoxic and infarcted regions were determined using Mann-Whitney test. Correlation between the numbers of lodged MS and the resulting brain hypoxic and infarcted regions was determined by Pearson’s test.

Due to inter-animal variation in the numbers of lodged MS and number of hypoxic areas, (cross) G- and K-functions were determined for each animal separately. Their Monte-Carlo H_0 G- and K-functions were plotted as mean ± confidence interval. Statistical inference of the experimental G- and K-functions versus the Monte-Carlo simulations was then determined by estimating the P value as (7):

$$\hat{P} = \frac{r+1}{n+1}$$ Equation 5

with r the number of simulations resulting in a higher value of G or K than the observed value in a specific bin and n the total number of simulations. $\hat{P}$ was determined per 50 µm distance bin. These estimates for each bin were then combined between experiments by Fischer's method:

$$F = -2\sum \ln(\hat{P})$$ Equation 6

where the summation is over the 6 animals. The experimental G- and K-functions were considered to differ statistically significant from the Monte-Carlo simulations for sufficiently low (G or K of data below simulation) or high values of F, which follows a chi-squared distribution with degrees of freedom equal to twice the number of experiments. Differences were considered statistically significant when $P \leq 0.05$. Statistical analyses and graphing were performed using GraphPad Prism 8 software (GraphPad Software, La Jolla, CA) and MATLAB R2018b software.

REFERENCES

1. van der Wijk, A. *et al.* Microembolus clearance through angiophagy is an auxiliary mechanism preserving tissue perfusion in the rat brain. *Acta Neuropathol Commun* **8**, 195 (2020).
2. Arslanian, R. A. *et al.* Complete clot ingestion with cyclical ADAPT increases first-pass recanalization and reduces distal embolization. *J Neurointerv Surg* **11**, 931-936 (2019).
3. Rapp, J. H. *et al.* Cerebral ischemia and infarction from atheroemboli. *Stroke* **34**, 1976-1980 (2003).
4. Luzzati, F., Fasolo, A. & Peretto, P. Combining confocal laser scanning microscopy with serial section reconstruction in the study of adult neurogenesis. *Front Neurosci* **5**, 70 (2011).
5. de Bakker, B. S. *et al.* An interactive three-dimensional digital atlas and quantitative database of human development. *Science* **354**, aag0053 (2016).
6. O'Sullivan, D. &Unwin, D. J. *Point Pattern Analysis*, (2010).
7. North, B. V., Curtis, D. & Sham, P. C. A note on calculation of empirical P values from Monte Carlo procedure. *Am J Hum Genet* **72**, 498-499 (2003).

SUPPLEMENTARY TABLES AND IMAGES

Table S1. *The number and percentage of microspheres (MS) found in the 500 µm thick reconstructed brain volumes as well as in the hemisphere (after extrapolation) per animal.*

Animal	nr of MS in reconstructed brain volume	nr of 15µm MS in reconstructed brain volume	nr of 25µm MS in reconstructed brain volume	nr of 50µm MS in reconstructed brain volume	% of total injected MS in reconstructed brain volume	Estimated nr of MS in hemisphere	Estimated % of total injected MS in hemisphere
1	190	161	27	2	0.61%	10615	35 %
2	81	63	18	0	0.26%	4897	16 %
3	43	39	4	0	0.14%	2307	9 %
4	79	41	37	1	0.25%	4345	16 %
5	115	103	12	0	0.37%	5950	19 %
6	105	79	23	3	0.34%	3940	12 %

Table S2. *Bregma coordinates of the selected coronal brain sections per animal.*

Animal	Bregma (distance in mm)
1	3.0-3.5
2	2.4-2.9
3	2.3-2.8
4	2.4-2.9
5	2.7-3.2
6	1.0-1.5

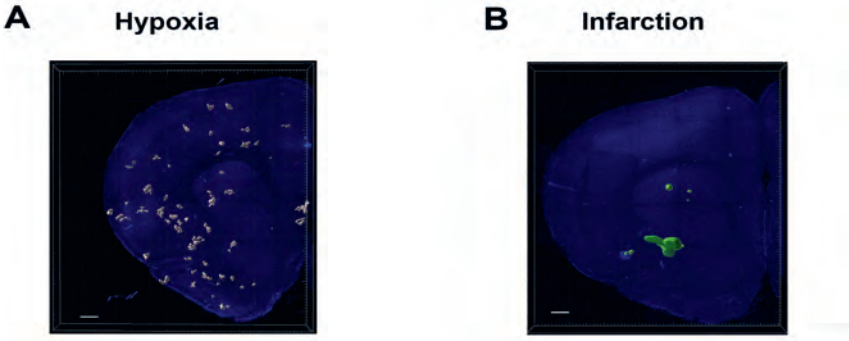

Figure S1. *Typical example of* **(A)** *multiple hypoxic (grey) or* **(B)** *sparsely distributed infarcted regions (green), in a 500 μm thick reconstructed brain volume (blue) of the intervention hemisphere. Scale bar = 500 μm. Reprinted from "Recovery of hypoxic regions in a rat model of microembolism," by T. Georgakopoulou, 2021, J Stroke Cerebrovasc Dis. 2021;30(6):105739. Reprinted with permission.*

Chapter 4

RECOVERY OF HYPOXIC REGIONS IN A RAT MODEL OF MICROEMBOLISM

Theodosia Georgakopoulou[1#], Anne-Eva van der Wijk[1#], Erik N. T. P. Bakker[1], Ed van Bavel[1], on behalf of the INSIST investigators

[1] Amsterdam UMC, University of Amsterdam, Biomedical Engineering and Physics, Amsterdam Cardiovascular Sciences, Meibergdreef 9, Amsterdam, The Netherlands

[#]Shared first authorship

J Stroke Cerebrovasc Dis. (2021) 30(6):105739

ABSTRACT

Endovascular treatment has become the standard of care for acute ischemic stroke. Despite successful recanalization, a limited subset of patients benefits from the new treatment. Human MRI studies have shown that during removal of the thrombus, a shower of microclots is released from the initial thrombus, possibly causing new ischemic lesions. The aim of the current study is to quantify tissue damage following microembolism. In a rat model, microembolism was generated by injection of a mixture of polystyrene fluorescent microspheres (15, 25 and 50 µm in diameter). The animals were killed at three time-points: day 1, 3 or 7. AMIRA and IMARIS software was used for 3D reconstruction of brain structure and damage, respectively. Microscopic analysis of 500 µm thick brain volumes revealed multiple ischemic, hypoxic and infarcted regions. Both the number and total volume of ischemic and hypoxic areas declined over time, whereas the infarcts remained. In conclusion, microembolism induces ischemia, hypoxia and infarction. Infarcted areas persist, but hypoxic regions recover over time suggesting that repair processes in the brain rescue the regions at risk.

INTRODUCTION

Acute ischemic stroke accounts for about 80% of stroke cases (1). The introduction of endovascular treatment (EVT), where a thrombus is removed by means of a retrieval device, has led to a breakthrough for the therapy of acute ischemic stroke (2). However, although in the large majority of cases successful recanalization of the occluded vessel is attained (3, 4), only one third of patients is left with a good clinical outcome, defined as modified Rankin Scale from 0 to 2 at 90 days follow-up (5).

This discrepancy between successful recanalization and poor clinical outcome has been attributed to, among others, poor collateral status (6), hyperglycemia and site of occlusion (4). Less attention is given to the release of emboli from the initial clot. There is evidence from human MRI studies that during and following removal of a thrombus, a shower of microclots releases from the initial thrombus and spreads in the arterial bed distal to the thrombus, possibly causing new ischemic lesions (7, 8). Based on *in vitro* simulations of EVT, hundreds of thousands of microemboli ranging in size from 10 µm to 1 mm were reported to be released into the cerebral circulation (9). Although new generation devices generate less microthrombi (9), the number is still substantial and may be related to poor clinical outcome. While release of mm-size thrombi should clearly be avoided, less is known on the effect of small but very numerous microthrombi. Such effects are relevant for future device design.

Several studies have evaluated tissue damage and neurological deficits caused by microembolism. It was shown that the number of microemboli determines brain tissue damage and neurological deficit (10, 11), and that the size of the particle determines the different injury patterns of cerebral infarction (12, 13). However, there is a lack of quantitative data regarding the course of brain damage in terms of ischemia, hypoxia and infarction as well as three-dimensional representations of tissue damage. This knowledge is needed to increase our understanding of stroke and improve EVT treatment.

The aim of the present study is to quantify tissue ischemia, hypoxia and infarction over time in a rat model of microembolism. We therefore injected at day (D) 0 a mixture of microspheres via the left common carotid artery and killed the animals at D1, 3 or 7. We hypothesize that microembolism relevant for EVT, ranging in size from 15-50 µm, is sufficient to cause brain damage. We found that microembolism induces ischemia, hypoxia and infarction, yet hypoxic regions became significantly less pronounced over time, indicating that the brain has the capacity to recover from hypoxic injury.

METHODS

Microembolism surgery

Female and male Wistar rats (16 to 20 weeks old, Charles River) were used. Microembolism was generated by injecting a mixture of polystyrene fluorescent microspheres (25000 of 15 µm, 5500 of 25 µm and 625 of 50 µm diameter). All experiments were performed under the approval of the local committee on the Ethics of Animal Experiments of the University of Amsterdam, Academic Medical Center (permit number: DMF321AA) and according

to the ARRIVE guidelines and European Union guidelines for the care of laboratory animals (Directive 2010/63/EU). The rats were housed in pairs in standard plastic cages with *ad libitum* food and water and a 12h:12h light-dark cycle. At D0 microembolism surgeries were performed under anesthesia (isoflurane mixed with 100% O_2). Anesthesia was induced at 4% isoflurane (Isoflutek 1000 mg/g; Laboratorios Karizoo SA, Barcelona, Spain) in 1 L/min O_2, hair was removed from the neck caudal to the mandibles and buprenorphine (Temgesic™, 0.05 mg/kg, Schering-Plough, Welwyn Garden City, Hertfordshire, UK) was injected s.c. 30 min pre-surgery as analgesic. After placing the rat in a supine position on a heating pad, anesthesia was maintained (at 2-2.5% isoflurane in 1 L/min O_2) and body temperature was kept at 37.0±0.5 ºC. Iodide was used to disinfect the skin and a ventral midline incision was made in the neck. The left common carotid artery, external carotid artery, and internal carotid artery were exposed. The external carotid artery and occipital artery were temporarily ligated with a 6.0 surgical suture. A mixture of fluorescent microspheres (DiagPoly™ Plain Fluorescent Polystyrene Particles, DFO-L011, DFO-L013, DFO-L016, λ Excitation 530 nm, λ Emission 582 nm, Creative Diagnostics®, Shirley, NY) was administered via the left common carotid artery using a 29G insulin needle over a period of 30 sec (15 µm, 25 µm and 50 µm microspheres, resuspended in a sterile 2% bovine serum albumin solution of phosphate buffered saline (PBS), in a total volume of 200 µl). The selected range of injected microspheres was based on the distribution of microemboli after *in vitro* EVT (9), but was limited only to sizes <50 µm to avoid whole brain infarct volumes. Microspheres ended up in the left hemisphere, leaving the contralateral side to serve as a control. Following removal of the needle, pressure was applied to the injection site to stop the bleeding. Finally, interrupted sutures (size 4-0) were made to close the wound and rats were allowed to recover on a heating pad before being placed back into their cages. Rats were randomly assigned to the three groups of D 1, 3 and 7.

Tissue preparation

Animals were killed on D1 (n=6; 3 female, 3 male), D3 (n=6; 2 female, 4 male) or D7 (n=7; 4 female, 3 male) post-surgery. For the detection of hypoxia, 60 mg/kg pimonidazole hydrochloride (Hypoxyprobe™ Pacific Blue Kit, HP15-x, Burlington, MA) was injected i.p. 90 minutes prior to euthanasia. To label the vasculature, DyLight 594 labeled tomato lectin (1 mg/kg; Vector Laboratories Cat# DL-1177) was administered via the tail vein and allowed to circulate for 5 min. Following injection of 100 µl heparin i.p. to avoid formation of blood clots, transcardial perfusion was done with heparinized PBS followed by tissue fixation with 4% paraformaldehyde at 80 mmHg. All aforementioned steps were performed while under anesthesia. Brains were then harvested for further processing.

Immunofluorescence staining

For immunofluorescent staining, brain sections (50 µm thick) were washed in PBS and incubated in blocking buffer (10% (v/v) normal goat serum (vector labs), 2% (v/v) TritonX-100 and 0.2% NaN_3 in PBS) for 1h at room temperature. Next, brain sections were

incubated overnight at room temperature with primary antibody mouse anti-NeuN (1:200; Millipore Cat# MAB377). After washing, secondary antibodies goat anti-mouse Cy5 (1:1000; Thermo Fisher Scientific Cat# A10524) and mouse anti-pimonidazole (1:500; Hypoxyprobe™ Pacific Blue Kit, HP15-x) were added and brain sections were incubated for 2h (for each antibody separately to avoid cross-reaction) at room temperature. All antibodies were incubated in blocking buffer. After washing, brain sections were sealed with fluorescence mounting medium (DAKO North America Inc., s3023). All staining procedures were performed under gentle agitation.

Confocal imaging and 3D analysis workflow

For each animal, ten consecutive coronal sections (50 µm thick) without cutting damage or major artefacts were selected within a distance between 1 and 5.5 mm from the bregma. The thickness of the sections and their distance from the bregma was chosen to facilitate 3D reconstruction (14). Tilescan images of whole brain sections and z-stack tilescan images of the intervention hemisphere were acquired using a confocal laser scanning microscope SP8 (Leica Microsystems, Wetzlar, Germany) with a 10x objective. The z-stacks (5 µm steps) of each 50 µm section were then converted to maximum intensity projection images using Image J (Rasband, W.S., ImageJ, U. S. National Institutes of Health, Bethesda, Maryland, USA). This conversion was needed to facilitate the alignment of the sections, using AMIRA software (Visage Imaging, Inc., San Diego, CA, USA) as described by De Bakker et al. (2016) (15). Each aligned maximum intensity projection section was inserted in IMARIS 9.3 software (Bitplane Inc., St. Paul, MN, USA) as an image of 50 µm thickness. As a result, a 500 µm thick brain volume was reconstructed per animal and further analyzed in IMARIS 9.3 software.

Lectin was injected intravenously to stain the endothelial luminal surface and the absence of lectin was used as a marker of ischemia. Pimonidazole hydrochloride (Hypoxyprobe™) binds to cells that have a partial oxygen pressure of ≤10 mmHg and was used as a marker of hypoxia. Anti-NeuN antibody binds to healthy neurons, and therefore absence of NeuN staining was used as a marker of infarction. For the hypoxic volume segmentation, the same batch of settings was applied to all brain volumes using the surface creation wizard of IMARIS 9.3. The ischemic and infarction volumes were segmented manually. The microspheres were automatically segmented using the spot creation wizard. Measurements of ischemic, hypoxic and infarcted volumes were performed in a randomized and blinded fashion regarding the day of sacrifice. The data are available from the corresponding author upon reasonable request.

Statistics

Normality of the data was tested by Shapiro-Wilk test. Normally distributed data are depicted as mean ± standard deviation and not normally distributed data as median and interquartile range. Differences between groups (D1, 3 and 7) were determined using analysis of variance followed by Tukey's test for multiple comparisons or Kruskal-Wallis followed by Dunn's test for multiple comparisons. Differences were considered

statistically significant when $P \leq 0.05$. Statistical analyses and graphing were performed using GraphPad Prism 6 software (GraphPad Software, La Jolla, CA) and IMARIS 9.3.

RESULTS

Microembolism causes ischemic, hypoxic and infarcted regions in the brain

Microembolism caused multiple focal lesions spread throughout the whole brain volume. Typical examples of individual coronal brain sections at different time-points are shown in Fig. 1A (white arrows indicate lesion locations). The lesions were characterized by ischemia (absence of lectin), hypoxia (hypoxyprobe) and infarction (absence of NeuN) (Supplementary Information Video S1) and were present at D1 (Fig. 1B top), D3 (Fig. 1B middle) and D7 (Fig. 1B bottom). In all cases, microspheres were confined to the intervention side, and no signs of tissue damage were found on the control side (Fig. 1B). In addition to the microscopic findings, macroscopic perivascular and point-like hemorrhages were regularly observed at all time-points when harvesting the brain (Supplementary Information Fig. S1).

Little but persistent neuronal damage 7 days following microembolism

To quantitatively assess tissue infarction, we reconstructed 500 µm thick brain volumes and quantified the number and volumes of the infarcted regions (absence of NeuN). Tissue infarction was present at all three time-points (Fig. 2A). The number of infarcted regions as well as the total infarcted volume did not significantly change over time (Fig. 2B, left graph; P=0.1599, right graph; P=0.1492 not significant Analysis of variance). In brief, following microembolism a small fraction of the brain (<1%) became infarcted and this neuronal damage persisted.

Local cerebral ischemia and hypoxia recover within 7 days following microembolism

Next to infarction, we detected ischemic (absence of lectin) and hypoxic (hypoxyprobe) regions which were present at all three time-points (Fig. 3A, 3C, Supplementary Information Video S2). The number and total volume of ischemic and hypoxic regions significantly reduced over time (Fig. 3B, left graph; D1 vs D3: P=0.0548, D1 vs D7: P=0.0132, D3 vs D7: P>0.9999, right graph; D1 vs D3: P=0.1344, D1 vs D7: P=0.0245, D3 vs D7: P>0.9999, Dunn's multiple comparison test after significant Kruskal-Wallis and Fig. 3D, left graph; D1 vs D3: P=0.0071, D1 vs D7: P<0.0003, D3 vs D7: P=0.3443, right graph; D1 vs D3: P=0.0129, D1 vs D7: P<0.0026, D3 vs D7: P=0.7983, Tukey's multiple comparison test after significant analysis of variance). Notably, ischemia and hypoxia at D7 was virtually absent, suggesting successful reperfusion and recovery of hypoxic tissue at risk.

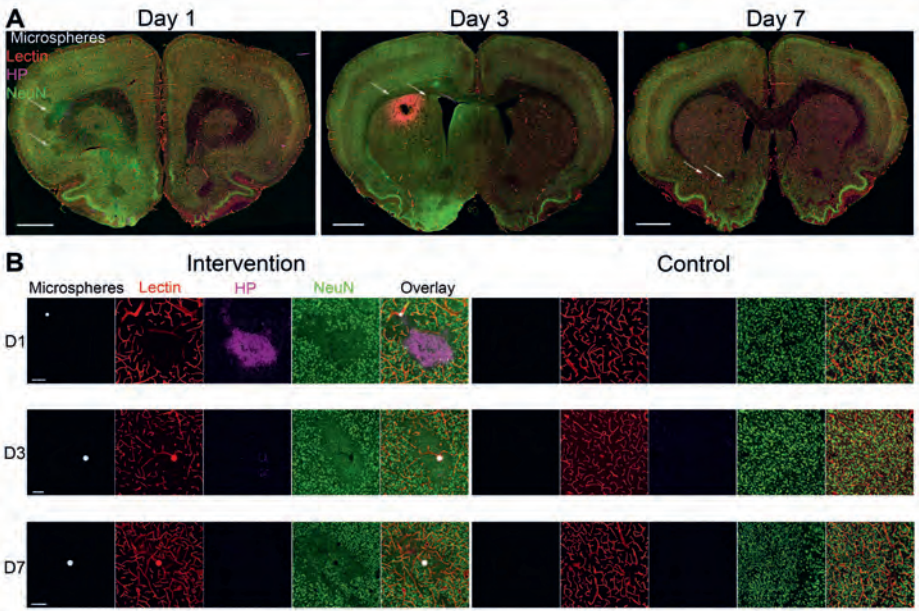

Figure 1. Multiple lesions following microembolism. ***(A)*** *Multiple ischemic (absence of lectin; red), hypoxic (HP: hypoxyprobe; magenta) and infarcted regions (white arrows, absence of NeuN; green) in the intervention hemisphere as compared to the intact control hemisphere at D1, 3 and 7. Scale bar = 1500 µm.* ***(B)*** *Example of a microsphere (white) causing ischemia (absence of lectin; red), hypoxia (magenta) and infarction (absence of NeuN; green) at D1, causing ischemia, hypoxia and infarction at D3 and causing infarction at D7. Control side showed no signs of damage. Scale bar = 100 µm.*

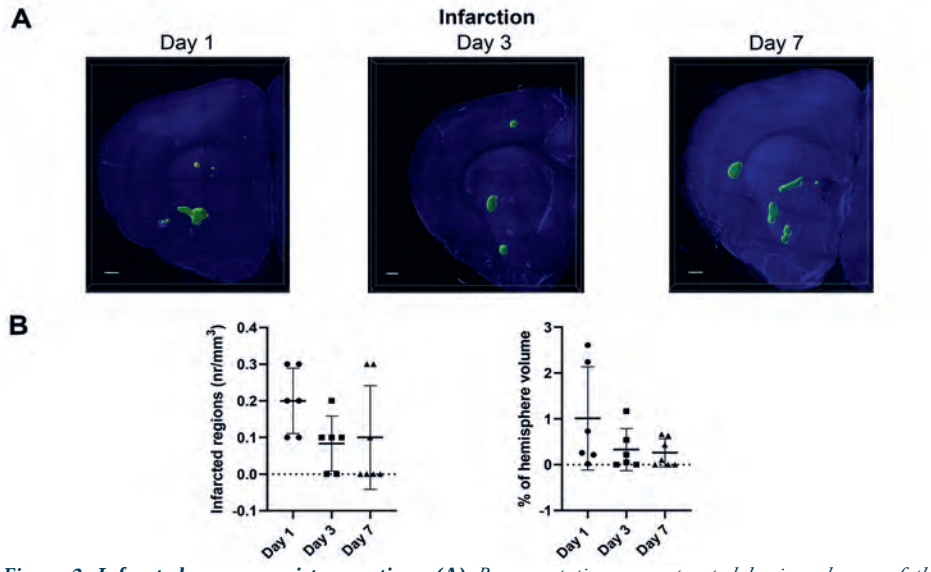

Figure 2. Infarcted areas persist over time. ***(A)*** *Representative reconstructed brain volumes of the intervention hemisphere (blue) with segmented infarcted regions (green) and lodged microspheres (red) at D1, 3 and 7. Scale bar = 500 µm.* ***(B)*** *Quantification of the number of infarcted regions per mm³ (left graph) and of the percentage of hemisphere being infarcted (right graph) at D1, 3 and 7. N=6-7 animals per time-point. Data are depicted as mean ± standard deviation. Analysis of variance with Tukey's multiple comparison test.*

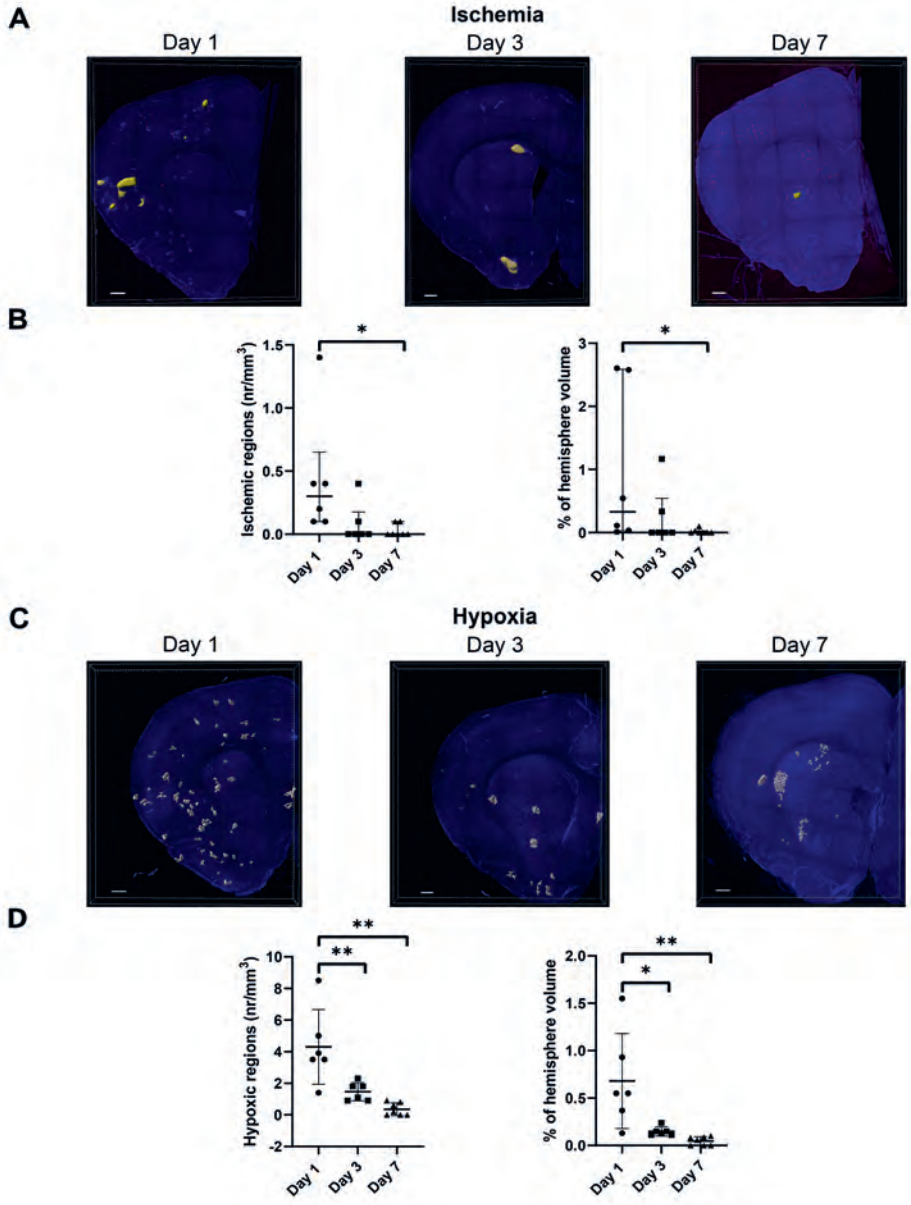

Figure 3. Ischemia and hypoxia decline over time. **(A)** *Representative reconstructed brain volumes of the intervention hemisphere (blue) with segmented ischemic regions (yellow) and lodged microspheres (red) at D1, 3 and 7. Scale bar = 500 µm.* **(B)** *Quantification of the number of ischemic regions per mm³ (left graph) and of the percentage of hemisphere being ischemic (right graph) at D1, 3 and 7. N=6-7 animals per time-point. Data are depicted as median and interquartile range. *P<0.05, D1 vs D7, Kruskal-Wallis with Dunn's multiple comparisons test.* **(C)** *Representative reconstructed brain volumes of the intervention hemisphere (blue) with segmented hypoxic regions (grey) and lodged microspheres (red) at D1, 3 and 7. Scale bar = 500 µm.* **(D)** *Quantification of the number of hypoxic regions per mm³ (left graph) and of the percentage of hemisphere being hypoxic (right graph) at D1, 3 and 7. N=6-7 animals per time-point. Data are depicted as mean ± standard deviation. **P<0.01, *P<0.05, D1 vs D3 and D1 vs D7. Analysis of variance with Tukey's multiple comparison test.*

DISCUSSION

To our knowledge, this is the first study to comprehensively map ischemia, hypoxia and infarction over time after cerebral microembolism. We found that microspheres of sizes relevant for EVT induced persistent neuronal damage, which did not change in terms of number and size over time. However, hypoxic and ischemic volumes had virtually disappeared after 7 days. These data suggest recovery of brain regions at risk within seven days.

In the majority of cases, EVT is preceded by thrombolysis with tissue plasminogen activator (rt-PA). However, the effectiveness of these agents is limited to the first 4.5h after symptom onset (16), while also considerable time elapses during transport from local centers performing the thrombolysis to specialized centers for EVT. rt-PA would only be able to dissolve the microclots after recanalization of the major thrombus. As a result, a substantial number of microthrombi could remain in the microcirculation without being lysed. In mice injected with fibrin-rich microclots, almost half of the injected clots were found in the blood vessels even after administration of tissue plasminogen activator (17).

This raises the question whether it would be sensible to perform thrombolysis also *after* the EVT. To our knowledge, no randomized clinical trials included rt-PA administration after EVT (18, 19), as can be appreciated because of the high risk of symptomatic intracranial hemorrhage (20), a common complication of the drug. The only data on the use of thrombolytic treatment after EVT come from case reports of patients with recurrent stroke within 90 days from their prior event (21, 22). Despite the contraindication of using rt-PA in this subset of patients, a small systematic review (23) concluded that repeated rt-PA administration may not be as harmful as initially thought. Due to the limited data it is hard to determine whether such treatment will be beneficial for patients. In addition, clots are very heterogeneous and can be rich in fibrin, but also in red blood cells, white blood cells and platelets (24) which may impair their susceptibility to thrombolysis (25). Moreover, since microthrombi cannot be visualized with the current clinical imaging modalities, their fate after such adjunctive therapy would remain unknown, and only functional outcome could be assessed. Following successful thrombus removal, rt-PA might have a higher likelihood of reaching the distal microthrombi, but there seem few arguments for performing clinical trials on this prior to more extensive translational research.

Next to thrombolysis, angiophagy is a complementary mechanism of the brain for vascular recanalization, where the embolus is enveloped by endothelial membrane projections and subsequently extravasated to the brain parenchyma (26, 27). In the present study, the reduction in number and size of ischemic volumes over time indicates successful local reperfusion. The mechanisms of local flow recovery were addressed in another study from our group, where we showed that at D7 almost half of the lodged microspheres are extravasated (28). Based on these findings, the successful local reperfusion found in the current study may relate to angiophagy.

The microembolism model we developed can be used to quantify transient and persistent effects of microemboli on the brain tissue, following EVT. The selection of microspheres instead of fibrin clots was made for two reasons. Firstly, microspheres are

not biodegradable and not susceptible to thrombolysis, covering a broad spectrum of persistent occluding materials. Secondly, the size, shape and number of microspheres can be controlled, making it possible to occlude the desired vascular level.

A limitation of this study is that we did not test the effect of individual sizes of microspheres. Lam et al. (2010) observed transient hypoxia but no infarctions for 10 or 15 µm microspheres in mice (26). It remains to be established whether the current infarctions are caused by the combination of different sizes or rather just the 25 and 50 µm microspheres. Also, future work needs to address the spatial relationship between embolus and brain damage, as well as the cooperative effects of multiple microspheres of varying size.

Here, we did not combine microembolism with a large vessel occlusion. We intentionally chose this approach in order to isolate the local consequences of microemboli. We expect that the local effects due to obstructed arterioles and capillaries will be analogous for rat and human, since the capillaries have the same diameter and arteriolar density is comparable for these species (29, 30). For the same reason we selected this particular range of microsphere sizes between 15 and 50 µm, although the emboli released after *in vitro* EVT also include larger sizes (9). It remains to be established how representative these data are for penumbral and healthy areas in stroke. A rat study found that unilateral proximal carotid occlusion is insufficient to cause stroke but strongly increases lesion sizes caused by 50 µm microspheres (31), suggesting mutual influence of local and global occlusions on cerebral injury.

In conclusion, our study demonstrated that microspheres with sizes resembling microthrombi in EVT induce irreversible micro-infarcts as well as areas of ischemia and hypoxia that recover within 7 days. These effects are relevant in major strokes for tissue damage progression, in areas of the target downstream territory with normal macroscopic perfusion, or in the penumbra.

CONFLICT OF INTEREST

The authors declare that the research was conducted in the absence of any commercial or financial relationships that could be construed as a potential conflict of interest.

AUTHOR CONTRIBUTIONS

ENTPB, EvB, AEvdW and TG designed the experiments; TG and AEvdW performed the surgeries; TG analyzed the data and wrote the manuscript; AEvdW, ENTPB and EvB contributed to editing of the manuscript. All authors read and approved the final version of the manuscript.

FUNDING

This project was funded from the European Union's Horizon 2020 research and innovation

program under grant agreement No 777072 (INSIST).

ACKNOWLEDGMENTS

We thank Jaco Hagoort of the Medical Biology Department (Amsterdam UMC) and Marjolijn Mertz of the Netherlands Cancer Institute for assisting with AMIRA and IMARIS respectively.

REFERENCES

1. Bamford, J., Sandercock, P., Dennis, M., Burn, J. & Warlow, C. Classification and natural history of clinically identifiable subtypes of cerebral infarction. *Lancet* **337**, 1521-1526 (1991).
2. Berkhemer, O. A. *et al.* A randomized trial of intraarterial treatment for acute ischemic stroke. *N. Engl. J. Med.* **372**, 11-20 (2015).
3. Nogueira, R. G. *et al.* PMC4176618; Trevo versus Merci retrievers for thrombectomy revascularisation of large vessel occlusions in acute ischaemic stroke (TREVO 2): a randomised trial. *Lancet* **380**, 1231-1240 (2012).
4. Bhaskar, S., Stanwell, P., Cordato, D., Attia, J. & Levi, C. PMC5771207; Reperfusion therapy in acute ischemic stroke: dawn of a new era? *BMC Neurol.* **18**, 8 (2018).
5. Munich, S. A., Vakharia, K. & Levy, E. I. Overview of Mechanical Thrombectomy Techniques. *Neurosurgery* **85**, S60-s67 (2019).
6. Berkhemer, O. A. *et al.* Collateral Status on Baseline Computed Tomographic Angiography and Intra-Arterial Treatment Effect in Patients With Proximal Anterior Circulation Stroke. *Stroke* **47**, 768-776 (2016).
7. Palombo, G. *et al.* Late evaluation of silent cerebral ischemia detected by diffusion-weighted MR imaging after filter-protected carotid artery stenting. *AJNR Am. J. Neuroradiol.* **29**, 1340-1343 (2008).
8. Zhu, L. *et al.* The distribution and size of ischemic lesions after carotid artery angioplasty and stenting: evidence for microembolization to terminal arteries. *J. Vasc. Surg.* **53**, 971-6 (2011).
9. Chueh, J. Y. *et al.* Reduction in distal emboli with proximal flow control during mechanical thrombectomy: a quantitative in vitro study. *Stroke* **44**, 1396-1401 (2013).
10. Atochin, D. N. *et al.* Mouse model of microembolic stroke and reperfusion. *Stroke* **35**, 2177-2182 (2004).
11. Winding, O. Cerebral microembolization following carotid injection of dextran microspheres in rabbits. *Neuroradiology* **21**, 123-126 (1981).
12. Tsai, M. J., Tsai, Y. H. & Kuo, Y. M. Characterization of the pattern of ischemic stroke induced by artificial particle embolization in the rat brain. *Biomaterials* **32**, 6381-6388 (2011).
13. Rapp, J. H. *et al.* Cerebral ischemia and infarction from atheroemboli. *Stroke* **34**, 1976-1980 (2003).
14. Luzzati, F., Fasolo, A. & Peretto, P. PMC3097380; Combining confocal laser scanning microscopy with serial section reconstruction in the study of adult neurogenesis. *Front Neurosci* **5**, 70 (2011).
15. de Bakker, B. S. *et al.* An interactive three-dimensional digital atlas and quantitative database of human development. *Science* **354** (2016).
16. Wardlaw, J. M. *et al.* PMC3386494; Recombinant tissue plasminogen activator for acute ischaemic stroke: an updated systematic review and meta-analysis. *Lancet* **379**, 2364-2372 (2012).
17. Grutzendler, J. *et al.* Angiophagy prevents early embolus washout but recanalizes microvessels through embolus extravasation. *Sci Transl Med* **6**, 226ra31 (2014).
18. Saver, J. L. & Adeoye, O. Intravenous Thrombolysis Before Endovascular Thrombectomy for Acute Ischemic Stroke. *JAMA* **325**, 229-231 (2021).
19. Phipps, M. S. & Cronin, C. A. Management of acute ischemic stroke. *BMJ* **368**, l6983 (2020).
20. Tsivgoulis, G., Kargiotis, O. & Alexandrov, A. V. Intravenous thrombolysis for acute ischemic stroke: a bridge between two centuries. *Expert Review of Neurotherapeutics* **17**, 819-837 (2017).
21. Alhazzaa, M. *et al.* Thrombolysis despite recent stroke: a case series. *Stroke* **44**, 1736-1738 (2013).
22. Yoo, H. S. *et al.* Repeated Thrombolytic Therapy in Patients with Recurrent Acute Ischemic Stroke. *J Stroke* **15**, 182-188 (2013).
23. Sarmiento, R. J. C., Diestro, J. D. B., Espiritu, A. I. & San Jose, M. C. Z. Safety and Efficacy of Repeated Thrombolysis with Alteplase in Early Recurrent Ischemic Stroke: A Systematic Review. *J Stroke Cerebrovasc Dis* **28**, 104290 (2019).
24. Fitzgerald, S. et al. PMC6910081; Platelet-Rich Emboli in Cerebral Large Vessel Occlusion Are Associated With a Large Artery Atherosclerosis Source. *Stroke* **50**, 1907-1910 (2019).

25. Wohner, N. *et al*. PMC3339800; Lytic resistance of fibrin containing red blood cells. *Arterioscler. Thromb. Vasc. Biol.* **31**, 2306-2313 (2011).
26. Lam, C. K., Yoo, T., Hiner, B., Liu, Z. & Grutzendler, J. PMC2879083; Embolus extravasation is an alternative mechanism for cerebral microvascular recanalization. *Nature* **465**, 478-482 (2010).
27. van der Wijk, A. E. *et al*. Extravasation of Microspheres in a Rat Model of Silent Brain Infarcts. *Stroke* **50**, 1590-1594 (2019).
28. van der Wijk, A. *et al*. Microembolus clearance through angiophagy is an auxiliary mechanism preserving tissue perfusion in the rat brain. *Acta Neuropathologica Communications* **8**, 195 (2020).
29. Reina-De La Torre, F., Rodriguez-Baeza, A. & Sahuquillo-Barris, J. Morphological characteristics and distribution pattern of the arterial vessels in human cerebral cortex: a scanning electron microscope study. *Anat. Rec.* **251**, 87-96 (1998).
30. Ngai, A. C. & Winn, H. R. Modulation of cerebral arteriolar diameter by intraluminal flow and pressure. *Circ. Res.* **77**, 832-840 (1995).
31. Omae, T., Mayzel-Oreg, O., Li, F., Sotak, C. H. & Fisher, M. Inapparent hemodynamic insufficiency exacerbates ischemic damage in a rat microembolic stroke model. *Stroke* **31**, 2494-2499 (2000).

SUPPLEMENTARY INFORMATION

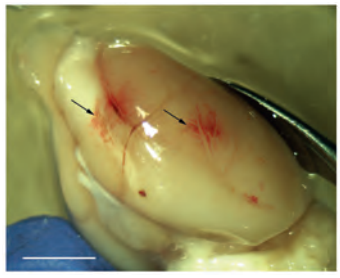

Figure S1. *Perivascular hemorrhages (black arrows) on the brain surface following microembolism. Ventrolateral view of a rat brain. Scale bar = 5mm.*

https://www.strokejournal.org/article/S1052-3057(21)00142-7/fulltext#supplementaryMaterial

Video S1. 3D reconstruction of lesions at D1. *Ischemic (absence of lectin; red), hypoxic (hypoxyprobe; magenta) and infarction (absence of NeuN; green) regions in the intervention hemisphere. The green arrow indicates one of the infarctions and the magenta arrow one of the hypoxic lesions. Ten serial coronal sections of the intervention hemisphere were aligned in AMIRA. Scale bar = 500 µm.*

Video S2. Segmented hypoxic lesions. *Representative reconstructed 500 µm thick brain volume of the intervention hemisphere (blue) with segmented hypoxic lesions (grey) and lodged microspheres (different colors based on their size) at D1. Ten serial coronal sections of the intervention hemisphere were aligned in AMIRA and analyzed in IMARIS.*

Chapter 5

PERIVASCULAR CLEARANCE OF BLOOD PROTEINS AFTER BLOOD-BRAIN BARRIER DISRUPTION IN A RAT MODEL OF MICRO-INFARCTS

Theodosia Georgakopoulou[1], Anne-Eva van der Wijk[1,2], Ed van Bavel[1,2,3], Erik N. T. P. Bakker[1,2,3]

[1] Amsterdam UMC, University of Amsterdam, Biomedical Engineering and Physics, Amsterdam Cardiovascular Sciences, Meibergdreef 9, Amsterdam, The Netherlands

[2] Amsterdam Cardiovascular Sciences, Microcirculation, Amsterdam, the Netherlands

[3] Amsterdam Neuroscience, Neurovascular disorders, Amsterdam, the Netherlands

Microvasc Res. (2023) 148:104515

ABSTRACT

Micro-infarcts result in a transient loss of the blood-brain barrier integrity in the ischemic territory. The transient blood brain barrier disruption leads to the extravasation of blood proteins into the brain parenchyma. It is not clear how these proteins are removed. Here we studied the role of perivascular spaces in brain clearance from extravasated blood proteins. Male and female Wistar rats were infused with microspheres of either 15, 25, or 50 µm in diameter (n=6 rats per group) via the left carotid artery. We infused either 25000 microspheres of 15 µm, 5500 of 25 µm, or 1000 of 50 µm. One day later, rats were infused with lectin and hypoxyprobe to label perfused blood vessels and hypoxic areas, respectively. Rats were then killed and perfusion-fixed. Brains were excised, sectioned, and analyzed using immunostaining and confocal imaging. Microspheres induced a size-dependent increase in ischemic volume per territory, but the cumulative ischemic volume was similar in all groups. The total volumes of ischemia, hypoxia and infarction affected 1-2% of the left hemisphere. Immunoglobulins (IgG) were present in ischemic brain tissue surrounding lodged microspheres in all groups. In addition, staining for IgG was found in perivascular spaces of blood vessels nearby areas of blood brain barrier disruption. About 2/3 of these vessels were arteries, while the remaining 1/3 of these vessels were veins. The subarachnoid space of the affected hemisphere stained stronger for IgG than the contralateral hemisphere in all groups. Microspheres of various sizes induce a local loss of blood brain barrier integrity, evidenced by parenchymal IgG staining. The presence of IgG in perivascular spaces of both arteries and veins distinct from the ischemic territories suggests that both contribute to the removal of blood proteins. The strong staining for IgG in the subarachnoid space of the affected hemisphere suggests that this perivascular route egresses via the cerebrospinal fluid. Perivascular spaces therefore play a previously unrecognized role in tissue clearance of fluid and extravasated proteins after blood brain barrier disruption induced by micro-infarcts.

INTRODUCTION

A clinically important consequence of stroke is edema. After an initial phase of cytotoxic edema, which is a consequence of energy depletion, vasogenic edema may develop in the course of hours after an ischemic insult (1). Vasogenic edema results from a loss of endothelial barrier function in the affected territories. Vasogenic edema involves extravasation of water and salts, but can also entail larger blood components, such as albumin and immunoglobulins (IgG). Resolution of edema is important as raised intracranial pressure may impair perfusion. In addition, blood components may elicit local inflammatory responses that can further exacerbate tissue damage.

We recently developed a rat model for micro-infarcts based on infusion of microspheres that recapitulates small ischemic strokes in terms of local ischemia, loss of barrier function, and edema (2). In that work we found that IgG extravasate from the vascular bed into the affected hemisphere, but are cleared in the course of days to weeks after the insult. The process of clearance of blood components is currently poorly understood. Specific transporters for proteins such as albumin have not yet been identified, and therefore other mechanisms need to be present.

In this study we addressed the role of perivascular spaces as a potential pathway for brain clearance after the induction of micro-infarcts. Perivascular spaces are part of a brain-wide clearance system, referred to as the glymphatic system (3). Impaired glymphatic function may contribute to neurodegenerative diseases associated with protein aggregation, such as Alzheimer's disease (4). Here we infused microspheres of various sizes into one hemisphere of rats via the carotid artery. We quantified the impact of local occlusions by determining the volumes of ischemic, hypoxic, and infarcted territories. The role of perivascular spaces was investigated using immunostaining for extravasated IgG and albumin. The data suggest that perivascular spaces of both arteries and veins nearby local micro-infarcts contribute to removal of blood components, which are subsequently transported to the cerebrospinal fluid.

METHODS

Animal surgery

All animal experiments were approved by the ethics committee of the Academic Medical Center (permit number: DMF321AA) and were carried out according to both the ARRIVE and the European Union guidelines for the care of laboratory animals (Directive 2010/63/EU). The animals had access to *ad libitum* food and water and were pair-housed in standard plastic cages with a 12h:12h light-dark cycle, in the animal facility (ARIA) of the Academic Medical Center. The surgical procedures applied here were previously described by Georgakopoulou et al. (2021) (5). Briefly, after anesthesia, the left common carotid artery (CCA) was exposed at the bifurcation level. Both the external carotid artery and occipital artery were temporarily ligated and polystyrene fluorescent microspheres (200 µl of DiagPoly Custom made Plain Fluorescent Microparticles, Excitation wavelength 656 nm, Emission wavelength 674 nm, Creative Diagnostics, Shirley, NY) were injected via the

left CCA. Group 15 received 25000 microspheres of 15 μm in diameter, group 25 received 5500 microspheres of 25 μm in diameter and group 50 received 1000 microspheres of 50 μm in diameter. The numbers of microspheres injected per group were based on scaling laws for arterial trees (6). According to this law, the volume/diameter relation is predicted with an exponent of 3. Rats were randomly assigned to the three groups (Group 15, 25, or 50). Totally, 26 Wistar rats (16–20 weeks old, Charles River) were used. However, one animal did not survive the first 24h post-surgery, in one animal the lectin injection was not successful, and in six animals microspheres injection was not successful. These animals were excluded. Eventually, 18 rats (50% female per group) were included in the analysis.

Tissue preparation and immunohistochemistry

Animals were killed 24h post-surgery. 90 minutes prior to euthanasia, pimonidazole hydrochloride (60 mg/kg; Hypoxyprobe Pacific Blue Kit, HP15-x, Burlington, MA) was injected intraperitoneally. Pimonidazole hydrochloride is a compound characterized by its affinity to bind to hypoxic cells (partial pressure of oxygen (PO_2) < 10 mmHg) and was used as a marker of hypoxia. Five minutes prior to euthanasia, lectin (1 mg/kg; DyLight 594 labeled lycopersicon Esculentum tomato, Vector Laboratories, DL-1177, Burlingame, CA) was injected intravenously. Lectin is a dye that stains perfused blood vessels and absence of staining was used as a marker of ischemia. Brain pre-processing and immunohistochemistry were performed exactly as described previously (5). For the immunohistological procedures, both 50 μm and 30 μm thick sections were cut. All staining procedures (anti-neuronal nuclei (NeuN), anti-glial fibrillary acidic protein (GFAP), anti-aquaporin 4 (AQP-4), anti-IgG, anti-pimonidazole and albumin) were performed on 50 μm sections. However, due to low tissue penetration, staining with anti-alpha smooth muscle actin (alpha-SMA) antibody was made on 30 μm thick sections and an extra first step of overnight incubation at room temperature in permeabilization solution was added in the staining protocol. The permeabilization solution was composed of 0.2 % v/v Triton X100 (Sigma Aldrich; X100), 2.3% w/v glycine (Sigma Aldrich; G8898) and 20% v/v Dimethyl Sulfoxide (DMSO) (Sigma Aldrich; D5879) in PBS. A summary of all primary and secondary antibodies used here, is listed in Table 1.

3D reconstruction of intervention hemisphere and quantification of brain ischemia, hypoxia and infarction

For the quantification of ischemia, hypoxia and infarction, a 500 μm thick volume of the intervention hemisphere was reconstructed based on confocal images, exactly as described previously (7). Briefly, tilescan images of ten consecutive coronal sections were made using a confocal laser scanning microscope SP8 (Leica Microsystems, Wetzlar, Germany). After alignment of the sections using AMIRA software (Visage Imaging, Inc., San Diego, CA, USA) segmentation of the damaged volumes were made in IMARIS 9.3, a 3D analysis software (Bitplane Inc., St. Paul, MN, USA). The volumes were exported in an excel document and used for the calculation of the total and mean damaged volumes.

Table 1. *Summary of primary and secondary antibodies.*

Antibody	Type	Working dilution	Species	Source
NeuN	Primary	1:500	Mouse	Millipore-MAB377
Alpha-SMA	Primary	1:200	Mouse	Abcam-AB7817
Anti-rat Cy3 (IgG staining)	Primary	1:500	Goat	Brunschwig-A10522
AQP-4	Primary	1:500	Rabbit	Millipore-AB2218
GFAP	Primary	1:500	Rabbit	Abcam-AB33922
Albumin	Primary	1:100	Sheep	Abcam-AB8940
Anti-Pimonidazole pacific blue	Secondary	1:500	Mouse	Hypoxyprobe, Pacific Blue Kit, HP15-x
Anti-mouse Cy3	Secondary	1:500	Goat	JIR-AB2338680
Anti-mouse FITC	Secondary	1:500	Goat	Abcam-AB6785
Anti-sheep Alexa-488	Secondary	1:500	Donkey	Abcam-AB150177
Anti-rabbit Alexa-488	Secondary	1:500	Goat	Invitrogen-A11034

Quantification of IgG leakage and IgG-positive vessels

Images of brain sections were captured using a confocal laser scanning microscope SP8 (Leica Microsystems, Wetzlar, Germany). Tilescan single-plane overview images of the coronal brain sections (50 µm thick) were taken with a 10× (air) objective (staining IgG, albumin). These images were used for the quantification of IgG leakage. Tilescan z-stack (z-step:2 µm) images of regions of interest (ROI's) on brain sections (30 µm thick) were captured with a 40× (oil) objective (staining IgG, and alpha-SMA). All IgG-positive perivascular spaces present on a brain section were captured. These images were used for the quantification of IgG-positive perivascular spaces of arteries and veins. Finally, tilescan z-stack (z-step:5 µm) images of IgG-positive perivascular spaces on brain sections (50 µm thick) were captured with a 40× (oil) objective (double staining IgG and GFAP, or IgG and AQP-4).

IgG leakage was assessed by determining mean pixel intensity in overview images. IgG leakage of either the whole intervention hemisphere, or different brain structures (corpus callosum, cortex, striatum and subarachnoid space (SAS)) was quantified and compared to the corresponding structures of the control hemisphere (contralateral side). In addition, the percentage of IgG-positive area was determined on the intervention hemisphere. For this analysis a fixed threshold was used in order to determine the area of the IgG-positive pixels and this IgG-positive pixel area was divided by the total area of the intervention hemisphere. Total IgG-positive area was also compared to the total ischemic area, both on the intervention hemisphere, in order to test whether there was a correlation. The individual ischemic areas were delineated manually. Note that IgG quantification was made on 2D images leading to areas (mm^2) and not volumes (mm^3). For all aforementioned analyses, FIJI software (version 1.8.0_172) was used. Finally, the number of IgG-positive arteries and veins was manually counted and evaluated by 2 experienced researchers, on maximum intensity projection images using Leica LAS X software (Leica Microsystems, Germany). Totally, 617 IgG-positive blood vessels were counted, of which 210 in group 15, 207 in group 25 and 200 in group 50. This analysis was assessed in a blinded fashion.

Statistical analysis

Normality of the data was tested by the Shapiro-Wilk test. Data are depicted as mean ± standard deviation (SD) or as median and interquartile range (IQR: box; whiskers: min–max), depending on their normality in distribution. Differences between intervention and control hemispheres were determined using a Wilcoxon signed rank or paired t-test. Differences between groups (15, 25 and 50), or between anatomical structures (cortex, striatum, corpus callosum) were determined using analysis of variance followed by Tukey's test for multiple comparisons, or Kruskal-Wallis followed by Dunn's test for multiple comparisons. Differences in the counts of IgG-positive arteries and veins were tested using a binominal test. Differences were considered statistically significant when $P \leq 0.05$. Correlation between total ischemic area and total IgG-positive area on the intervention hemisphere were determined using either Spearman or Pearson test. Statistical analyses and graphing were performed using GraphPad Prism 9.1 software (GraphPad Software, La Jolla, CA).

RESULTS

Impact of microspheres on perfusion, hypoxia and neurological deficits

In the present study we found that 25000 microspheres of 15 µm caused a comparable amount of cumulative damage as 5500 of 25 µm and 1000 of 50 µm in terms of ischemia and hypoxia (~2% of the intervention hemisphere). The cumulative volume of infarcted brain tissue tended to be larger in the 50 µm group (p=0.09 vs 15 µm; p=0.10 vs 25 µm), but this did not reach statistical significance (Fig. 1A). As expected, the 15 µm group had smaller but more numerous ischemic and infarcted volumes compared to the 50 µm group (Table 2 and Fig. 1B). In contrast, we found smaller mean hypoxic regions in the 50 µm group compared to the 25 µm (Table 2 and Fig. 1B middle graph).

In terms of neurological function, assessed by the Bederson score, two out of six animals in each group had severe defects (Grade 3: lethargic, circling behavior). However, in the 50 µm group the neurological deficits were even more severe, in addition to the two animals with grade 3, two animals had paralysis (Grade 5: paralysis), and two had no stroke symptoms. One animal did not survive the first 24h post-surgery (not included in the analysis). When all groups were combined, almost half of the animals had obvious signs of stroke (8 out of 18), of which 6 were female. Thus, microspheres causing infarction to 1-2% of the brain hemisphere are sufficient to cause obvious neurological deficits in a substantial portion of the studied animals.

Table 2. *Number of ischemic, hypoxic and infarcted volumes per group. Data are shown as mean with standard deviation (SD). 15 µm microspheres lead to more ischemic volumes as compared to 50 µm. *** indicates P<0.001 for 25 µm vs 15 µm, ****indicates P<0.0001 for 50 µm vs 15 µm.*

	15 µm	**25 µm**	**50 µm**
Number of ischemic volumes ± SD	92±25	38±16***	16±7****
Number of hypoxic volumes ± SD	712±1054	114±58	896±1203
Number of Infarction volumes ± SD	42±39	24±8	11±8

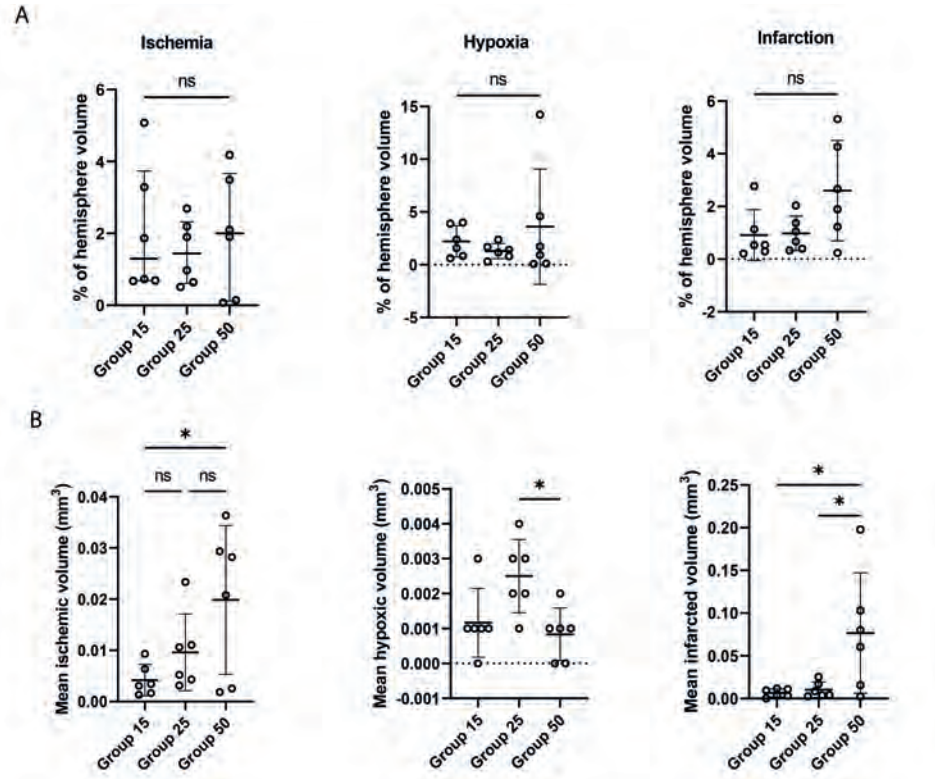

Figure 1. Impact of microspheres on brain perfusion parameters. (A) *Data show total volumes of brain tissue affected by ischemia, hypoxia, and infarction, respectively, as percentage of the hemisphere. The cumulative volume was the same for all sizes of microspheres.* ***(B)*** *The mean volumes of individual territories affected by ischemia and infarction was larger in the 50 µm group as compared to the 15 µm group. The mean hypoxic volume was larger in brains infused with microspheres of 25 µm as compared to 50 µm. N = 6 animals per group. Data are depicted as mean ± standard deviation. Analysis of variance with Tukey's multiple comparison test. * indicates P<0.05, ns=not significant.*

IgG leakage into brain parenchyma after microembolization with different microsphere sizes

Microembolization may lead to blood brain barrier (BBB) disruption, which can be detected by the leakage of blood components such as IgG or albumin, into the brain parenchyma. Indeed, microspheres of all sizes were found to induce leakage of IgG into the affected hemisphere, with occasionally some leakage in border zones between the control and intervention hemisphere. We found a similar leakage pattern for both IgG and albumin (Supplementary Information Fig. S1), but due to the simpler procedure for IgG detection continued the analysis only with IgG. The pattern of IgG leakage was found to be more dispersed in the smaller microsphere sizes (15, 25 µm) and more localized in the 50 µm group (Fig. 2A-C). In group 15, IgG leakage led to both higher mean intensity (Fig. 2B) and larger IgG-positive area (mm²) (Fig. 2C) compared to group 50. In all cases, the mean IgG intensity was significantly higher on the intervention hemisphere as compared to the control (Fig. 2B) and the IgG-positive area correlated with total ischemic area (Supplementary Information Fig. S2).

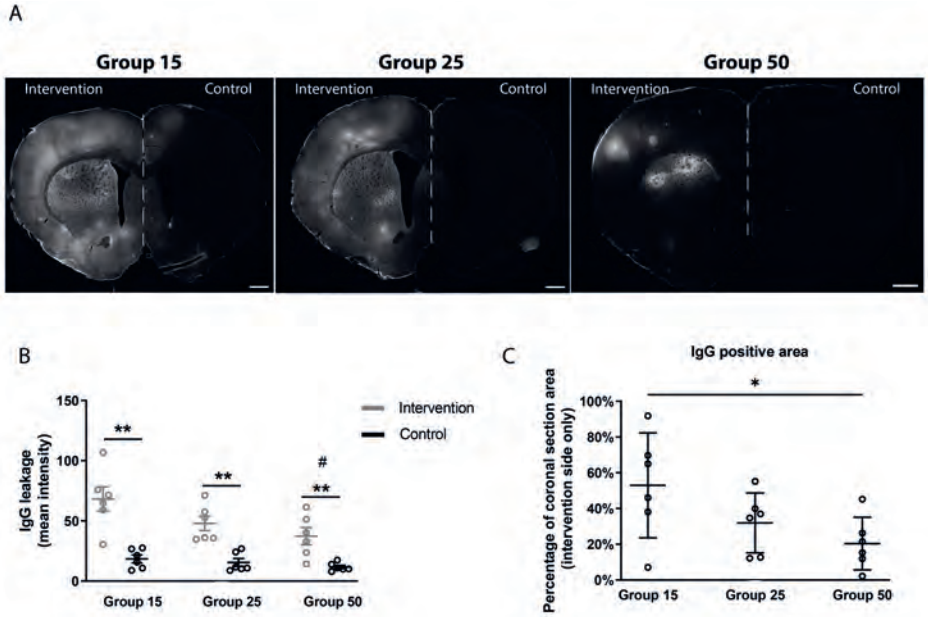

Figure 2. IgG leakage appears in a more diffuse pattern in the 15 µm group. ***(A)*** *Representative example per group (15, 25, 50 µm) of a coronal brain section showing IgG leakage on the intervention hemisphere (left side). Scale bar = 1000 µm.* **(B)** *Quantification of IgG leakage (mean intensity) per group (15, 25, 50 µm) and comparison to the control hemisphere. Data are depicted as mean with standard deviation. Paired t-test between hemispheres. ** indicates P<0.01. Ordinary One-way ANOVA between groups with Tukey's multiple comparison test. # indicates P<0.05 and refers to differences between group 50 and 15. N = 6 animals per group.* **(C)** *IgG-positive area of the intervention hemisphere as determined on a single coronal brain section. 15 µm microspheres lead to a larger area of IgG leakage as compared to 50 µm microspheres. Data are shown as the average percentage ± standard deviation being IgG-positive. * indicates P<0.05. N = 6 animals per group.*

We then questioned whether gray and white matter are affected differently by micro-infarcts with respect to IgG leakage. We divided the coronal brain sections into 3 anatomical structures namely cortex, striatum and corpus callosum (Fig. 3A). Cortex represents gray matter, striatum a combination of gray and white matter, and corpus callosum consists of white matter. Corpus callosum had a lower mean intensity of IgG signal compared to striatum and cortex in all groups (Fig. 3B). In addition, there was significantly higher IgG intensity in the intervention hemisphere compared to control for each anatomical structure.

IgG is present in the perivascular space of arteries and veins that surround ischemic regions

After careful examination of the intervention hemisphere, we detected IgG accumulation around blood vessels in addition to the aforementioned diffuse IgG leakage in the brain parenchyma associated with microspheres (Fig. 4). To gain more insight in the precise anatomical location of the IgG-positive staining, associated with blood vessels, we performed additional stainings. We used GFAP as an astrocytic marker and AQP-4 as a marker of the water channels located on the astrocytic endfeet. This GFAP and AQP-4 staining showed that IgG accumulated within perivascular spaces of cerebral vasculature

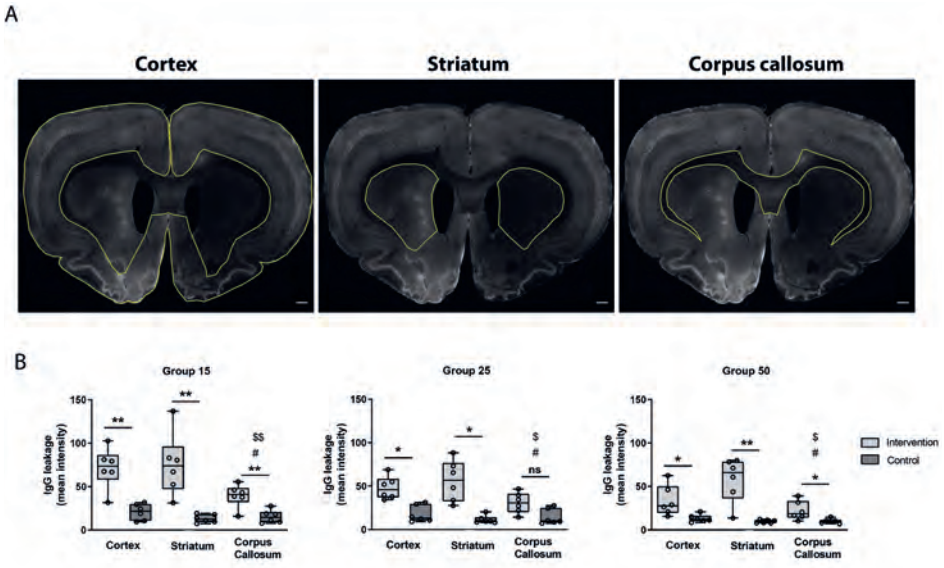

Figure 3. IgG leakage was less prominent in white matter (corpus callosum). (A) *Anatomical structures indicated in the same coronal brain section. From left to right: cortex, striatum, corpus callosum. Scale bar = 500 µm.* ***(B)*** *Quantification of IgG leakage in the different anatomical structures, for both the control and intervention hemisphere per group (15, 25, 50 µm). N = 6 animals per group. For a better comparison, all data are depicted as median with interquartile range, although only group 25 is not normally distributed. Paired t-test, or Wilcoxon test between hemispheres. * indicates P<0.05, ** indicates P<0.01. Ordinary One-way ANOVA between anatomical structures with Tukey's multiple comparison test. $ indicates P<0.05, $$ indicates P<0.01 and refers to differences between Corpus callosum and Cortex. # indicates P<0.05 and refers to differences between Corpus callosum and Striatum.*

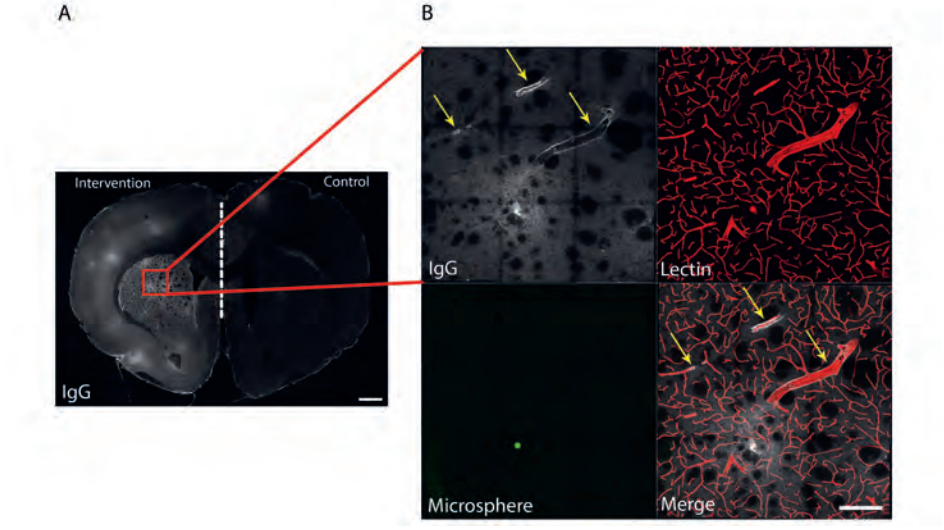

Figure 4. (A) *IgG-positive coronal brain section with IgG-positive vessels on the intervention side. Scale bar = 1000 µm.* ***(B)*** *Detail of IgG-positive staining along blood vessels (arrows) in the vicinity of an ischemic region (absence of lectin) caused by a microsphere (green). Scale bar = 200 µm.*

(Fig. 5). Next, we examined whether IgG was located in the perivascular space of arteries or veins. Using alpha-SMA as a marker of arteries, we found IgG-positive perivascular spaces of both arteries and veins (Fig. 6A, B). After quantification of the IgG-positive vessels we found that ~70% were arteries and the remaining ~30% were veins (Fig. 6C).

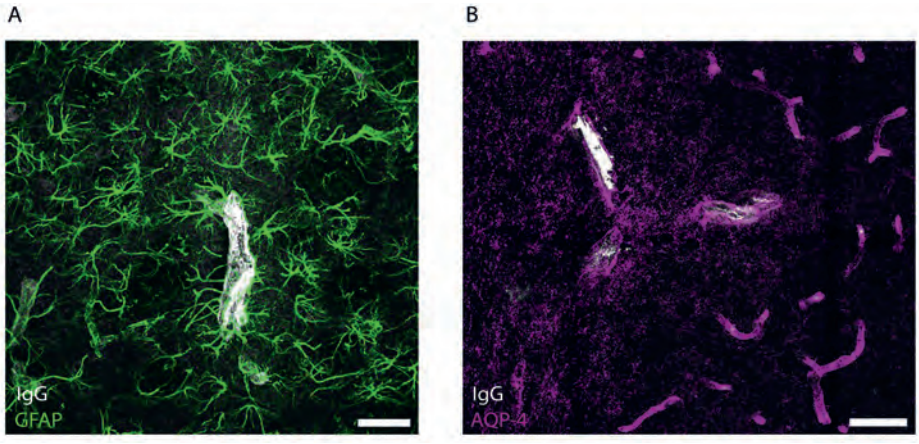

Figure 5. IgG-positive perivascular spaces. *IgG staining was found to be within the boundaries of the perivascular space, delineated by astrocyte endfeet (GFAP staining)* ***(A)*** *and aquaporin-4 channels (AQP-4 staining)* ***(B)****. Scale bar = 100 µm.*

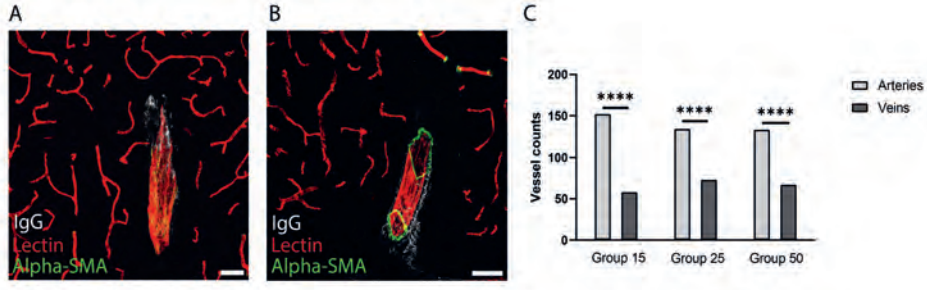

Figure 6. *IgG-positive perivascular spaces of veins* ***(A)****, arteries* ***(B)*** *and their quantification* ***(C)****. In each group, the majority of IgG-positive perivascular spaces were identified along arteries. Scale bar = 50 µm. Binominal test between arteries and veins.**** indicates P<0.0001.*

Presence of IgG in the subarachnoid space (SAS)

To study the fate of IgG that leaked into brain tissue, we also quantified the staining for IgG in the SAS of both the intervention and control hemisphere. In each group, the intensity was higher in the intervention hemisphere (Fig. 7).

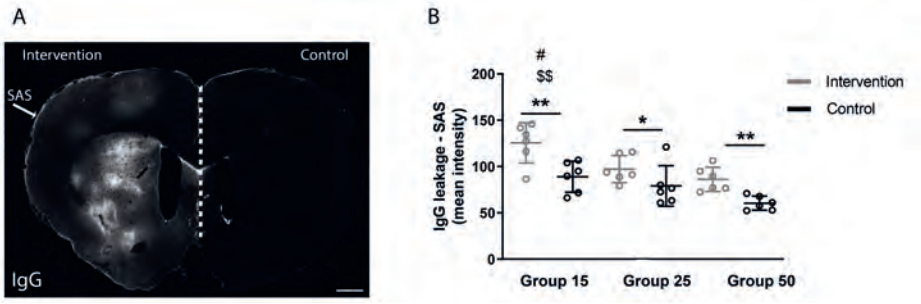

Figure 7. The role of subarachnoid space (SAS) in clearance of IgG. (A) *IgG intensity in the SAS of a coronal rat brain section (of group 50). Scale bar = 1000 µm.* **(B)** *Quantification of IgG intensity in the SAS per group. The SAS of the intervention side has a significantly higher mean IgG intensity as compared to the control side. Data are depicted as mean with standard deviation. Paired t-test between hemispheres. * indicates P<0.05, ** indicates P<0.01. Ordinary One-way ANOVA between groups with Tukey's multiple comparison test.. ^{ss} indicates P<0.01 and refers to differences between group 15 and 50. $^{\#}$ indicates P<0.05 and refers to differences between group 15 and 25.*

DISCUSSION

In this study we addressed the role of perivascular spaces in the clearance of IgG. This protein was investigated as representative for blood components that leak across the BBB of ischemic territories into brain tissue. We found that one day after infusion of microspheres, IgG leakage was prominent in the affected hemisphere, with some spillover of IgG into the adjacent control hemisphere. This spillover may result from perfusion territories of blood vessels at the border zone that extend into the control hemisphere. Alternatively, microspheres may have passed from the circulation of the intervention hemisphere to the control hemisphere via collaterals. IgG leakage into the interstitium was patchy, as expected from local occlusions. A novel finding was the presence of IgG and albumin in the perivascular spaces of blood vessels in the intervention hemisphere.

The presence of IgG in perivascular spaces was substantiated by staining for AQP-4 and GFAP, which we used to delineate astrocyte endfeet. The presence of IgG-positive staining between the astrocyte endfeet and the vessel wall clearly demonstrated that IgG was present in the perivascular space. An important finding in the present study was that IgG staining was found along both arteries and veins, which suggests that the perivascular spaces of both types of vessels are involved in the transport of proteins that leaked into the brain tissue. An obvious limitation of the current work however, is that postmortem staining does not allow direct assessment of directionality of transport along the perivascular spaces.

The route of IgG clearance was further studied by analysis of IgG staining at the level of the SAS. Here we found that staining was stronger in the intervention hemisphere, which suggests that net transport of IgG occurred from tissue to the SAS, for which the most plausible route would be along both arteries and veins towards the brain surface. This route (under ischemic conditions) would imply a deviation from the physiological route of brain clearance according to the glymphatic theory (3). This route along both arteries and veins, could be the result of a change in the direction and magnitude of the

driving forces that occur due to the pathological leakage of water and solutes in the affected hemisphere. This hypothesis fits well with the observations of Wang et al. (2017) (8) who showed that entry of fluorescent dye from the cerebrospinal fluid (CSF) compartment into brain tissue was abolished three days after infusion of cholesterol crystals as a model for micro-infarcts. Of note, the difference in fluorescence intensity between the control and intervention hemisphere indicates that apparently, mixing of CSF between both hemispheres at the level of the SAS is limited.

Recent work by Mestre et al. (2020) (9) showed that within minutes after an ischemic challenge induced by middle cerebral artery occlusion, CSF influx via perivascular spaces contributes to local edema. Local vasoconstriction and expansion of the perivascular space play a role herein. Our data were obtained one day after induction of ischemia, which could represent the start of the resolution phase. We previously showed that parenchymal IgG staining gradually disappears in the course of days and weeks in this model (2, 10). We think it is unlikely that perivascular staining as found in our experiments reflects remaining IgG and albumin from the initial CSF influx. The physiological levels of IgG and albumin in CSF is relatively low and elicits weak staining, as can be seen in the control hemisphere. The strong staining in the perivascular spaces and SAS of the intervention hemisphere does not fit with this. It thus appears that after initial CSF influx, the perivascular spaces contribute to the efflux of water and solutes after an ischemic insult in the resolution phase.

IgG that leak into brain tissue are normally quickly eliminated across the BBB via Fc receptors (11). It may be that this pathway is overwhelmed or perhaps not fully functional in the intervention hemisphere. We also found that IgG staining was less in white matter as compared to tissue consisting of gray matter, or a mixture of the two types of brain tissue. This finding could simply be a reflection of the reduced vascular density of white matter, which we previously found in rats (12). Alternatively, it could be explained by an increase in clearance rate. A lower vulnerability to BBB damage in white matter as compared to gray matter seems unlikely, as white matter is more often implicated in injury after stroke (13).

We used microspheres of different sizes, ranging from 15 μm, to 25 μm, and 50 μm. The number of microspheres was lowered with the increase in microsphere diameter, to inflict a comparable burden to the affected hemispheres. The data on the cumulative volumes of ischemia indicate that this goal was achieved in terms of impaired perfusion. In terms of IgG leakage, we observed that the group infused with 50 μm microspheres was associated with lower cumulative IgG signal in the affected hemisphere. Possibly, the fewer occlusions and slow diffusion rate of IgG into brain tissue could explain these findings. Interestingly, the mean hypoxic volume was largest in the group infused with microspheres of 25 μm. Possibly, ischemic territories induced by this size of microspheres elicit hypoxic territories that may still survive, whereas occlusions in the group with 50 μm, hypoxic areas advance to infarction.

In conclusion, we found that micro-infarcts induced by a range of microsphere sizes are associated with perivascular staining for IgG and albumin. This involves both arteries and veins in the vicinity of micro-infarcts. These blood proteins may derive from a local

disruption of the BBB and reflect a clearance pathway towards the SAS. The clinical implication of this work is that the role of perivascular clearance from blood components, and presumably also fluid, deserves further attention as a potential target for treatment after an ischemic insult. At present, therapeutic strategies that target this brain clearance system are lacking, but the impact of postural changes (14), sleep (15) and the impact of different types of anesthesia (16, 17) may be fruitful areas for future research in this respect.

FUNDING

This project was funded by the European Union's Horizon 2020 research and innovation program under grant agreement No 777072 (INSIST) and Neuroscience Amsterdam (project number NDIS-2019-03).

AUTHORS' CONTRIBUTIONS

TG: design, data acquisition, analysis, and interpretation, drafted the manuscript. AEvdW: design, data acquisition. EvB: design, data interpretation, revised the manuscript. EB: design, data analysis and interpretation, drafted the manuscript. All authors approved submission of the work.

REFERENCES

1. Jessen, N. A., Munk, A. S., Lundgaard, I. & Nedergaard, M. PMC4636982; The Glymphatic System: A Beginner's Guide. *Neurochem. Res.* **40**, 2583-2599 (2015).
2. van der Wijk, A. E. *et al*. PMC7671188; Microembolus clearance through angiophagy is an auxiliary mechanism preserving tissue perfusion in the rat brain. *Acta Neuropathol Commun* **8**, 195 (2020).
3. Iliff, J. J. *et al.* PMC3551275; A paravascular pathway facilitates CSF flow through the brain parenchyma and the clearance of interstitial solutes, including amyloid β. *Sci Transl Med* **4**, 147ra111 (2012).
4. Braun, M. & Iliff, J. J. The impact of neurovascular, blood-brain barrier, and glymphatic dysfunction in neurodegenerative and metabolic diseases. *Int. Rev. Neurobiol.* **154**, 413-436 (2020).
5. Georgakopoulou, T., van der Wijk, A. E., Bakker, E. & vanBavel, E. Recovery of Hypoxic Regions in a Rat Model of Microembolism. *J Stroke Cerebrovasc Dis* **30**, 105739 (2021).
6. Huo, Y. & Kassab, G. S. PMC3223633; Intraspecific scaling laws of vascular trees. *J R Soc Interface* **9**, 190-200 (2012).
7. Xue, Y. *et al*. PMC9385041; Quantification of hypoxic regions distant from occlusions in cerebral penetrating arteriole trees. *PLoS Comput Biol* **18**, e1010166 (2022).
8. Wang, M. *et al.* PMC5354332; Focal Solute Trapping and Global Glymphatic Pathway Impairment in a Murine Model of Multiple Microinfarcts. *J. Neurosci.* **37**, 2870-2877 (2017).
9. Mestre, H. *et al.* PMC7375109; Cerebrospinal fluid influx drives acute ischemic tissue swelling. *Science* **367** (2020).
10. van der Wijk, A. E. *et al.* Extravasation of Microspheres in a Rat Model of Silent Brain Infarcts. *Stroke* **50**, 1590-1594 (2019).
11. Schlachetzki, F., Zhu, C. & Pardridge, W. M. Expression of the neonatal Fc receptor (FcRn) at the blood-brain barrier. *J. Neurochem.* **81**, 203-206 (2002).
12. Naessens, D. M. P., de Vos, J., VanBavel, E. & Bakker, E. PMC6151927; Blood-brain and blood-cerebrospinal fluid barrier permeability in spontaneously hypertensive rats. *Fluids Barriers CNS* **15**, 26 (2018).
13. Wang, Y. *et al.* PMC5677601; White matter injury in ischemic stroke. *Prog. Neurobiol.* **141**, 45-60 (2016).
14. Lee, H. *et al*. PMC4524974; The Effect of Body Posture on Brain Glymphatic Transport. *J. Neurosci.* **35**, 11034-11044 (2015).
15. Xie, L. *et al*. PMC3880190; Sleep drives metabolite clearance from the adult brain. *Science* **342**, 373-377 (2013).
16. Benveniste, H. *et al*. PMC5685871; Anesthesia with Dexmedetomidine and Low-dose Isoflurane Increases Solute Transport via the Glymphatic Pathway in Rat Brain When Compared with High-dose Isoflurane. *Anesthesiology* **127**, 976-988 (2017).
17. Stanton, E. H. *et al.* Mapping of CSF transport using high spatiotemporal resolution dynamic contrast-enhanced MRI in mice: Effect of anesthesia. *Magn. Reson. Med.* **85**, 3326-3342 (2021).

SUPPLEMENTARY INFORMATION

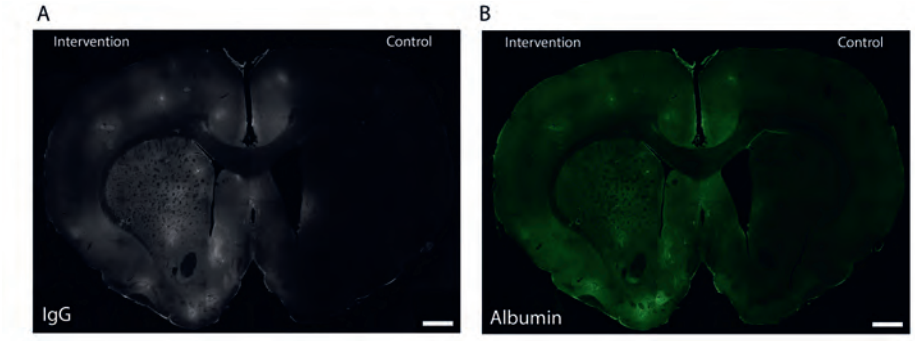

Figure S1. *IgG* ***(A)*** *and albumin* ***(B)*** *staining show similar patterns of leakage in the brain parenchyma. Scale bar = 1000 µm.*

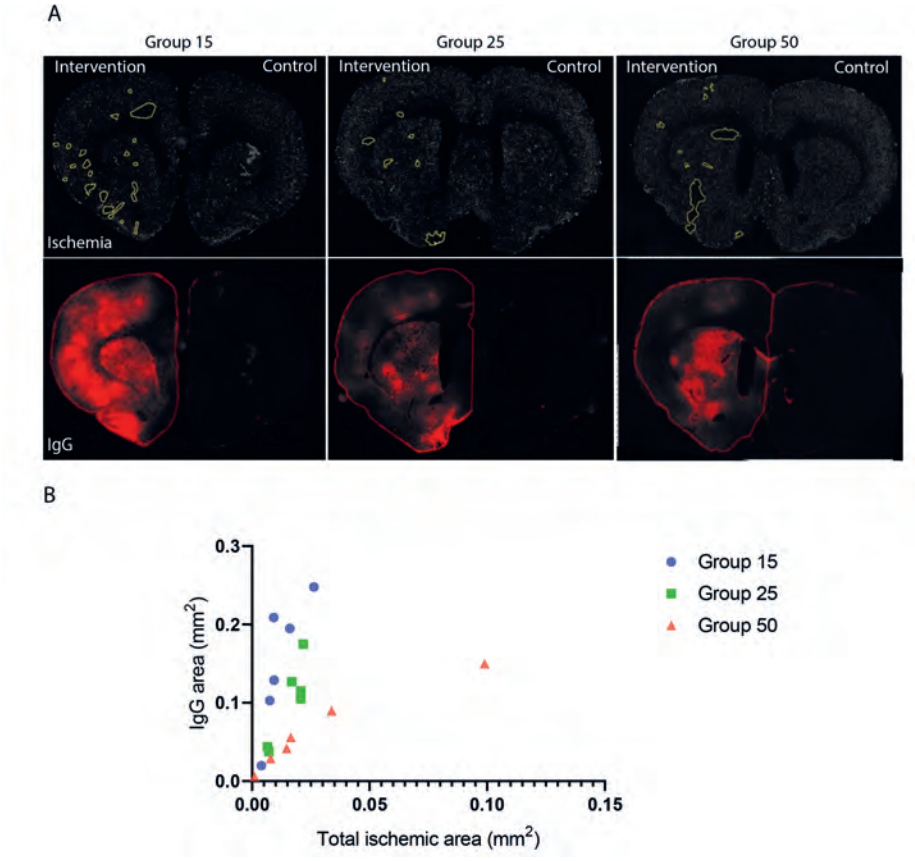

Figure S2. (A) *Quantification of ischemic areas (yellow demarcated regions; upper panel) and IgG leakage (red thresholded regions; lower panel) per group on the intervention hemisphere.* ***(B)*** *Correlation between total ischemic area and total area of IgG leakage. Group 15: $R^2 = 0.67$ (Pearson correlation, $p<0.05$), Group 25: $R^2 = 0.80$ (Pearson correlation, $p<0.05$), Group 50: $r = 1$ (Spearman correlation, $p<0.01$). N = 6 animals per group.*

Chapter 6

MICROEMBOLUS CLEARANCE THROUGH ANGIOPHAGY IS AN AUXILIARY MECHANISM PRESERVING TISSUE PERFUSION IN THE RAT BRAIN

Anne-Eva van der Wijk[1*], Theodosia Georgakopoulou[1*], Jisca Majolée[2], Jan S.M. van Bezu[2], Miesje M. van der Stoel[3], Bert J. van het Hof[4], Helga E. de Vries[4], Stephan Huveneers[3], Peter L. Hordijk[2], Erik N.T.P. Bakker[1], Ed van Bavel[1]

[1] Amsterdam UMC, University of Amsterdam, Biomedical Engineering and Physics, Amsterdam Cardiovascular Sciences, Meibergdreef 9, Amsterdam, The Netherlands

[2] Amsterdam UMC, Vrije Universiteit Amsterdam, Physiology, Amsterdam Cardiovascular Sciences, De Boelelaan 1117, Amsterdam, The Netherlands

[3] Amsterdam UMC, University of Amsterdam, Medical Biochemistry, Amsterdam Cardiovascular Sciences, Meibergdreef 9, Amsterdam, The Netherlands

[4] Amsterdam UMC, Vrije Universiteit Amsterdam, Molecular Cell Biology and Immunology, Amsterdam Neuroscience, De Boelelaan 1117, Amsterdam, The Netherlands

* Shared first authorship

Acta Neuropathol Commun. (2020) 8(1):195

ABSTRACT

Considering its intolerance to ischemia, it is of critical importance for the brain to efficiently process microvascular occlusions and maintain tissue perfusion. In addition to collateral microvascular flow and enzymatic degradation of emboli, the endothelium has the potential to engulf microparticles and thereby recanalize the vessel, through a process called angiophagy. Here, we set out to study the dynamics of angiophagy in relation to cytoskeletal remodeling *in vitro* and reperfusion *in vivo*. We show that polystyrene microspheres and fibrin clots are actively taken up by (brain) endothelial cells *in vitro*, and chart the dynamics of the actin cytoskeleton during this process using live cell imaging. Whereas microspheres were taken up through the formation of a cup structure by the apical endothelial membrane, fibrin clots were completely engulfed by the cells, marked by dense F-actin accumulation surrounding the clot. Both microspheres and fibrin clots were retained in the endothelial cells. Notably, fibrin clots were not degraded intracellularly. Using an *in vivo* microembolization rat model, in which microparticles are injected into the common carotid artery, we found that microspheres are transported by the endothelium from the microvasculature into the brain parenchyma. Microembolization with microspheres caused temporal opening of the blood-brain barrier and vascular nonperfusion, followed by microsphere extravasation and restoration of vessel perfusion over time. Taken together, angiophagy is accompanied by active cytoskeletal remodeling of the endothelium, and is an effective mechanism to restore perfusion of the occluded microvasculature *in vivo*.

INTRODUCTION

Although the brain comprises only 2% of the body weight, it is responsible for approximately 20% of the total body's energy expenditure (1). Since the brain has no substantial local energy storage, it has a critical need for a constant cerebral blood flow. In order to maintain sufficient perfusion to meet its energy demands, the brain has a uniquely organized vascular network. The cerebral cortex is supplied and drained by interconnected pial arteriolar and venular networks, connected through penetrating arterioles and venules with the three-dimensional microvascular network feeding the parenchyma (2). This intricate microvascular network ensures tissue perfusion throughout the brain, with every neuron positioned within <15 μm from a capillary (3).

Obstruction of the cerebral microvasculature impairs local perfusion and leads to ischemic damage. Such obstruction can result from brain embolization, with microemboli originating from various sources. For instance, patients with atrial fibrillation have a substantial burden of vascular brain lesions (4), of which a large portion may be caused by cardioembolic events. Although many of the lesions are clinically unnoticed, they are associated with decreased cognitive function (4). Recently, it became clear that (micro) embolization of the brain may be a major complication of the infectious disease COVID-19 (5). Furthermore, the introduction of intra-arterial thrombectomy in the treatment of acute ischemic stroke has surfaced a major challenge in the field. Recanalization of the occluded artery is achieved in the large majority of patients after thrombectomy, yet the procedure itself may result in emboli showers dislodging from the main thrombus (6-8), causing widespread microvascular perfusion deficits distal of the initial event (8).

Microembolus composition and location determine the extent of tissue damage caused by an occlusion. Microemboli may be rich in red blood cells, have different characteristics depending on thickness and density of fibrin strands (9), or consist mainly of cholesterol (10), calcified material (11) or white blood cells (12). This specific composition makes clots more or less prone to degradation, hence affecting the resolution of tissue ischemia. In addition, the extent of collateralization of the vascular plexus where the occlusion or embolus occurs determines whether alternative pathways for perfusion are available (13, 14) or not (14, 15), and thus, whether local tissue perfusion is maintained.

Considering its intolerance to ischemia, it is very important for the brain to efficiently process small emboli and maintain tissue homeostasis. Although the three-dimensional microvasculature is highly interconnected, collateral microvascular flow is not always sufficient to maintain tissue perfusion. Whereas the brain has endogenous fibrinolytic capacity (8, 16), many emboli are poorly susceptible to this enzymatic degradation (17), with prolonged vessel occlusion and hypoxia as a result. Notably, the endothelium has the potential to engulf microparticles from the circulation and extrude them on the abluminal side, in a process called angiophagy. This extravasation of microparticles was found in the brain and other organs and with emboli of different sources in mice (18, 19), rats (20) and in the human retina (18, 21). Crucially, angiophagy may be a protective mechanism of the brain to reestablish blood flow through vessel recanalization (19).

Here, we show that microparticle uptake is associated with active cytoskeletal

remodeling of endothelial cells *in vitro*, using fibrin clots and polystyrene microspheres. Furthermore, we quantified the percentage of perfused vessels after microembolization and demonstrate that embolus extravasation *in vivo,* or angiophagy, is needed to restore vessel perfusion in a microembolization model in rats.

METHODS

Cell culture and *in vitro* endothelial uptake experiments

Human umbilical vein endothelial cells (HUVECs; Lonza, Verviers, Belgium, passage 2-5) were grown to confluence on 5 µg/ml fibronectin-coated glass coverslips (Menzel™, ThermoFisher, Amsterdam, The Netherlands) and kept in Endothelial Cell Medium (ECM) supplemented with singlequots (ScienCell Research Laboratories, Carlsbad, CA) at 5% CO_2 at 37ºC. Human cerebral microvascular endothelial cells (hCMEC/D3, passage 29-31) were grown in type I collagen-coated Ibidi slides in EGM™-2 BulletKit™ Medium (Lonza). Microspheres (15 µm; 10,000 per well (surface area 1.9 cm^2)) or Texas Red-conjugated fibrin clots (~2,700 per well (surface area 1.9 cm^2); see Supplementary Materials and Methods), were added to the cells in a volume of 50 µl. Based on approximate cell numbers in confluent HUVEC cultures and added microspheres, this is 1 microsphere per ~10 cells. After 4 or 24h cells were fixed with 4% paraformaldehyde for 15 min and immunofluorescence staining was done (Supplementary Materials and Methods).

Images were recorded using a confocal laser scanning microscope SP8 (Leica Microsystems, Wetzlar, Germany) with a 63x 1.40 NA oil objective. Microparticles were imaged at five random locations per well and z-stacks were made based on phalloidin signal with z-steps of 0.30 µm. Images were deconvolved using Huygens Professional version 19.04 (Scientific Volume Imaging, The Netherlands, http://svi.nl) and 3D images were rendered using LAS X 3D software (version 3.7.0; Leica Microsystems).

Lentiviral transductions and live cell imaging

Lentiviral particles were generated by transfecting HEK293T cells with the lentiviral expression construct with 3rd generation packaging plasmids using *Trans*IT®-LT1 transfection reagents (Mirus Bio LLC, Madison, WI). The supernatant containing the lentiviral particles was harvested 48-72h post transfection. HUVECs were transduced with LifeAct-mTurquoise construct (as described in Goedhart et al. (2012) (22)) cloned into a Lentiviral vector (pLV) overnight, selected with puromycin and grown to confluence on fibronectin-coated Lab-Tek Chambered 1.0 borosilicate coverglass slides (ThermoFisher) in EGM™-2 medium (Lonza). Live cell imaging was done with an inverted NIKON Eclipse Ti equipped with a 60x 1.49 NA Apo TIRF (oil) objective, perfect focus system, CFP and mCherry filter cubes and an Andor Zyla 4.2 plus sCMOS camera. An Okolab cage incubator and humidified CO_2 gas chamber set to 37ºC and 5% CO_2 were used during imaging. Frames were taken every minute for 4-8h.

Animals

The animal experiments in this study were conducted in female and male Wistar rats (16 to 20 weeks old, Charles River). Rats were housed in pairs under a 12h light-dark cycle and fed *ad libitum* with standard laboratory chow and free access to water. All surgical procedures were conducted under isoflurane inhalation anesthesia mixed with oxygen while the body temperature was monitored with a feedback-regulated heating pad. Adequate depth of anesthesia was verified by absence of toe-pinch reflex.

Cerebral embolization procedure

On the day of surgery, animals were weighed and anesthetized with isoflurane (induction 4%, maintenance 2-2.5% in 1 L/min O_2). Buprenorphine (0.05 mg/kg) was administered subcutaneously 30 min prior to the first incision for analgesia. The rat was placed in a supine position on a homeostatic heating pad, hair was removed from the skin caudal to the mandibles and iodide was used to disinfect the skin. A midline incision was made from below the mandible to the sternal notch. To expose the left carotid artery around the bifurcation, the superficial fascia, salivary glands and the muscle layers were blunt dissected. The left common carotid (CCA), the internal carotid (ICA) and external carotid (ECA) artery were exposed and the ECA and occipital artery were temporarily ligated with 6-0 surgical sutures. Next, a mixture of fluorescent microspheres (DiagPoly™ Plain Fluorescent Polystyrene Particles, λ Ex 530 nm, λ Em 582 nm, Creative Diagnostics®, Shirley, NY) or fibrin clots (10,000 particles; Supplementary Information Materials and Methods and Fig. S1) was injected into the left CCA using a 29G insulin needle (25,000 of 15 µm (14.1±1.2), 5,500 of 25 µm (26.3±3.0) and 625 of 50 µm (50.4±3.3) microspheres, resuspended in sterile 2% bovine serum albumin in phosphate buffered saline (PBS), in a total volume of 200 µl). No microparticles were injected in the right CCA, and therefore the right hemisphere served as the untreated control. To stop the bleeding after removal of the needle, pressure was applied to the injection site. Subsequently, threads were removed. The wound was closed with sutures and rats were allowed to recover on a heating pad before returning to their cages. One animal had to be killed directly after the surgery because it did not recover well from anesthesia and was excluded from analysis. Two sham animals, in which the ECA and occipital artery were ligated and 2% bovine serum albumin in PBS was injected in the CCA, were killed one day after surgery to serve as a control for surgery and anesthesia effects on edema and Immunoglobulins (IgG) extravasation but not included in the final analysis.

Tissue preparation and immunofluorescence staining

Animals injected with microspheres were killed on day (D) 1 (n=8), 3 (n=8) or 7 (n=8) after surgery, and animals injected with fibrin clots were killed on D1 (n=4) or within an hour (n=1) after surgery. After induction of anesthesia, the vasculature was labeled by an intravenous injection of DyLight 594 labeled tomato lectin (1 mg/kg; DyLight 594 labeled lycopersicon Esculentum tomato, Vector Laboratories, Burlingame, CA) and allowed to circulate for 5 min. Rats were given 100 µl heparin i.p. and after increasing isoflurane to 5%

animals were transcardially perfused with heparinized PBS followed by tissue fixation with 4% paraformaldehyde at 80 mmHg. Tissue preparation and immunofluorescence staining are further described in Supplementary Materials and Methods. Images of brain sections were captured using a confocal laser scanning microscope SP8 (Leica Microsystems) with a 10x 0.5 NA (air) or 20x 0.75 NA (oil) objective.

Image analysis

Five animals were excluded from analysis because the microsphere injections were not successful (i.e. no or very few microspheres were found in the brain – both vessels and parenchyma), resulting in the analyses being done on D1 (n=6), D3 (n=6) and D7 (n=7). Quantification of microsphere extravasation was performed on sections stained for laminin. Microsphere extravasation was scored as "in" (microspheres are inside a vessel), "going out" / extraluminal (in the process of extravasation, in many cases observed as a vessel with lectin perfusion yet with the microsphere still contained within the extracellular matrix, often seen as a laminin bulge); or "out" / parenchymal (outside of the vessel lumen and the extracellular matrix) by two independent researchers blinded to the identity of the specimen. An extravasation score was calculated for each animal to enable statistical analysis, where microspheres scored as "in" were given 0, "going out" 1 and "out" 2. Vessel nonperfusion was quantified in the same samples, and a vessel was identified as "nonperfused" when there was no lectin distal and/or proximal from the occluding microsphere. Midline shift was calculated by measuring the width of the control and treated hemispheres starting from the midline, and divided by the total width from ex vivo coronal sections in FIJI (version 2.0.0-rc-69/1.52m). Three sections were measured and averaged per animal. IgG leakage, glial fibrillary acidic protein (GFAP) and ionized calcium-binding adaptor molecule 1 (Iba1) signal intensity was assessed by determining mean pixel intensity in overview images, while excluding ventricles using threshold analysis in FIJI (all pixels with "0" were excluded). All analyses on animal brain sections were quantified in a blinded fashion.

Statistics

Data are depicted as median ± interquartile range (IQR: box; whiskers: min – max) or mean ± standard deviation (SD). Data was tested for normality using a QQ-plot and a Shapiro-Wilk test and depending on the outcome, a parametric or nonparametric test was performed. Differences between treated and untreated hemispheres were determined using a Wilcoxon signed rank or paired t-test. Differences between groups (D1, 3 and 7) were determined using analysis of variance (ANOVA) followed by Tukey Kramer's test for multiple comparisons, or by Kruskal-Wallis with Dunn's test for multiple comparisons. Between-size (15 μm and 25 μm microspheres) differences were tested with a repeated measures 2-way ANOVA and association of categorical variables was tested with a Chi-square test. Differences were considered statistically significant when $P \leq 0.05$. Statistical analyses and graphing were performed using GraphPad Prism 6 software (GraphPad Software, La Jolla, CA).

RESULTS

Microparticles are taken up by endothelial cells *in vitro*

To determine whether microparticles are taken up by endothelial cells *in vitro*, we added microspheres (15 µm) and fibrin clots (10-40 µm) to HUVEC monolayers followed by fixation after 4 and 24h. Already after 4h, we observed that the endothelial cells generate apical membrane protrusions, forming cups around the microspheres. In all cases, F-actin- and VE-cadherin-positive "caps" were observed on top of the microspheres in addition to F-actin in the basal plane of the cup structures (Fig. 1A and Supplementary Information Video S1), indicating that the microspheres were completely engulfed by the endothelial cell. In Fig. 1B, we quantified the fluorescence profile for the adherens junction protein VE-cadherin and F-actin in the z direction, demonstrating location of these caps at +15 µm relative to the apical membrane. Cell-cell contacts remained intact despite uptake of microspheres, as deduced from the VE-cadherin signal at intercellular junctions (Supplementary Information Video S1). In addition, we observed that fibrin clots in many cases were completely internalized by HUVECs already after 4h, with dense F-actin concentrations in the apical membrane (Fig. 1C and Supplementary Information Video S1). In some cases, this was a joint effort performed by multiple cells, as shown by intact adherens junctions between cells engulfing the clot (Fig. 1C). HUVECs are endothelial cells of peripheral, macrovascular origin, and may respond differently to stimuli compared to barrier-forming, microvascular endothelium of the central nervous system (23). Therefore, we also used hCMEC/D3 cells, often used as a simplified model of the human blood-brain barrier (BBB) (24). Similar to HUVECs, endothelial membrane protrusions and "caps" were found surrounding the microspheres (Supplementary Information Fig. S2A, B), and fibrin clots were encapsulated by F-actin rich membrane protrusions (Supplementary Information Fig. S2C).

Engulfed microparticles are retained intracellularly in live cells

Using a lentiviral approach, we transduced HUVECs with LifeAct-mTurquoise to visualize the F-actin cytoskeleton dynamics during microparticle uptake in live cells. Similar to what we observed with immunofluorescence staining, addition of microspheres to the cells induced the formation of an endothelial apical, F-actin rich cup, surrounding the microsphere (Video 1). This cup generally formed within 2-4h after microsphere addition, and microspheres were retained by the endothelial cell that had taken up the particle, even during cell locomotion and division. For fibrin clots, we observed F-actin-rich points of contact, taking hold of the clot at multiple sites, and F-actin accumulation around the clot (indicated with open arrow in Video 2). Once taken up inside the cell, we consistently observed an imprint of the fibrin clot in the F-actin cytoskeleton (indicated with filled arrow in Video 2). Of note, fibrin clots were not degraded intracellularly, but were carried along by the cell that had taken up the particle, similar to the microspheres. Taken together, these *in vitro* data show that microparticles are retained intracellularly once they are taken up and fibrin clots are not degraded by endothelial cells.

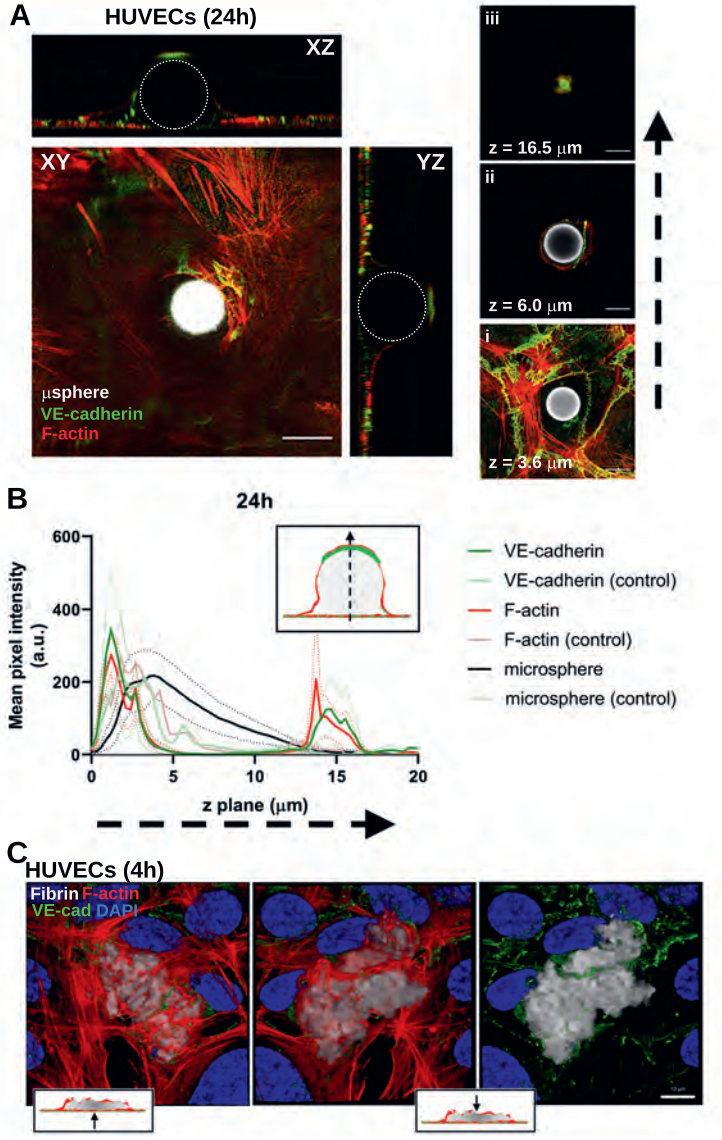

Figure 1. Microspheres are taken up by HUVECs. (A) *XZ and YZ orthogonal view of a z-stack shows a cup structure of phalloidin (F-actin; red) surrounding the microsphere (white; in XZ and YZ depicted with dashed line), and F-actin- and VE-cadherin-positive "caps" on top of the microsphere. Different z planes are shown in i, ii and iii. Note the F-actin and VE-cadherin (green) surrounding the microsphere in ii, and the cap on top of the microsphere in iii. Scale bar = 10 μm.* **(B)** *Quantification of signal intensity for F-actin, VE-cadherin and microsphere (dark-colored lines) in the z direction shows a peak in signal intensity after z = 15 μm, which is the cap structure on top of the microsphere. Light-colored lines are signal intensity in control location, i.e. of a region where no microsphere was bound. Signal intensity was quantified from 2-4 images averaged from n=3 independent experiments. Data are depicted as mean ± standard deviation (dashed lines).* **(C)** *Three-dimensional rendering of a fibrin clot, encapsulated by the cytoskeleton with intact adherens junctions. Left panel is the view from below the cellular monolayer, middle panel is the view from above the monolayer. Right panel shows that the fibrin clot is taken up by two cells, demonstrated by the intact adherens junction between cells across the clot. Cell nuclei are blue (DAPI). Scale bar = 10 μm.*

https://actaneurocomms.biomedcentral.com/articles/10.1186/s40478-020-01071-9#additional-information

Video 1. Live cell imaging showing microsphere uptake by HUVECs. *HUVECs were transduced with lentiviral LifeAct (green) to visualize the cytoskeleton and images were taken every 2 minutes over 8h in xy. Left panel: LifeAct (green) and a 15 µm microsphere (white; coming in from the left) and fibrin clot (white; coming in from the right). Right panel: only LifeAct signal in grey. The endothelium generates protrusions and a F-actin rich cup structure surrounding the microsphere, occurring after ± 4h after microsphere addition (red arrow indicates the endothelial cup).*

https://actaneurocomms.biomedcentral.com/articles/10.1186/s40478-020-01071-9#additional-information

Video 2. Live cell imaging showing fibrin clot uptake by HUVECs*. HUVECs were transduced with lentiviral LifeAct (green) to visualize the cytoskeleton and images were taken every minute over 8h in xy. Left panel: LifeAct (green) and fibrin clot (white). Right panel: only LifeAct signal in grey. Fibrin clots are taken up by the cell through multiple F-actin-rich points of contact (open arrow) and, once taken up in the cell, leave an imprint in the F-actin cytoskeleton (filled arrow). Fibrin clots are retained by the cell, despite cell locomotion and division, and are not degraded intracellularly.*

Microparticles do not affect endothelial barrier function *in vitro*

We assessed possible endothelial barrier loss by microparticles using Electric Cell-Substrate Impedance Sensing (ECIS). We found that the addition of microspheres and fibrin clots did not alter electrical resistance of HUVEC monolayers (Fig. 2A, B), except for 2 of the 5 experiments where endothelial barrier function was negatively influenced after addition of the highest amount of microspheres (green bar, Fig. 2B). However, this amount exceeded the amount used in the experiments (Fig. 1), which corresponds to the red bar in Fig. 2B. To test for preservation of endothelial cell responses, we used a thrombin receptor activating peptide 24h after the addition of microparticles, which caused a rapid drop and recovery of electrical resistance similar to that seen in control cells (data not shown). This finding suggests that microparticles did not affect endothelial reactivity or viability.

Timing of microsphere extravasation *in vivo*

In our previous work, we established that microspheres (15 µm) can extravasate from the vessel lumen in the rat cerebral microcirculation (20). Here, we injected a mixture of different microsphere sizes (15, 25 and 50 µm) into the internal carotid artery of rats to determine whether there is a size limit for emboli to undergo extravasation and if size

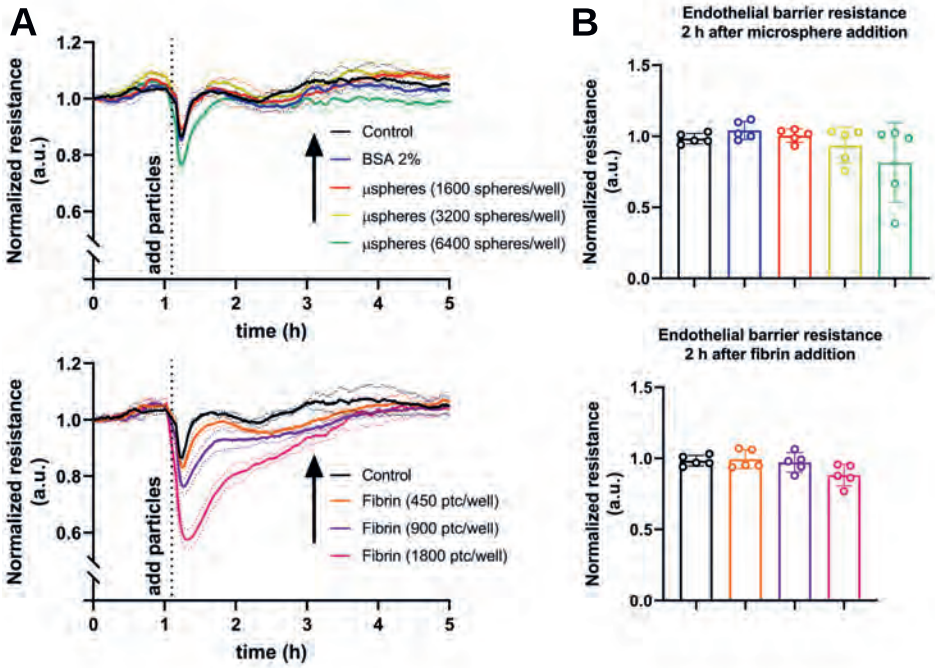

Figure 2. Impedance measurements with ECIS after addition of microparticles to HUVECs. (A) *Example tracing of an ECIS experiment after addition of different amounts of microspheres or fibrin clots to endothelial cells. Tracings are shown as normalized electrical resistance, where t_0 is the baseline electrical resistance of ~1h prior to addition of microparticles. Baseline electrical resistance at 400 Hz was 1086 Ω (median; range 633–1513 Ω). The arrows indicate the time point used for quantification in B.* ***(B)*** *Quantification of electrical resistance at 400 Hz 2h after addition of microparticles. N = 5 independent experiments done in triplo. Data are depicted as mean ± standard deviation. One-way ANOVA with Tukey–Kramer's test for multiple comparisons.*

affects extravasation rate. In Supplementary Information Table S1, percentages of microspheres injected and detected in the brain are given. We only occasionally observed 50 µm microspheres in the brain parenchymal vessels. We injected 625 50 µm microspheres per animal as to not induce severe neurological damage, and it is possible that a large portion of these microspheres remained in the pial vasculature as was demonstrated previously with magnetic resonance imaging (25), and that we were unable to detect them in our coronal sections. Because of the low number of observed 50 µm microspheres, we limited our analysis to the smaller microspheres.

Based on staining for the extracellular matrix component laminin (Fig. 3A and Supplementary Information Video S2), we scored 15 and 25 µm microspheres as being inside a vessel ("in"); in the process of extravasation ("going out" / extraluminal); or outside of the vessel lumen and the extracellular matrix ("out" / parenchymal; see "Methods" section). Virtually all microspheres were inside the vessels at D1. At D3, a small percentage of microspheres was in the process of extravasation, or had extravasated from the vessel. At D7, we found that for microspheres of 15 µm and 25 µm around half of the scored particles was either extraluminal or already parenchymal (Fig. 3B and Supplementary Information Table S2).

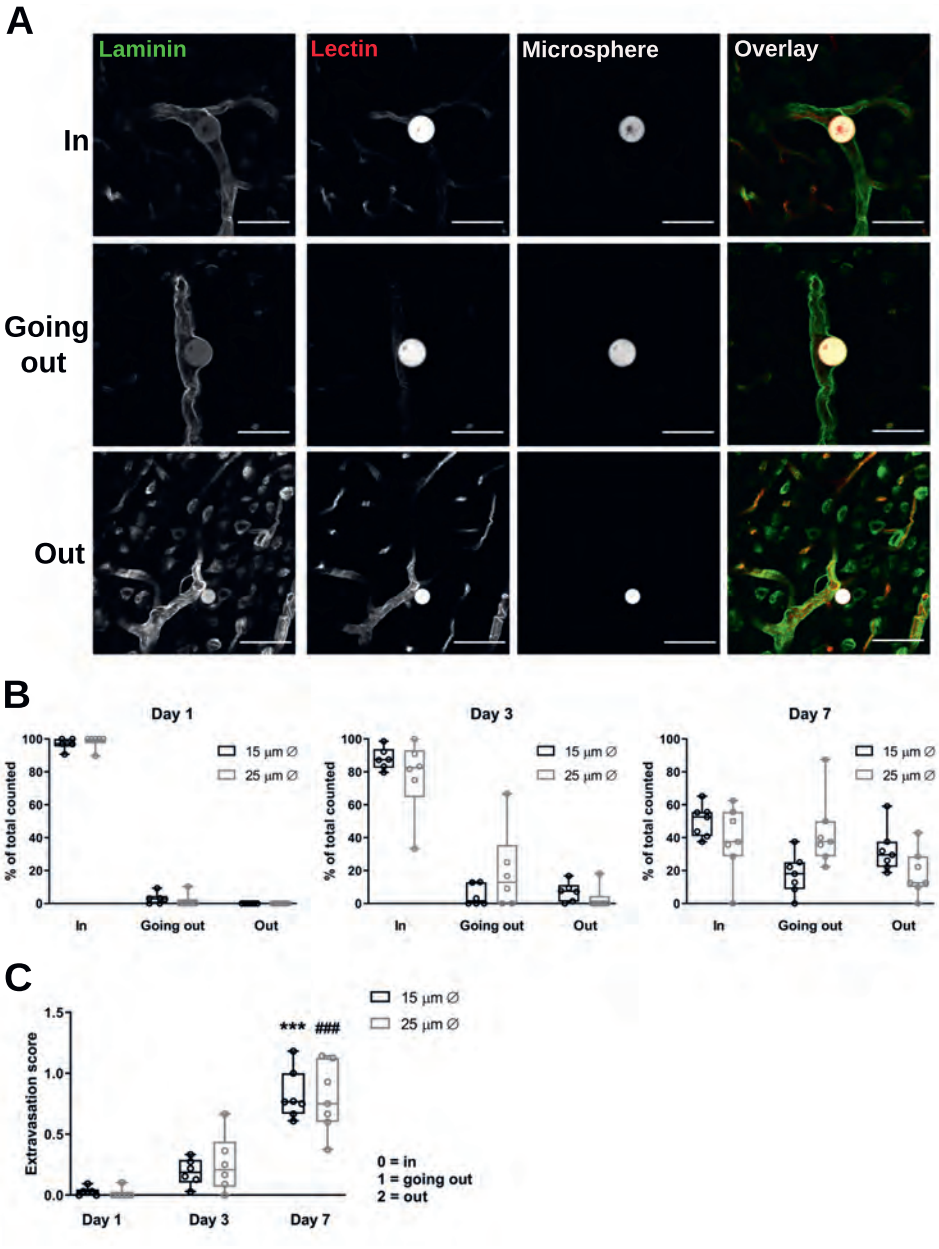

Figure 3. Microsphere extravasation in vivo is independent of size. **(A)** *Examples of microspheres (white) scored as "in" (top panel), "going out" (middle panel) and "out" (bottom panel) in coronal brain sections stained postmortem for laminin (green) and i.v. lectin (red) before killing. Scale bar = 50 µm.* **(B)** *Quantification of microsphere extravasation at D1, 3 and 7 for 15 µm (black boxes) and 25 µm microspheres (grey boxes). N = 6–7 animals per time point. Data are depicted as median and IQR (min–max).* **(C)** *An extravasation score between 0 and 2 was calculated per rat to determine whether extravasation rate was dependent on time point and microsphere size ("in" was weighed as 0, "going out" as 1 and "out" as 2). N = 6–7 animals per time point. Data are depicted as median and IQR (min–max). ***P < 0.001, 15 µm D1 versus D7; ###P < 0.001, 25 µm D1 versus D7, Kruskal–Wallis with Dunn's multiple comparison test.*

We calculated an extravasation score, reflecting the average phase of extravasation per rat per day (see "Methods" section), for 15 µm and 25 µm microspheres. For both sizes of microspheres, the extravasation score was significantly higher at D7 compared to D1 (Fig. 3C; P=0.0004 for 15 µm and P=0.0007 for 25 µm microspheres, respectively). However, there was no effect of microsphere size on extravasation score (Fig. 3C, P=0.8339, two-way RM ANOVA), suggesting that extravasation rate is similar for microspheres of 15 and 25 µm.

Lastly, since embolus composition may affect extravasation rate, we injected fluorescently-labeled fibrin clots ranging from ~10-40 µm and killed the rats at D1 (n=4). To our surprise, we did not detect any fibrin clots or fragments inside the vessels or the brain parenchyma (Fig. 4A), nor did we find any fibrin in the retina, choroid plexus of the eye or the lungs (data not shown). In order to ascertain that the injections were successful, we added microspheres to the fibrin suspension and observed microspheres in the brain, but not fibrin clots. In contrast, we did detect fibrin clots occluding microvessels at 1h after injection (Fig. 4B and Supplementary Information Video S3), ruling out a technical problem with fluorescent fibrin clots entering the brain. This finding suggests that fibrin clots may be processed within 24h by the brain after intra-carotid injection, yet precludes the use of these emboli to further study angiophagy in our model.

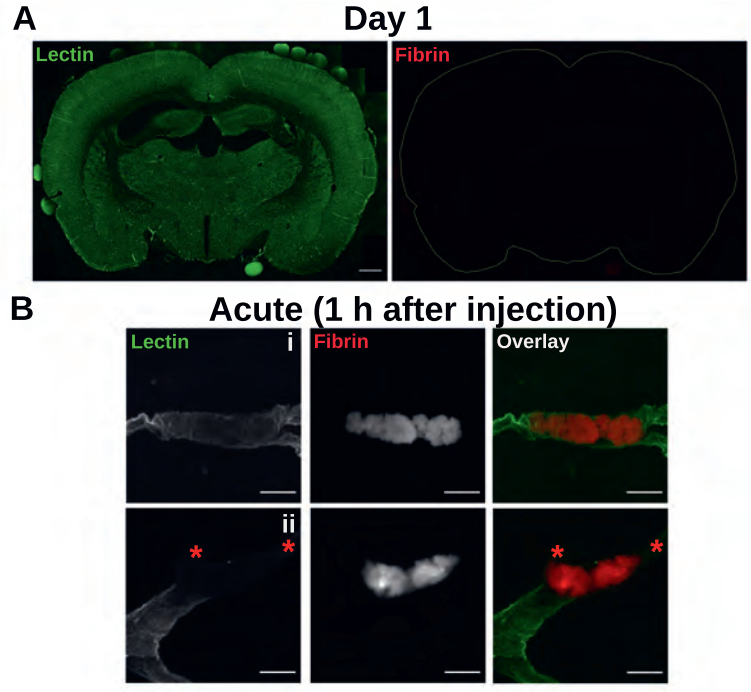

Figure 4. Microembolization with fibrin clots in vivo. (A) *Fibrin clots (red) were not found in the brain vasculature (lectin; green), nor in the brain parenchyma at D1 after embolization. Scale bar = 1 mm.* ***(B)*** *Example (maximum intensity projections) of fibrin clots in the brain vasculature in an acute experiment, i.e. the rat was killed 1h after injection with fibrin clots. (i) Fibrin clot (red) with lectin perfusion (green), and (ii) a fibrin clot occluding the vessel and hampering lectin perfusion. Scale bar = 10 µm.*

Microsphere extravasation is associated with vascular perfusion *in vivo*

Using an intravenous lectin injection on the day of killing and a postmortem laminin staining, we calculated the percentage of nonperfused vessels after microembolization with microspheres in rats. Figure 5A shows two examples of a vessel occluded by a microsphere enveloped by extracellular matrix (laminin): one with lectin perfusion despite the presence of a microsphere, and one lacking lectin signal, suggesting there was no vascular perfusion. Microembolization resulted in vascular nonperfusion in 72.9% and 80.0% of the scored vessels at D1 for 15 µm and 25 µm microspheres, respectively (IQR 64.2-77.7% for 15 µm and 62.5-87.5% for 25 µm; Fig. 5B). For both sizes of microspheres, the percentage of nonperfused vessels decreased significantly over time, with only 38.5% and 33.8% of nonperfusion at D7, respectively (IQR 28.9-53.5%; P=0.0004, D7 vs D1 for 15 µm and IQR 26.5-42.5%; P=0.0075, D7 vs D1 for 25 µm).

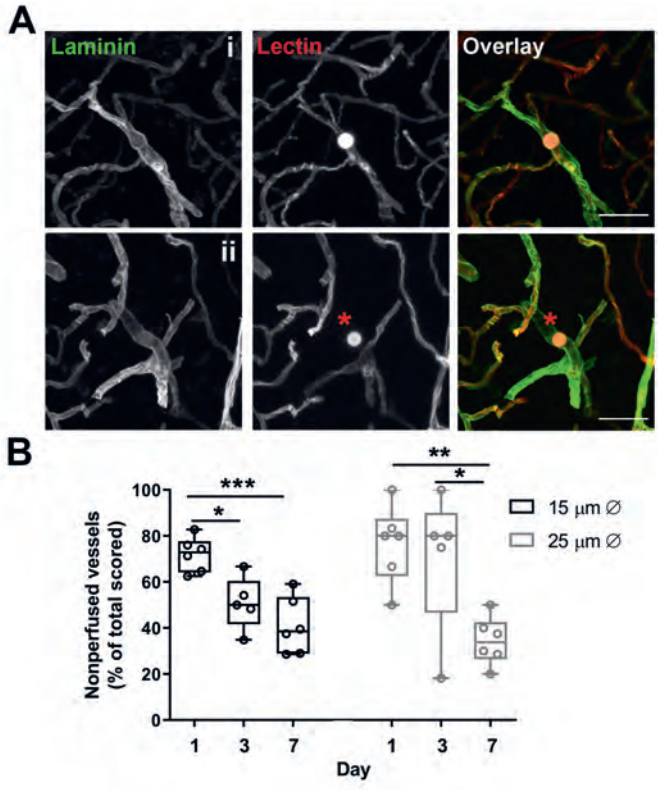

Figure 5. Quantification of perfused vessels after microembolization in vivo. (A) *Example (maximum intensity projections) of (i) a microsphere (white) with lectin perfusion despite the presence of a microsphere, and (ii) a microsphere causing vascular nonperfusion (asterisk) using i.v. lectin (red) at the day of killing and postmortem laminin staining (green). Scale bar = 50 µm.* ***(B)*** *Quantification of vascular nonperfusion at D1, 3 and 7 for 15 µm (black boxes) and 25 µm microspheres (grey boxes). Three animals were excluded from perfusion analysis because the i.v. lectin injection failed, resulting in n=5-6 animals per time point. Data are depicted as median and IQR (min – max). *P<0.05, **P<0.01, ***P<0.001, one-way ANOVA with Tukey Kramer's test for multiple comparisons.*

In Table 1, the scored microspheres are categorized according to their extravasation status per day per size, and further classified into “perfused” or “nonperfused”. Using a Chi-square test, we found that extravasation status and perfusion were strongly associated variables at all time points, showing that microsphere extravasation is associated with vessel reperfusion.

Table 1. *Nonperfusion of vessels is related to extravasation status. ns=not significant, *P<0.05, **P<0.01, ***P<0.001.*

	Perfused (#)	Nonperfused (#)	Total scored (#)	nonperfused (%)	p-value (X^2)
D1 (n=6)					
15 µm					
In	40	120	160	75.0	0.0016 (**)
Going out	5	1	6	16.7	
Out	0	0	0	n/a	
25 µm					
In	5	26	31	83.9	0.6620 (ns)
Going out	0	1	1	100	
Out	0	0	0	n/a	
D3 (n=5)					
15 µm					
In	79	83	162	51.2	0.0013 (**)
Going out	9	6	15	40.0	
Out	11	0	11	0.0	
25 µm					
In	9	21	30	70.0	0.0242 (*)
Going out	3	2	5	40.0	
Out	2	0	2	0.0	
D7 (n=6)					
15 µm					
In	24	76	100	76.0	<0.0001 (****)
Going out	25	4	29	13.8	
Out	62	4	66	6.1	
25 µm					
In	7	13	20	65.0	0.0003 (***)
Going out	18	6	24	25.0	
Out	9	0	9	0.0	

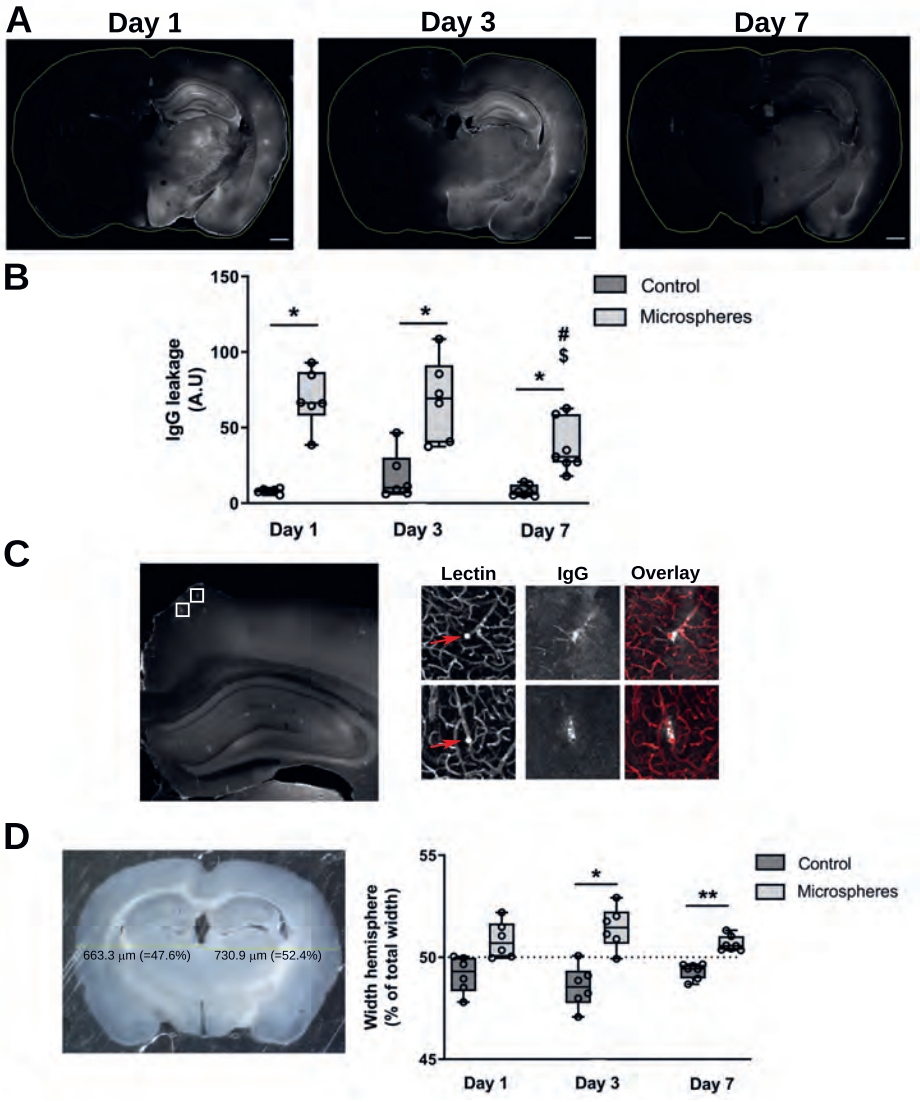

Figure 6. Microspheres induce BBB opening in vivo. **(A)** *There was widespread IgG extravasation (white) throughout the injected hemisphere, whereas this was not the case in the control hemisphere. Scale bar = 1 mm.* **(B)** *Quantification of IgG signal intensity at D1, 3 and 7 in the control (dark grey) and injected (light grey) hemispheres. N=6-7 animals per time point. Data are depicted as median and IQR (min – max). *P<0.05, between hemispheres, Wilcoxon matched-pairs signed rank test; #,$ P<0.05, D1 vs D7 and D3 vs D7, Kruskal-Wallis with Dunn's multiple comparison test.* **(C)** *Accumulation of IgG was occasionally observed at places where microspheres had lodged (boxed regions in left overview image are enlarged in the right panel, microspheres are indicated by red arrows).* **(D)** *Width of control and treated hemispheres were measured in ex vivo coronal sections and quantification demonstrated that the treated hemisphere (light grey) expanded at the expense of the control hemisphere (dark grey). N=6-7 animals per time point. Data are depicted as median and IQR (min – max). *P<0.05, **P<0.01, between hemispheres, paired t-test.*

Microspheres induce BBB opening *in vivo*

It takes several days for polystyrene microspheres to be extruded from the cerebral microvasculature (Fig. 3). The microsphere extravasation process itself, or the lack of perfusion of the occluded vessels, may lead to BBB disruption. Indeed, we observed widespread extravasation of IgG in the hemisphere in which we injected microspheres (Fig. 6A), indicative of a loss of BBB integrity. IgG signal intensity was significantly higher at all time points in the hemisphere injected with microspheres as compared to the control hemisphere (Fig. 6B). Signal intensity had decreased at D7, compared to D1 (P=0.0279) and D3 (P=0.0279), indicating that BBB opening may be temporary. IgG extravasation was observed throughout the entire hemisphere, yet with occasional accumulation at places where microspheres had lodged (Fig. 6C). Next, we measured the width of control and injected hemispheres in *ex vivo* coronal brain sections and found that the extensive BBB opening was accompanied by a midline shift, where the injected hemisphere expanded at the expense of the control hemisphere (Fig. 6D).

Finally, we observed mild reactive gliosis in the hemispheres injected with microspheres, demonstrated by immunostaining for reactive astrocytes with GFAP and activated microglia with Iba1. GFAP was expressed at higher levels in the hemisphere injected with microspheres as compared to the control hemisphere, peaking at D1 and D3, indicating the reactivity of surrounding astrocytes. Although expression appeared to have normalized at D7 (Supplementary Information Fig. S3A), quantification of the signal intensity showed sustained GFAP upregulation (Supplementary Information Fig. S3B). Iba1 expression increased in the hemisphere with microspheres at D3 and remained upregulated at D7 (Supplementary Information Fig. S3C, D). Moreover, microglia surrounding microspheres sometimes had a more amoeboid morphology, which is typical of an activated microglial phenotype, compared to the ramified morphology of quiescent microglia (Supplementary Information Fig. S3D). Taken together, microembolization and angiophagy are accompanied by transient BBB opening and mild gliosis.

DISCUSSION

Using a combination of *in vitro* and *in vivo* approaches, we here show in detail the extravasation of microspheres and fibrin clots. We found that processing of particles by endothelial cells is different for fibrin and microspheres, with uptake of fibrin clots through multiple F-actin-rich contact points and complete encapsulation by the cell. Microspheres on the other hand, are taken up by the endothelial cell through endothelial membrane protrusions and tunnel formation. The uptake of both microspheres and fibrin clots appears to occur anywhere in the cell, suggesting a preference for transcellular over paracellular transport. It was recently demonstrated that flow is required for endothelial cell remodeling and subsequent extravasation of tumor cells (26), in a mechanism similar to what we observed here. In that study, tumor cells were engulfed by endothelial cells which showed increased protrusions when kept under flow, yet this engulfment did not take place under static conditions (26). In our hands, fibrin engulfment takes place under static conditions as

shown by live cell imaging and immunofluorescence staining, and even inert polystyrene microspheres induce endothelial cell remodeling in the absence of flow. Thus, we show that flow is not a prerequisite for fibrin and microsphere uptake – in line with lack of flow in an occluded vessel *in vivo* – although it may very well enhance this process. In addition, polystyrene microspheres lack specific affinity to endothelial cells, and thus, microsphere uptake is independent of receptor-binding. Collectively and in line with previous studies (18, 19, 26), our results show that embolus uptake, transcellular transport and extravasation is associated with active remodeling of the endothelium.

In our rat model, we found that microembolization was accompanied by IgG extravasation and the affected hemisphere was enlarged at the expense of the control hemisphere, which is suggestive of edema. BBB opening was most prominent at early time points, when the large majority of microspheres occluded the vessels. Whether it is the vessel occlusion, or the process of angiophagy that is causing BBB opening is not clear from this study, but we suggest that BBB opening is temporary and will resolve once angiophagy proceeds and all microspheres have extravasated, as was shown previously (20). Moreover, we observed mild reactive gliosis and activated microglia in the embolized hemisphere. Upon an insult, ramified microglia can transform into an amoeboid form and have the potential to become phagocytic (27). The timing of microglial activation coincided with the first signs of microsphere extravasation, and thus may have been induced by the presence of foreign material in the brain parenchyma. Although we found no signs of microglial uptake of microspheres, it may very well be that microglia, or other perivascular cells such as pericytes, are involved in the post-extravasation degradation of more natural occurring microparticles on the tissue side (19).

Recently, it was demonstrated that cortical capillaries quite regularly undergo spontaneous obstruction (28), by what may be leukocytes or red blood cells (12). To mimic such capillary obstructions and investigate what happens to occluded capillaries, microspheres of 4 µm were injected through the tail vein. In this study, the authors showed that over two-third is cleared by dislodgement of the microsphere back into the circulation, and only 2% through angiophagy (28). However, microspheres of 4 µm can pass through the smallest capillaries (2), unlike microspheres sized >15 µm as used in the present study, which occlude arterioles. Thus, small obstructions such as seen by Reeson et al. (2018) (28) may be cleared by dislodgment before angiophagy can take place.

Studies using optical methods such as focal photothrombosis to occlude single vessels (14, 15) showed that single capillary occlusions did not lead to detectable tissue damage, consistent with an interconnected microvascular network where flow loss can be compensated for by anastomosing vascular branches (14). Although in our model we could not discriminate between what was proximal and distal from the microsphere, the fact that even at D1 a portion (about 20-30%) of the scored vessels had lectin perfusion despite the presence of an occluding microsphere, is in line with the idea that flow loss in the capillary bed may be partly compensated for by interconnected capillaries. However, we show that microvascular perfusion improves significantly over time and is strongly associated with extravasation status, with restored lectin perfusion in the vast majority of cases where

microspheres have undergone or are in the process of extravasation. This finding argues for the importance of angiophagy in microvascular perfusion, and it being a protective mechanism of the brain, at times when collateral flow and enzymatic degradation are insufficient.

A limitation of our study is that we were unable to capture extravasation of fibrin clots *in vivo*. Whereas fibrin clots were found to occlude vessels and hamper lectin perfusion in an acute experimental setting (i.e. within 1h after fibrin injection, Fig. 4 and Supplementary Information Video S3), we could not detect any fibrin in the brain at 1 day after surgery, indicating that fibrin clots are processed rapidly and efficiently in rats. This finding was surprising, as studies in mice reported the presence of fibrin clots in the circulation or brain parenchyma until 8 days after injection (18, 19). In the rat brain, the clots likely have undergone either intraluminal degradation or rapid angiophagy, followed by interstitial degradation. Previously, it was demonstrated in mice with *in vivo* two-photon imaging that both processes take place simultaneously, but that efficacy of enzymatic degradation decreased dramatically after the first 3h after embolization, leaving the brain still with a substantial microembolic burden (18). Similarly, another study found that only 40 to 50% of fibrin clots dissolved spontaneously in the mouse cerebral vasculature within 3h, and this was paralleled with a sustained reduction in cerebral blood flow (29). Therefore, we hypothesize that fibrin clots that have escaped enzymatic degradation were engulfed by the endothelium, extruded on the abluminal side and degraded in the interstitial space. This hypothesis is strengthened by several observations. Firstly, we did not find any evidence that particles that have been taken up are released back into the circulation (or the apical side *in vitro*). Since *in vitro* culture on glass coverslips is a limiting factor for the cells to extrude internalized particles as large as our fibrin clots or microspheres on the basolateral side, we found instead that both fibrin clots and microspheres are retained intracellularly (Video 1, 2). This internalization of fibrin took place within minutes, and *in vivo*, would hamper accessibility to blood-borne proteolytic enzymes, as was also suggested by Grutzendler et al. (2014) (18). Therefore, it would be a feasible scenario that *in vivo*, the internalized particles are taken up and extruded basolaterally, as is the case with microspheres. Secondly, fibrin clots are not degraded by endothelial cells (Video 2, Fig. 1C). However, endothelial cells and perivascular cells such as pericytes produce proteolytic enzymes (30), which may enhance fibrinolysis once the fibrin clots have been extruded. In fact, it was suggested that angiophagy is mediated by matrix metalloproteinases (19), which are also implicated in plasminogen-independent degradation of fibrin (31). However, future studies are needed to thoroughly address the involvement of angiophagy in clearing of microthrombi that escaped enzymatic degradation, e.g. in models where fibrinolysis is impaired.

Conclusions

Taken together, although angiophagy was associated with endothelial remodeling, temporary BBB opening and mild gliosis, our data suggest that it represents an important auxiliary mechanism of the cerebral vasculature to process emboli that cause widespread vessel occlusion. Considering that even inert, non-degradable microspheres are taken up by

the endothelium, we believe that angiophagy takes place independent of receptor-binding, and embolic material of any source can be taken up and extruded by the microvessels. Thus, delineating its dynamics and underlying mechanisms is important and may lead to future interventions promoting angiophagy in the brain, reducing local hypoxia, edema and loss of function following an embolic event.

FUNDING

This work was supported by the Amsterdam Cardiovascular Sciences (project number SH352009). This project was partially funded from the European Union's Horizon 2020 research and innovation program under grant agreement No 777072 (INSIST). The funding bodies had no role in the design of the study and collection, analysis and interpretation of data, nor in writing of the manuscript.

AUTHOR'S CONTRIBUTIONS

AEvdW, TG, ENTPB, PLH and EvB conceived and designed the experiments; TG and AEvdW performed the surgeries; AEvdW, JM, JSvB, AJvH, MMvdS performed *in vitro* experiments; AEvdW analyzed the data and wrote the manuscript; HEdV and SH contributed to discussion and ENTPB, EvB and PLH contributed to editing of the manuscript. All authors read and approved the final version of the manuscript.

REFERENCES

1. Sokoloff, L. in (eds Field, J., Magoun, H. W. & Hall, V. E.) 1843-1864 (American Physiological Society, Washington, DC, 1960).
2. Blinder, P. *et al.* PMC4141079; The cortical angiome: an interconnected vascular network with noncolumnar patterns of blood flow. *Nat. Neurosci.* **16**, 889-897 (2013).
3. Tsai, P. S. *et al.* PMC4972024; Correlations of neuronal and microvascular densities in murine cortex revealed by direct counting and colocalization of nuclei and vessels. *J. Neurosci.* **29**, 14553-14570 (2009).
4. Conen, D. *et al.* Relationships of Overt and Silent Brain Lesions With Cognitive Function in Patients With Atrial Fibrillation. *J. Am. Coll. Cardiol.* **73**, 989-999 (2019).
5. Klok, F. A. *et al.* PMC7192101; Confirmation of the high cumulative incidence of thrombotic complications in critically ill ICU patients with COVID-19: An updated analysis. *Thromb. Res.* (2020).
6. Chueh, J. Y. *et al.* Reduction in distal emboli with proximal flow control during mechanical thrombectomy: a quantitative in vitro study. *Stroke* **44**, 1396-1401 (2013).
7. Chueh, J. Y., Puri, A. S. & Gounis, M. J. An in vitro evaluation of distal emboli following Lazarus Cover-assisted stent retriever thrombectomy. *J Neurointerv Surg* **9**, 183-187 (2017).
8. Wang, C. X., Yang, T. & Shuaib, A. Clot fragments formed from original thrombus obstruct downstream arteries in the ischemic injured brain. *Microcirculation* **13**, 229-236 (2006).
9. Duffy, S. *et al.* Novel methodology to replicate clot analogs with diverse composition in acute ischemic stroke. *J Neurointerv Surg* **9**, 486-491 (2017).
10. Rapp, J. H. *et al.* Microemboli composed of cholesterol crystals disrupt the blood-brain barrier and reduce cognition. *Stroke* **39**, 2354-2361 (2008).
11. Rapp, J. H. *et al.* Cerebral ischemia and infarction from atheroemboli. *Stroke* **34**, 1976-1980 (2003).
12. Cruz Hernandez, J. C. *et al.* PMC6508667; Neutrophil adhesion in brain capillaries reduces cortical blood flow and impairs memory function in Alzheimer's disease mouse models. *Nat. Neurosci.* **22**, 413-420 (2019).
13. Schaffer, C. B. *et al.* PMC1324794; Two-photon imaging of cortical surface microvessels reveals a robust redistribution in blood flow after vascular occlusion. *PLoS Biol* **4**, e22 (2006).
14. Shih, A. Y. *et al.* PMC3952571; The smallest stroke: occlusion of one penetrating vessel leads to infarction and a cognitive deficit. *Nat. Neurosci.* **16**, 55-63 (2013).

15. Nishimura, N., Schaffer, C. B., Friedman, B., Lyden, P. D. & Kleinfeld, D. PMC1765467; Penetrating arterioles are a bottleneck in the perfusion of neocortex. *Proc. Natl. Acad. Sci. U. S. A.* **104**, 365-370 (2007).
16. Takashima, S., Koga, M. & Tanaka, K. PMC2072169; Fibrinolytic activity of human brain and cerebrospinal fluid. *Br. J. Exp. Pathol.* **50**, 533-539 (1969).
17. Murciano, J. *et al.* Platelets inhibit the lysis of pulmonary microemboli. *Am J Physiol Lung Cell Mol Physiol* **282**, 529 (2002).
18. Grutzendler, J. *et al.* Angiophagy prevents early embolus washout but recanalizes microvessels through embolus extravasation. *Sci Transl Med* **6**, 226ra31 (2014).
19. Lam, C. K., Yoo, T., Hiner, B., Liu, Z. & Grutzendler, J. PMC2879083; Embolus extravasation is an alternative mechanism for cerebral microvascular recanalization. *Nature* **465**, 478-482 (2010).
20. van der Wijk, A. E. *et al.* Extravasation of Microspheres in a Rat Model of Silent Brain Infarcts. *Stroke* **50**, 1590-1594 (2019).
21. Cho, K. H. *et al.* The Characteristics of Retinal Emboli and its Association With Vascular Reperfusion in Retinal Artery Occlusion. I*nvest. Ophthalmol. Vis. Sci.* **57**, 4589-4598 (2016).
22. Goedhart, J. *et al.* PMC3316892; Structure-guided evolution of cyan fluorescent proteins towards a quantum yield of 93%. *Nat Commun* **3**, 751 (2012).
23. van der Wijk, A. E., Vogels, I. M. C., van Noorden, C. J. F., Klaassen, I. & Schlingemann, R. O. TNFalpha-Induced Disruption of the Blood-Retinal Barrier In Vitro Is Regulated by Intracellular 3',5'-Cyclic Adenosine Monophosphate Levels. *Invest. Ophthalmol. Vis. Sci.* **58**, 3496-3505 (2017).
24. Weksler, B., Romero, I. A. & Couraud, P. O. PMC3623852; The hCMEC/D3 cell line as a model of the human blood brain barrier. *Fluids Barriers CNS* **10**, 16 (2013).
25. Zhu, L. *et al.* Do microemboli reach the brain penetrating arteries? *J. Surg. Res.* **176**, 679-683 (2012).
26. Follain, G. *et al.* Hemodynamic Forces Tune the Arrest, Adhesion, and Extravasation of Circulating Tumor Cells. *Dev Cell* **45**, 33-52 e12 (2018).
27. Davalos, D. *et al.* ATP mediates rapid microglial response to local brain injury in vivo. *Nat Neurosci* **8**, 752-758 (2005).
28. Reeson, P., Choi, K. & Brown, C. E. PMC5919759; VEGF signaling regulates the fate of obstructed capillaries in mouse cortex. *Elife* **7** (2018).
29. Atochin, D. N. *et al.* Mouse model of microembolic stroke and reperfusion. *Stroke* **35**, 2177-2182 (2004).
30. Harkness, K. A. *et al.* Dexamethasone regulation of matrix metalloproteinase expression in CNS vascular endothelium. *Brain* **123** (Pt 4), 698-709 (2000).
31. Hiraoka, N., Allen, E., Apel, I. J., Gyetko, M. R. & Weiss, S. J. Matrix metalloproteinases regulate neovascularization by acting as pericellular fibrinolysins. *Cell* **95**, 365-377 (1998).

SUPPLEMENTARY INFORMATION

SUPPLEMENTARY METHODS

Fibrin clots

Fibrin clots were made as described by Lam et al. (2010) (1). In short, fibrinogen from bovine plasma (Cat #F8630, Sigma-Aldrich; 100 mg/ml) was dissolved in PBS and conjugated with Texas Red succinimidyl ester (Cat #T6134, ThermoFisher; 5 mg/ml in DMSO) for 1h at room temperature. Next, bovine thrombin (500 U/ml in 0.1% BSA; Cat #112374, Merck Millipore) was added to the fibrinogen (62.5 U/ml end concentration), immediately vortexed and incubated at 40 ºC overnight. The resulting fibrin clot was fragmented into small pieces by crude mechanical disruption and sonication, washed with

ethanol to remove unbound ester, resuspended in PBS and filtered through cell strainers to eliminate debris and small particles, in order to get fibrin clots in the 10-40 µm range (Supplementary Information Fig. S1).

Immunofluorescence staining of cells

Cells were carefully washed in PBS and permeabilized with 0.2% TritonX-100 for 3 min, washed in PBS and blocked with 1% human serum albumin (HSA) for 1h. Next, cells were incubated in rabbit anti-VE cadherin (D87F2) XP® (1:400, Cat #2500, Cell Signaling, Danvers, MA) diluted in 1% HSA for 2h. After three wash steps (3 times 5 min in PBS), cells were incubated for 1h in goat anti-rabbit Alexa Fluor 488 (1:100, Invitrogen), a phalloidin probe (Acti-stain 555 phalloidin, 1:200, Cat #PHDH1, Cytoskeleton, Heerhugowaard, The Netherlands) and 4',6-diamidino-2-phenylindole (DAPI; 1:500) for nuclear staining diluted in 1% HSA. Cells were washed (three times 5 min in PBS) and coverslips were mounted with Mowiol® 4-88/DABCO solution (Sigma-Aldrich). All staining procedures were performed at room temperature.

Electric cell-substrate impedance sensing (ECIS)

Endothelial barrier function was assessed with electric cell-substrate impedance sensing (ECIS; Applied BioPhysics, Inc., Troy, NY). HUVECs were isolated as described previously (2) and seeded on 1% gelatin-coated gold electrode arrays (96W10idf; Applied BioPhysics). Impedance was measured during monolayer formation at 4 kHz with ECIS software (Applied BioPhysics). After formation of a stable endothelial barrier, microparticles were added to the cell medium in different concentrations (1600, 3200 or 6400 microspheres per well (surface area 0.32 cm^2) and 450, 900 or 1800 fibrin particles per well (surface area 0.32 cm^2) and impedance was measured for another 24h. For microspheres, a 2% BSA control was included, in addition to control wells where only PBS was added to the medium. Five independent experiments were done in triplo.

Rat brain preparation and immunofluorescence staining

The brain was removed and further processed as described previously (3). Brain sections (100 µm thick) were stained as described previously (3), with the following adjustments: a different blocking buffer was used (5% normal goat serum, 2% Triton X-100 and 0.2% NaN3 in PBS), all steps were done at room temperature and brain sections were incubated in secondary antibody for 2h. The following antibodies were used: (primary) rabbit polyclonal anti-laminin antibody (diluted 1:500, Cat #L9393; Sigma-Aldrich, Zwijndrecht, The Netherlands), mouse monoclonal anti-GFAP antibody (diluted 1:200, Cat #4650-0309, Bio-Rad, Oxford, UK), rabbit polyclonal anti-Iba1 antibody (diluted 1:1000, Cat #019-19741, Wako, Neuss, Germany) and (secondary) goat-anti-mouse Cy5 or goat-anti-rabbit Alexa 488; diluted 1:200) diluted in blocking buffer. The IgG staining was done by incubating brain sections with a goat anti-rat-IgG conjugated to Cy5 (diluted 1:250, Cat #A21208, ThermoFisher, Landsmeer, The Netherlands) overnight at room temperature. Specificity of the staining was checked by excluding the primary antibody.

SUPPLEMENTARY TABLES

Table S1. *Microsphere distribution.*

Microsphere diameter:	**15 µm**	**25 µm**	**50 µm**
Injected (#)	25,000	5,500	625
% of total	80.3	17.7	2.0
Scored per animal (#)	40 ± 21	9 ± 5	0 ± 1
Scored per animal (%)	79.2 ± 7.9	20.2 ± 7.8	0.6 ± 1.1

n=19 rats, *total of 937 microspheres. mean ± standard deviation.*

Table S2. *Microsphere extravasation status.*

	In (#)	**Going out (#)**	**Out (#)**	**Total scored (#)**
D1 (n=6)				
15 µm	187	7	0	194
25 µm	54	4	0	57
D3 (n=6)				
15 µm	250	17	15	282
25 µm	52	6	2	60
D7 (n=7)				
15 µm	112	39	75	226
25 µm	28	31	13	72

SUPPLEMENTARY FIGURES AND VIDEO LEGENDS

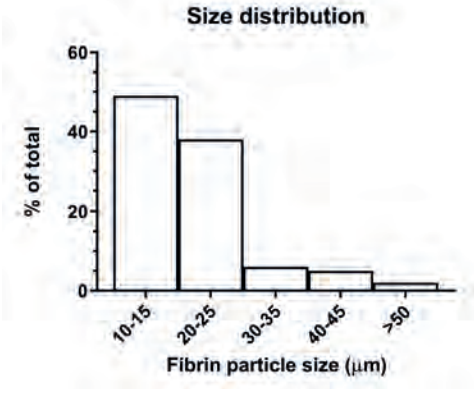

Figure S1. Size distribution of fibrin particles.

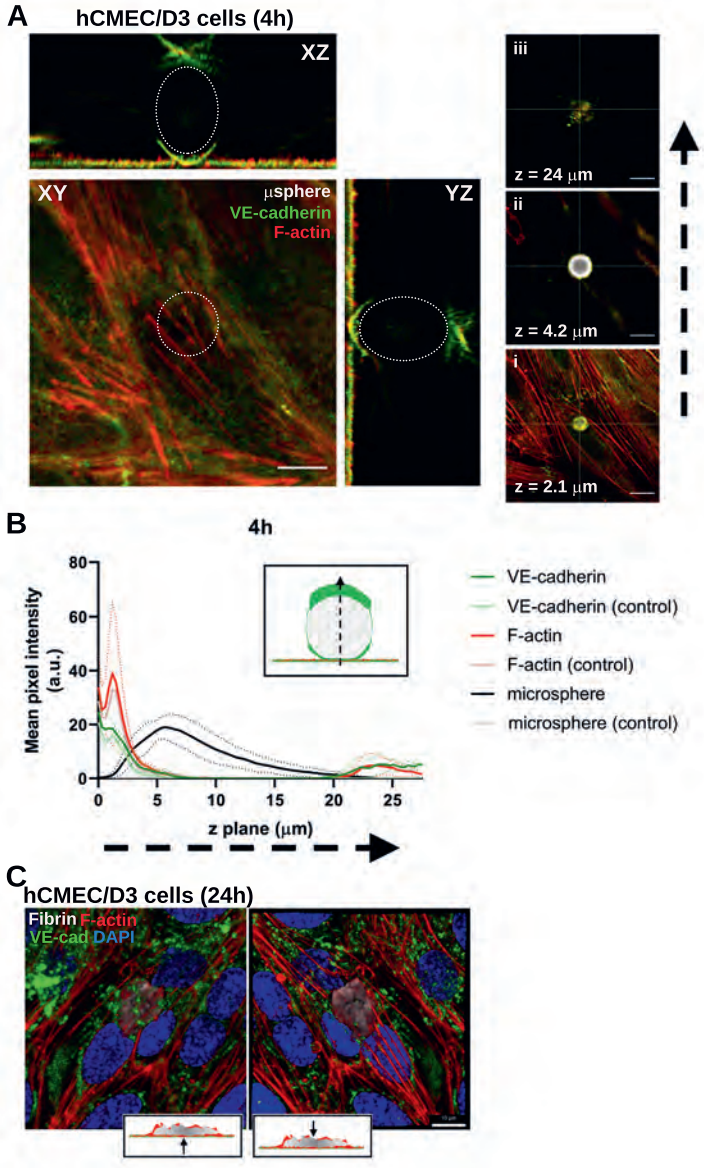

Figure S2. Microspheres are taken up by hCMEC/D3 cells. (A) *XZ and YZ orthogonal view of a z-stack shows a cup structure of phalloidin (F-actin; red) surrounding the microsphere (white; in XZ and YZ depicted with dashed line), and F-actin- and VE-cadherin-positive "caps" on top of the microsphere. Different z planes are shown in i, ii and iii. Note the F-actin and VE-cadherin (green) surrounding the microsphere in ii, and the cap on top of the microsphere in iii. Scale bar = 10 μm.* ***(B)*** *Quantification of signal intensity for F-actin, VE=cadherin and microsphere in the z direction shows a peak in signal intensity after the microsphere, which is the cap structure on top of the microsphere. Light-colored lines are signal intensity in control location, i.e. of a region where no microsphere was bound. Signal intensity was quantified from 2-4 images averaged from n = 3 independent experiments. Data are depicted as mean ± standard deviation (dashed lines).* ***(C)*** *Three-dimensional rendering of a fibrin clot, encapsulated by the cytoskeleton. Left panel is the view from below the cellular monolayer, right panel is the view from above the monolayer. Right panel shows that the fibrin clot is taken up by two cells, demonstrated by the two cell nuclei (DAPI; blue). Scale bar = 10 μm.*

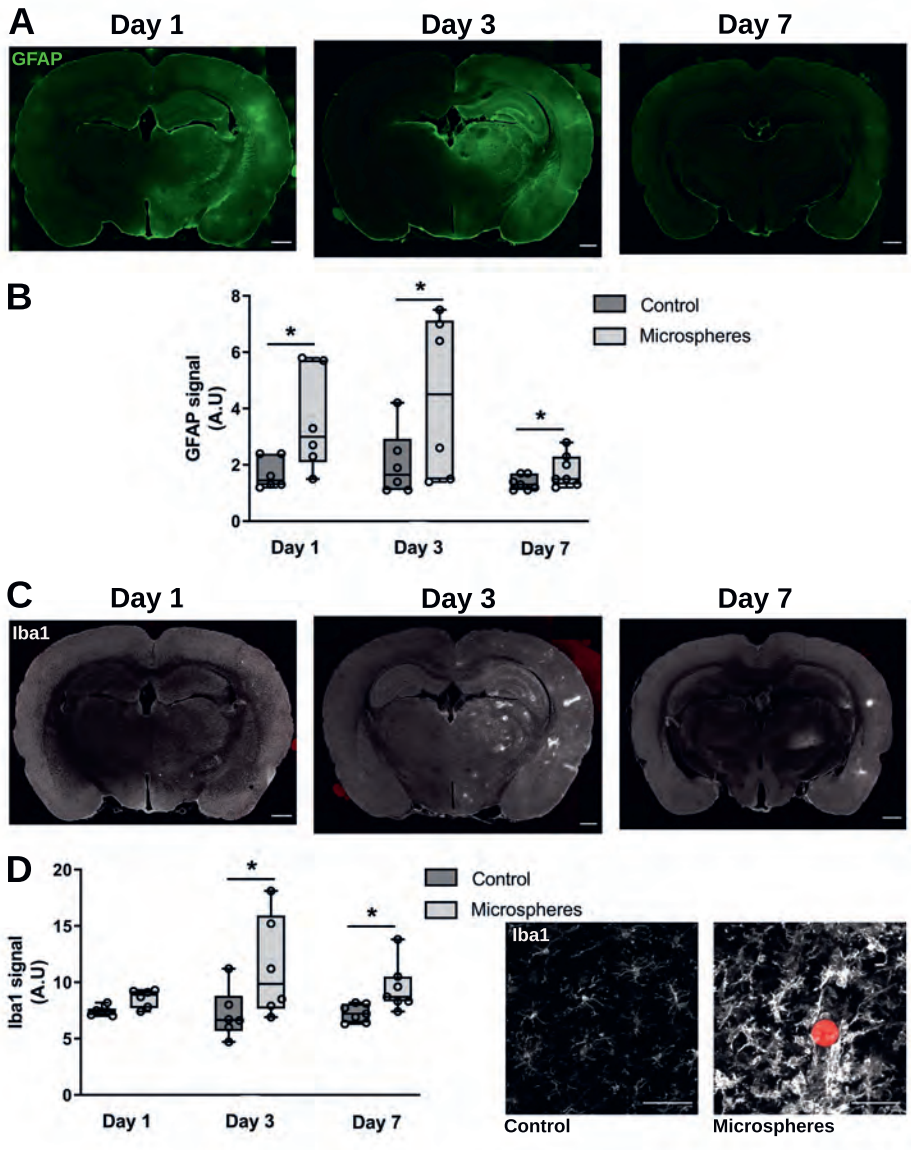

Figure S3. Microspheres induce mild reactive gliosis in vivo. (A) *GFAP staining (green) was increased in the treated hemisphere. Scale bar = 1 mm.* ***(B)*** *Quantification of GFAP signal intensity at D1, 3 and 7 in the control (dark grey) and injected (light grey) hemispheres. N=6-7 animals per time point. Data are depicted as median and IQR (min – max). *P<0.05, between hemispheres, Wilcoxon matched-pairs signed rank test.* ***(C)*** *Iba1 staining (white) was increased in the treated hemisphere. Scale bar = 1 mm.* ***(D)*** *Quantification of Iba1 signal intensity at D1, 3 and 7 in the control (dark grey) and injected (light grey) hemispheres. N=6-7 animals per time point. Data are depicted as median and IQR (min – max). *P<0.05, between hemispheres, Wilcoxon matched-pairs signed rank test. Reactive microglia (Iba1; white) were observed surrounding microspheres (red) with a changed morphology (from ramified in the control hemisphere to amoeboid surrounding microspheres). Scale bar = 50 µm.*

https://actaneurocomms.biomedcentral.com/articles/10.1186/s40478-020-01071-9#additional-information

Video S1. *Three-dimensional rendering of a microsphere (left panel) and fibrin clot (right panel) being taken up by HUVECs. Cells were stained for F-actin (red), VE-cadherin (green) and nuclei (DAPI, blue). Microsphere and fibrin clot are white. Scale bar = 20 µm.*

https://actaneurocomms.biomedcentral.com/articles/10.1186/s40478-020-01071-9#additional-information

Video S2. *Three-dimensional rendering of examples of a microsphere inside a vessel ("in"; left panel), microsphere inside a vessel but with a laminin bulge and restored perfusion ("going out" / extraluminal; middle panel) and outside the vessel lumen and extracellular matrix ("out" / parenchymal; right panel). Laminin (green) and microsphere (white). Scale bar = 50 µm.*

https://actaneurocomms.biomedcentral.com/articles/10.1186/s40478-020-01071-9#additional-information

Video S3. *Three-dimensional view of a fibrin clot (red) occluding a cerebral vessel visualized by i.v. lectin perfusion (green) prior to killing in an acute experimental setting (i.e. animal was killed within 1h after embolization surgery, n=1). Note the lack of lectin perfusion distal from the fibrin clot. Scale bar = 20 µm.*

REFERENCES

1. Lam, C. K., Yoo, T., Hiner, B., Liu, Z. & Grutzendler, J. Embolus extravasation is an alternative mechanism for cerebral microvascular recanalization. *Nature* **465**, 478-482 (2010).
2. Majolée, J. *et al.* CSN5 inhibition triggers inflammatory signaling and Rho/ROCK-dependent loss of endothelial integrity. *Sci Rep* **9**, 8131 (2019).
3. van der Wijk, A. E. *et al.* Extravasation of Microspheres in a Rat Model of Silent Brain Infarcts. *Stroke* **50**, 1590-1594 (2019).

Chapter 7

EXTRAVASATION OF BIODEGRADABLE MICROSPHERES IN THE RAT BRAIN: A PLATFORM FOR SUSTAINED DRUG DELIVERY?

Anne-Eva van der Wijk[1], Theodosia Georgakopoulou[1], Rob Steendam[2], Johan Zuidema[2], Peter L. Hordijk[3], Erik N.T.P. Bakker[1], Ed vanBavel[1]

[1] Amsterdam UMC, University of Amsterdam, Biomedical Engineering and Physics, Neuroscience Amsterdam, Amsterdam Cardiovascular Sciences, Meibergdreef 9, Amsterdam, The Netherlands

[2] InnoCore Pharmaceuticals, L.J. Zielstraweg 1, Groningen, The Netherlands

[3] Amsterdam UMC, Vrije Universiteit Amsterdam, Physiology, Amsterdam Cardiovascular Sciences, De Boelelaan 1117, Amsterdam, The Netherlands

Drug Deliv. (2023) 30(1):2194579

ABSTRACT

Drug development for neurological disease is greatly impeded by the presence of the blood-brain barrier (BBB). We and others previously reported on extravasation of micrometer-sized particles from the cerebral microcirculation – across the BBB – into the brain tissue over the course of several weeks. This mechanism could potentially be used for sustained parenchymal drug delivery after extravasation of biodegradable microspheres. Here, we set out to evaluate the extravasation potential of three classes of biodegradable microspheres with drug-carrying potential, having a median diameter of 13 µm (80% within 8-18 µm) and polyethylene glycol concentrations of 0%, 24% and 36%. Extravasation, capillary recanalization and tissue damage were determined in a rat cerebral microembolization model at day 14 after microsphere injection. Microspheres of all three classes had the potential to extravasate from the vessel into the brain parenchyma, with microspheres without polyethylene glycol extravasating the fastest. Microembolization with biodegradable microspheres led to impaired local capillary perfusion, which was substantially restored after bead extravasation. We did not observe overt tissue damage after microembolization with any microsphere: we found very limited BBB disruption (IgG extravasation), no microgliosis (Iba1 staining) and no large neuronal infarctions (NeuN staining). In conclusion, biodegradable microspheres with different polymer compositions can extravasate into the brain parenchyma while causing minimal tissue damage, demonstrating their potential to be used for sustained release drug delivery into the brain interstitium.

INTRODUCTION

One of the major challenges in the neurological field is the development of therapeutics for brain diseases. In the past decades, clinical trials for treatment of brain disorders ranging from Alzheimer disease (1) to glioblastoma (2) have led to failure, almost without exception. This failure is largely due to the presence of the blood-brain barrier (BBB), which is a major hurdle for delivery of drugs from the blood to the brain interstitium, since the BBB only allows for passage of small molecules that are both lipid-soluble and have a molecular weight of <400 Da (3). This precludes the use of ~98% of all small molecules, and all large molecule therapeutics (such as monoclonal antibodies, recombinant proteins, gene therapeutics) (3). Many attempts have been made to re-engineer drugs in order to circumvent the BBB, e.g. through nanocarriers (4), receptor-mediated transport (5) or ultrasound-induced BBB disruption (6), but with limited success. Thus, a drug delivery platform to transport therapeutics across the BBB, where they can exert their effects locally in the brain parenchyma, would be a major step forward in this field.

In previous studies we observed that flow-obstructing, polystyrene particles with diameters of 15 to 50 micrometer that were injected intra-arterially into the rat brain extravasated from the vessel into the brain tissue over the course of several weeks (7, 8). This process was previously observed in the mouse brain, lungs, heart and retina (9, 10), and in human retina (11) and was coined angiophagy (9). Extravasation of polystyrene microspheres was associated with restoration of blood flow (7-10) and, importantly, caused only mild and transient tissue damage (7, 8). Of note, these microspheres are several orders of magnitude larger than nanoparticles that are being used in drug delivery studies (12) and their extravasation does not require specific endothelial receptor binding, but rather physical entrapment of the particle in the smaller arterioles and capillaries (7). In the present study, we set out to assess whether this extravasation mechanism could potentially be exploited to deliver drugs across the BBB into the brain parenchyma, using biodegradable microspheres. Such a microsphere would need to be transported across the endothelium, followed by slow release of the drug. As a first step, we studied the transendothelial transport of several fluorescent biodegradable microspheres.

Biodegradable microspheres are widely used as long-acting injectable (LAI) depot formulations to treat chronic diseases. Typically, LAI microspheres are composed of polymers that release their bioactive cargo over a specific time frame, related to polymer swelling, increasing porosity and hydrolytic degradation. They are usually injected subcutaneously or intramuscularly. The released drugs have local or remote targets (13-15). Physicochemical properties of copolymer blocks can be varied to adjust drug elution profiles and degradation characteristics. Here, we used SynBiosys® (InnoCore Pharmaceuticals, Groningen, The Netherlands) poly(ether ester urethane) multi-block copolymers composed of various combinations of lactide, glycolide, ε-caprolactone, dioxanone and polyethylene glycol. The composition of these multi-block copolymers can be customized to meet specific needs regarding their physical characteristics, including degradation, hydrophilicity, swelling degree, drug release kinetics and erosion kinetics.

The aim of this study was to evaluate the potential of biodegradable microspheres as a drug delivery platform to target the brain in neurological disease, by determining 1) whether

fluorescent biodegradable microspheres extravasate through angiophagy from the cerebral microcirculation in rats, 2) whether there is a difference in extravasation speed between biodegradable microspheres of varying composition, and 3) how microembolization with biodegradable microspheres affects brain tissue.

METHODS

Polymer synthesis and characterization

SynBiosys® multiblock copolymers (InnoCore Pharmaceuticals, The Netherlands) were synthesized and characterized as described before (16). The polymer for microsphere M1, abbreviated as 50GL20L40, consisted of a poly(DL-lactide-co-glycolide) block with a molecular weight (MW) of 2,000 g/mole (GL20) and a poly(DL-lactide) block, MW 4,000 g/mole (L40) in a 50/50 wt.% block ratio. The polymer for M2, abbreviated as 50CP10C20-D25, consisted of a poly(ε-caprolactone)-(polyethylene glycol)-poly(ε-caprolactone) block, MW 2000 g/mole containing 50 wt.% of PEG MW 1000 g/mole (CP10C20) and a poly(p-dioxanone) block, MW 2,500 g/mole (D25) in a 50/50 wt.% block ratio. The total PEG fraction of polymer B was 24 wt.%. The polymer for M3, abbreviated as 50CP30C40-LL40, consisted of a poly(ε-caprolactone)-polyethyleneglycol-poly(ε-caprolactone) block, MW 4000 g/mole containing 75 wt.% of PEG MW 3000 g/mole (CP10C20) and a poly(L-lactide) block, MW 4,000 g/mole (LL40) in a 50/50 wt.% block ratio. The total PEG fraction of polymer C was 36.4 wt.%. The composition of the polymers as determined by 1H NMR and intrinsic viscosity are listed in Table 1.

Table 1. *Polymer composition and properties used for microspheres M1, M2 and M3.*

Polymer	50GL20L40, M1	50CP10C20-D25, M2	50CP30C40-LL40, M3
PEG MW (g/mole)	-	1000	3000
PEG wt.%	0.0	24.0	36.4
Lactide wt.%	71.6	0.0	47.2
Glycolide wt%	20.3	0.0	0.0
Caprolactone wt.%	0.0	23.3	12.1
Dioxanone wt.%	0.0	45.7	0.0
BDO wt.%	3.2	1.6	1.0
BDI wt.%	4.9	5.4	3.3
IV (dl/g)	0.76	0.73	0.78

PEG: polyethylene glycol, MW: molecular weight, wt%: weight percentage, BDO: 1,4 butanediol, BDI: 1,4-butanediisocyanate, IV: intrinsic viscosity.

Preparation of microspheres

Microspheres with narrow particle size distributions (M1, M2, M3) were prepared via membrane emulsification using an oil-in-water single emulsion solvent extraction / evaporation method. For the purpose of this study, all microspheres were loaded with 1 wt.% of the fluorescent molecule Lumogen red 305 (BASF Color & Effers GmbH) to facilitate visualization in the rat brain. Polymers were dissolved in dichloromethane

(DCM) to a concentration of 10 w/w% and Lumogen red 305 was added, where after the solution was filtered (PTFE, 0.2 µm). Subsequently, the filtered solution was pumped (5.0 mL/min) through a stainless steel membrane with a pore size of 5 µm into a continuous phase consisting of an aqueous solution containing 0.4 % polyvinyl alcohol. The obtained emulsion was collected in a 1 L beaker glass and stirred for 3 h (200 rpm, magnetic stirrer) to evaporate DCM. The hardened microspheres were subsequently washed with Millipore water, collected by filtration (5 µm filter) and dried via lyophilization. Dried microspheres were stored at -20°C and analyzed for particle size.

The microspheres were suspended in an aqueous 0.6 % sodium carboxymethyl cellulose solution at a concentration of 0.283 mg/mL, representing approximately 200,000 particles per mL, as based on their weight, volume averaged particle size and polymer density. Microsphere suspensions were stored and shipped refrigerated at ~5°C.

Characterization of microspheres

The surface morphology of the microspheres was examined by scanning electron microscopy (SEM) using a Jeol JCM-5000 Neoscope (Jeol, Tokio, Japan). Samples of microspheres were adhered to a sample holder using double-sided adhesive carbon conductive tape and sputter coated with a thin layer of gold. Samples were then imaged using a 10 kV electron beam. In addition, confocal images of suspended microspheres were made.

Average size and particle size distribution (PSD) of the microspheres was measured by laser diffraction using a Horiba LA-960 Laser Diffraction Particle Analyzer (Horiba, Japan). In brief, a suspension of the microspheres in demineralized water was added to a 15 mL measuring cell combined with a stirring magnet to disperse the particles. Microsphere concentration was adjusted to have a transmittance within 70 to 90%. Two light sources were used in the system, one laser with a wavelength of 650nm and one LED with a wavelength of 405nm. Together with multiple detectors, the scattering pattern of the particles in solution was determined. Using the Fraunhofer theory, the PSD was calculated within a range of 10 nm- 5000 µm. A single fold measurement of 20 seconds was recorded. The coefficient of variation (C.V.) of the particle size distribution was calculated according to Eq. 1:

$$C.V. = \frac{Std.Dev.}{D_v(50)} \qquad \text{Equation 1}$$

Where $D_v(50)$ is the volume-based mean diameter, and Std.Dev. the standard deviation of this diameter. The span of the particle size distribution was calculated using Eq. 2:

$$Span = \frac{D_v(90) - D_v(10)}{D_v(50)} \qquad \text{Equation 2}$$

where $D_v(10)$, $D_v(50)$ and $D_v(90)$ represent volume-based particle sizes for 10%, 50% and 90% undersize, respectively.

Ethics statement

The experiments in this study were conducted in female and male Wistar rats (21 to 23 weeks old, Charles River). Rats were housed in pairs under a 12h light-dark cycle and fed *ad libitum* with standard laboratory chow and free access to water. All experiments were

conducted in accordance with the ARRIVE guidelines and European Union guidelines for the care of laboratory animals (Directive 2010/63/EU). The surgical protocols in this study were performed with approval of the local committee on the Ethics of Animal Experiments of the University of Amsterdam, Academic Medical Center (permit number: 18-5484-1-02). All surgical procedures were conducted under isoflurane inhalation anesthesia mixed with oxygen while the body temperature was monitored with a feedback-regulated heating pad.

Cerebral embolization procedure

Cerebral embolization was done as described in van der Wijk et al. (2020) (7) under isoflurane inhalation anesthesia (induction 4%, maintenance 2-2.5% in 1 L/min O_2) and subcutaneous buprenorphine (0.05 mg/kg) for analgesia. In short, the left common carotid (CCA), the internal carotid (ICA) and external carotid (ECA) artery were exposed and the ECA and occipital artery were temporarily ligated. M1, M2 or M3 Lumogen Red-loaded fluorescent microspheres with a median diameter of 12.7-12.9 µm (see Table 2) were then injected using a 29G insulin needle. Considering their size, these microspheres are expected to lodge in small arterioles and capillaries (17). Based on previous studies (7, 8) and pilot experiments (data not shown) we injected around 40,000 microspheres in a total volume of 200 µl physiological buffer into the common carotid artery of rats to ensure sufficient microsphere infusion and initiation of extravasation, while causing minimal tissue damage. Intra-carotid microsphere injection leads to a stochastic distribution of microspheres throughout the intervention hemisphere, whereas the control hemisphere is not affected, barring an occasional contralateral microsphere close to the midline (18). The right CCA was not injected, and therefore the right hemisphere served as the untreated control. One animal was excluded from all analyses because microsphere injection failed due to extensive bleeding after the intra-arterial injection.

Table 2. *Microsphere characteristics.*

Microsphere group	**M1**	**M2**	**M3**
Polymer grade	50GL20L40	50CP10C20-D25	50CP30C40-LL40
Lumogen red 305 content (wt.%)	1.0	1.0	1.0
Particle concentration	40,000 / 200 µl	40,000 / 200 µl	40,000 / 200 µl
$D_v(10)$* (µm)	7.8	8.2	7.6
$D_v(50)$* (µm)	12.7	12.9	12.7
$D_v(90)$* (µm)	18.6	18.2	18.8
span	0.85	0.77	0.88
CV (%)	32.7%	29.6%	33.7%

**$D_v(10)$, $D_v(50)$ and $D_v(90)$ represent volume-based particle sizes for 10%, 50% and 90% undersize, respectively.*

Tissue preparation and immunofluorescence staining

Animals were killed on day (D) 14 (n=6-8 per group) after surgery. After induction of

anesthesia, the vasculature was labeled by an intravenous injection of DyLight 488 labeled tomato lectin (1 mg/kg; DyLight 488 labeled lycopersicon Esculentum tomato, Vector Laboratories, Burlingame, CA), which was allowed to circulate for 5 min. Rats were given 100 µl heparin i.p. and after increasing isoflurane to 5% animals were transcardially perfused with heparinized PBS followed by tissue fixation with 4% paraformaldehyde at 80 mmHg. Tissue preparation and immunofluorescence staining was done as described previously (7), with the following adjustments: blocking buffer contained 5% normal goat serum and 0.1% Triton X-100 in PBS. The following antibodies were used: (primary) rabbit polyclonal anti-laminin antibody (diluted 1:500, Cat #L9393; Sigma-Aldrich, Zwijndrecht, The Netherlands), rabbit polyclonal anti-Iba 1 antibody (diluted 1:1000, Cat #019-19741, Wako, Neuss, Germany), mouse anti-NeuN antibody (NEUronal Nuclei, clone A60; diluted 1:200, Cat #MAB377, Millipore BV, Amsterdam, The Netherlands), and (secondary) goat-anti-mouse Cy5 (diluted 1:500) or goat-anti-rabbit Cy5; diluted 1:200) diluted in blocking buffer. The IgG staining was done by incubating brain sections with a goat anti-rat-IgG conjugated to Cy5 (diluted 1:250, Cat #A21208, ThermoFisher, Landsmeer, The Netherlands) overnight at room temperature. Specificity of the staining was checked by excluding the primary antibody. Images of 100 µm thick brain sections were captured using a confocal laser scanning microscope SP8-X DLS Lightsheet (Leica Microsystems) with a 10x 0.5 NA (air) objective for Iba1, NeuN and IgG, or SP8-X (Leica Microsystems) with a 20x 0.75 NA (oil) objective for laminin.

Image analysis

Quantification of microsphere extravasation was performed on sections stained for laminin. Microsphere extravasation was scored as “in”, “going out” or “out” for at least 30 microspheres per rat (Suplementary Information Table S1), based on their position in laminin and lectin images (7). From these data an extravasation score was calculated for each animal, where microspheres scored as “in” were assigned 0, “going out” 1 and “out” 2; i.e. a higher extravasation score indicates a higher rate of microsphere extravasation. Vessel perfusion was quantified in the same samples, and a vessel was identified as “nonperfused” when there was no lectin distal and/or proximal from the occluding microsphere. One animal was excluded from these analyses because the i.v. lectin injection had failed, and thus we were not able to assess extravasation status and vessel perfusion.

IgG leakage and Iba1 signal intensity was quantified by determining mean pixel intensity in single plane overview images, while excluding ventricles using threshold analysis in FIJI (version ImageJ 1.53c).

All analyses on animal brain sections were quantified in a blinded fashion. Total n of animals per group are indicated in the figure legends.

Statistics

Data are depicted as median ± interquartile range (IQR; whiskers represent min – max). Data was tested for normality using a QQ-plot and a Shapiro-Wilk test and depending on the outcome, a parametric or nonparametric test was performed. Differences between groups

(M1, M2 and M3) were determined using Kruskal-Wallis with Dunn's test for multiple comparisons, or by analysis of variance (ANOVA) followed by Tukey Kramer's test for multiple comparisons. Association of the categorical variables "Vessel perfusion" (yes/no) and "Extravasation status" (in/going out/out) was tested with a Chi-square test for trend. Differences between intervention and contralateral hemispheres were determined using a Wilcoxon signed rank or paired t test. Sex differences were evaluated stratified by M1, M2 and M3 with an ordinary 2-way ANOVA with the factors "Sex" and "Microsphere", and pooled for M1, M2 and M3 per sex with an unpaired t-test. Differences were considered statistically significant when $P \leq 0.05$. Statistical analyses and graphing were performed using GraphPad Prism 9.1.0 software (GraphPad Software, La Jolla, CA).

RESULTS

In vitro microspheres size distribution and characteristics

Scanning electron microscopy (Supplementary Information Fig. S1A) showed that all microspheres were spherical and had a smooth (M1, M2) or somewhat rawer (M3) non-porous surface morphology. Figure S1B (Supplementary Information) shows the particle size distributions of the three microsphere groups as illustrated by laser diffraction. The volume average particle sizes, $D_v(50)$, of the three groups were almost identical (12.7 - 12.9 µm) (Table 2) as were the values for the coefficient of variance (C.V. 29.6 – 33.7%) and span (0.77 – 0.88).

Biodegradable microspheres extravasate from the cerebral microcirculation

We previously found that polystyrene microspheres of 15 or 25 µm in diameter are cleared from microvessels over the course of several weeks (7, 8). We hypothesized that such angiophagy can take place independent of receptor binding, and therefore embolic material of any source may be taken up and extruded by the microvessels. In line with this hypothesis, we observed that biodegradable microspheres from all three groups extravasated from the vessel into the brain at D14 post-injection (Fig. 1A, B). Figure 1A shows examples of three stages of microsphere extravasation. Extravasation status was assessed based on i.v. lectin injection before killing the animal to visualize the lumen of still perfused vessels, and post-mortem staining for the extracellular matrix protein laminin, which clearly outlines the vessel wall (7). At D14, the majority of microspheres was still located inside the vessels ("in" or intraluminal), yet there was also a significant portion of microspheres either in the process of extravasation ("going out" or extraluminal) or already extravasated ("out" or parenchymal; Fig. 1B, Supplementary Information Table S2). The extravasation score of the group that received M1 microspheres (0.59, IQR 0.50-0.64) was significantly higher compared to the group that received M2 (0.26, IQR 0.24-0.28; P=0.034 M1 vs. M2) or M3 microspheres (0.23, IQR 0.22-0.35; P=0.0090 M1 vs. M3), indicating that the M1 microspheres had the highest extravasation capacity at D14 (Fig. 1C).

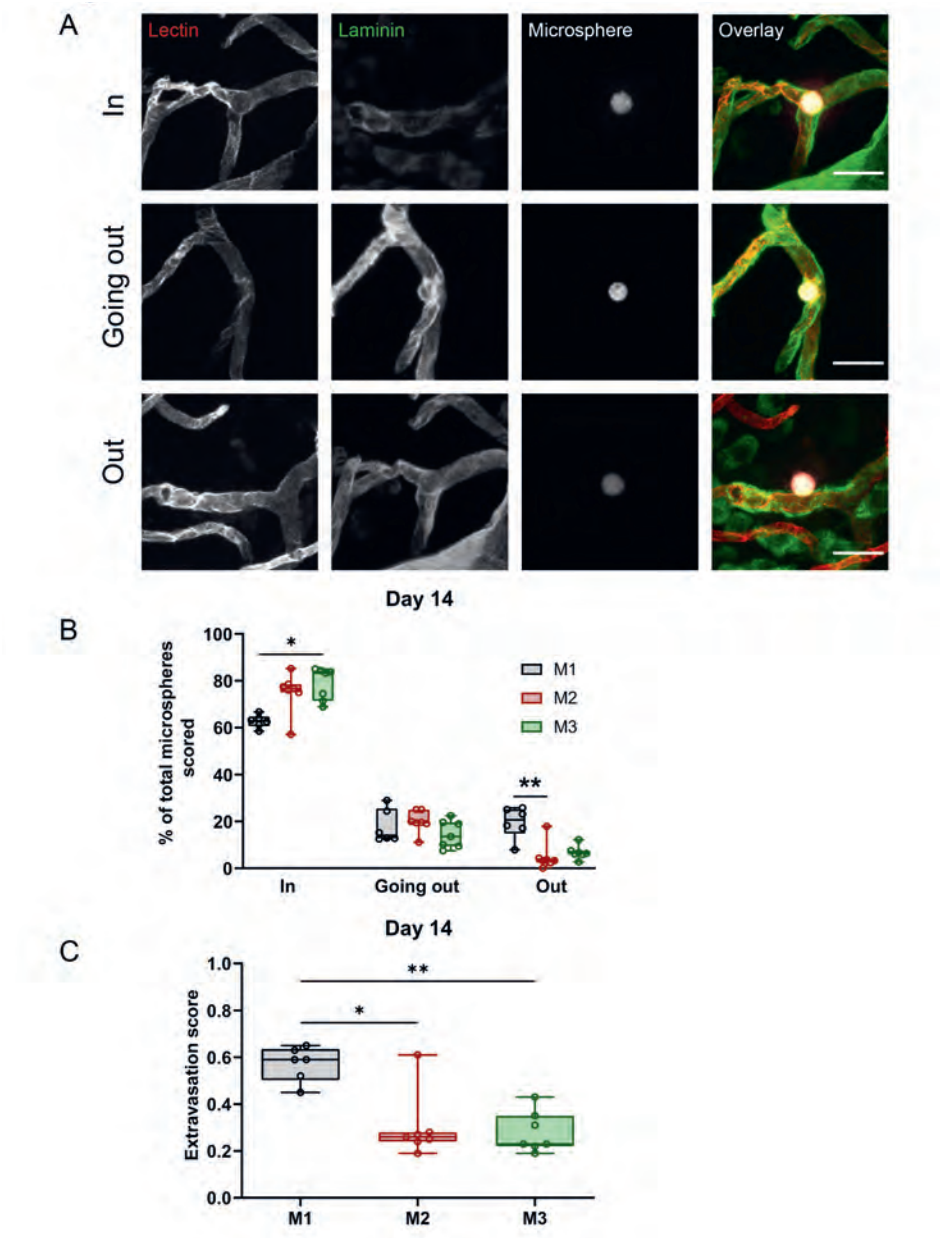

Figure 1. Extravasation of biodegradable microspheres at D14. (A) *Examples of biodegradable microspheres (white in overlay) scored as "in", "going out" and "out" in coronal brain sections stained by i.v. injected lectin (red) before killing, and postmortem for laminin (green). Scale bar = 25 µm.* ***(B)*** *Quantification of microsphere extravasation of M1 (black), M2 (red), and M3 (green) microspheres at D14.* ***(C)*** *An extravasation score between 0 and 2 was calculated per rat ("in" was weighed as 0, "going out" as 1 and "out" as 2).* ***(B)*** *and* ***(C)*** *M1: n=6, M2: n=7, M3: n=7 animals (one M2 animal was excluded from the extravasation analysis because the i.v. lectin injection failed). Data are depicted as median ± IQR (box) and min – max (whiskers), each data point represents an individual animal. *P<0.05, **P<0.01, Kruskal-Wallis with Dunn's multiple comparison test.*

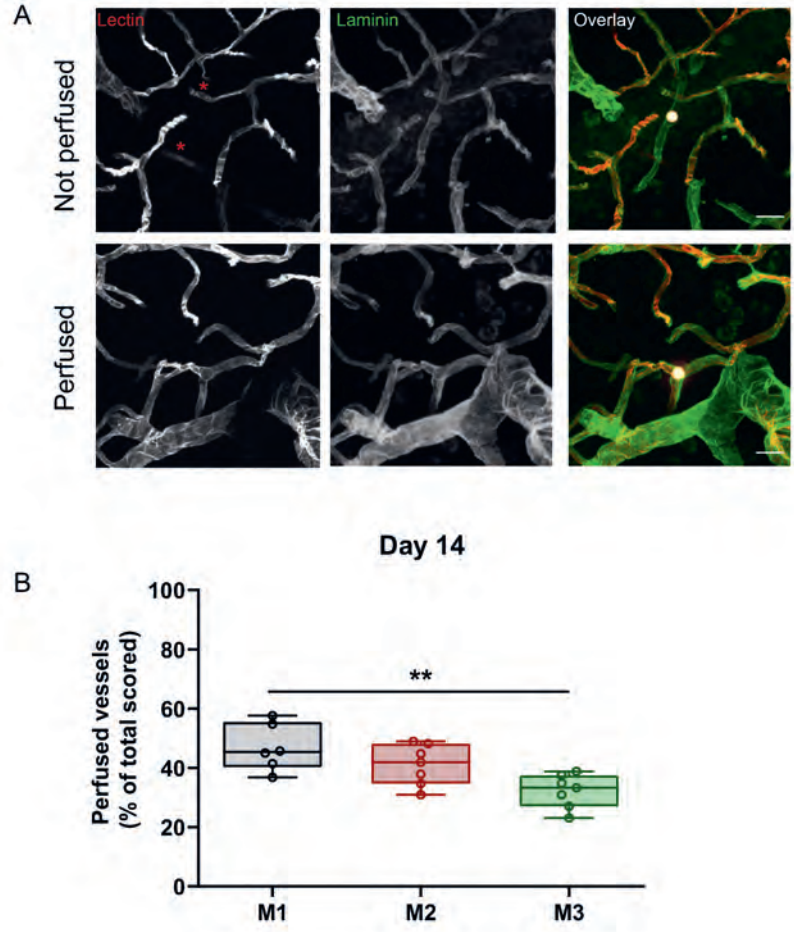

Figure 2. Perfused vessels after microembolization with biodegradable microspheres at D14. (A) *Examples of vessels obstructed with biodegradable microspheres. Top panel shows a nonperfused vessel, indicated by lack of i.v. lectin perfusion (red; indicated by asterisks) proximally and distally of the microsphere (white), while the vessel wall is clearly outlined by laminin (green). Bottom panel shows a perfused vessel, despite the presence of a microsphere. Scale bar = 25 µm.* **(B)** *Quantification of vessel perfusion after microembolization with M1 (black), M2 (red), and M3 (green) microspheres at D14. M1: n=6, M2: n=7, M3: n=7 animals (one M2 animal was excluded from the perfusion analysis because the i.v. lectin injection failed). Data are depicted as median ± IQR (box) and min – max (whiskers), each data point represents an individual animal. **P<0.01, ANOVA with Tukey's multiple comparison test.*

Vessel perfusion is associated with extravasation status

Microembolization of the brain inevitably leads to perfusion deficits of the obstructed microvessels. We used i.v. injected lectin as a proxy for tissue perfusion in the rat brain, and observed that the majority of obstructed vessels lacked lectin staining either proximally, distally or on both sides of the blocking microsphere (Fig. 2A). In some cases however, there was lectin perfusion despite the presence of an obstruction (Fig. 2A). Vessel perfusion was often restored when microspheres were extraluminal or parenchymal. Fig. 2B shows the quantification of vessel perfusion of all the scored microsphere-containing vessels, i.e.

irrespective of extravasation status. The M1 group had the most perfused vessels (45.4%, IQR 40.3-55.5%), compared to M2 (41.9%, IQR 34.7-48.2%; P=0.2951, n.s., M1 vs. M2) and M3 (33.3%, IQR 27.0-37.5%; P=0.0032, M1 vs. M3; P=0.0644, n.s., M2 vs. M3). We categorized the scored microspheres according to extravasation (in/going out/out) and perfusion status (yes/no), and found that the two parameters were strongly associated variables for all three microsphere groups (Supplementary Information Table S2). This indicates that extravasation of microspheres leads to restoration of vessel perfusion.

Biodegradable microspheres induce very limited BBB disruption

The BBB tightly regulates the entry of molecules from blood into the brain parenchyma, and is generally impermeable to plasma proteins. Whereas it is a major hurdle for drug delivery, the BBB is crucial to maintain tissue homeostasis in physiological conditions (19). To assess whether microembolization with biodegradable microspheres affects BBB function, we stained the rat brain for endogenous IgG after flushing all the blood from the vessels during perfusion-fixation (Fig. 3A). This revealed a small but significant increase in IgG staining in the embolized hemisphere as compared to the control hemisphere for groups that received M1 and M2 microspheres (Fig. 3B).

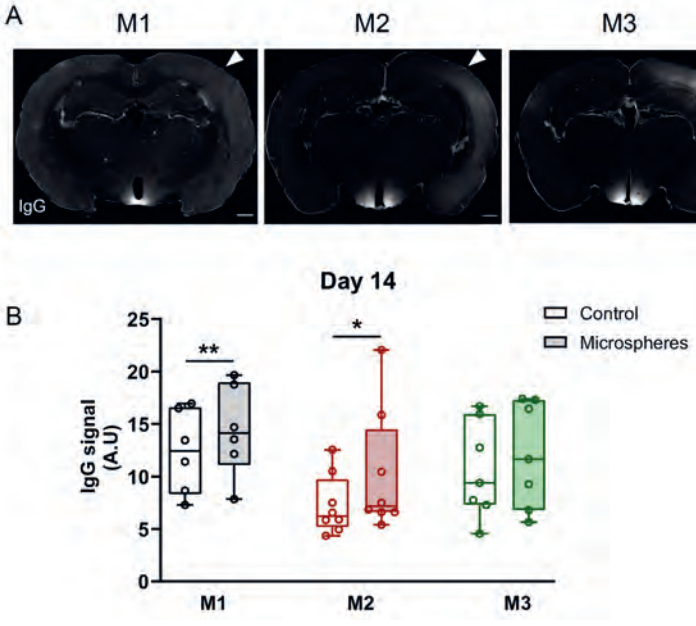

Figure 3. Biodegradable microspheres induce very limited BBB opening at D14. (A) *Representative overview images of endogenous IgG staining (white) in coronal sections of a rat brain injected with M1 (black), M2 (red), and M3 (green) microspheres at D14. The IgG signal was very low in both hemispheres (arrowhead indicates intervention side; brightness was increased equally in all images to aid visualization). Scale bar = 1 mm.* ***(B)*** *Quantification of IgG signal intensity in the control (open boxes) and intervention (filled boxes) hemispheres after microembolization with M1 (black), M2 (red) and M3 (green) microspheres at D14. M1: n=6, M2: n=8, M3: n=7 animals. Data are depicted as median ± IQR (box) and min – max (whiskers), each data point represents an individual animal. **P<0.01, paired t-test, *P<0.05, Wilcoxon signed rank.*

Biodegradable microspheres do not induce overt tissue damage

We previously demonstrated that brain embolization with small polystyrene microspheres (15 µm) caused only mild and transient tissue damage (8), but that a combination of 15 µm microspheres with larger microspheres (25 and 50 µm) induced hypoxia and neuronal infarction within 24h (18). To determine whether microembolization with biodegradable microspheres ± 13 µm in size can be done without causing brain infarctions, we stained the rat brains for NeuN, a neuronal marker (Fig. 4A). No large neuronal infarctions were observed in any of the animals after microembolization in all three groups. Most animals did have some micro-infarcts – most often found in the cortex – presenting as a small region where NeuN signal was absent, in most cases accompanied by a nonperfused region, yet not always in close vicinity to a microsphere (Fig. 4B).

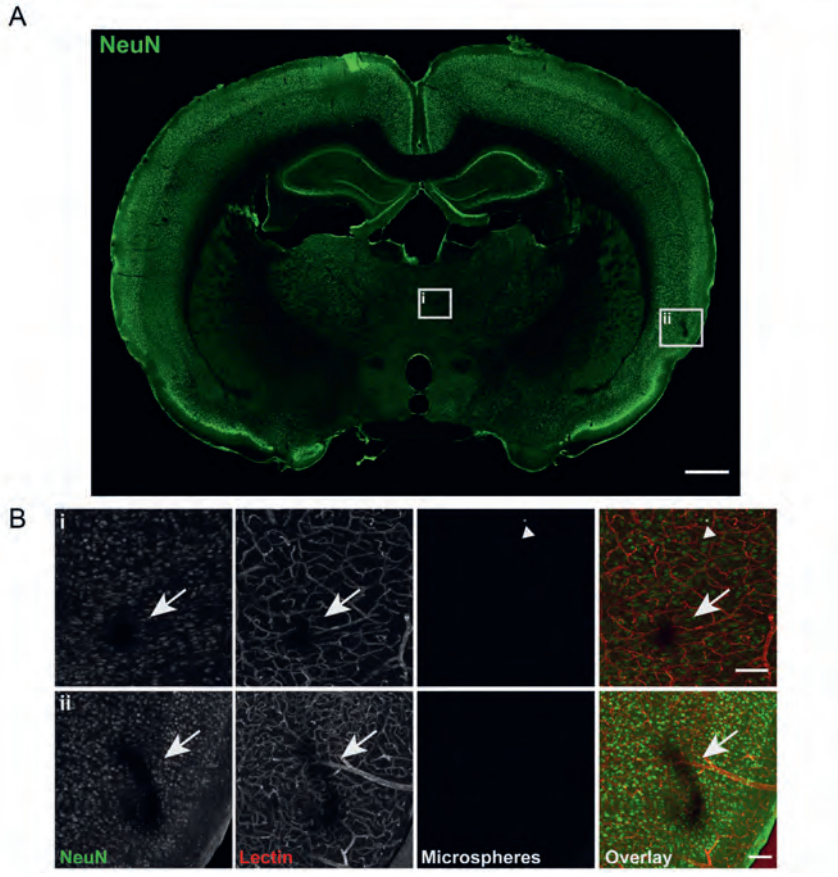

Figure 4. Biodegradable microspheres do not induce overt neuronal damage. (A) *Overview image of a coronal brain section stained for the neuronal marker NeuN (green). Two insets show minor infarcted areas in the intervention side, enlarged in (B). This image is from an animal injected with M3 microspheres. Scale bar = 1 mm.* ***(B)*** *Enlarged images of the minor infarcts from (A). i: Infarcted region in the striatum, accompanied by local nonperfusion (red; lack of lectin perfusion), with a microsphere in the vicinity (white; arrow head). ii: Infarcted region in the cortex, accompanied by local nonperfusion, but no microsphere in the near vicinity (in this brain section). This is an example of one of the larger infarcts found, yet it is still relatively small. Scale bar is 100 µm for both images. Arrow: infarcted region, arrowhead: microsphere.*

In addition to the limited neuronal damage, we did not observe microgliosis in these animals (Fig. 5A), as shown by staining for the microglial marker Iba1. Microglia had a quiescent morphology (Fig. 5A, enlarged images in lower panel) and Iba1 signal was similar in the intervention hemisphere and the control hemisphere in all three groups (Fig. 5B). Taken together, these data suggest that microembolization with biodegradable microspheres does not cause major tissue damage in the rat brain.

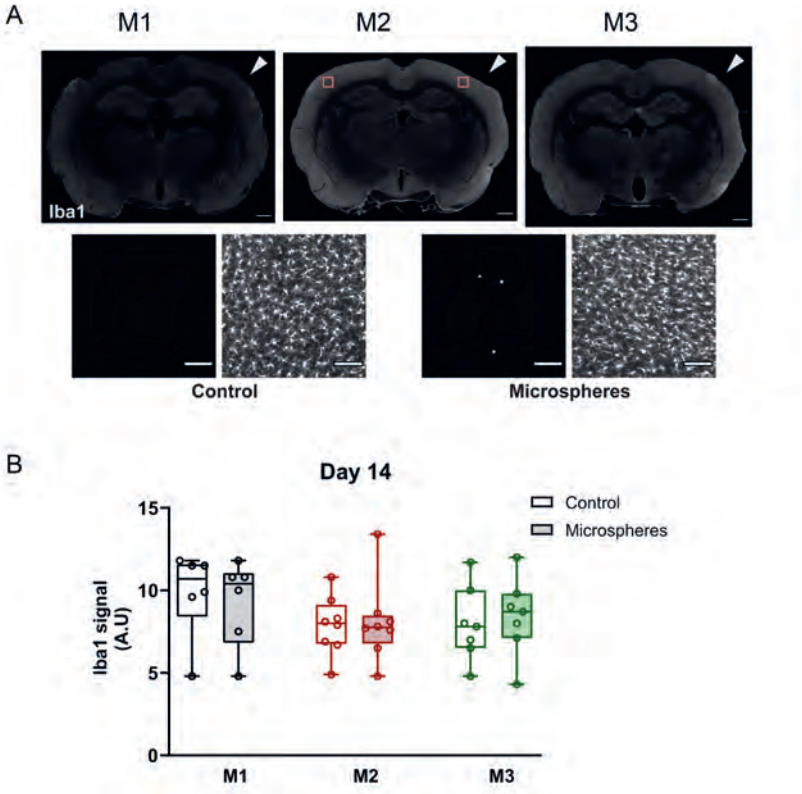

Figure 5. Biodegradable microspheres do not induce microgliosis at D14. (A) *Representative overview images of Iba1 staining (marker of microglia; white) in coronal sections of a rat brain injected with M1 (black), M2 (red), and M3 (green) microspheres at D14. Iba1 staining was similar in both hemispheres (arrowhead indicates intervention side; brightness was increased equally in all images to aid visualization). Scale bar = 1 mm. Lower panel images are an enlargement of the boxed regions of the M2 coronal section and show microglia with a quiescent (ramified) morphology in the cortex of the control and intervention hemisphere, also in the near vicinity of microspheres (white). Scale bar = 100 µm.* ***(B)*** *Quantification of the Iba1 signal intensity in the control (open boxes) and intervention (filled boxes) hemispheres after microembolization with M1 (black), M2 (red) and M3 (green) microspheres at D14. M1: n=6, M2: n=8, M3: n=7 animals. Data are depicted as median ± IQR (box) and min – max (whiskers), each data point represents an individual animal.*

Sex has no effect on outcome after brain microembolization

We used two-way ANOVA with “Sex” and “Microsphere” as independent variables to evaluate whether sex affects the outcome of extravasation score, vessel perfusion, IgG and Iba1 signal intensity in the intervention hemisphere for animals stratified as groups that received M1, M2 or M3 microspheres. For both extravasation score (Supplementary

Information Fig. S2A) and vessel perfusion (Supplementary Information Fig. S2B), there was no effect of sex, nor was there an interaction between sex and microsphere determining these parameters. For IgG (Supplementary Information Fig. S3A) and Iba1 signal intensity (Supplementary Information Fig. S3B) in the intervention hemisphere, there was no main effect of microspheres and sex, nor was there an interaction effect. Since the groups are rather small when stratified by microsphere class, we also pooled the microsphere classes to assess whether there is a difference between male and female rats – this was not the case for either of the outcome variables (Supplementary Information Fig. S2C-D and Fig. S3C-D). Together, these data suggest that sex does not affect extravasation, vessel perfusion or effects on the brain tissue after microembolization with biodegradable microspheres.

DISCUSSION

Currently, there are very few options available to locally treat neurodegenerative diseases such as Alzheimer's disease, but also mental disorders, brain tumors or to apply adjunctive therapy in acute ischemic stroke patients. Progress to treat neurological disease is hampered by the BBB, which blocks entry of almost all therapeutics after systemic delivery (3). This blockage is illustrated by aducanumab (20), a human monoclonal antibody that is administered through i.v. infusions and that selectively reacts with amyloid-β (Aβ) aggregates. In patients, aducanumab reduced Aβ plaques. However, the brain:plasma concentration ratio, although higher than previously reported for other systemically delivered Aβ antibodies (<0.1% brain penetration, (21)) was still only 1.3% (22), meaning that very high systemic doses are needed to attain any clinical effect. Thus, there is still much room for improvement in drug delivery.

In the present study, we demonstrate that the process of angiophagy may have potential to be exploited for drug delivery into the brain through long-acting drug-loaded biodegradable microspheres. To this end, microspheres need to be administered intra-arterially, which is invasive. Moreover, microembolization of the brain is potentially harmful and may lead to tissue damage. Clearly, these safety concerns should be evaluated. In the rat brain, we observed minimal tissue damage after embolization with biodegradable microspheres of all three classes. There was virtually no sign of IgG leakage in the embolized hemisphere, which indicates that the BBB was largely intact at D14 after embolization, although we cannot exclude transient opening at earlier time points (7). We performed pilot experiments with polystyrene microspheres to assess the optimal number of microspheres injected for particle extravasation, while limiting adverse effects to the brain. We found some small neuronal micro-infarctions, mostly localized to the cortical layers (data not shown). It has been reported in rats that cortical micro-infarcts consequential to single vessel occlusions of penetrating arterioles may result in cognitive dysfunction (23), however the median diameter of most micro-infarcts found in the present study was about six times smaller compared to that study (data not shown). There were also no signs of microgliosis in the intervention side of animals, suggesting absence of ongoing inflammation. Taken together, microembolization of the rat brain with biodegradable microspheres sized ~13 μm appears

to be feasible without overt tissue damage. Future studies should include *in vivo* imaging (e.g. MRI) and cognitive tests to further evaluate tolerability and safety of the procedure.

Intra-arterial application of drug-loaded microspheres is not unprecedented: trans-arterial chemoembolization with microspheres is the gold standard to treat intermediate stage hepatocellular carcinoma (24). This method is well suited for local delivery of chemotherapeutic drugs at the site of the tumor, while at the same time depriving the tumor's blood supply through arterial obstruction. This method is accomplished by microspheres that are much larger (~100-300 µm), which elute their content into the vessel lumen at the site of the occluded vessel, from where it diffuses into the liver parenchyma (25). While this method is different from the current strategy of relying on microsphere extravasation, it illustrates a clear case where the disadvantage of intra-arterial administration is acceptable considering the severity of the disease and treatment outcome. It clearly remains to be established for which specific neurological diseases the current strategy could be realistic.

We found that microembolization with biodegradable microspheres led to vessel obstruction and consequent nonperfusion in a large percentage of obstructed vessels. Vessel perfusion was strongly associated with angiophagy, and given more time, restoration of blood flow may take place when a larger portion of microspheres have extravasated into the brain parenchyma (8). Based on previous studies (7-10), we had expected that the majority of injected biodegradable microspheres would have been cleared from the vessels at D14 post-surgery. This was however not the case, as in the present study only ~20-35% of microspheres (M1, M2 or M3) was in the process of extravasation, or had extravasated at D14. In contrast, about 50-80% of polystyrene microspheres had cleared from the microvessels at D7 (7, 8), and virtually all had undergone angiophagy at D28 after microembolization (8). These data suggest that microsphere (polymer) composition may have an effect on extravasation capacity, in line with the fact that we also observed differences between M1, M2 and M3 microspheres.

We prepared microspheres of multiblock copolymers containing different weight fractions and molecular weight of polyethylene glycol. By incorporating increasing amounts of hydrophilic polyethylene glycol (PEG) and PEG segments of increasing molecular weight, the swelling degree and water absorption capacity of multiblock copolymers increases (26); M1 microspheres composed of lactide / glycolide based multiblock copolymer without any PEG hardly swell under aqueous conditions and are therefore most suited for delivery of small molecules and peptides (27), whereas M2 (24 wt.% PEG1000) and M3 (36.4 wt.% PEG3000) microspheres, due to the higher swelling degree of these polymers, are suited for delivery of larger molecules, such as proteins (28, 29). Although all tested microspheres had the potential to be transported over the BBB, we found that M1 microspheres showed the largest extravasation capacity and highest reperfusion rate at D14. It remains to be established which properties determine the rate of extravasation. The rapidly extravasating polystyrene microspheres in our previous studies are very hydrophobic. Possibly, the water uptake by M2 and M3 microspheres impairs their extravasation due to the increased hydrophilicity, but this needs further study.

It is becoming increasingly recognized that sex differences in pathogenesis, progression

and symptoms of disease are strongly understudied in the neuroscience field (or almost any biomedical field for that matter) (30, 31). Yet, we did not find significant effects of sex on extravasation, vessel perfusion or effects on the brain tissue after microembolization with biodegradable microspheres, justifying the pooling of data from male and female rats.

Limitations of the study

In the present study, we took the first steps in determining potential safety hazards of microembolization in the brain. A more extensive safety profile should be made in future studies, e.g. to assess whether the micro-infarcts that we observed in the present study are benign or, despite their minute size, affect cognition and behavior in these animals.We found that a large percentage of biodegradable microspheres was still confined within the microvasculature at D14. Transport of biodegradable microspheres across the BBB and cargo unloading in the brain parenchyma is needed in order to exert truly local effects of therapeutics in the brain. Longitudinal data on microsphere extravasation of all classes would be needed to further develop biodegradable microspheres as a drug delivery platform, e.g. to determine optimal timing of drug release and polymer resorption, and hence copolymer block composition.

We did not study the cellular mechanisms of microsphere extravasation. Our previous work on polystyrene spheres has revealed involvement of endothelial actin cytoskeleton remodeling (7, 8). A better understanding of these mechanisms could help optimizing extravasation by adjusting polymer composition or even by simultaneously targeting endothelial actin dynamics. While we demonstrated extravasation of the microspheres, we did not address release and transport of their cargo in the parenchyma, let alone the biological effectiveness of released compounds.

Conclusion

In conclusion, we show here that biodegradable microspheres composed of different multiblock copolymers have the potential to extravasate from the cerebral microcirculation into the brain parenchyma. The use of sufficiently small microspheres limited tissue damage due to microembolization, thereby enabling a possible therapeutic window for sustained drug release over time in the brain tissue without side effects due to local anoxia. The observed differences in extravasation capacity between the three microsphere compositions warrant further optimization towards the use of such microspheres as a drug delivery platform for the sustained release of small molecules, proteins and antibodies to the brain in future studies.

AUTHOR'S CONTRIBUTIONS

AEvdW, ENTPB, PLH and EvB conceived and designed the experiments; AEvdW and TG performed the surgeries; AEvdW acquired the experimental data, analyzed the data. AE and EvB wrote the manuscript, RS and JZ were involved in the design and manufacturing of the biodegradable microspheres; all authors contributed to editing of the manuscript. All authors read and approved the final version of the manuscript.

CONFLICT OF INTEREST

RS and JZ are employed by InnoCore Pharmaceuticals, Groningen, The Netherlands. The SynBiosys® multi-block copolymer platform is patent protected and owned by InnoCore Pharmaceuticals.

REFERENCES

1. Cummings, J. PMC5866992; Lessons Learned from Alzheimer Disease: Clinical Trials with Negative Outcomes. *Clin Transl Sci* **11**, 147-152 (2018).
2. Jacus, M. O. *et al.* PMC4761278; Pharmacokinetic Properties of Anticancer Agents for the Treatment of Central Nervous System Tumors: Update of the Literature. *Clin. Pharmacokinet.* **55**, 297-311 (2016).
3. Pardridge, W. M. PMC539316; The blood-brain barrier: bottleneck in brain drug development. *NeuroRx* **2**, 3-14 (2005).
4. Beduneau, A., Saulnier, P. & Benoit, J. P. Active targeting of brain tumors using nanocarriers. *Biomaterials* **28**, 4947-4967 (2007).
5. Giugliani, R. *et al.* PMC6034233; Neurocognitive and somatic stabilization in pediatric patients with severe Mucopolysaccharidosis Type I after 52 weeks of intravenous brain-penetrating insulin receptor antibody-iduronidase fusion protein (valanafusp alpha): an open label phase 1-2 trial. *Orphanet J Rare Dis* **13**, 110 (2018).
6. Carpentier, A. *et al.* Clinical trial of blood-brain barrier disruption by pulsed ultrasound. *Sci Transl Med* **8**, 343re2 (2016).
7. van der Wijk, A. E. *et al.* PMC7671188; Microembolus clearance through angiophagy is an auxiliary mechanism preserving tissue perfusion in the rat brain. *Acta Neuropathol Commun* **8**, 195 (2020).
8. van der Wijk, A. E. *et al.* Extravasation of Microspheres in a Rat Model of Silent Brain Infarcts. *Stroke* **50**, 1590-1594 (2019).
9. Grutzendler, J. *et al.* Angiophagy prevents early embolus washout but recanalizes microvessels through embolus extravasation. *Sci Transl Med* **6**, 226ra31 (2014).
10. Lam, C. K., Yoo, T., Hiner, B., Liu, Z. & Grutzendler, J. PMC2879083; Embolus extravasation is an alternative mechanism for cerebral microvascular recanalization. *Nature* **465**, 478-482 (2010).
11. Cho, K. H. *et al.* The Characteristics of Retinal Emboli and its Association With Vascular Reperfusion in Retinal Artery Occlusion. Invest. *Ophthalmol. Vis. Sci.* **57**, 4589-4598 (2016).
12. Lam, F. C. *et al.* PMC5959860; Enhanced efficacy of combined temozolomide and bromodomain inhibitor therapy for gliomas using targeted nanoparticles. *Nat Commun* **9**, 1991 (2018).
13. Nkanga, C. I. *et al.* Clinically established biodegradable long acting injectables: An industry perspective. *Adv. Drug Deliv. Rev.* **167**, 19-46 (2020).
14. Steendam, R., van der Laan, A. & Hissink, D. Bioresorbable drug-eluting stent coating formulations based on SynBiosys biodegradable multi-block copolymers. *J. Control. Release* **116**, 94 (2006).
15. Teekamp, N. *et al.* Polymeric microspheres for the sustained release of a protein-based drug carrier targeting the PDGFβ-receptor in the fibrotic kidney. *Int. J. Pharm.* **534**, 229-236 (2017).
16. Stanković, M. *et al.* Tailored protein release from biodegradable poly(ε-caprolactone-PEG)-b-poly(ε-caprolactone) multiblock-copolymer implants. *Eur. J. Pharm. Biopharm.* **87**, 329-337 (2014).
17. Blinder, P. *et al.* The cortical angiome: an interconnected vascular network with noncolumnar patterns of blood flow. *Nat. Neurosci.* **16**, 889-897 (2013).
18. Georgakopoulou, T., van der Wijk, A. E., Bakker, E. & vanBavel, E. Recovery of Hypoxic Regions in a Rat Model of Microembolism. *J Stroke Cerebrovasc Dis* **30**, 105739 (2021).
19. Abbott, N. J., Patabendige, A. A., Dolman, D. E., Yusof, S. R. & Begley, D. J. Structure and function of the blood-brain barrier. *Neurobiol. Dis.* **37**, 13-25 (2010).
20. U.S. Food & Drug Administration (FDA). (2021).
21. Levites, Y. *et al.* PMC1307561; Anti-Abeta42- and anti-Abeta40-specific mAbs attenuate amyloid deposition in an Alzheimer disease mouse model. *J. Clin. Invest.* **116**, 193-201 (2006).
22. Sevigny, J. *et al.* The antibody aducanumab reduces Abeta plaques in Alzheimer's disease. *Nature* **537**, 50-56 (2016).
23. Shih, A. Y. *et al.* The smallest stroke: occlusion of one penetrating vessel leads to infarction and a cognitive deficit. *Nat. Neurosci.* **16**, 55-63 (2013).
24. Lencioni, R., Petruzzi, P. & Crocetti, L. PMC3700789; Chemoembolization of hepatocellular carcinoma. *Semin Intervent Radiol* **30**, 3-11 (2013).

25. Namur, J. *et al*. Drug-eluting beads for liver embolization: concentration of doxorubicin in tissue and in beads in a pig model. *J. Vasc. Interv. Radiol.* **21**, 259-267 (2010).
26. Bezemer, J. M., Grijpma, D. W., Dijkstra, P. J., van Blitterswijk, C. A. & Feijen, J. A controlled release system for proteins based on poly(ether ester) block-copolymers: polymer network characterization. *J. Control. Release* **62**, 393-405 (1999).
27. Lockwood, N. A. *et al*. In vitro and in vivo characterization of novel biodegradable polymers for application as drug-eluting stent coatings. *J. Biomater. Sci. Polym. Ed.* **21**, 529-552 (2010).
28. Hughes, P. *et al*. Poly-dioxanone multi-block copolymer for ocular protein delivery. World Intellectual Property Organization, International publication number WO2021/067388, available at https://nl.espacenet.com, accessed September 14, 2022. (2021).
29. Steendam, R. *et al*. Dosage form for extended release of an antibody or large protein. European patent office, European patent application EP4051233, published September 7, 2022, available at https://nl.espacenet.com. (2022).
30. Becker, J. B., Prendergast, B. J. & Liang, J. W. PMC4962440; Female rats are not more variable than male rats: a meta-analysis of neuroscience studies. *Biol Sex Differ* **7**, 34 (2016).
31. Mazure, C. M. & Swendsen, J. PMC4864429; Sex differences in Alzheimer's disease and other dementias. *Lancet Neurol* **15**, 451-452 (2016).

SUPPLEMENTARY INFORMATION

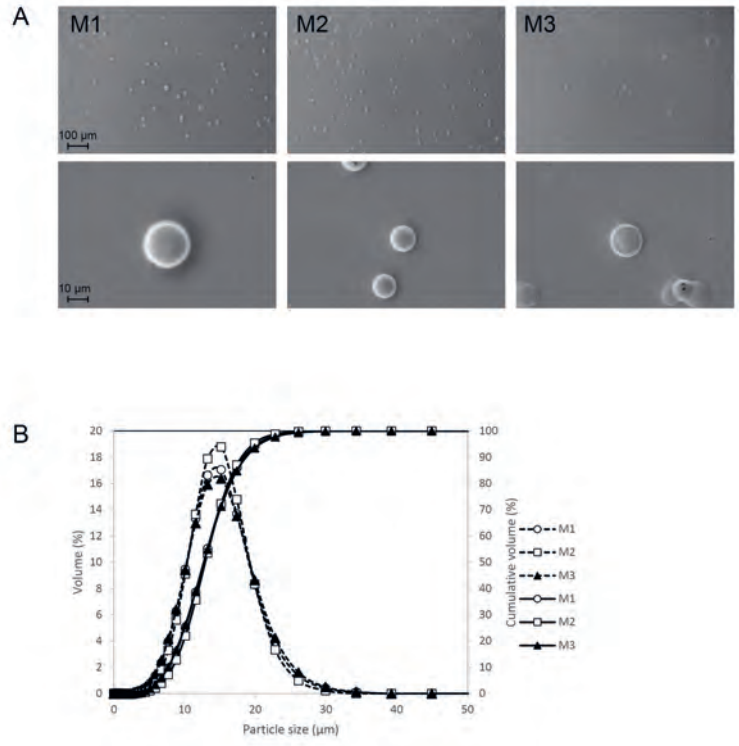

Figure S1. ***(A)*** *SEM images of M1, M2 and M3 show a round shape of these microspheres, with smooth surface for M1 and M2 and a somewhat rougher surface for M3.* ***(B)*** *Particle size distribution of microspheres M1, M2 and M3 with volume percentage on the left axis (dashed lines) and cumulative volume percentage on the right axis (solid lines).*

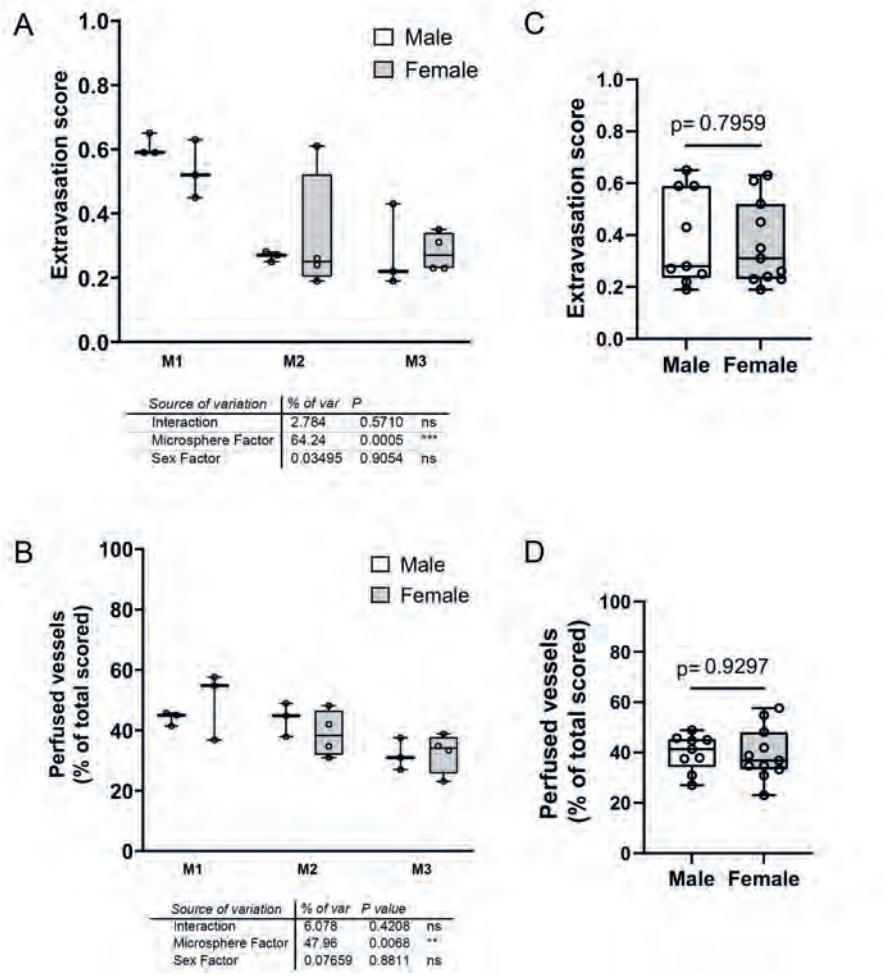

Figure S2. Sex has no effect on extravasation score and vessel perfusion. *Two-way ANOVA was performed for animals stratified by the independent variables "Sex" (male; open boxes, female; filled boxes) and "Microspheres" to assess whether sex affects* **(A)** *extravasation score and* **(B)** *vessel perfusion. Since the groups are rather small when stratified by microsphere class, animals were pooled for microsphere class to assess whether there is a difference in* **(C)** *extravasation score and* **(D)** *vessel perfusion between male and female rats with an unpaired t-test. Data are depicted as median ± IQR (box) and min – max (whiskers), each data point represents an individual animal. (A) and (B) Male M1: n=3, female M1: n=3, male M2: n=3, female M2: n=4, male M3: n=3, female M3: n=4. (C) and (D) Male: n=9, female: n=11.*

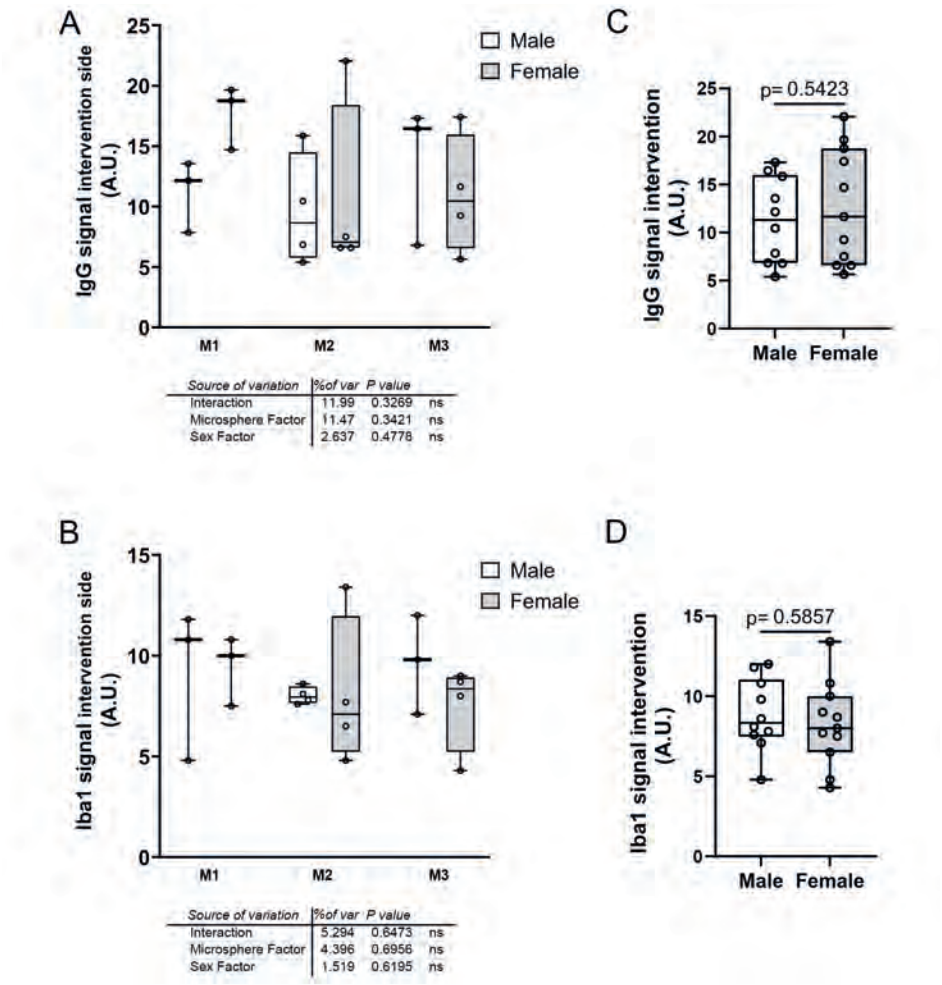

Figure S3. Sex has no effect on IgG and Iba1 signal intensity. *Two-way ANOVA was performed for animals stratified by the independent variables "Sex" (male; open boxes, female; filled boxes) and "Microspheres" to assess whether sex affects* **(A)** *IgG signal intensity in the intervention side and* **(B)** *Iba1 signal intensity in the intervention side. Since the groups are rather small when stratified by microsphere class, animals were pooled for microsphere class to assess whether there is a difference in* **(C)** *IgG signal intensity in the intervention side and* **(D)** *Iba1 signal intensity in the intervention side between male and female rats with an unpaired t-test. Data are depicted as median ± IQR (box) and min – max (whiskers), each data point represents an individual animal. (A) and (B) Male M1: n=3, female M1: n=3, male M2: n=4, female M2: n=4, male M3: n=3, female M3: n=4. (C) and (D) Male: n=10, female: n=11.*

Table S1. *Absolute numbers scored for extravasation status at day 14.*

	Total scored (#)		
	M1 (n=6)	**M2 (n=7)**	**M3 (n=7)**
In	134	201	241
Going out	39	50	49
Out	41	12	23
TOTAL	214	263	313

Table S2. *Percentage extravasation status at day 14.*

	M1 (n=6)	**M2 (n=7)**	**M3 (n=7)**
In	62.8 (60.6-64.8)*	76.7 (75.0-78.6)	83.3 (71.4-84.4)
Going out	14.1 (12.7-25.5)	19.6 (19.1-25.0)	13.5 (9.4-19.6)
Out	20.7 (14.8-25.2)**	3.3 (2.4-4.3)	6.3 (5.9-7.5)

*Data is depicted as median (IQR). *P=0.0134, M1 vs M3; **P=0.0021, M1 vs M2; Kruskal-Wallis with Dunn's multiple comparisons test*

Chapter 8

GENERAL DISCUSSION

GENERAL DISCUSSION

This thesis focuses on brain damage and recovery following multiple obstructions of the cerebral microvasculature. Using a rat model of microembolization, we performed a multi-faceted analysis by following the pathological events induced by local occlusions over time, and in relation to their topography. In addition, recovery mechanisms, such as resolution of edema and reperfusion due to angiophagy, as well as therapeutic innovations were addressed.

Spatial analysis: Distant effects of micro-occlusions and the importance of cerebral vascular anatomy

One of our main findings is that micro-occlusions may cause distant effects in terms of hypoxia and infarction, up to millimeters away from the occlusion site. We came to this conclusion in both **chapter 2** and **chapter 3**, which describe our findings after injecting either a single size of microspheres (25 µm diameter; **chapter 2**) or a mixture of microsphere sizes (15-50 µm diameter; **chapter 3**) in the cerebral circulation. The distant effects could be explained by a phenomenon entitled as coalescence, which has been described by Shih et al. (2013) (1). Using a photothrombotic approach, Shih et al. could selectively block multiple descending arterioles. According to their brain tissue perfusion experiments, each penetrating arteriole provides blood to a distinct cortical column of brain tissue (2, 3). After quantification of the damage, they found that neighboring cortical columns surrounding the damaged area showed signs of decreased perfusion and degeneration, although these areas were served by arterioles that were not photothrombotically occluded (1). This process of coalescence could be due to delayed thrombosis in the microcirculation. We believe that this phenomenon is also the case in our experimental model. Thus, when multiple small arterioles are occluded, an expansion of brain damage due to a negative impact on neighboring territories may lead to distant effects as found in **chapters 2** and **3**.

In the next chapters, we evaluated brain damage volumes. Since we were interested in the impact of microemboli on brain tissue perfusion and survival, as well as brain function, we quantified the total infarction and evaluated the corresponding neurological deficit. In **chapter 5**, infusion of a single microsphere size per group (group 15: 25000 microspheres of 15 µm, group 25: 5500 microspheres of 25 µm and group 50: 1000 microspheres of 50 µm) resulted in approximately 1% of cumulative infarction volume in all cases. The number of microspheres used was based on scaling laws for vascular trees. The scaling laws predict the volume–diameter power relation with a theoretical exponent of 3 (4). Thus, for instance, a 25 µm artery supplies with blood a 4.5-fold larger region than a 15 µm artery. In other words, by blocking 4.5-fold more 15 µm arterioles than 25 µm arterioles we would cause equal brain damage. The validity of these scaling laws was confirmed by our experiments, where we found a similar cumulative infarction volume. In terms of brain function, we found that when only 1% of the intervention hemisphere is infarcted, severe neurological deficits can develop. This burden caused by a shower of microemboli may also be (partially) responsible for the poor recovery of acute ischemic stroke (AIS) patients after thrombectomy. Collectively, we can conclude that potential release of microemboli

should be taken into account for future device design, especially after an AIS event where the patient's health is already compromised.

An unexpected finding was that, when combining all microsphere sizes together in **chapter 4** (25000 of 15 µm, 5500 of 25 µm and 500 of 50 µm), it did not lead to a greater cumulative infarction volume as compared to the experiments with single microsphere sizes (**chapter 5**). Although speculative, since we did not include the topology of cerebral vasculature in the analysis and given that all possible factors that may affect outcome were similar between the animals (collateralization, age, intervention), we believe that this finding may be explained by the fact that a typical vascular tree was simultaneously blocked at different levels. To visualize this hypothesis, we added a schematic representation of a typical cortical arterial tree (Fig. 1). However, a better understanding of lesion progression could be gained if the architecture of the cerebral vasculature is included in the analysis pipeline.

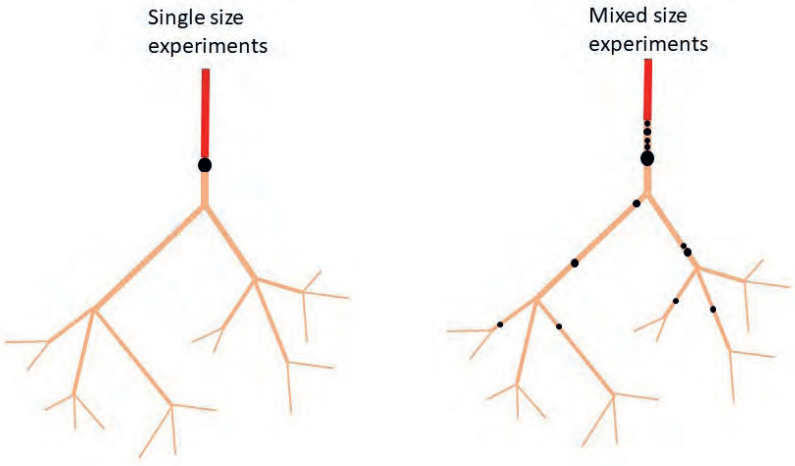

Figure 1. Schematic of a typical cortical arterial tree with perfused (red) and non-perfused parts (light orange). *Left: Occlusion with a single microsphere size (black filled circle) Right: Multiple occlusions with a mixture of microsphere sizes (black filled circles).*

We initially aimed to correlate the structure of the vascular tree to tissue damage. The reconstruction of the cerebral vasculature proved to be very difficult, so in our analysis, the topology of the rat cerebral vasculature was not taken into account (**chapter 2-4**). Our 3D reconstruction of the intervention hemisphere was based on the alignment of 10 consecutive coronal brain sections, 50 µm thick each. Technical issues and the detrimental nature of micro-occlusions affected the quality of the 3D reconstruction. Micro-occlusions also resulted in tissue decomposition due to brain (micro-) infarctions. In addition, several steps of the reconstruction procedure, from fixation of brain tissue in 4% PFA to placing the brain sections on glass microscope slides required manually processing and treatment of the tissue with chemicals. Despite gentle handling, brain sections were subjected to a different degree of deformation and shrinkage, which in turn made the reconstruction of the cerebral vasculature a mission impossible. We therefore decided to use the contours of

the affected regions (hypoxic, infarcted) and the gross brain anatomy (ventricles, midline, and cerebral cortex) in order to make the 3D reconstruction of the intervention hemisphere (**chapter 2-4**). In **chapter 2**, we incorporated *in silico* cortical columns in our analysis in order to overcome the obstacle of the 3D visualization of the rat cerebral vasculature. Although there were some limitations in the study (human vs. rodent, acute effects vs. 24h effects, multiple occlusions vs. single arteriole occlusion), we were able to show that *in silico* models could improve our understanding regarding the impact of microemboli on tissue perfusion and oxygenation. In addition, using two different approaches (*in vivo* and *in silico*), we showed that blocking the arterioles with 25 μm (diameter) microspheres leads to both local and distant effects. However, there were some discrepancies regarding the percentage of distant and local effects between *in vivo* and *in silico* experiments that could only be explained when taking into account the actual topology of the rat cerebral vasculature.

To visualize the rat brain vascular anatomy, we attempted to use a technique known as tissue clearing (5, 6). Tissue clearing is based on chemical treatment of brain tissue samples (parts or whole) in order to make the tissue transparent. This process consequently allows for a high-resolution assessment of vascular reconstruction (6, 7) since no tissue cutting is needed. During these pilot experiments, we became aware of the following challenges. Firstly, polystyrene microspheres were susceptible to the chemicals of the clearing protocol and did not survive the process. Secondly, the clearing protocol may work very well on the mouse brain tissue (7) but not on the rat, which was our animal model (8). Lastly, the clearing quality depends on tissue size, and lipid composition. Although we managed to find custom-made microspheres that met the requirements of this experimental setup and we followed an optimized clearing protocol (8), we were not satisfied with the clearing quality of the whole brain tissue and decided to clear smaller brain samples. Due to time restrictions, we did not finish the clearing experiments and did not include it in the current thesis. However, this is work in progress and remains a challenge for the future.

A 3D visualization of the cerebral vasculature is essential if we want to understand the biological relationships between structure and function. In case of an occlusion, the existence of a collateral connection (9) may supply the affected area with blood and thus influence tissue survival. In humans, evidence of the significance of the collateral circulation on brain function comes from AIS patients, where a good collateral status is a prognostic marker for good clinical outcome (10). The collateral status of AIS patients is determined by the thrombolysis in cerebral infarction (TICI) score (0: no perfusion – 3: complete perfusion). Although the TICI score is a widely used number to evaluate the degree of reperfusion following thrombectomy, it gives no direct information on vascular architecture (11). In addition, studies on the brain collateral circulation often focus either more proximally at the circle of Willis (neuroimaging techniques on living human patients) (12), or at the microscopic scale of capillaries and arterioles (microscopic techniques on brain cadaver tissue samples) (13, 14). Secondary pathways such as the leptomeningeal anastomoses, a network of small connecting branches between two major cerebral arteries at the pial surface, are poorly investigated. Given that imaging techniques (MRI, CT) have a low resolution (0.5-2 mm) (15), the most common way to gain knowledge on the

anatomy of leptomeningeal anastomoses is from experiments on brain cadavers. However, the human brain surface is characterized by folds (gyri) and grooves (sulci) and that makes the mapping of the pial surface collateralization extremely challenging. The most comprehensive work on leptomeningeal anastomoses remains the work of Duvernoy et al. from 1981, which examined brain cadaver material after injecting ink (14). Unfortunately, 3D reconstructions and quantitative data of the human leptomeningeal anastomotic network remain scarce (16-18). We tried to visualize the pial surface architecture using cadaver brains. By filling the vessels with a fluorescent gelatin via the carotid arteries and scanning of the brain in a 3D imaging cryomicrotome, we aimed to provide a 3D reconstruction and quantification of the pial collaterals. The restrictions due to coronavirus affected our experiments and we could only fill two human cadaver brains, using two different filling protocols. Only one brain was successfully filled with gelatin. Quantification of the vessel characteristics is not completed yet and therefore not included in this thesis. Such data of detailed information on the architecture of the leptomeningeal collaterals may be used for computer simulations that predict clinical outcome after AIS.

Temporal and functional analysis: The role of angiophagy and glymphatics in tissue recovery

In **chapters 4** and **6**, we looked at the progression of brain tissue damage caused by a shower of microemboli in a follow-up period of 7 days. We confirmed that infarction was irreversible, but ischemia, hypoxia and edema were reduced or even virtually disappeared within 7 days. The tissue recovery could be attributed to two mechanisms also studied in the current thesis, namely angiophagy (**chapter 6**) and the clearance of debris via the glymphatic pathway (**chapter 5**). Other processes not addressed here like angiogenesis and the regrowth of new blood vessels (19) could also contribute to brain tissue recovery after micro-occlusions but these are beyond the scope of this thesis. Angiophagy is the extravasation of microemboli into the brain parenchyma and reestablishes tissue reperfusion. By using both *in vivo* and *in vitro* techniques and different microemboli compositions, we tried to further elucidate the process of microembolus extravasation. We demonstrated that angiophagy was accompanied by active cytoskeletal remodeling of the endothelium. However, the factors that promote angiophagy and the molecular mechanism still needs further investigation. If we take a closer look at the role of glymphatics on brain clearance, we showed that the perivascular space and the subarachnoid space play a vital role in the clearance of surplus endogenous IgG from the brain parenchyma (**chapter 5**). Immunoglobulin (IgG) is a common blood component that leaks into the brain parenchyma as a result of the transient increase in bloob brain barrier (BBB) permeability. In more detail, it became clear that the perivascular spaces around arteries and veins are responsible for transporting the excess of blood components towards the subarachnoid space. This finding is, however, not in line with the currently accepted theory of glymphatics. According to this theory, under physiological conditions cerebrospinal fluid enters the brain parenchyma from the perivascular space around arteries and exits through perivascular space around veins (20) However, the fact that we studied the process of glymphatic clearance under

pathological conditions could explain the altered directionality of brain fluids. Taken together, we found that the glymphatic system and the process of angiophagy both contribute to tissue recovery after micro-infarcts (**chapter 6**).

FUTURE DIRECTIONS

The knowledge gained in this thesis is applicable to both thrombotic and embolic stroke and potentially extend to other brain disorders. Our analysis looked at different aspects of micro-occlusions ranging from immediate effects, such as the acute response of blood flow and oxygen transport, to long-term effects like lesion progression, tissue recovery and potential treatment. In the following paragraphs, the relevance of our experiments to unravel and treat brain disorders is further elucidated.

In silico models for brain damage prediction after arterial occlusions

For the comparison between animal experiments and computer models (**chapter 2**), we used hemisphere reconstructions (7000×500×8000 μm) versus cortical columns (375×375×1500 μm) of brain tissue, respectively. We still have to develop *in silico* models of the brain cortex made up by multiple cortical columns and block them with multiple microemboli (rather than one), in order to first, fine-tune the *in silico* model and second, understand the coalescent nature of tissue damage after multiple arterial occlusions (1). In our *in silico* analysis we assumed that blood flow and oxygen transport were steady and passive processes and did not take into account pathological events following micro-occlusions, such as cerebral edema, pericyte constriction and neuronal cell death. All aforementioned events occur and develop in the first hours after AIS and could affect blood flow and consequently tissue oxygenation (21-23). These additions and improvements of the *in silico* model are needed in order to deliver a comprehensive work regarding damage evolution after micro-occlusions and further in the context of AIS be able to predict the impact caused by a shower of microemboli after thrombectomy. In conclusion, because of the complex nature of infarct growth, we primarily focused on the *in silico* model on the acute effects of micro-occlusions on blood flow and tissue oxygenation. If we aim to place our experiments within the INSIST (*IN Silico* clinical trials for the treatment of acute Ischemic STroke) pipeline, several aspects should be further evaluated first. To run a complete *in silico* clinical trial of virtual patients we need to incorporate other pathological events like BBB permeability, immune responses, neuronal tissue death and the corresponding neurological deficits depending on stroke location, but also intrinsic recovery mechanisms such as the fibrinolytic system, angiophagy, angiogenesis and glymphatics.

Glymphatics during stroke

Our experimental setup could not catch the dynamic nature of IgG clearance from the brain parenchyma (**chapter 5**). Our findings are largely based on immunohistological procedures on post-mortem material and focus on 24h after microembolization. It would be interesting to follow the process real time in order to get a picture of the timing and the

mechanisms of brain clearance from the brain parenchyma. Using the same animal model of microembolization in combination with two-photon microscopy, we could gain more insight on the role of glymphatics in case of micro-occlusions. Two-photon microscopy enables live imaging and has a higher penetration depth compared to single-photon microscopy (24). With a cranial window on the skull of the animal model, it is possible to follow in time pathological responses of the brain. The microembolization model is suitable for this purpose because micro-occlusions cause extensive IgG leakage into the brain parenchyma without necessarily leading to neuronal cell death and neurological deficits (25). For this reason, it is possible to follow the events chronically at different time points with little animal suffering, which could be achieved by imaging leakage of fluorescent dyes from the vasculature into the tissue. Such data could be relevant for other diseases that cause BBB permeability and may contribute to the design of new therapeutics that stimulate brain clearance.

Angiophagy: 'Trojan horse' strategy of drug transport across the BBB?

Crossing the BBB remains one of the main challenges regarding the treatment of brain disorders. The uptake of pharmaceutical compounds in the brain is inhibited because of the selective permeability of the BBB (26). As presented in **chapter 7**, angiophagy can be considered as a potential mechanism of drug delivery from the systemic circulation into the brain parenchyma. Such a drug delivery treatment strategy relies on three distinct processes: (i) transport across the BBB through angiophagy, (ii) microsphere degradation and (iii) release of the encapsulated drug into the brain parenchyma. This strategy where a pharmaceutical compound that does not have the ability to cross the BBB is encapsulated within another material in order to pass the BBB, is called a 'Trojan horse' (27). Using three different types of polymeric biodegradable microspheres, each having another degree of hydrophilicity, we looked at the extravasation rate in order to evaluate whether the material composition affects the timing of angiophagy. However, evaluating the extravasation rate is only a first step towards the exploitation of angiophagy as a drug delivery mechanism. Future research may focus on other physical and chemical properties that possibly affect extravasation rate (e.g. surface charge) and biodegradation (e.g. liposomes) (28). Both timing of extravasation and duration of biodegradation determine the uptake of the drug from the brain parenchyma. Depending on the nature of the pathological condition and the required therapy duration, different combinations of composition materials could be used to deliver drugs into the brain parenchyma. Another aspect of such a treatment strategy that needs further investigation is the drug release. Here, we filled the microspheres with a fluorescent dye, but in the future, pharmaceutical compounds should be tested as filling materials. Finally, angiophagy in general is a poorly investigated mechanism and still needs to be further understood. To date, it has been shown in various organs in mice, in the rat brain and the piglet lungs (25, 29, 30). Evidence of angiophagy in humans comes from cadaver lung samples of patients that suffered from chronic thromboembolic diseases (29). Whether angiophagy can take place in the human brain, is still an open question. Taken together, angiophagy may be exploited for drug delivery into the brain parenchyma in order to treat various neurological disorders.

CONCLUSION

In this thesis, we studied the impact of micro-occlusions on brain tissue and the intrinsic mechanisms of the brain that are involved in recovery of tissue at risk. The analysis can be divided into three sections, the spatial (**chapter 2, 3**), the temporal (**chapter 4, 6**) and the functional analysis (**chapter 5-7**), each focusing on different aspects of the micro-occlusion effects. From our spatial analysis both *in vivo* and *in silico* we can conclude that multiple micro-occlusions cause distant effects on brain tissue and not only local damage as initially thought. Our temporal analysis revealed that tissue hypoxia following microembolization of the cerebral microcirculation is of transient nature and that the mechanism of angiophagy may play a pivotal role in the recovery of hypoxic tissue. Finally, with our functional analysis, we laid the foundation for a potential new therapy for brain disorders (cancer, dementia) by exploiting the extravasation capacity of angiophagy. Further, our functional analysis shed light on the role of the glymphatic system to the clearance of brain edema after microembolization, highlighting the contribution of subarachnoid space and of perivascular space (both around arteries and veins) to debris elimination. Taken together, this thesis addressed the detrimental effects of micro-occlusions on brain tissue, evaluated potential recovery mechanisms such as angiophagy and glymphatics and suggested novel approaches for therapies of brain disorders in general.

REFERENCES

1. Shih, A. Y. *et al.* PMC3952571; The smallest stroke: occlusion of one penetrating vessel leads to infarction and a cognitive deficit. *Nat. Neurosci.* **16**, 55-63 (2013).
2. Blinder, P., Shih, A. Y., Rafie, C. & Kleinfeld, D. PMC2906564; Topological basis for the robust distribution of blood to rodent neocortex. *Proc. Natl. Acad. Sci. U. S. A.* **107**, 12670-12675 (2010).
3. Drew, P. J. *et al.* PMC3204312; Chronic optical access through a polished and reinforced thinned skull. N*at Methods* **7**, 981-984 (2010).
4. Huo, Y. & Kassab, G. S. PMC3223633; Intraspecific scaling laws of vascular trees. *J R Soc Interface* **9**, 190-200 (2012).
5. Zhang, L. Y. *et al.* PMC5963347; CLARITY for High-resolution Imaging and Quantification of Vasculature in the Whole Mouse Brain. *Aging Dis* **9**, 262-272 (2018).
6. Richardson, D. S. *et al.* Tissue clearing. *Nature Reviews Methods Primers* **1**, 84 (2021).
7. Lugo-Hernandez, E. *et al.* PMC5624395; 3D visualization and quantification of microvessels in the whole ischemic mouse brain using solvent-based clearing and light sheet microscopy. *J. Cereb. Blood Flow Metab.* **37**, 3355-3367 (2017).
8. Branch, A. *et al.* An optimized tissue clearing protocol for rat brain labeling, imaging, and high throughput analysis. *bioRxiv*, 639674 (2021).
9. Faber, J. E., Chilian, W. M., Deindl, E., van Royen, N. & Simons, M. PMC4140974; A brief etymology of the collateral circulation. *Arterioscler. Thromb. Vasc. Biol.* **34**, 1854-1859 (2014).
10. Ribo, M. *et al.* Extending the time window for endovascular procedures according to collateral pial circulation. *Stroke* **42**, 3465-3469 (2011).
11. Tung, E. L. *et al.* Rethinking Thrombolysis in Cerebral Infarction 2b: Which Thrombolysis in Cerebral Infarction Scales Best Define Near Complete Recanalization in the Modern Thrombectomy Era? *Stroke* **48**, 2488-2493 (2017).
12. Dhakal, P. *et al.* PMC8028512; Anatomical Variations in Circle of Willis in Patients Undergoing CT Cerebral Angiography in a Tertiary Hospital in Nepal: A Descriptive Cross-sectional Study. *JNMA J Nepal Med Assoc* **58**, 1065-1068 (2020).
13. Cassot, F. *et al.* Branching patterns for arterioles and venules of the human cerebral cortex. *Brain Res.* **1313**, 62-78 (2010).
14. Duvernoy, H. M., Delon, S. & Vannson, J. L. Cortical blood vessels of the human brain. Brain Res. Bull. 7, 519-579 (1981).
15. Lin, E. & Alessio, A. PMC4752333; What are the basic concepts of temporal, contrast, and spatial resolution in cardiac CT? *J Cardiovasc Comput Tomogr* **3**, 403-408 (2009).

16. Cassot, F., Lauwers, F., Fouard, C., Prohaska, S. & Lauwers-Cances, V. A novel three-dimensional computer-assisted method for a quantitative study of microvascular networks of the human cerebral cortex. *Microcirculation* **13**, 1-18 (2006).
17. Helthuis, J. H. G. *et al*. Branching Pattern of the Cerebral Arterial Tree. *Anat. Rec.* **302**, 1434-1446 (2019).
18. Payne, S. J. in Cerebral Blood Flow and Metabolism.
19. Hatakeyama, M., Ninomiya, I. & Kanazawa, M. PMC6862417; Angiogenesis and neuronal remodeling after ischemic stroke. *Neural Regen Res* **15**, 16-19 (2020).
20. Hablitz, L. M. & Nedergaard, M. PMC8603752; The Glymphatic System: A Novel Component of Fundamental Neurobiology. *J. Neurosci.* **41**, 7698-7711 (2021).
21. Gautam, J. & Yao, Y. PMC6300777; Roles of Pericytes in Stroke Pathogenesis. *Cell Transplant.* **27**, 1798-1808 (2018).
22. Campbell, B. C. *et al.* PMC3734777; Failure of collateral blood flow is associated with infarct growth in ischemic stroke. *J. Cereb. Blood Flow Metab.* **33**, 1168-1172 (2013).
23. Klatzo, I. Blood-brain barrier and ischaemic brain oedema. *Z. Kardiol.* **76** Suppl 4, 67-69 (1987).
24. Rubart, M. Two-Photon Microscopy of Cells and Tissue. *Circ. Res.* **95**, 1154-1166 (2004).
25. van der Wijk, A. E. *et al*. Extravasation of Microspheres in a Rat Model of Silent Brain Infarcts. *Stroke* **50**, 1590-1594 (2019).
26. Pardridge, W. M. PMC3494002; Drug transport across the blood-brain barrier. *J. Cereb. Blood Flow Metab.* **32**, 1959-1972 (2012).
27. Warren, K. E. Beyond the Blood:Brain Barrier: The Importance of Central Nervous System (CNS) Pharmacokinetics for the Treatment of CNS Tumors, Including Diffuse Intrinsic Pontine Glioma. *Frontiers in Oncology* **8** (2018).
28. Hersh, A. M., Alomari, S. & Tyler, B. M. Crossing the Blood-Brain Barrier: Advances in Nanoparticle Technology for Drug Delivery in Neuro-Oncology. *International Journal of Molecular Sciences* **23**, 4153 (2022).
29. Perros, F. *et al*. PMC7696066; Description, Staging and Quantification of Pulmonary Artery Angiophagy in a Large Animal Model of Chronic Thromboembolic Pulmonary Hypertension. *Biomedicines* **8** (2020).
30. Grutzendler, J. Angiophagy: mechanism of microvascular recanalization independent of the fibrinolytic system. *Stroke* **44**, 84 (2013).

Chapter 9

SUMMARY

SAMENVATTING

AUTHOR AFFILIATIONS

PORTFOLIO

CURRICULUM VITAE

DANKWOORD

SUMMARY

The mammalian brain depends on a well-controlled delivery of nutrients and oxygen in order to function properly. These components reach the brain via the blood circulation through a network of cerebral arteries, arterioles and capillaries. Obstructions of the cerebral vasculature can cause disturbance of homeostasis and lead to severe neurological deficits. In this thesis we evaluated the spatiotemporal effects of multiple occlusions at the arteriole level on brain tissue and investigated intrinsic mechanisms of blood flow restoration and debris clearance.

After a general introduction in **chapter 1**, the impact of occlusions on brain tissue perfusion and oxygenation is studied in **chapter 2**. We used both *in vivo* and *in silico* approaches to elucidate the relationship between occlusion site and resulting ischemia and hypoxia. In a rat model of microembolization, infusion of 25 µm (diameter) microspheres resulted in multiple occlusions of penetrating arterioles. In computer models of human cortical arterial trees, the penetrating arterioles were occluded by microspheres of the same size and the oxygen transport was simulated using a Green's function method. After segmenting the microspheres and hypoxic regions, their spatial correlation was quantified. Comparison between *in vivo* and *in silico* experiments revealed distant effects of micro-occlusions. Distant effects were also found in **chapter 3**, after infusion of a mixture of microsphere sizes (15, 25 and 50 µm diameter) in the cerebral circulation. After a 3D reconstruction of the intervention hemisphere and segmentation of the damaged regions, we applied a novel point-pattern spatial analysis between occlusion site and the hypoxic or infarcted regions. We found effects of micro-occlusions extending to thousands of micrometers away from the occlusion site. In **chapter 4**, using the same experimental setup as **chapter 3** we monitored and quantified brain lesions in terms of ischemia, hypoxia and infarction for a period of seven days. We found that infarction persists, but ischemia and hypoxia decrease over time. These findings suggest that recovery mechanisms rescue the tissue at risk. Possible recovery mechanisms were investigated in the following chapters. **Chapter 5** focuses on the blood brain barrier (BBB) disruption, a severe complication of (micro-)occlusions and on the mechanisms that restore homeostasis. Microembolization of the cerebral circulation with a single size of microspheres (15, 25, 50 µm diameter), resulted in all cases in BBB disruption and entrance of blood components (albumin, Immunoglobulin (IgG)) in the brain parenchyma. Our histological analysis based on immunostainings and confocal imaging, demonstrated that the glymphatic system is recruited to clear the extravasated blood components from the brain parenchyma. In particular, IgG is cleared through perivascular spaces surrounding the cerebral arteries and veins and ends up into the subarachnoid space. Another intrinsic mechanism that contributes to brain tissue recovery is angiophagy, the extravasation of microspheres to the brain parenchyma. In **chapter 6,** we studied angiophagy using both *in vitro* and *in vivo* experiments. By introducing polystyrene microspheres or fibrin clots on the surface of human (brain) endothelial cell cultures, we followed in time the process of embolus engulfment with live cell imaging. We showed that angiophagy occurs *in vitro* and is accompanied by active cytoskeletal remodeling of the endothelium. In our animal model of microembolization, we quantified the process of

angiophagy in a course of 7 days. We found that approximately 50% of the microspheres was in the process of extravasating or extravasated at day 7, which led to reperfusion of previously occluded brain regions. Since microemboli are actively transferred to the brain parenchyma through angiophagy, we investigated in **chapter 7** whether this mechanism can be exploited for the transfer of therapeutic compounds through the BBB. We therefore infused three types of biodegradable microspheres having the same diameter (~13 µm), but different surface characteristics. Quantification of extravasated microspheres revealed that hydrophilicity affects the extravasation rate. Finally, the findings of this thesis, future perspectives and conclusions are presented in **chapter 8**.

SAMENVATTING

De hersenen zijn afhankelijk van een goed geregelde aanvoer van voedingsstoffen en zuurstof om optimaal te kunnen functioneren. Deze componenten bereiken de hersenen via de bloedcirculatie door een netwerk van slagaders, arteriolen en haarvaten. Obstructies van de cerebrale vasculatuur kunnen een verstoring van de homeostase veroorzaken en leiden tot ernstige neurologische stoornissen. In dit proefschrift evalueerden we de spatiële en temporele effecten van meerdere occlusies op het niveau van de arteriolen op het hersenweefsel. Daarnaast onderzochten we intrinsieke mechanismen van bloedstroom herstel en transport van afvalstoffen.

Hoofdstuk 1 vormt een inleiding op het proefschrift. Hierin beschrijf ik het belang van homeostasis in het brein en hoe deze aangetast kan worden door micro-occlusies. In **hoofdstuk 2** wordt de impact van occlusies op de perfusie en oxygenatie van het hersenweefsel beschreven. We hebben zowel *in vivo* als *in silico* technieken gebruikt om de relatie tussen de occlusielocatie en resulterende ischemie en hypoxie op te helderen. In een rattenmodel van micro-embolisatie resulteerde infusie van 25 µm (diameter) microsferen in een groot aantal occlusies van penetrerende arteriolen. In computermodellen van menselijke corticale arteriële vaatbomen werden de penetrerende arteriolen afgesloten door microsferen van dezelfde grootte en werd het zuurstoftransport gesimuleerd met behulp van de Green's functie-methode. Na het segmenteren van de microsferen en hypoxische gebieden, werd hun spatiële correlatie gekwantificeerd. Vergelijking tussen *in vivo* en *in silico* experimenten onthulde dat micro-occlusies effecten kunnen hebben op een relatief grote afstand van de occlusielocatie. Dit was ook het geval in **hoofdstuk 3**, na infusie van een mix van microsferen (15, 25 en 50 µm diameter) in de cerebrale circulatie. Na een 3D-reconstructie van de interventie hemisfeer en segmentatie van de beschadigde regio's, hebben we een spatiële analyse (point-pattern analysis) toegepast op de occlusielocatie en de hypoxische of geïnfarceerde regio's. We vonden effecten van micro-occlusies die zich uitstrekken tot duizenden micrometers verwijderd van de occlusielocatie. In **hoofdstuk 4** hebben we, gebruikmakend van dezelfde experimentele aanpak als **hoofdstuk 3**, gedurende zeven dagen de hersenschade in termen van ischemie, hypoxie en infarct gevolgd en gekwantificeerd. We vonden dat een infarct definitief is, maar dat ischemie en hypoxie in de loop van de tijd afnemen. Deze bevindingen suggereren dat herstelmechanismen

het hypoxische weefsel kunnen redden. In de volgende hoofdstukken zijn mogelijke herstelmechanismen onderzocht. In **hoofdstuk 5** wordt de nadruk gelegd op de verstoring van de bloedhersenbarrière, een ernstige complicatie van (micro-)occlusies. Daarnaast onderzochten we de mechanismen die de homeostase herstellen. Micro-embolisatie van de cerebrale circulatie met een enkele grootte van microsferen (15, 25, 50 µm diameter), resulteerde in alle gevallen in bloedhersenbarrière-verstoring en extravasatie van bloedcomponenten (albumine, IgG) in het hersenparenchym. Onze histologische analyse op basis van immunokleuring en confocale beeldvorming toonde aan dat het glymfatische systeem wordt gerekruteerd om het surplus van bloedcomponenten uit het hersenparenchym te verwijderen. In het bijzonder wordt IgG geklaard door perivasculaire ruimtes die de cerebrale slagaders en aders omringen, waarna het terecht komt in het subarachnoïdale ruimte. Een ander intrinsiek mechanisme dat bijdraagt aan het herstel van weefselperfusie is angiofagie, d.w.z. de extravasatie van microsferen naar het hersenparenchym. In **hoofdstuk 6** hebben we angiofagie bestudeerd met zowel *in vitro* als *in vivo* experimenten. Door polystyreen microsferen of fibrinestolsels op het oppervlak van menselijke (hersen) endotheelcelculturen te introduceren, volgden we in de tijd het proces van angiofagie met live-beeldvorming van de cellen. We toonden aan dat angiofagie *in vitro* gepaard gaat met actieve cytoskeletale remodellering van het endotheel. In ons diermodel van micro-embolisatie hebben we het proces van angiofagie gekwantificeerd over een periode van 7 dagen. We ontdekten dat op dag 7 voor ongeveer 50% van de microsferen extravasatie gaande of afgerond was, wat leidde tot reperfusie van eerder afgesloten hersengebieden. Omdat microsferen actief worden overgebracht naar het hersenparenchym via angiofagie, hebben we in **hoofdstuk 7** onderzocht of dit mechanisme kan worden benut voor de overdracht van geneesmiddelen. We hebben daarom drie soorten biologisch afbreekbare microsferen geïnjecteerd in ons ratmodel via de carotis arterie. De microsferen hadden dezelfde diameter (~13 µm), maar verschillende oppervlaktekenmerken. Kwantificatie van geëxtravaseerde microsferen liet zien dat hydrofiliciteit de extravasatiesnelheid beïnvloedt. Ten slotte worden de bevindingen van dit proefschrift, toekomstperspectieven en conclusies gepresenteerd in **hoofdstuk 8**.

AUTHOR AFFILIATIONS

Anne-Eva van der Wijk
Amsterdam UMC, Biomedical Engineering and Physics, Amsterdam Cardiovascular Sciences, University of Amsterdam, Meibergdreef 9, Amsterdam, The Netherlands.

Bert J van Het Hof
Amsterdam UMC, Molecular Cell Biology and Immunology, Amsterdam Neuroscience, Vrije Universiteit Amsterdam, De Boelelaan, 1117, Amsterdam, The Netherlands.

Erik N.T.P. Bakker
Amsterdam UMC, Biomedical Engineering and Physics, Amsterdam Cardiovascular Sciences, University of Amsterdam, Meibergdreef 9, Amsterdam, The Netherlands.

Ed van Bavel
Amsterdam UMC, Biomedical Engineering and Physics, Amsterdam Cardiovascular Sciences, University of Amsterdam, Meibergdreef 9, Amsterdam, The Netherlands.

Helga E de Vries
Amsterdam UMC, Molecular Cell Biology and Immunology, Amsterdam Neuroscience, Vrije Universiteit Amsterdam, De Boelelaan, 1117, Amsterdam, The Netherlands.

Jan S M van Bezu
Amsterdam UMC, Physiology, Amsterdam Cardiovascular Sciences, Vrije Universiteit Amsterdam, De Boelelaan, 1117, Amsterdam, The Netherlands.

Jisca Majolée
Amsterdam UMC, Physiology, Amsterdam Cardiovascular Sciences, Vrije Universiteit Amsterdam, De Boelelaan, 1117, Amsterdam, The Netherlands.

Johan Zuidema
InnoCore Pharmaceuticals, L.J. Zielstraweg 1, Groningen, The Netherlands

Miesje M van der Stoel
Amsterdam UMC, Medical Biochemistry, Amsterdam Cardiovascular Sciences, University of Amsterdam, Meibergdreef 9, Amsterdam, The Netherlands.

Peter L Hordijk
Amsterdam UMC, Physiology, Amsterdam Cardiovascular Sciences, Vrije Universiteit Amsterdam, De Boelelaan, 1117, Amsterdam, The Netherlands.

Rob Steendam
InnoCore Pharmaceuticals, L.J. Zielstraweg 1, Groningen, The Netherlands

Stephan Huveneers
Amsterdam UMC, Medical Biochemistry, Amsterdam Cardiovascular Sciences, University of Amsterdam, Meibergdreef 9, Amsterdam, The Netherlands.

Stephen J Payne
Institute of Biomedical Engineering, Department of Engineering Science, University of Oxford, Oxford, United Kingdom.
and
Institute of Applied Mechanics, National Taiwan University, Taipei, Taiwan.

Tamás I Józsa
Institute of Biomedical Engineering, Department of Engineering Science, University of Oxford, Oxford, United Kingdom.

Theodosia Georgakopoulou
Amsterdam UMC, Biomedical Engineering and Physics, Amsterdam Cardiovascular Sciences, University of Amsterdam, Meibergdreef 9, Amsterdam, The Netherlands.

Yidan Xu
Institute of Biomedical Engineering, Department of Engineering Science, University of Oxford, Oxford, United Kingdom.

INSIST investigators

WP1: Management
Charles Majoie[1], Henk Marquering[2], Ed van Bavel[2], Alfons Hoekstra[3]

WP2: Population and morphology models
Charles Majoie[1], Diederik Dippel[4], Hester Lingsma[5], Aad van der Lugt[6], Noor Samuels[4,5,6], Nikki Boodt[4,5,6], Yvo Roos[1], Simon F De Meyer[7], Senna Staessens[7], Sarah Vandelanotte[7], Henk Marquering[2], Praneeta Konduri[2], Nerea Arrarte Terreros[2]

WP3: *In silico* models for thrombosis and thrombolysis
Bastien Chopard[8], Franck Raynaud[8], Remy Petkantchin[8], Mikhail Panteleev[9], Alexey Shibeko[9], Karim Zouaoui Boudjeltia[10], Vanessa Blanc-Guillemaud[11]

WP4: *In silico* models for thrombectomy
Francesco Migliavacca[12], Gabriele Dubini[12], Giulia Luraghi[12], Jose Felix Rodriguez Matas[12], Sara Bridio[12], Patrick Mc Garry[13], Michael Gilvarry[14], Ray McCarthy[14], Kevin Moerman[13], Behrooz Fereidoonnezhad[13], Anushree Dwivedi[14], Sharon Duffy[14]

WP5: *In silico* models of perfusion defects and tissue damage
Stephen Payne[15], Ed van Bavel[2], Alfons Hoekstra[3], Tamas Jozsa[15], Wahbi El Bouri[15], Sissy Georgakopoulou[2], Raymond Padmos[3]

WP6: Integration and validation
Alfons Hoekstra[3], Victor Azizi[3], Claire Miller[3], Max van der Kolk[3], Raymons Padmos[3]

Affiliations INSIST investigators
[1] Department of Radiology and Nuclear Medicine, Amsterdam University Medical Centers, Location AMC, Amsterdam, The Netherlands.
[2] Department of Biomedical Engineering & Physics, Amsterdam University Medical Centers, location AMC, Amsterdam, The Netherlands.
[3] Computational Science Lab, Faculty of Science, Institute for Informatics, University of Amsterdam, Amsterdam, Netherlands.
[4] Department of Neurology, Erasmus MC University Medical Center, PO Box 2040, 3000 CA Rotterdam, the Netherlands.
[5] Department of Public Health, Erasmus MC University Medical Center, PO Box 2040, 3000 CA Rotterdam, the Netherlands.
[6] Department of Radiology, Erasmus MC University Medical Center, PO Box 2040, 3000 CA Rotterdam, the Netherlands.
[7] Laboratory for Thrombosis Research, KU Leuven Campus Kulak Kortrijk, Kortrijk, Belgium.
[8] Computer Science Department, University of Geneva, CUI, 7 route de Drize, 1227 Carouge, Switzerland.
[9] Faculty of Computational Mathematics and Cybernetics, Moscow.
[10] Laboratory of Experimental Medicine (ULB222), Faculty of Medicine, Université libre de Bruxelles, CHU de Charleroi, Belgium.
[11] Institut de Recherches Internationales Servier, Coubevoie Cedex, France.
[12] Department of Chemistry, Materials and Chemical Engineering 'Giulio Natta', Politecnico di Milano, Piazza Leonardo da Vinci 32, 20133 Milano, Italy.
[13] National Centre for Biomedical Engineering Science, School of Engineering, National University of Ireland Galway, Ireland.
[14] Cerenovus, Galway Neuro Technology Centre, Galway, Ireland.
[15] Department of Engineering Science, University of Oxford, Parks Road, Oxford OX1 3PJ, UK.

PORTFOLIO

Name PhD student: Theodosia Georgakopoulou
PhD period: July 2018 – April 2022
Names of PhD supervisor(s): A.G.J.M. van Leeuwen, H.A. Marquering
& co-supervisor(s): Dr. N.T.P. Bakker

1. PHD TRAINING

	Year	ECTS
General courses		
Cellular Imaging: Basic Microscopy	2018	1.6
Practical Biostatistics	2019	1.4
Didactical skills	2021	0.4
Specific courses		
Image J / Fiji	2018	0.6
Seminars, workshops and master classes		
TLC Masterclass Onderwijs/Opleiden	2021	0.2
TLC Masterclass Oog voor studentenwelzijn	2021	0.2
TLC Masterclass Zorg ICT, wat kun je ermee?	2021	0.2
TLC Masterclass Toetsen als een Aristoteles. Filosofisch oordelen voor beginners	2021	0.2
TLC Workshop: Toetsing - toetsvragen maken	2022	0.2
Presentations		
Cardiovascular Engineering meeting	2018-2022	4.0
All hands INSIST meeting, Oxford, United Kingdom	2018	0.6
WP5 INSIST meeting, Oxford, United Kingdom	2018	0.2
All hands INSIST meeting, Milan, Italy	2019	0.6
WP5 INSIST meeting, Amsterdam, Netherlands	2019	0.2
All hands INSIST meeting, Rotterdam, Netherlands	2019	0.6
WP5 INSIST meeting, Oxford, United Kingdom	2019	0.2
All hands INSIST meeting, Moscow, Russia (Virtual)	2020	0.6
WP5 INSIST meeting, Amsterdam, Netherlands (Virtual)	2020	0.2
All hands INSIST meeting, Galway, Scotland (Virtual)	2020	0.6
WP5 INSIST meeting, Oxford, United Kingdom (Virtual)	2020	0.2
All hands INSIST meeting, Virtual	2021	0.6
WP5 INSIST meeting, Amsterdam, Netherlands	2021	0.2
All hands INSIST meeting, Geneva, Switzerland	2021	0.6
All hands INSIST meeting, Amsterdam, Netherlands	2022	0.6
(Inter)national conferences		
Dutch Endothelial Biology Society (DEBS) meeting, Amsterdam, The Netherlands	2018	0.8
26th Congress of the European Society of Biomechanics ESB, Milan, Italy (poster)	2021	1.4
Other		
INSIST lecture series (Winterschool)	2021	0.8

2. TEACHING

	Year	ECTS
Lecturing		
Imaging the brain, Bachelor Psychobiology	2019-2022	2.0
Heart and Circulation, Master Cardiovascular Research	2018-2019	1.0
Tutoring, Mentoring		
-		
Supervising		
Master student – Medical Natural sciences, VU	2018	1.5
Bachelor student – Bachelor of Science in Medicine, VU	2018	0.5
Bachelor student – Bachelor Applied Physics, Haagse Hogeschool	2019-2020	2.0
Bachelor student – Bachelor Medical Natural Sciences, VU	2020	1.5
Bachelor student – Bachelor Biology Medical Laboratory Research, InHolland	2021-2022	2.0
Master student – Master Computational Science, VU-UvA	2021-2022	2.0
Other		
-		

3. PARAMETERS OF ESTEEM

	Year
Grants -	
Awards and Prizes -	

4. PUBLICATIONS

	Year
Peer reviewed Michailidou I, Jongejan A, Vreijling JP, Georgakopoulou T, de Wissel MB, Wolterman RA, Ruizendaal P, Klar-Mohamad N, Grootemaat AE, Picavet DI, Kumar V, van Kooten C, Woodruff TM, Morgan BP, van der Wel NN, Ramaglia V, Fluiter K, Baas F. Systemic inhibition of the membrane attack complex impedes neuroinflammation in chronic relapsing experimental autoimmune encephalomyelitis. Acta Neuropathol Commun. 2018 May 3;6(1):36. doi: 10.1186/s40478-018-0536-y. PMID: 29724241; PMCID: PMC5932802.	2018
van der Wijk AE*, Georgakopoulou T*, Majolée J, van Bezu JSM, van der Stoel MM, van Het Hof BJ, de Vries HE, Huveneers S, Hordijk PL, Bakker ENTP, van Bavel E. Microembolus clearance through angiophagy is an auxiliary mechanism preserving tissue perfusion in the rat brain. Acta Neuropathol Commun. 2020 Nov 17;8(1):195. doi: 10.1186/s40478-020-01071-9. PMID: 33203478; PMCID: PMC7671188. *Equal contribution • **Authors' contributions:** AEvdW, TG, ENTPB, PLH and EvB conceived and designed the experiments; TG and AEvdW performed the surgeries; AEvdW, JM, JSvB, AJvH, MMvdS performed in vitro experiments; AEvdW analyzed the data and wrote the manuscript; HEdV and SH contributed to discussion and ENTPB, EvB, TG and PLH contributed to editing of the manuscript. All authors read and approved the final version of the manuscript.	2020
Georgakopoulou T*, van der Wijk AE*, Bakker ENTP, van Bavel E; INSIST investigators. Recovery of Hypoxic Regions in a Rat Model of Microembolism. J Stroke Cerebrovasc Dis. 2021 Jun;30(6):105739. doi: 10.1016/j.jstrokecerebrovasdis.2021.105739. Epub 2021 Mar 23. Erratum in: J Stroke Cerebrovasc Dis. 2021 Nov;30(11):105967. PMID: 33765634. *Equal contribution • **Authors' contributions:** TG, AEvdW, ENTPB, and EvB conceived and designed the experiments; TG and AEvdW performed the animal surgeries; TG analyzed the data and wrote the manuscript; All authors contributed to editing of the manuscript and read and approved the final version of the manuscript.	2021
Georgakopoulou T, van der Wijk AE, Bakker ENTP, van Bavel E; INSIST investigators. Quantitative 3D analysis of tissue damage in a rat model of microembolization. J Biomech. 2021 Nov 9;128:110723. doi: 10.1016/j.jbiomech.2021.110723. Epub 2021 Sep 2. PMID: 34509910. • **Authors' contributions:** TG and EvB conceived and designed the experiments; TG and AEvdW performed the animal surgeries; TG and EvB analyzed the data; TG wrote the manuscript; All authors contributed to editing of the manuscript and read and approved the final version of the manuscript.	2021
Xue Y*, Georgakopoulou T*, van der Wijk AE, Józsa TI, van Bavel E, Payne SJ. Quantification of hypoxic regions distant from occlusions in cerebral penetrating arteriole trees. PLoS Comput Biol. 2022 Aug 5;18(8):e1010166. doi: 10.1371/journal.pcbi.1010166. Epub ahead of print. PMID: 35930591. *Equal contribution • **Authors' contributions:** TG, YX, SJP and EvB conceived and designed the experiments; TG and AEvdW performed the animal surgeries; YX performed the *in silico* experiments; TG and YX analyzed the data; TG and YX wrote the manuscript; All authors contributed to editing of the manuscript and read and approved the final version of the manuscript.	2022

Other Anne-Eva van der Wijk, Theodosia Georgakopoulou, Rob Steendam, Johan Zuidema, Peter L. Hordijk, Erik N.T.P. Bakker, Ed vanBavel. Overcoming barriers: microsphere extravasation for drug delivery in the rat brain. In preparation. • **Authors' contributions:** AEvdW, TG, ENTPB and EvB conceived and designed the experiments; TG and AEvdW performed the animal surgeries; AEvdW analyzed the data; AEvdW wrote the manuscript; All authors contributed to editing of the manuscript and read and approved the final version of the manuscript.	2022
Theodosia Georgakopoulou, Anne-Eva van der Wijk, Ed vanBavel, Erik N T P Bakker. Clearance of endogenous IgG through perivascular spaces in the brain following micro-occlusions. In Preparation. • **Authors' contributions:** TG, ENTPB and EvB conceived and designed the experiments; TG and AEvdW performed the animal surgeries; TG analyzed the data; TG and ENTPB wrote the manuscript; All authors contributed to editing of the manuscript and read and approved the final version of the manuscript.	2022

CURRICULUM VITAE

Theodosia Georgakopoulou werd op 5 juli 1984 geboren in Katerini, Griekenland. In 2003 begon ze met haar studie Civiele Techniek aan de Aristoteles Universiteit in Thessaloniki. Na het behalen van haar bachelor en master diploma heeft ze een periode als ingenieur civiele techniek in Griekenland gewerkt. In 2010 besloot ze naar Nederland te komen om verder te studeren in de Civiele Techniek. Gezondheidsredenen hebben haar ambities vertraagd en uiteindelijk een andere wending gegeven. Een foutieve diagnose van haar huisarts heeft haar getriggerd om naar de medische wereld over te stappen. Nadat ze binnen 9 maanden de Nederlandse taal heeft geleerd aan het Horizon College Alkmaar, is ze in 2013 begonnen met de bachelor Biomedische Wetenschappen aan de Vrije Universiteit van Amsterdam. In het laatste jaar van haar bachelor heeft ze stage gelopen bij het Center of Neurogenomics and Cognitive Research (CNCR) met als onderzoeksonderwerp de moleculaire basis van depressie. In 2016 begon ze aan haar master Neurosciences aan de Universiteit van Amsterdam. Tijdens deze master heeft ze twee stages gelopen, de eerste bij Amsterdam UMC, locatie AMC, waar ze gekeken heeft naar mogelijke therapeutische targets van multiple sclerose. Haar tweede stage heeft ze gedaan bij het Leids Universitair Medisch Centrum waar ze onderzoek deed naar de rol van bepaalde hersenreceptoren in het reguleren van slaap. In 2018 heeft ze haar master cum laude afgerond. Vanaf juli 2018 is ze begonnen met haar promotie op de afdeling Biomedical Engineering and Physics in het AMC, wat resulteerde in dit proefschrift. Sinds mei 2022 werkt ze als docent bij HBO Inholland.

DANKWOORD

Promotie is meer dan de verdediging van een proefschrift. Als PhD kandidaat ben je verantwoordelijk voor het bedenken van experimenten, inplannen van operaties, administratie bijhouden, en managen van het project. Naast operaties met proefdieren, data analyse, artikelen schrijven en publiceren, horen studenten begeleiden en lesgeven er ook bij. Een promotieonderzoek en alles dat daarbij hoort is altijd het resultaat van een teamprestatie. Voor dit werkstuk zijn mensen uit verschillende disciplines bijeengekomen om van mening te wisselen, ideeën te bedenken en creatieve oplossingen toe te passen. Sommige mensen hebben aan dit werk bijgedragen buiten hun besef, met hun lach, goed humeur en positiviteit. In mijn promotiereis ben ik obstakels en uitdagingen tegengekomen die ik uiteindelijk samen met jullie heb kunnen overwinnen. Ik wil bij deze iedereen bedanken voor haar/zijn inspanning, advies, tips, gesprekken, hulp en steun. Ik heb bewust gekozen om geen namen te benoemen zodat ik niemand vergeet. Nogmaals bedankt!